Characterizing Ocean Turbulence from Argo, Acoustic Doppler, and Simulation Data

KATHERINE MCCAFFREY
B.A., Applied Mathematics, University of Saint Thomas, 2009
M.S., Atmospheric and Oceanic Sciences, University of Colorado, 2011

A thesis submitted to the Faculty of the Graduate School
of the University of Colorado in partial fulfillment
of the requirements for the degree of
Doctor of Philosophy
in the Department of Atmospheric and Oceanic Sciences.
2014

Advisor: Baylor Fox-Kemper
Committee: Chris Fairall, Peter Hamlington, Levi Kilcher,
Julie Lundquist, Jeff Weiss

This thesis entitled:

Characterizing Ocean Turbulence from Argo, Acoustic Doppler, and Simulation Data

written by Katherine McCaffrey

has been approved for the Department of Atmospheric and Oceanic Sciences

Baylor Fox-Kemper

Peter Hamlington

May 2, 2014

The final copy of this thesis has been examined by the signatories, and we find that both the content and the form meet acceptable presentation standards of scholarly work in the above mentioned discipline.

Abstract

McCaffrey, Katherine (PhD, Atmospheric and Oceanic Sciences)
Characterizing Ocean Turbulence from Argo, Acoustic Doppler, and Simulation Data
Thesis directed by: Baylor Fox-Kemper, Assistant Professor, Department of Geological Sciences, Brown University, and the Cooperative Institute for Research in Environmental Sciences, University of Colorado at Boulder

Turbulence is inherently chaotic and unsteady, so observing it and modeling it are no easy tasks. The ocean's sheer size makes it even more difficult to observe, and its unpredictable and ever-changing forcings introduce additional complexities. Turbulence in the oceans ranges from basin scale to the scale of the molecular viscosity. The method of energy transfer between scales is, however, an area of active research, so observations of the ocean at all scales are crucial to understanding the basic dynamics of its motions. In this collection of work, I use a variety of datasets to characterize a wide range of scales of turbulence, including observations from multiple instruments and from models with different governing equations.

I analyzed the largest scales of the turbulent range using the global salinity data of the Argo profiling float network. Taking advantage of the scattered and discontinuous nature of this dataset, the second-order structure function was calculated down to $2000m$ depth, and shown to be useful for predicting spectral slopes. Results showed structure function slopes of $\frac{2}{3}$ at small scales, and 0 at large scales, which corresponds with spectral slopes of $-\frac{5}{3}$ at small scales, and -1 at large scales. Using acoustic Doppler velocity measurements, I characterized the meter- to kilometer-scale turbulence at a potential tidal energy site in the Puget Sound, WA. Acoustic Doppler current profiler (ADCP) and acoustic Doppler velocimeter (ADV) observations provided the data for an analysis that includes coherence, anisotropy, and intermittency. In order to more simply describe these features, a parameterization was done with four turbulence metrics, and the anisotropy magnitude, introduced here, was shown to most closely capture the coherent events. Then, using both the NREL TurbSim stochastic turbulence generator and the NCAR large-eddy simulation (LES) model, I calculated turbulence statistics to validate the accuracy of these methods in reproducing the tidal channel. TurbSim models statistics at the height of a turbine hub ($5m$) well, but do not model coherent events, while the LES does create these events, but not realistically in this configuration, based on comparisons with observations.

Each of the datasets have disadvantages when it comes to observing turbulence. The Argo network is sparse in space, and few measurements are taken simultaneously in time. Therefore spatial and temporal averaging is needed, which requires the turbulence to be homogeneous and stationary if it is to be generalized. Though the acoustic Doppler current profiler provides a vertical profile of velocities, the fluctuations are dominated by instrument noise and beam spread, preventing it from being used for most turbulence metrics. ADV measurements have much less noise, and no beam spread, but the observations are made at one point in space, limiting us to temporal statistics or an assumption of "frozen turbulence" to infer spatial scales. As for the models, TurbSim does not have any real-world forcing, and uses parameterized spectra, and coherence functions and randomizes phase information, while LES models must make assumptions about sub-grid scales, which may be inaccurate. Additionally, all models are set up with idealizations of the forcing and domain, which may make the results unlike observations in a particular location and time. Despite these difficulties in observing and characterizing turbulence, I present several quantities that use the imperfect, yet still valuable observations, to attain a better description of the turbulence in the oceans.

Acknowledgments

This dissertation was made possible by the National Oceanic and Atmospheric Administration's Earth Systems Research Laboratory (NOAA-ESRL) and the Cooperative Institute for Research in Environmental Sciences (CIRES) Graduate Research Fellowship. I am grateful for this funding, and for the opportunities that working with these institutes provided.

First and foremost, I want to thank my advisor, Baylor Fox-Kemper for his support through my PhD work. His advising was consistently helpful and encouraging to me. Despite the move across the country, Baylor continued to keep my progress as a priority and was always available and willing to help. I could not have asked for a better teacher and mentor!

Thanks are also due to Peter Hamlington who, in many ways, acted as my advisor while Baylor was at Brown, and the time spent in Hamlington Group meetings was invaluable. A large portion of the introduction to this dissertation was guided by the class notes from his fantastic Turbulence class. Thank you to my other committee members, Levi Kilcher, Julie Lundquist, Chris Fairall, and Jeff Weiss, who were always willing to meet, and were enormously helpful.

I also want to thank Gael Forget of the Massachussetts Institute of Technology for sharing his quality-controlled Argo float dataset and OCCA climatology, and the preliminary code for computing structure functions. Also, a huge thank you goes to Jim Thomson of the University of Washington and the Applied Physics Laboratory and his group for the use of their hard-earned data from the Puget Sound. Thanks also to Spencer Alexander of CU-Boulder Mechanical Engineering for running his LES model to the specifications I requested.

Contents

List of Tables

List of Figures

Chapter 1

Introduction

1.1 What is turbulence?

Turbulence is a fascinating phenomenon that has been studied for centuries, but is so complex that there still remains much to be understood about it. The state of being turbulent is defined by Merriam-Webster.com (2014) as:

a : great commotion or agitation,

b : irregular atmospheric motion especially when characterized by up-and-down currents,

c : departure in a fluid from a smooth flow.

Causing "great agitation" among fluid dynamicists since the 16th century, the chaotic and unpredictable nature of turbulence has been both the attracting and deterring factor in its study. With variations from a smooth flow occurring in both space and time over a large range of scales, turbulent flows occur in many different forms in the world we live. Beyond the most familiar atmospheric turbulence experienced by almost anyone who has flown in an airplane, turbulence is present in many applications including: boundary layers of vehicles, blood flow through arteries, internal combustion engine cylinders, wakes of air and sea craft, industrial emissions and pollution, and in the magnetic fields in the Earth's core or on the Sun.

A fluid is defined as turbulent in fluid dynamic terms when the Reynolds number is in the range

$$Re \equiv \frac{UL}{\nu} = \frac{(L/T)L}{\nu} = \frac{L^2/T}{\nu} \approx O(10^4 - 10^8), \tag{1.1}$$

where U, L, T, and ν, are the velocity, length, time, and molecular viscosity scales of the fluid (Pope, 2000). The Reynolds number is the ratio of the non-linear inertial to linear viscous effects, which determines whether the flow is dominated by viscosity and is therefore smooth and laminar (low Reynolds number), or dominated by inertia, and therefore is complex and turbulent (high Reynolds number). The complexity of turbulence is such that the flows span a range of length and time scales, from a largest, "outer" scale, δ, to the smallest "inner" scale set by the viscosity, λ_ν. The relationship between the two scales is set by the outer scale Reynolds number ($L = \delta$ in Equation 1.1) as $\delta/\lambda_\nu = O(10^{-1})Re_\delta^{3/4}$ (Pope, 2000). In the ocean, $\delta \sim 1000km$, and $\lambda_\nu \sim 1mm$, resulting in a range of more than *five* orders of magnitude (Jimenez, 1997).There is also a range of time scales in every turbulent flow, from a longest scale, $T_\delta \equiv \delta/u$, to the shortest scale, $T_\nu \equiv \lambda_\nu/u$. The ratio of longest to shortest time scales is also $T_\delta/T_\lambda = O(10^{-1})Re_\delta^{3/4}$, again resulting in a range of five orders of magnitude in the ocean.

However, most turbulent flows are not the same at all locations ($u = u(\mathbf{x})$, and $\delta = \delta(\mathbf{x})$), so the Re_δ becomes a function of the location in the flow, i.e. $Re_\delta = Re_\delta(\mathbf{x})$ (Pope, 2000). A flow is homogeneous when the statistics are the same in all locations in the flow, and a flow is isotropic when statistics are the same in all directions. Thus, the statistics of most turbulent flows (e.g. $\overline{u'^2}$, $\overline{v'^2}$, or $\overline{w'^2}$) are globally inhomogeneous and anisotropic. Turbulence can also be non-stationary, or changing on long time scales. Section 1.2 will discuss the importance of removing the slowly-changing signal to identify the turbulence that may be considered stationary. The non-stationarity, heterogeneity and anisotropy in turbulent flows contribute to their difficulty to observe, analyze, and predict.

The most commonly used method of analyzing turbulence comes from the seminal work of A.N. Kolmogorov (1941) (commonly referred to as "K41"). In this work, K41 makes three hypotheses. The first states that,

> *When looking at a small volume $L \ll \delta(x)$ with characteristic time dimension T much less than $\delta(x)/u$, the turbulence can be approximated as being locally homogeneous, isotropic, and stationary.*

The second states that,

> *In that small volume with characteristic dimension L and over the same short duration T, the turbulence will be essentially universal, depending only on the local values of the kinetic energy dissipation rate ε, the viscosity ν, and the spatial scale r (or wavenumber k).*

And the final hypothesis is that,

> *For r between the local inner and outer scales ($r < \delta(x)$ but $r > \lambda_k(x)$), the turbulence statistics become independent of ν and thus depend only on the dissipation rate ε and the scale r (or wavenumber k).*

Most turbulence theories that have followed K41 are based on this assumption of homogeneous, isotropic, stationary turbulence, with analyses of the kinetic energy spectrum, shown in Figures 1.1&1.2. This spectrum can be divided into sections as shown, with forcing at large scales (small k), dissipation at small scales (large k), and an inertial range where energy is neither created or destroyed, but simply transferred from large to small scales. The spectral slope, λ, of the inertial range in this forward energy cascade (commonly plotted on log-log axes) has been analyzed in laboratory experiments and found to support the K41 hypotheses (Gibson and Schwarz, 1963; Grant et al., 1962; Lumley, 1964).

Before the work of K41, and through observing and forecasting the weather, Lewis Fry Richardson (1922) spoke very eloquently:

Big whirls have little whirls that feed on their velocity,
    and little whirls have lesser whirls and so on to viscosity.

Following the foundational work of K41, subsequent work has shown that the turbulent cascade over an inertial range can also be applied to other isotropic, homogenous flows.

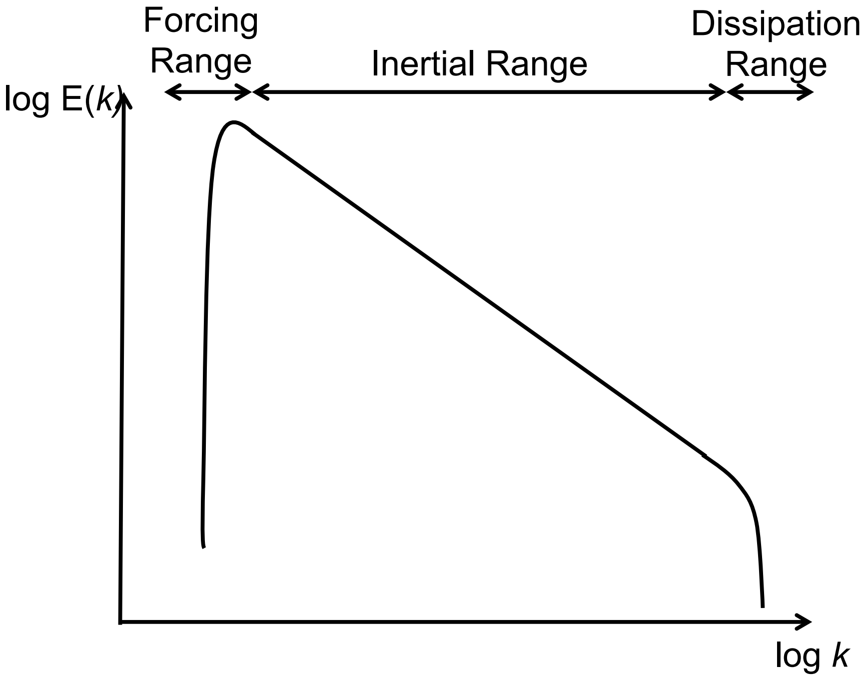

Figure 1.1: A schematic of a kinetic energy spectrum, with the forcing, inertial and dissipation ranges shown.

Obukhov (1949) and Corrsin (1951) theorized about the variance spectra of passive tracers in a three-dimensional flow. They found that a tracer will follow the same slope behavior as the kinetic energy spectrum that carries the tracer, with a spectral slope of $\lambda = -\frac{5}{3}$. Soon after, Batchelor (1959) predicted the tracer variance spectrum between the viscous scale, when energy is dissipated, and the diffusivity scale, where the tracer is dissipated. In this small scale, the now-called "Batchelor spectrum" follows a spectral slope of $\lambda = -1$. With a similar argument, Vallis (2006) showed that, in a flow dominated by one eddy-turnover time scale, the passive tracer spectrum has a forward cascade with slope of $\lambda = -1$. Research continues to investigate other turbulent regimes where spectral slopes can be expected to differ. The ocean itself has many different regimes, which will be introduced briefly below, and investigated further with observations in Chapter 2.

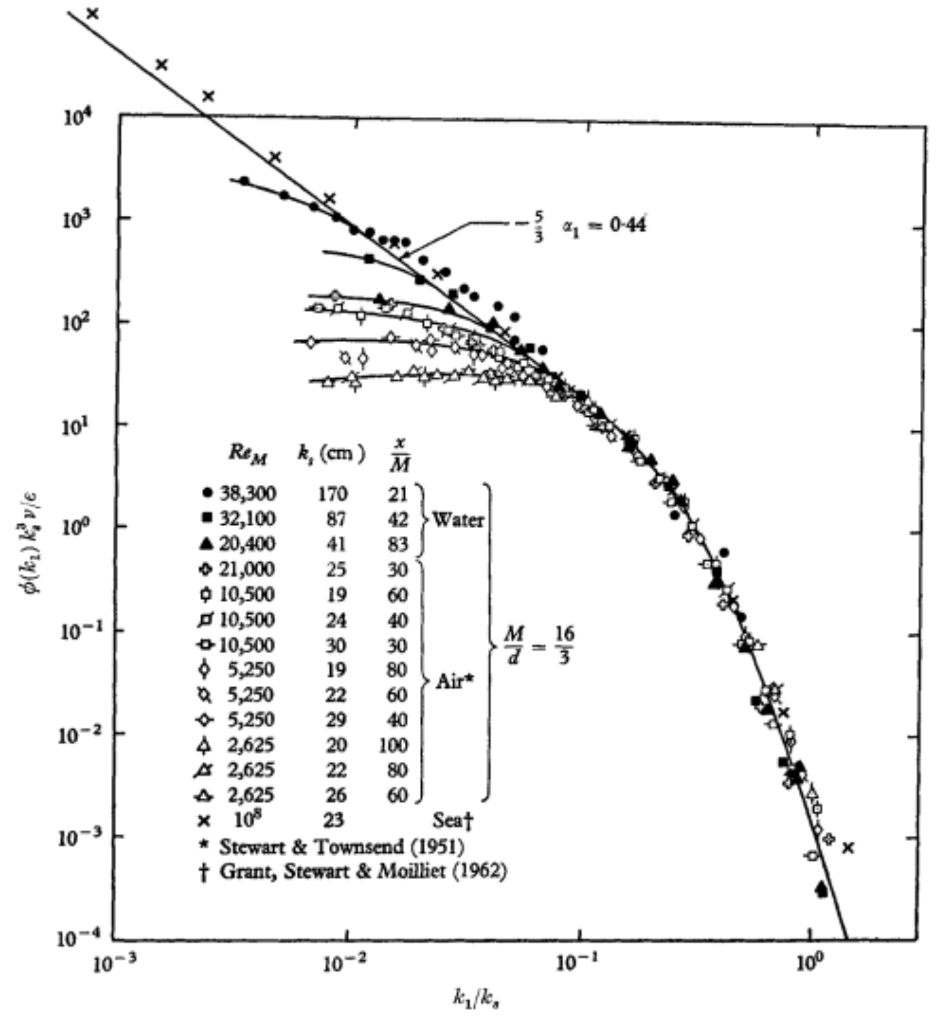

Figure 1.2: Normalized velocity spectra at differing Reynolds numbers, from Gibson (1963).

1.1.1 Geophysical Turbulence - Oceans

In many ways, the highly complex ocean is no different from the theoretical or laboratory flows that are more simple to analyze. It has the same basic kinetic energy spectrum, with forcing, inertial or transport, and dissipation ranges of motion. The ocean is forced at the largest scales by the temperature gradient between the unevenly-heated equator and poles (Stewart, 2004). Winds also provide forcing on the oceans by transferring momentum at the air-sea interface, and the gravitational and rotational forces of the Earth force tides and geostrophic currents. At the smallest scales, energy is dissipated at the molecular level through friction. In between, mesoscale and submesoscale eddies form the inertial range of turbulent motions. The spectral slope differs depending on the particular turbulent regime and forcings, and in certain regimes, can include an enstrophy (vorticity squared) cascade with different slopes. For example, in 2D turbulence, energy and enstrophy are both conserved, so there is also an enstrophy cascade that cannot overlap with the energy cascade, resulting in an inverse energy cascade with spectral slope of $\lambda = -\frac{5}{3}$ to large scales from a central wavenumber, and a forward enstrophy cascade with spectral slope of $\lambda = -3$ to small scales (Kraichnan, 1967). The ocean can sometimes be nearly 2D because stratification, rotation, and depth can limit vertical motions. Non-dimensional parameters, like the Rossby number which compares rotational and inertial forces ($Ro = U/fL$, where $f = \Omega cos\theta$ is the Coriolis parameter for rotation rate Ω and latitude θ) and the Prandtl ratio which compares rotation and buoyancy ($Pr = f/N$, where N^2 is the Brunt-Väisälä, or buoyancy, frequency), define regimes in the oceans when particular forces are important (or not) (Vallis, 2006). When horizontal scales are near the deformation radius ($L_R = \sqrt{gD}/f_0$, where g is the acceleration due to gravity, D is the water depth, and f_0 is the Coriolis parameter at a particular latitude) and thus horizontal motions are much larger than vertical ones, variations in f are small, Ro is small, the ocean is considered to be *quasi-geostrophic*. Charney (1971) showed that quasi-geostrophic motions are very similar to 2D, and therefore share the inverse energy cascade slope of $\lambda = -\frac{5}{3}$ and the forward enstrophy cascade with slope of $\lambda = -3$. The difference between 2D and QG is in the vertical boundaries in QG, as identified in Salmon (1980), and Blumen (1982) identified the surface-forced QG (surface quasi-geostrophy, or SQG) scenarios with an inverse energy cascade with spectral slope of $\lambda = -2$ and a forward temperature variance cascade with slope of $\lambda = -8/3$. Each of these predictions for spectral slopes is based on theory, and in many ways, the actual ocean is more complicated than the simplified theories, so observations are needed to answer which theory is correct, and if multiple theories' slopes are observed in different regions or ranges of scales, what the determining factors are.

1.2 Observing Ocean Turbulence

An analysis of the spectrum of turbulence in the oceans requires observations at many spatial and temporal scales. The largest spatial scales may be the easiest to observe with the use of satellites, while the smallest can only be observed in localized studies. The longest time scales are impossible to study since they are much longer than a human lifetime, but decadal scales are observable by satellites. The shortest timescales can again only be observed locally. Intermediate spatial and temporal scales are observed to varying degrees.

Observing turbulence requires a span of temporal and spatial scales of observations, so that mean and fluctuating components can be separated. The averages used for the statistical description can be temporal, spatial, or ensemble, depending on the nature of the problem at hand. From the average, a fluctuating value can be obtained, as in a Reynolds decomposition,

$$\mathbf{u} = \overline{\mathbf{u}} + \mathbf{u}', \tag{1.2}$$

where $\mathbf{u}$ is the full flow property (e.g., velocity or temperature), $\overline{\mathbf{u}}$ is the mean, and $\mathbf{u}'$ is the fluctuation (Pope, 2000). From this definition, it is also true that $\overline{\overline{\mathbf{u}}} = \overline{\mathbf{u}}$, and $\overline{\mathbf{u}'} = 0$.

When making observations of turbulent flows, the spatial and temporal sampling resolution as well as averaging intervals are not trivial. For a flow with a characteristic fluctuation time scale τ and outer time scale T, the averaging time interval, δt, used to remove the background state must satisfy $\tau < \delta t < T$. Similarly, the spatial averaging scale must be larger than the smallest length scale of the fluctuations and smaller than the forcing length scale. This requirement has two major implications: first, about the sampling resolution, and second, about the averaging scales. The sampling frequency of an instrument is often non-negotiable, so the appropriate instrument is needed for the desired information. For example, an acoustic Doppler current profiler (ADCP) has a sampling frequency of $O(1\ Hz)$, while an acoustic Doppler velocimeter (ADV) has sampling frequencies higher than 10 Hz (Nortek USA, LLC, 2014). The ADV can, therefore, measure smaller structures in the flow than an ADCP. For some applications, those small-scale fluctuations may be important, but for others, the lower resolution may be sufficient.

When choosing an appropriate averaging interval, an analysis of the scale separations is necessary. An example analysis done on ADCP velocity measurements from a tidal strait to illustrate this procedure. In decomposing the velocity signal into a temporal mean and perturbation, the goal is to capture the small-scale (in time and space) turbulent effects aside from the large-scale (in time and space) tidal effects. Taylor's "frozen turbulence" hypothesis of the relationship between the time and length scales is assumed, which assumes that the mean flow is slower than the turbulent flow, so, for a given mean velocity scale, u, the time and length scales of the turbulence are related directly to the mean velocity as $U \sim L/T$ (Taylor, 1938). This requires that, for turbulence at larger spatial scales, a longer time scale is needed to capture the motions, and vice versa. With a goal of capturing the large, coherent structures in the tidal flow, the largest δt possible is desirable. However, the tidal signal impacts the flow at longer time scales, so a careful analysis was needed to separate the two.

Figure 1.3a shows a 10.5-hour segment of velocities with different δt means, and Figures 1.3b and c show the resulting perturbations ($\delta t = 60, 30$, and 20 minutes in Figure 1.3b and $\delta t = 10$ and 5 minutes in Figure 1.3c). From these plots, it is clear that the 60, 30 and

20-minute averages are too long because a significant trend remains over the intervals where the tide is changing direction. That trend is therefore being included in the "turbulence," though it is actually the tidal signal.

The variance for each segment in the entire sample for different δt values was computed, and is shown in Figure 1.4. For the smallest values of δt, there are higher variances seen, with a decrease as δt increases to about $\delta t = 5$. Ignoring the outliers, the range of variances stays about constant until approximately $\delta t = 35$ when it increases again. Using this range of ideal δt values, as well as the information in Figure 1.3, the higher end of this range is known to be too large. Therefore, after this analysis, the interval length, δt, for the mean-perturbation decomposition was chosen to be 10 minutes. This captures the largest scales of turbulence without contaminating it with the tidal signal.

Unfortunately the availability of observations often forces averaging on inopportune scales. The global Argo dataset, for example, has large spatial coverage, but the closest floats are only $O(1-10km)$ apart, disabling the Argo floats from being used for any submesoscale observations. The following section introduces several examples of ocean turbulence observations, explaining how the available observations can be used, as well as their limitations.

1.2.1 Relevant Observations

Observations of ocean turbulence are largely limited to specific regions where a particular phenomenon is occurring. Global observations are fairly limited, with the exception of the recent Argo project (Argo Science Team, 1998). Typically global ocean observations are constrained to the ocean surface though the use of satellites. Localized observational campaigns involving autonomous gliders, floats, and tow-yos have been completed more extensively. An introduction to different turbulence characterization methods based on observations is done below with a selection of studies (an excellent review of similar observations can be found in Callies and Ferrari (2013)).

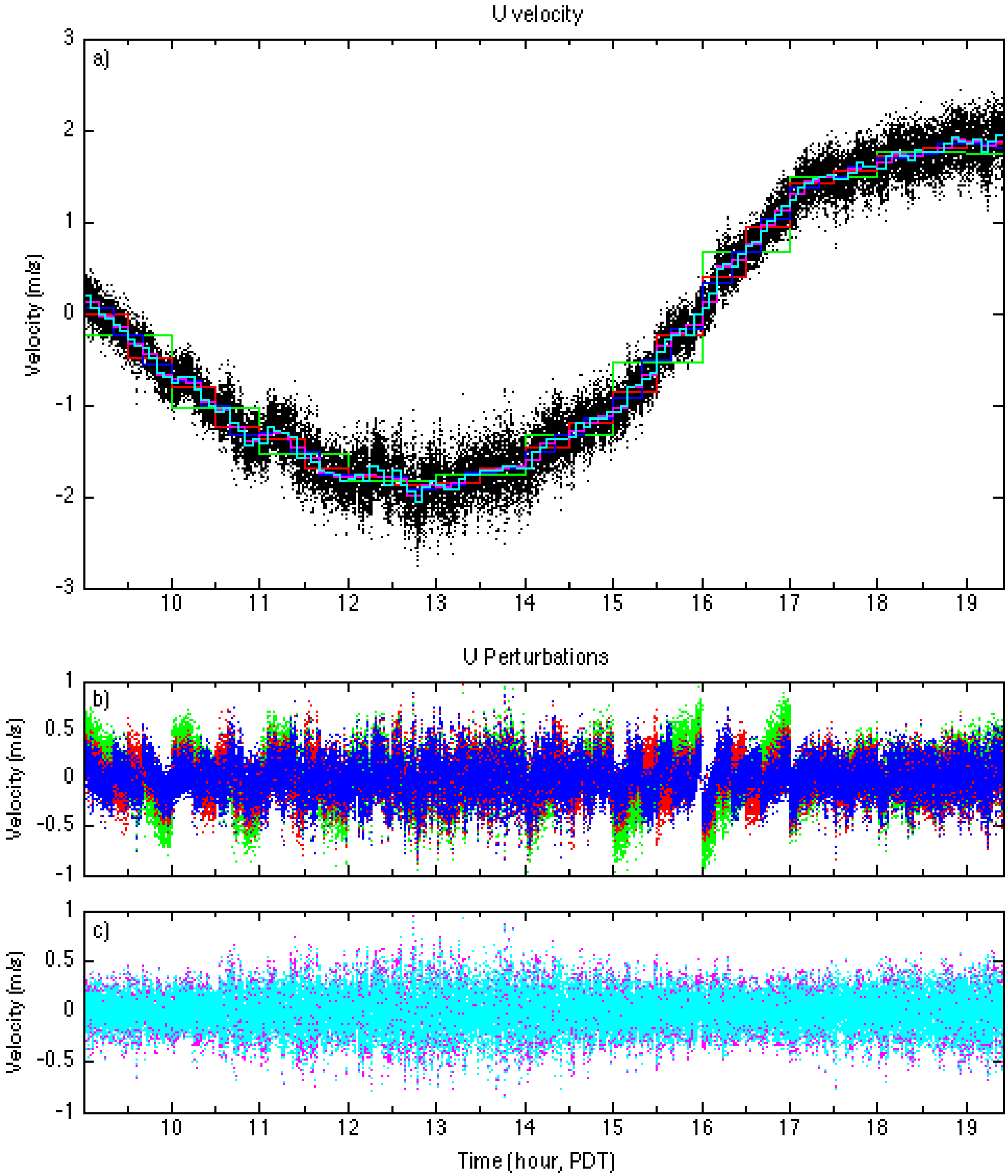

Figure 1.3: a) Velocity (black) over a 10.5-hour segment with averages shown in color: δt = 60-minute: green, δt = 30-minute: red, δt = 20-minute: blue, δt = 10-minute: magenta, δt = 5-minute: cyan. Perturbation from the mean are shown in b) and c) for $\delta t = 60,\ 30$ and $20min$, and $\delta t = 10$ and $5min$, respectively, with the same colors as a).

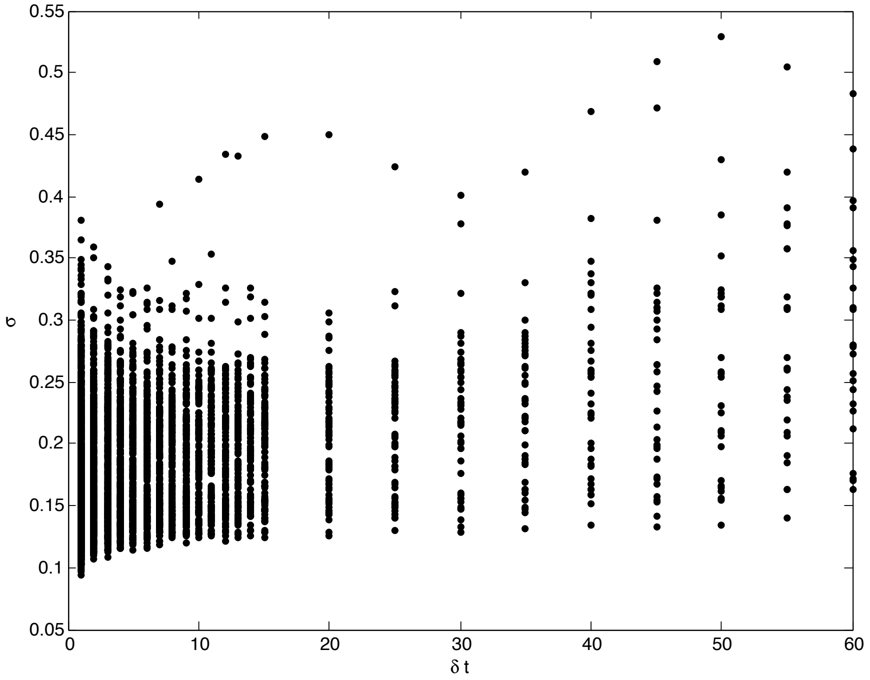

Figure 1.4: Variances for each segment with δt varying.

Global turbulence estimates from satellite data

Satellites provide a significant amount of information about the ocean surface with their repeated measurements over the entire globe. Satellite programs include sea-surface temperature (SST, e.g., *Aqua, Envisat*), sea-surface salinity (SSS, e.g., *Aquarius*), sea-surface height (SSH, e.g., *Jason 1* and *2*), ocean color for chlorophyll (e.g., *Aqua*), and sea-ice cover (e.q., *Aqua*) (JPL, 2014; NASA, 2014). From SSH, surface velocities can be computed, assuming geostrophy (motions balanced between the pressure gradient from SSH and rotation), and it is possible to infer turbulence quantities from other data like SST and SSS. Wunsch and Stammer (1995) used two years of TOPEX/POSEIDON altimetric measurements to calculate global wavenumber spectra (Figure 1.5). They calculated global maps of SSH variability from the data, which is obtained in each location on the Earth's surface every 10 days. In the along-track wavenumber spectra, they observed slopes of $\lambda = -5/2$ below the deformation radius and a shallower slope at larger scales, with errors possibly including the slope of $\lambda = -3$ of the enstrophy cascade. Scott and Wang (2005) also used SSH observations to

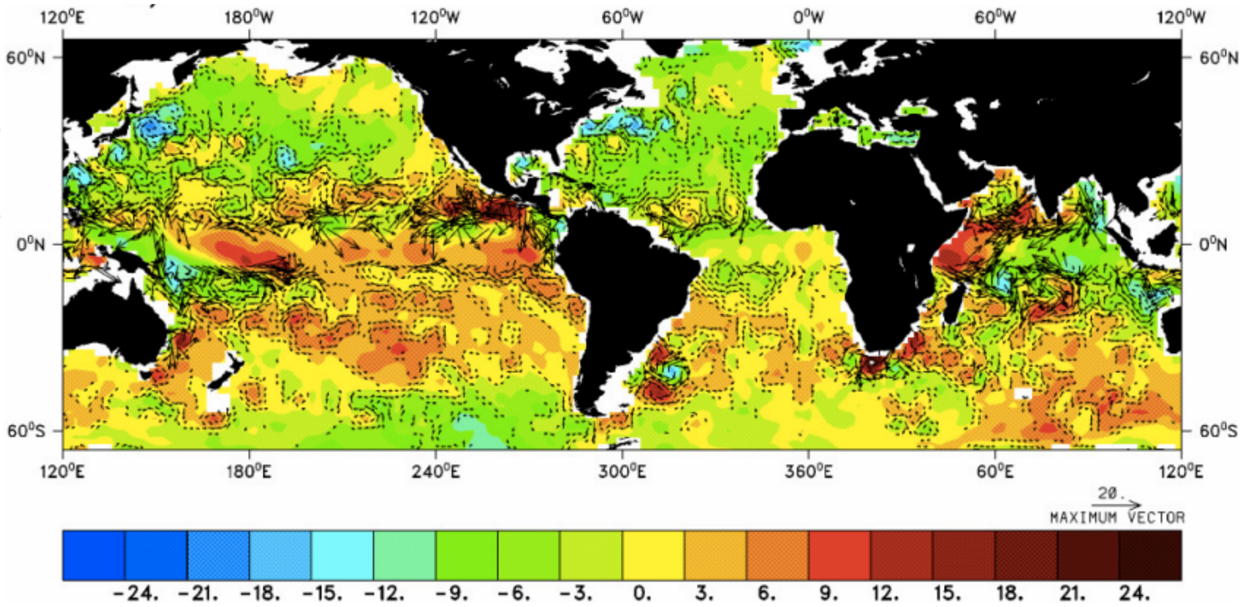

Figure 1.5: Figure 6b from Wunsch and Stammer (1995): Example of the anomaly of elevation $\eta' = \eta - \overline{\eta}$, relative to four-year mean $\overline{\eta}$ during one 10-day period (March 10-20, 1993). The geostrophic flow vectors corresponding to the elevation anomaly are superposed. Wavelengths shorter than about $500km$ have been omitted to permit some visual clarity. The actual anomaly field is far more complex and visually dominated by the omitted small scales.

analyze the two-dimensional energy cascade, seeing an inverse cascade, though it is limited to scales only just above the deformation radius. Using satellite data to gain information about ocean turbulence is very useful, but it gives no sub-surface information. Only recently have satellite altimetry spectra supported SQG (not QG) dynamics, which inform the subsurface (Le Traon et al., 2008). Also, spectra from altimetry measurements are limited by the assumption of geostrophy needed to obtain velocity from SSH, excluding all ageostrophic (i.e., turbulent) motions.

Regional turbulence estimates from gliders, floats, and tow-yos

Focusing on particular regions where interesting dynamics are known or predicted to occur can provide information to extend on larger scales. Wang et al. (2010) and Ferrari and Rudnick (2000) used ship-board ADCPs and towed instruments on transects between

New York and Bermuda, and in the subtropical North Pacific, respectively. Callies and Ferrari (2013) analyzed the data at scales smaller than $200km$ (submesoscale) from both campaigns and found spectral slopes indicating interior QG dynamics in the Gulf Stream region, while neither interior nor surface QG dynamics appear in the more quiescent tropical North Pacific. Cole and Rudnick (2012) also obtained more than two years of observations from an underwater glider in the central subtropical North Pacific, north of the Hawaiian islands. They investigated thermohaline fluctuations by computing spectra of salinity variations along constant density surfaces (isopycnals) between the scales of $15 - 1300\ km$. This creates a passive tracer cascade, since salinity and density are independent (temperature changes balance salinity changes to keep density constant). Their results showed spectral slopes of $\lambda = -1$ at the scales observed, and on isopycnals down to $25.8\ kg\ m^{-3}$. Another localized study in the North Atlantic used relative dispersion theory to predict the probability of the location of neutrally buoyant subsurface drifters over time (LaCasce and Bower, 2000). Their results shown evidence of an inverse energy cascade in the western basin, but not in the east. Klymak and Moum (2007) used a horizontally-towed vehicle equipped with a microstructure profiler in the Kauai Channel in Hawaii to measure turbulent dissipation rates, as well as spectra of pressure, isopycnal displacement, temperature, and isopycnal slope. This horizontal spectral information was compared to vertical measurements to quantify the Garrett-Munk internal wave spectrum (Garrett and Munk, 1972). Each of these observational campaigns was conducted with a slightly different purpose and instruments, highlighting the vast range of measurement techniques used for observing ocean turbulence. However, global coverage with these methods and instruments is unreasonable.

Local estimates of turbulence with acoustic instruments

Thomson et al. (2012) characterize of turbulence at two tidal energy sites in the Puget Sound, WA using ADCP and ADV data. With only the availability of a time series of observations at one point (ADV) or in a vertical profile (ADCP), Taylor's hypothesis is employed to gain spatial information from temporal data. This hypothesis requires that the turbulence is advected at a faster rate than it changes, so the time scales are directly proportional to the length and velocity scales ($L = UT$) (Taylor, 1938). The fractional turbulence intensity, or the intensity of turbulence at different spatial scales, is calculated by a change in variables from frequency to length scale in the horizontal velocity spectra (representative of the velocity variance at a particular scale), divided by the mean speed. Spectral slopes of $\lambda = -\frac{5}{3}$ were seen, with length scales of about $70m$ containing the most turbulence intensity at the Nodule Point location in the Puget Sound. With only a time series available, the only way to gather length scale information is through an assumption about the flow which may not be valid for all, if any, real-world tidal flows.

1.3 Modeling Ocean Turbulence

With the lack of observations to adequately characterize turbulence in many cases, numerical models are used to fill in the gaps in time and in space. Since the statistics of the energy spectrum are based on the large scale flow (δ and u), only the mean flow needs to be resolved and then turbulence statistics can be obtained from the large-scale motions (Kolmogorov, 1941). The goal of modeling is to predict, from solving particular mathematical equations, the future state of a flow based on specific initial and boundary conditions. The continuity and Navier-Stokes (NS) equations for fluid motion (Equation 1.3) are first ensemble-averaged (direct-numerical simulations compute the fully-resolved NS equations, but are extremely computationally expensive and not reasonable for flows with a large range of scales), in order to solve for the mean flow (Equation 1.4, called the Reynolds-Averaged Navier-Stokes, or RANS, equations).

$$\frac{\partial u_i}{\partial x_i} = 0; \; \frac{\partial u_i}{\partial t} = -u_j\frac{\partial u_i}{\partial x_j} - \frac{1}{\rho}\frac{\partial p}{\partial x_i} + \nu\frac{\partial^2 u_i}{\partial x_j \partial x_j} \tag{1.3}$$

$$\frac{\partial \overline{u}_i}{\partial x_i} = 0; \; \frac{\partial \overline{u}_i}{\partial t} = -\overline{u}_j\frac{\partial \overline{u}_i}{\partial x_j} - \frac{1}{\rho}\frac{\partial \overline{p}}{\partial x_i} + \frac{1}{\rho}\frac{\partial}{\partial x_j}\left[\mu\left(\frac{\partial \overline{u}_i}{\partial x_j} + \frac{\partial \overline{u}_j}{\partial x_j}\right) - \rho\overline{u_i'u_j'}\right] \tag{1.4}$$

(Pope, 2000). However, even the equations for the mean flow include higher-order terms (i.e., $\overline{u_i'u_j'}$) that prevent closure, so the biggest challenge in modeling turbulence is adequately representing the higher-order terms while obtaining a closed equation set to solve. Those higher-order terms are the turbulence that we want to most accurately capture, and extensive work is still being done to improve the methods of modeling this term. In many models, the gradient transport theorem is used, which relates the turbulent flux of a quantity ψ by the fluctuating component u_i' to the mean gradient of ψ by a proportionality constant diffusivity:

$$\overline{u_i'\psi'} = -D\frac{\partial\overline{\psi}}{\partial x_i}. \tag{1.5}$$

In the case of $\psi = u_j$, the diffusivity, D is equal to the eddy viscosity, ν_T. Several models predict the behavior of ν_T, including mixing-length theory models (Smagorinsky, 1963; Lomax and Baldwin, 1978), and $k-\varepsilon$ and $k-\omega$ models (Launder and Spalding, 1974). Without going into the details of these models, the important point is that whichever estimation of ν_T is used, the equation set is now closed, and can therefore be solved at all points in a chosen volume.

Another method of solving the NS equations is large-eddy simulations (LES). This method applies a low-pass filter to solve the NS equations at low computational cost. A sub-grid scale (SGS) model is then used for the smaller, unresolved scales. This method is based on the assumption that the most energetic eddies are the large ones, and that the smaller eddies receive their energy through the cascade, are independent of the flow geometry or forcing mechanisms, and can therefore by modeled (if the cut-off scale lies in the inertial range) (Moeng, 1984). The chosen parameterization scheme is much less sensitive than in the RANS model since only the small eddies are parameterized, as opposed to all of them. The most popular SGS model is that of Smagorinsky (1963), using a nonlinear eddy viscosity. Other SGS models include those of Germano et al. (1991); Bardina et al. (1980); Domaradzki and Saiki (1997), and Scotti and Meneveau (1999).

An additional way to solve the closure problem is to avoid it altogether and solve a different set of equations which use the statistical properties of the flow, instead of the physical ones. Since the kinetic energy spectrum is a statistical property that relies only on the first two moments (the mean and standard deviation), this can be the starting point for a stochastic turbulence model, such as the National Renewable Energy Laboratory's TurbSim model (Jonkman, 2009). Defining a spectral model, then computing an inverse Fourier transform can provide the velocity perturbations to be added to a more basic mean flow. This method is very simplified, making it very computationally cheap, but it also misses strongly coherent or intermittent features of flow that may be important (Mücke et al., 2011). The work herein includes an analysis of both a stochastic-turbulence generating model and LES, with the aim of understanding which model more accurately creates turbulence that can be relied on.

1.4 Why is ocean turbulence important?

The global ocean energy budget is not fully understood, but is important for many reasons, a sampling of which are presented here. First, the role that the oceans play in determining the global climate is paramount. Nearly half of the sun's radiation is absorbed by the oceans, and, with its large heat capacity, a great deal of it gets mixed deeper by the winds and transported poleward as part of the "global conveyor belt" of ocean circulation (Broecker, 1991; Stocker et al., 2013). Trenberth and Solomon (1994) estimated the amounts of heat transported northward (Figure 1.6) in each basin, but with very large error bars. The amount of energy that gets transported by the main global circulation is determined by the amount of eddy activity and energy transfer to smaller scales, and ultimately dissipated. The locations where large and small amounts of energy exist determine the climatological properties of the Earth. With the current changes to global climate that we are seeing, it is becoming increasingly important to understand the mechanisms behind how the ocean's

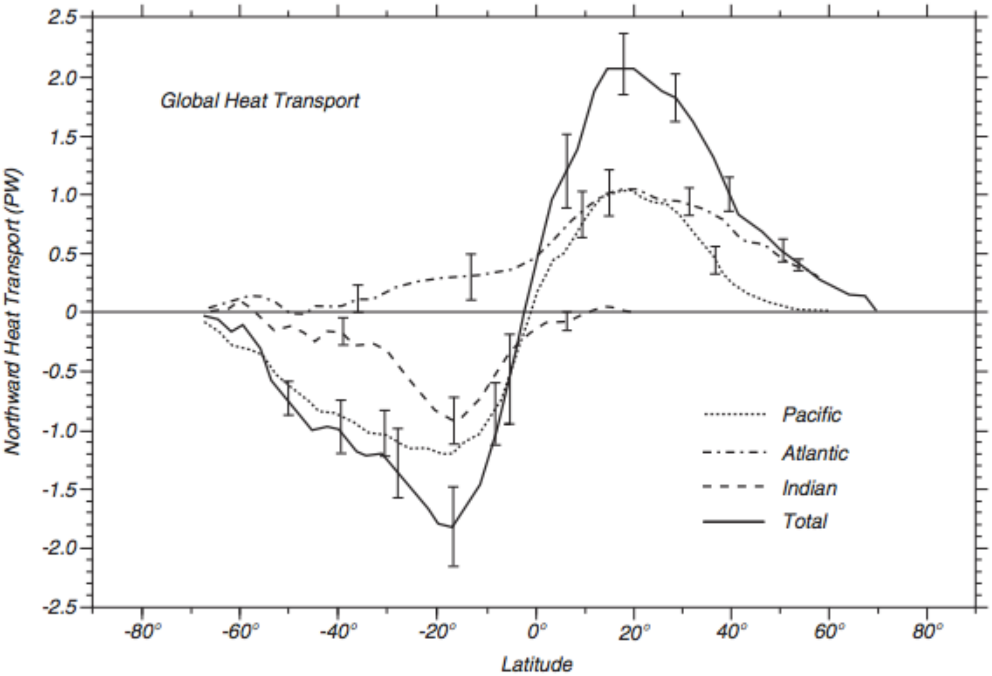

Figure 1.6: The poleward ocean heat transports in each ocean basin and summed over all oceans (total), as computed from the net flux through the ocean surface, integrated from 65N and adjusted south of 30°S, for 1988 (Trenberth and Solomon, 1994).

heat is transported (i.e., by turbulence) in order to continually improve global climate models (GCMs). A more complete understanding of the ocean will allow models to predict future states with better precision. For this reason, many studies have set out to determine the spectral behavior of the energy transfer between large and small scales from observations in different locations in the oceans. With the knowledge of the rates of forcing, transfer, and dissipation, GCMs can more accurately parameterize the smaller scales of turbulence that they cannot resolve, and the greater number of observations allows for better model validation and reliability.

Another important reason for studying ocean turbulence that drives parts of this research is the usage of ocean energy for power generation. Much like the strong winds in parts of the world, there are ocean currents that surpass 1 $m\ s^{-1}$, which, with the density of water 1000× that of the air, can produce substantial amounts of energy (O'Rourke et al., 2010). Marine renewable energy comes in four main types: ocean thermal, wave, tidal, and ocean current

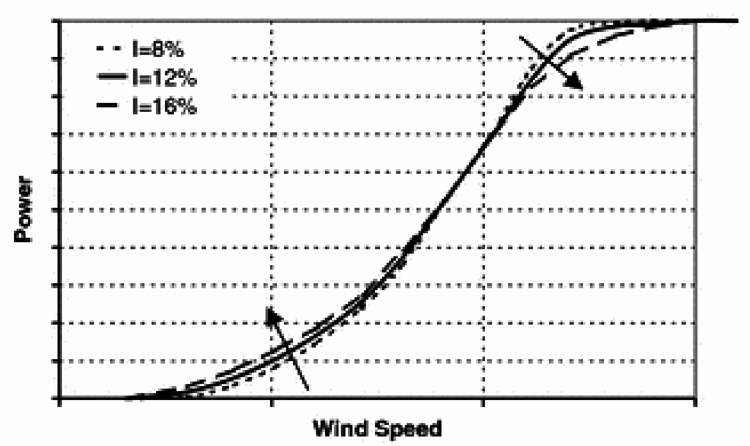

Figure 1.7: General behavior of the wind power curve with changes in turbulence intensity (Figure 28.1 from Kaiser et al. 2007).

energy conversion (the 3 later forms are marine hydrokinetic, or MHK, energy sources). The focus of the research here will be tidal energy conversion. Turbulence plays an important role in the generation of power through its impacts on a turbine and the mean flow (Legrand, 2009). In some cases, a fast flow with strong turbulence may be less desirable than a slower flow with weaker turbulence. The importance of turbulence effects on wind turbines is becoming increasingly appreciated as experience increases. Intense coherent turbulent structures can be structurally harmful to turbines, can decrease the capacity to generate power, and can increase the overall cost of power production. Elliott and Cadogan (1990), Kaiser et al. (2007), and Rareshide et al. (2009) showed that increased turbulence intensity decreases the power generated by a turbine at high wind speeds and slightly increases it at low wind speeds (Figure 1.7). Sutherland (2002), Frandsen et al. (2007), and Mücke et al. (2011) quantified the loading response of the turbine to turbulent flows, showing increased loads that decrease the lifetime of the turbines. With increased observations and improved numerical models, more specific features (e.g., size, shape, frequency) and their impacts on power generation can be better understood.

There are, of course, many other interesting problems inside the realm of ocean turbulence, but the applications presented above are the ones motivating the work in the following chapters of this dissertation. I set out to answer these questions, with a collection of observations and models as my tools. Each of the tools has its disadvantages and cannot do a complete characterization on its own, but much useful information can be gained from the imperfect data nonetheless.

Chapter 2

Observations of Macro-turbulence from the Global Argo Profiling Float Network

Since the global coverage of satellite observations is limited to the surface of the oceans, the Argo global network of subsurface floats is providing the very first observations on a global scale down to $2000m$. This groundbreaking dataset opens the doors for much greater understanding of the large-scale circulation, and the growing density of data coverage will extend the information to smaller scales as time passes. Only one study, by Roullet et al. (2013), has used Argo data for turbulence, introducing the second moment of the potential density probability density function as a diagnostic of mesoscale turbulence. This chapter will analyze large-scale turbulence with the global coverage of the Argo profiling float dataset, using methods proven to characterize turbulence in the atmosphere. This work introduces a new method that can be used for GCM validation, providing more than just the point comparisons at depth that Argo provides, but addressing the turbulent motions as well. The contents of the chapter have been submitted for publication in the Journal of Physical Oceanography (McCaffrey et al., 2014a & b).

2.1 Observations from Argo Profiling Floats

The large, and ever-increasing, spatial and temporal extent of Argo's dataset provides an unprecedented tool for observing the large-scale ocean circulation and global changes, as well as providing the observations needed to validate GCMs. The temporal resolution of the Argo float network also provides greater accuracy for climatologies and data re-analysis products which use any observations available and, with the use of dynamical models, interpolate to cover the entire globe (Kanamitsu et al., 2002). One such example of a climatology utilizing the extensive Argo float network is the Ocean Comprehensive Atlas, or OCCA, climatology of Forget (2010). Having a high-quality climatology allows for a better understanding of anomalous events in the oceans, like a hurricane which mixes and de-stratifies the ocean as it passes. When investigating the approximate re-stratification time for the ocean mixed layer after a hurricane has passed, scalings are needed based on the differences of the temperature between the wake and the surrounding waters, as well as the mixed layer (restratification) depth. The OCCA climatology, using Argo, provided the climatological temperatures under non-hurricane conditions for use in calculating the depth to which the mixed layer needs to re-stratify (see Appendix B and Haney et al. (2012)).

The Argo profiling float network was organized in 2000 from a less consolidated set of floats, and has been increasing in float density since (Argo Science Team, 1998). With more than 3500 floats routinely measuring the oceans down to $2000m$, the oceans are being observed in much greater detail than ever before. The Argo float network provides temperature, salinity and pressure measurements around the world, as seen in Figure 2.1. Each Argo float descends to $1000m$, where it drifts for 9 days until descending to the full $2000m$. As it ascends to the surface, the temperature and salinity profile is recorded, and then transmitted to a satellite. Near-real time observations are then made available, as well as a quality-controlled dataset after analysis. For more detail on the observational methods and instrumentation, please see Argo Science Team (1998).

The availability of such a large number of observations down to $2000m$ allows an inves-

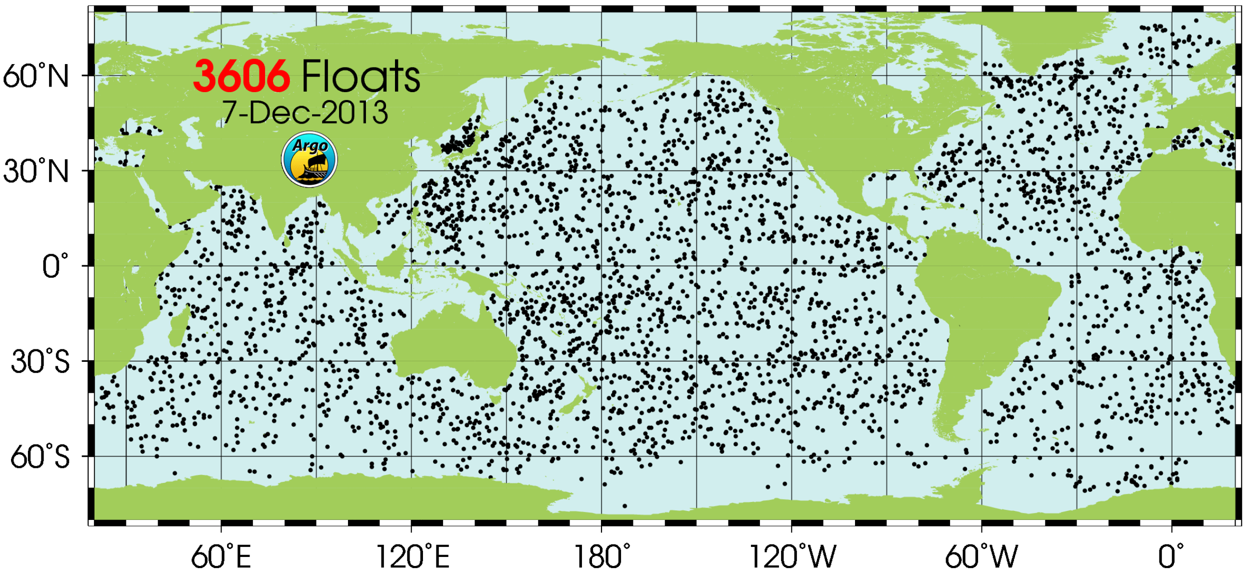

Figure 2.1: The locations of all 3606 operating Argo floats on 7 December 2013. *http : //www.argo.ucsd.edu/*

tigation of previously indescribable processes. The measurements from Argo floats span a large range of scales, from $O(10km)$ to $O(1000km)$, allowing analysis of temperature and salinity in a spectrum over that range. Unfortunately, traditional spectral analysis by Fourier methods requires continuous measurements in time and space, which are very rare in the ocean (Ferrari and Rudnick, 2000; Klymak and Moum, 2007; Cole and Rudnick, 2012; Callies and Ferrari, 2013). The structure function analysis of Frehlich and Sharman (2010b) introduced a method of calculating spectral slopes from rawinsonde (weather balloon) data. This method used second-order horizontal structure functions of temperature and velocity from randomly spaced rawinsonde profiles, and inferred spectral slopes that matched the results of the previous spectral analysis of Nastrom and Gage (1985) in the atmosphere. With Argo floats taking randomly spaced vertical profiles, analogous to a balloon in the atmosphere, here, we apply the rawinsonde method to the extensive Argo dataset to investigate the spectral behavior of the oceans.

2.2 Structure Function Analysis

Here, and in Appendix C and McCaffrey et al. (2014), I introduce the method of using structure functions from Argo data to characterize large-scale turbulence. Utilizing the available salinity observations from Argo, the second-order salinity structure function (Equation 2.1) was calculated in locations varying in depth, latitude, basin, and eddy activity:

$$D_S(\mathbf{s}, \mathbf{x}) \equiv \overline{[S'(\mathbf{x}) - S'(\mathbf{x}+\mathbf{s})]^2} \rightarrow D_S(s) = \overline{[S'(x) - S'(x+s)]^2}, \tag{2.1}$$

where S' is salinity perturbation from a mean, $\mathbf{s}$ is the separation distance vector between simultaneous observations, and $\mathbf{x}$ is the location vector, and the overbar represents an average over x and time (Kolmogorov, 1941). The OCCA monthly-mean climatology was chosen as the background state to determine the fluctuating component of the salinity. A monthly mean was chosen to eliminate the large-scale forcing of the annual cycle but keep the faster, turbulent scales. As discussed in Chapter 1, the choice of averaging intervals is critical to an accurate description of the ocean's turbulent flows. With the sparse Argo floats, the structure function, which is an average in space and time, acts to smooth over the scales smaller than the intervals. The spatial averages in the structure function are determined by the assumptions of stationary, homogeneous, isotropic turbulence which is the basis for the power-law scalings of theoretical turbulence (Kolmogorov, 1941). The assumption of homogeneous turbulence allows averaging over all locations (i.e., $D(\mathbf{s}, \mathbf{x}) = D(\mathbf{s})$), and isotropy allows averaging over all directions (i.e., $D(\mathbf{s}) = D(s)$). The time averaging intervals for stationarity, however, require special attention when using Argo data. For the structure function average, the time differences between observations also needed to be accounted for. Only very few Argo floats measure at the exact same time, so a limit was set, dependent on an advection velocity of ocean signals and the distance between measurement locations. I experimented with the limiting velocity and determined that $1m\ s^{-1}$ - a speed faster than most ocean currents - maintained the structure function slope of the faster velocity (which

Reference	Theory	λ	γ
Obukhov (1949), Corrsin (1951)	Passive or active tracer cascade in energy cascade	$-\frac{5}{3}$	$\frac{2}{3}$
Batchelor (1959), Vallis (2006)	Passive tracer cascade in enstrophy cascade or other single dominant timescale	-1	0
Klein et al. (1998)	Surface frontogenesis active or passive tracer cascade	-2	1

Table 2.1: Several theories of spectral slope, λ, and structure function slope, γ, for different turbulent regimes.

allowed more observations, but may include subsequent profiles from the same float, or the same eddy sampled multiple times), but was smoother than a slower velocity, which drastically decreased the number of pairs entering the average.

Assuming a homogeneous, isotropic turbulence spectrum with power-law behavior over a range of wavenumbers, then a related scaling law for the structure function is expected (Webb, 1964). If the power law of the salinity spectrum is given by $B(k) = \alpha_B k^{\lambda}$, with spectral slope, λ, the structure function will also have a polynomial form: $D_\theta(s) = c_D s^{\gamma} + C_0$ with structure function slope, γ, and a constant C_0 representing contributions from other portions of the spectrum not adhering to the $B(k) = \alpha_B k^{\lambda}$ law (shown to be negligible in Webb (1964)). The relationship between the two slopes is

$$\gamma = -\lambda - 1. \tag{2.2}$$

In the case when two discernible spectral slopes are present, the equivalent structure function can be written as

$$D_\theta(s) = c_1 s^{\gamma_1} + c_2 s^{\gamma_2}, \tag{2.3}$$

where the relationship in Equation 2.2 applies to γ_1 at small scales (large wavenumber), and γ_2 at large scales (small wavenumber) (McCaffrey et al., 2014).

As introduced in Section 1.1.1, several theories of spectral and structure function slopes exist, so the goal of this study is to identify which theory, or theories, may describe the behavior in the regions analyzed. See Table 2.1 for a summary of these theories. The behavior of active tracers varies from those of passive tracers, so structure functions were calculated along both isobars and isopycnals, distinguishing between the active and passive tracer behavior of the oceans. We compared structure functions varying in depth, latitude, eddy activity, and basin to determine the dependence on physical properties of the flow.

2.3 Structure Function Results

The full results are included as Appendix C and McCaffrey et al. (2014a), but the major findings are summarized here. Unfortunately the assumption of homogeneity that underlies each of these turbulent theories is seen to be mostly untrue. Salinity variance, defined as the average difference squared between the OCCA climatology and the Argo observations, $\overline{(S_{OCCA} - S_{Argo})^2}$, was calculated and mapped along constant pressure and density surfaces, and is shown in Figure 2.2a and b, respectively. (Figure 3 in McCaffrey et al. (2014) maps the depth of isopycnals to show that steep isopycnal slopes exist in some locations.) "Homogeneous" regions were chosen along the $5m$ isobar (solid line in Figure 2.2a) and the 25.9 $kg\ m^{-3}$ isopycnal (2.2b) for a comparative analysis, with homogeneity defined as a difference in salinity variance of less than two orders of magnitude (shown on Figures 2.2a & b, with subplots showing variance in the region). The resulting structure functions in the homogeneous regions were compared to those in strongly heterogeneous regions (like the dashed box in Figure 2.2a) in order to assess the importance of this assumption.

The homogeneous region chosen on the isobar of $5m$ was in the Kuroshio current region of the northwest Pacific Ocean (defined in Appendix A of McCaffrey et al. (2014a)). The region spans scales up to 4000 km, and contains 7000 salinity profiles (though only $O(1000)$ pairs are "simultaneous"). Figure 2.3a shows the salinity structure functions on isobars from the surface ($5m$) to $2000m$. At small scales, below about 200 km, a slope of $\gamma = \frac{2}{3}$ is seen, with slopes of $\gamma = 0$ at larger scales. This slope behavior is constant with depth,

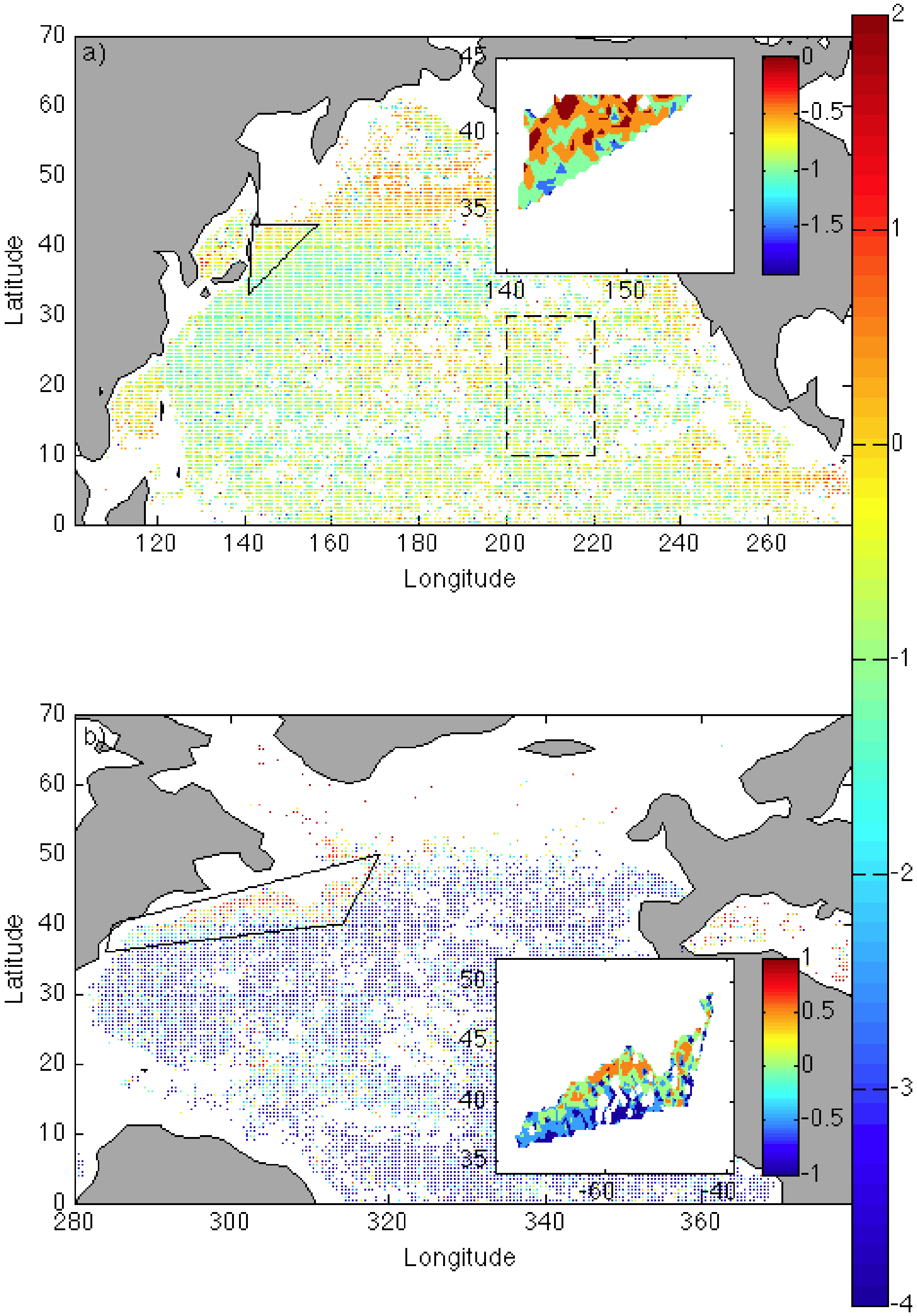

Figure 2.2: The log of salinity "variance" at (a) $5m$, where the homogeneous region of the Kuroshio (solid line) was chosen and analyzed in Figure 2.3, and (b) at 25.8 $kg\ m^{-3}$, where the homogeneous region of the Gulf Stream was chosen and analyzed in Figure 2.4. The heterogeneous region analyzed in Figure 2.5 is shown in the dotted line in a). Subplots show the variance in each region, with the color bars spanning only 2 orders of magnitude.

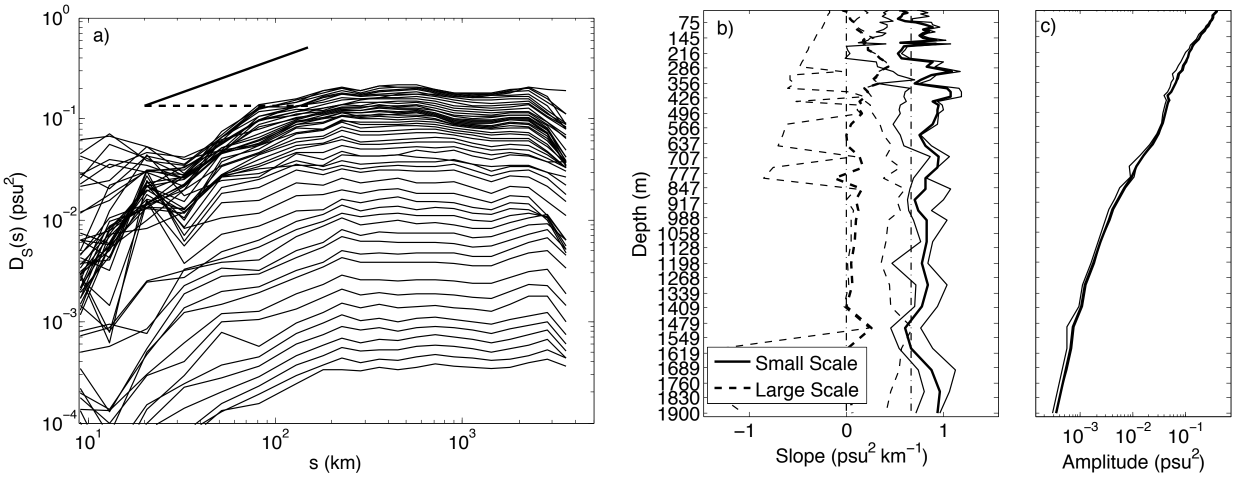

Figure 2.3: Salinity structure function, $D_S(s)|_p$, (a) in the Kuroshio uniform variance region at depths from $5m$ (top-most line) to $2000m$ (bottom-most). The slopes of the small scale (solid) and large scale (dashed) fit lines (b), and the amplitude (c) is plotted with depth in pressure in meters. A 95% bootstrap interval is also shown in thin lines in (b) and (c) for slopes and amplitude.

as seen in Figure 2.3b. However, the amplitude of the structure functions decreases with increasing pressure, with a fairly constant mixed layer at the surface to 75 km (Figure 2.3c). Because this region is homogeneous, it is reasonable to infer the spectral-structure function relationship. These slopes are consistent with the slopes predicted by Obukhov (1949) and Corrsin (1951) for the active tracer cascade in the energy cascade at smaller scales, with a spectral slope of $\lambda = -\frac{5}{3}$. The large-scale slope of $\gamma = 0$ is not predicted by any theories, but a random signal has a slope of 0 (see the appendix in Appendix C), which suggests that above 200 km, the salinity signal is noise.

Along the 25.8 $kg\ m^{-3}$ isopycnal, the homogenous region was chosen in the northwest Atlantic, near the Gulf Stream current (defined in Appendix A of McCaffrey et al. (2014a)). The region spans scales up to 3500 km, and contains 6000 salinity profiles (though fewer than 1000 pairs are "simultaneous"). The isopycnal salinity structure function, shown in Figure 2.4a, exhibits different behavior from the isobaric structure functions at small scales. The large-scale slope of $\gamma = 0$ is seen on all isopycnals, but at small scales, a slope is often not discernible. This may be a result of a smaller number of observations in that region at small scales (see large confidence intervals on Figure 2.4b). There is similar depth dependence along isopycnals as isobars, with the structure function amplitude decreasing with increasing density below a constant mixed layer down to 26.4 $kg\ m^{-3}$. Again, since this region is considered homogeneous, the spectral slope is inferred from the structure function. The slopes for the isopycnal structure function are consistent with the theories of Obukhov (1949) and Corrsin (1951) for the passive tracer cascade in the energy cascade, with a spectral slope of $\lambda = -\frac{5}{3}$. This is consistent with the slopes seen in the isobaric structure functions as well. The large-scale slopes of $\gamma = 0$ are consistent with the theory of Vallis (2006) for a passive tracer cascade in the case when stirring is done by the largest eddies, and the flow is dominated by a single timescale of those eddies, producing a forward enstrophy cascade above the largest length scale where $\lambda = -1$. It is worth noting that only the bottom 4 structure function lines are along isopycnals that exists all year. In this region, the 27.4 $kg\ m^{-3}$ isopycnal reaches the surface in the wintertime. There is no discernible difference between the structure functions of salinity along the isopycnals that do and do not outcrop each year.

Once the assumption of homogeneity is no longer valid, like between 10-30N and 140-160W in the Pacific Ocean where there is a large variation in salinity variance, the spectral slope cannot be inferred from the structure function slope, but the structure function must be used on its own as a statistic. The comparison between the depth dependence of the isobaric and isopycnal structure functions then becomes an interesting study to identify the effect of internal waves in the structure function (Figure 2.5). Since internal waves are fluctuations of isopycnals, following an isopycnal removes that signal, thus removing internal waves from the isopycnal structure function. Both isobaric and isopycnal structure functions have a slope of $\gamma = \frac{2}{3}$ at the surface at all scales. However, deeper, the isobaric structure functions flatten out to $\gamma = 0$ at large scales, with small scales steeper than $\gamma = 0$ but shallower than $\gamma = \frac{2}{3}$. Only the deepest isopycnal slopes flatten out to $\gamma = 0$, while most remain shallower than $\gamma = \frac{2}{3}$. The uniform behavior across all scales in the isopycnal structure functions

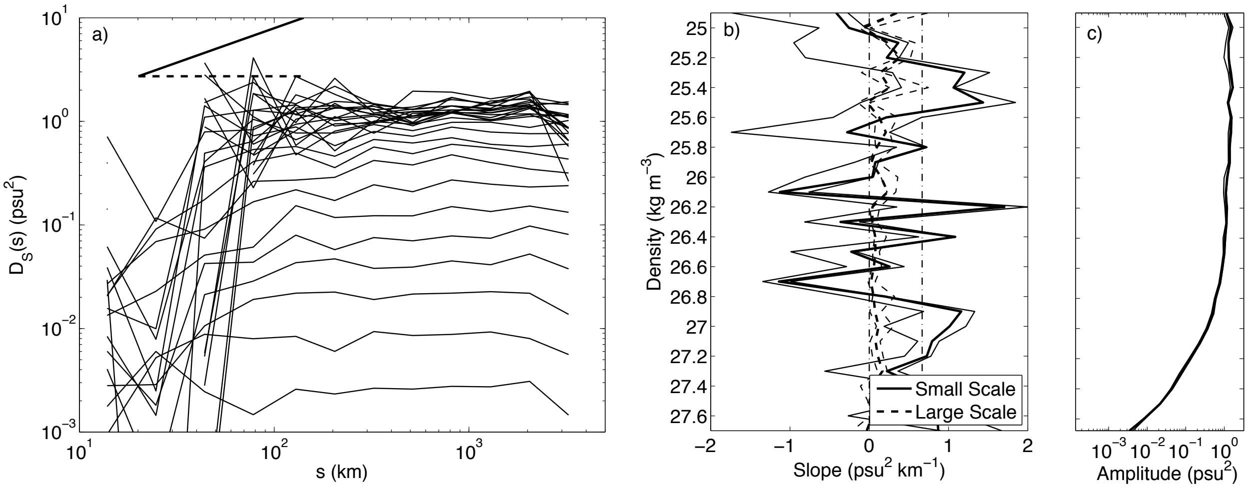

Figure 2.4: Salinity structure function, $D_S(s)|_\sigma$, in the Gulf Stream uniform variance region at densities 24.4 $kg\ m^{-3}$ to 27.8 $kg\ m^{-3}$, binned by 0.1 $kg\ m^{-3}$. The slopes of the small scale (solid) and large scale (dashed) fit lines (b), and the amplitude (c) is plotted with depth, with pressure in meters on the left axis and the average density on the right. A 95% bootstrap interval is also shown in thin lines in (b) and (c) for slopes and amplitude.

makes sense since there is no dominant length scale in the heterogeneous region. However, the internal waves impose a length scale on the isobaric structure functions, giving them the slight difference seen between small- and large-scale slopes.

When comparing structure functions on pressure and potential density surfaces, the flat slopes of the isopycnals may be misleading. It may seem that the isopycnal structure functions are flat due to atmospheric noise, like the isobaric structure functions above the dominant forcing scale. However, the flattening of the deeper isopycnals suggests that there is a different mechanism at work there from the isobaric structure functions. The mixing of passive and active tracers identifies this difference, as described in Vallis (2006).

The latitude dependence of the structure functions along isobars and isopycnals was also analyzed. Latitude is hypothesized to affect the structure function by changing the largest small-scale slope according to the Rossby deformation radius, which decreases with the sine of latitude (Chelton et al., 1998). Additionally, geographical features like subtropical or subpolar gyres vary with latitude. Figure 2.6 shows the structure functions along isobars

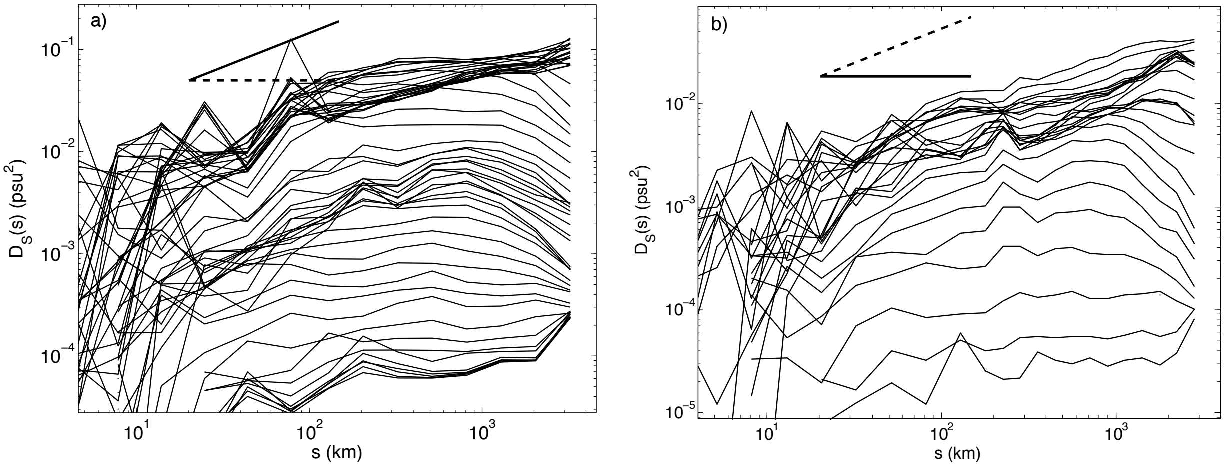

Figure 2.5: Salinity structure functions, $D_S(s)$, between 10-30N and 140-160W in the Pacific Ocean (a heterogeneous region with high and low salinity variance) on (a) pressure surfaces $(5 - 2000m)$ and (b) density surfaces $(25.1 - 27.7\ kg\ m^{-3}$, the isopycnals that persist all year). Bold reference lines show a slope of $\gamma = \frac{2}{3}$ (solid) and 0 (dashed).

at $5m$ (top left) and $1900m$ (top right), and isopycnals at 25.8 $kg\ m^{-3}$ (bottom left) and 27.8 $kg\ m^{-3}$ (bottom right). On isobars, at the surface, there is a peak in amplitude at the equator, suggesting high eddy and internal wave activity, and low points in the amplitude in the center of the subtropical gyres between 25-35 N and S. At all latitudes at small scales, a slope between $\gamma = 0$ and $\gamma = \frac{2}{3}$ is seen, but that slope flattens to $\gamma = 0$ at high latitudes and remains constant nearer to the equator. At $1900m$, the peak amplitude is at the high latitudes, with the lowest amplitude seen at the equator. Most latitude bands have a slope of approximately $\gamma = 0$ at all scales except when $\gamma = \frac{1}{3}$ at the non-equatorial low latitudes.

The latitude dependence of the isopycnal structure functions encourages more investigation into its mechanics. The isopycnal of 25.8 $kg\ m^{-3}$ (bottom left panel of Figure 2.6) is near the surface at high latitudes, and below the thermocline at the low latitudes. The amplitudes of the structure functions act as expected, with higher amplitudes at higher latitudes where the isopycnal is closer to the surface. However, the peak at the equator suggests either a shallower isopycnal, or additional eddy activity at depth. The asymmetry with latitude in structure function amplitude but not in isopycnal depth (see Figure 3 of McCaffrey et al. (2014)) encourages further investigation into the difference between the northern and southern hemispheres. This asymmetry is much larger on the 27.8 $kg\ m^{-3}$ isopycnal, with flatter slopes and much higher amplitude in the northern hemisphere. A hypothesis to account for this behavior is that the northern Atlantic is the site of a large seasonal injection of temperature and salinity variations on isopycnals (called “spice”). Yeager and Large (2007) proposed that the wintertime injection of spice increases salinity variability that then is subducted and transported southward by the meridional overturning circulation. The shallow depth of the 27.8 $kg\ m^{-3}$ isopycnal in the northern Atlantic supports this theory since it is more likely to reach the deep wintertime mixed layer where spice is injected. The asymmetry of the structure function amplitudes may be explained by this process, as salinity variations are highest in the northern Atlantic and decrease to the south. This process happens along isopycnals where salinity is a passive tracer, so this behavior is not expected to be seen in the isobaric structure functions.

To analyze the role of eddies in the structure function, we compared regions high in eddy kinetic energy (EKE) and those low in EKE, as identified from maps of Aviso EKE (Figure 2.7). Both high-EKE and low-EKE regions are nearly homogenous, but the high-EKE regions have a large-scale preferred flow direction, making it less isotropic than the low-EKE regions. We only calculated the isopycnal structure function in order to isolate the eddy activity apart from internal wave activity. The comparison is done in Figure 2.8. In low-EKE regions (Figures 2.8b and d), there are slopes of $\gamma = \frac{2}{3}$ at all scales at the surface, with flatter slopes at depth at large scales. In high-EKE regions (Figures 2.8a and c), the surface structure functions in the Gulf Stream and Kuroshio are the same, with slopes of $\gamma = \frac{2}{3}$ at small scales and $\gamma = 0$ at large scales. However, the two western boundary currents are different along deeper isopycnals. The slope of $\gamma = \frac{2}{3}$ extends to the largest scales at depth in the Gulf Stream, but in the Kuroshio, the surface large-scale slope of $\gamma = 0$ extends in the smaller scales. Though it is possible that a lack of observations introduces noise that is distorting the slope at small scales, this may indicate that the eddy activity extends deeper

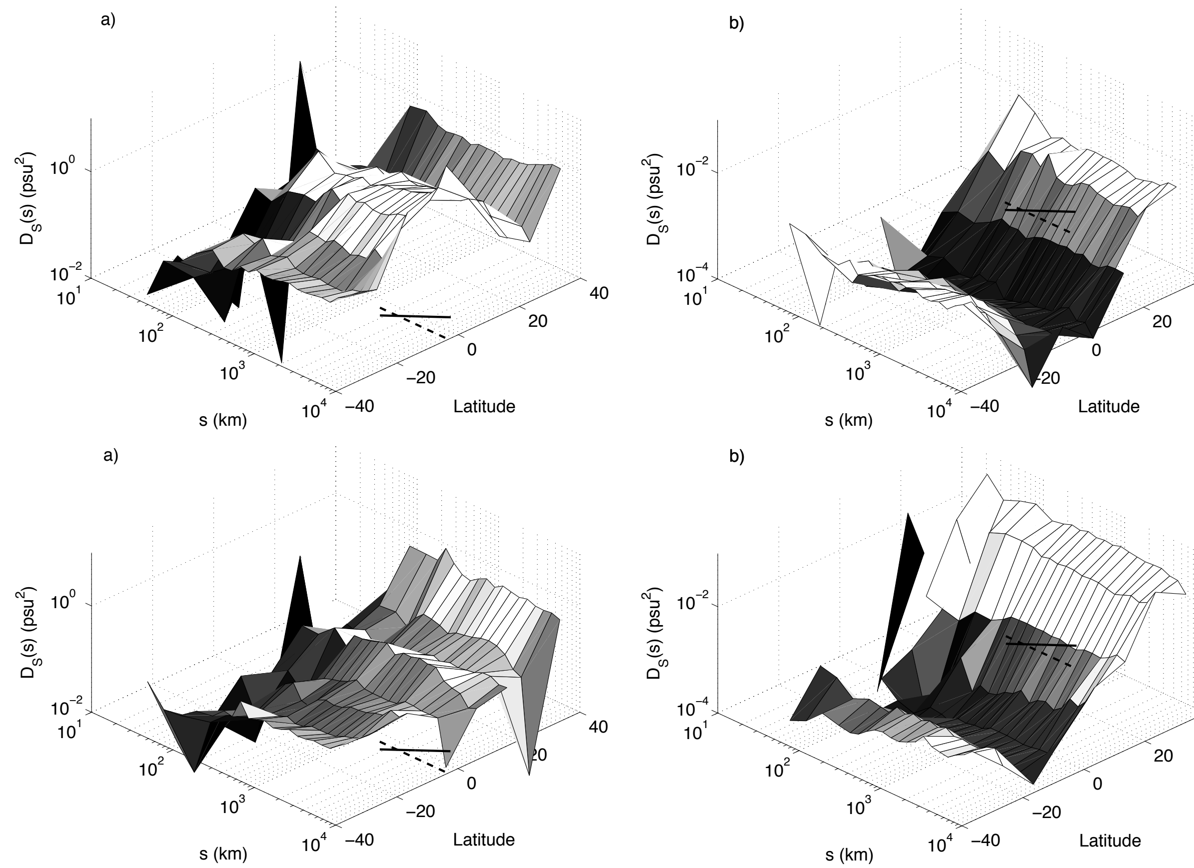

Figure 2.6: Salinity structure function, $D_S(s)|_p$, at $5m$ (top left) and $1900m$ (top right), and $D_S(s)|_\sigma$, at 25.8 $kg\ m^{-3}$ (bottom left) and 27.8 $kg\ m^{-3}$ (bottom right), with $D(s)$ on the z-axis, and separation distance and latitude on the horizontal axes.

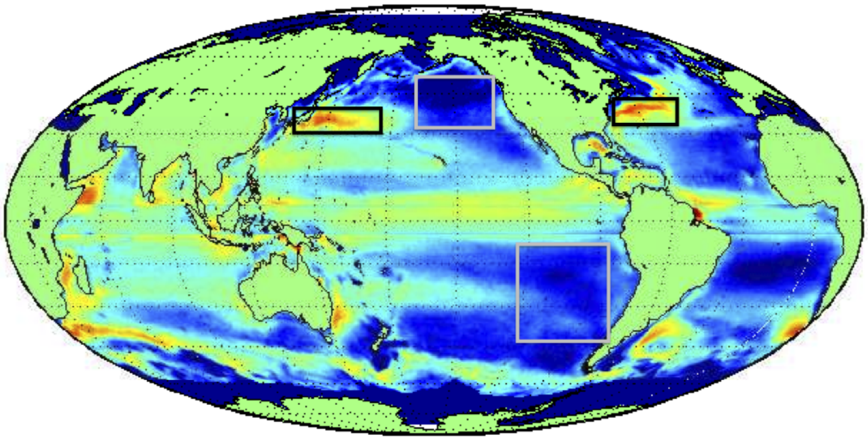

Figure 2.7: Log_{10} of eddy kinetic energy ($cm^2\ s^{-2}$) on the surface from AVISO satellite altimetry measurements from 1993-2010. Chosen high-EKE are shown in black boxes, and low-EKE regions in gray boxes.

in the water column in the Gulf Stream than it does in the Kuroshio.

A comparison of the amplitudes of the structure functions in the high-EKE and low-EKE regions illuminates the higher variance seen at the surface in the high-EKE regions that is missing in the low-EKE regions. At the deepest isopycnals, the two low-EKE regions and the Kuroshio have similar amplitudes, suggesting that the surface mixing adds salinity variance only on the isopycnals with structure functions that have a changing slope. The higher amplitude even at the deepest isopycnals in the Gulf Stream supports the hypothesis that the eddy activity extends throughout the water column in this region, but not the others.

The structure function is also a tool to identify characteristics of ocean basins, like the location of deep water formation, which occurs in the North Atlantic, but not the North Pacific. Figure 2.9 compares the deep and shallow isobaric structure functions for the North and South Atlantic and Pacific. All eight structure functions have a small-scale slope of approximately $\gamma = \frac{2}{3}$ and large-scale slope of $\gamma = 0$ (a 95% bootstrap confidence interval, described in Appendix B of McCaffrey et al. (2014a), is shown for each to support statistical significance of these results). The amplitude of the surface structure functions in both basins are similar, but the deep structure functions act quite differently. The amplitude in the North Pacific is much smaller than that of the North Atlantic. The southern oceans' structure functions also show the small amplitude, like that of the North Pacific. These results may be the indicator of the highly saline deep water that is formed in the North Atlantic, or the presence of the highly saline Mediterranean outflow ("Meddies") (Reid, 1994).

2.4 Conclusions from Structure Functions

Though it was shown that the assumption of homogeneity is rarely true, the comparison between the structure functions in homogeneous and heterogenous regions shows that this differentiation is not necessary. Comparing the homogeneous isopycnal structure function in the Gulf Stream western boundary current (Figure 2.4a) to the heterogeneous isopycnal

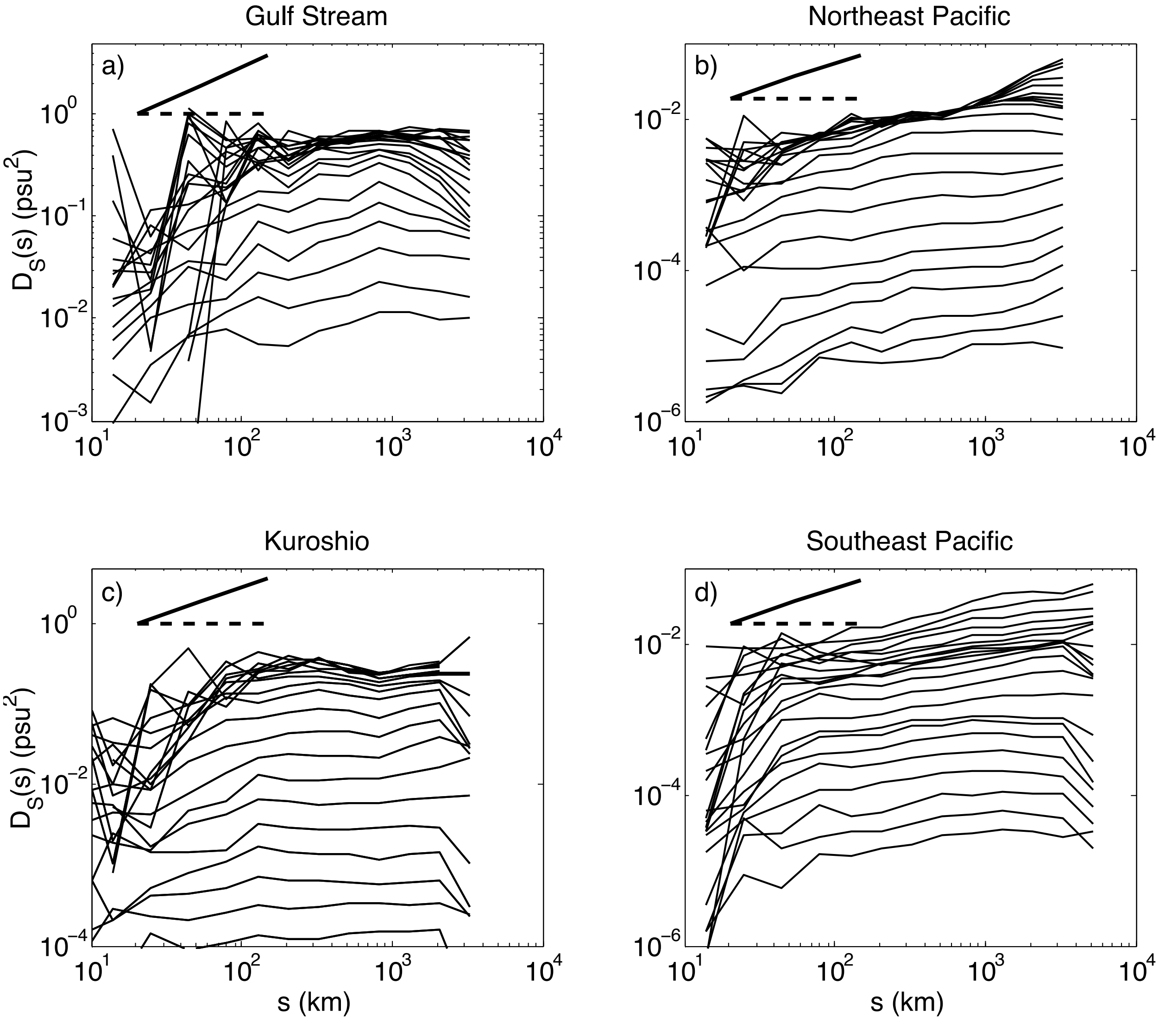

Figure 2.8: Salinity structure function, $D_S(s)|_\sigma$, in high-EKE regions of the Gulf Stream (a) and Kuroshio (c), and low-EKE regions of the northeast Pacific (b) and southeast Pacific (d) at from the surface (top line) to 27.8 $kg\ m^{-3}$ (bottom line). Reference slopes of $\gamma = 0$ (dashed) and $\frac{2}{3}$ (solid) are shown in bold. Note: axes are identical on all four plots.

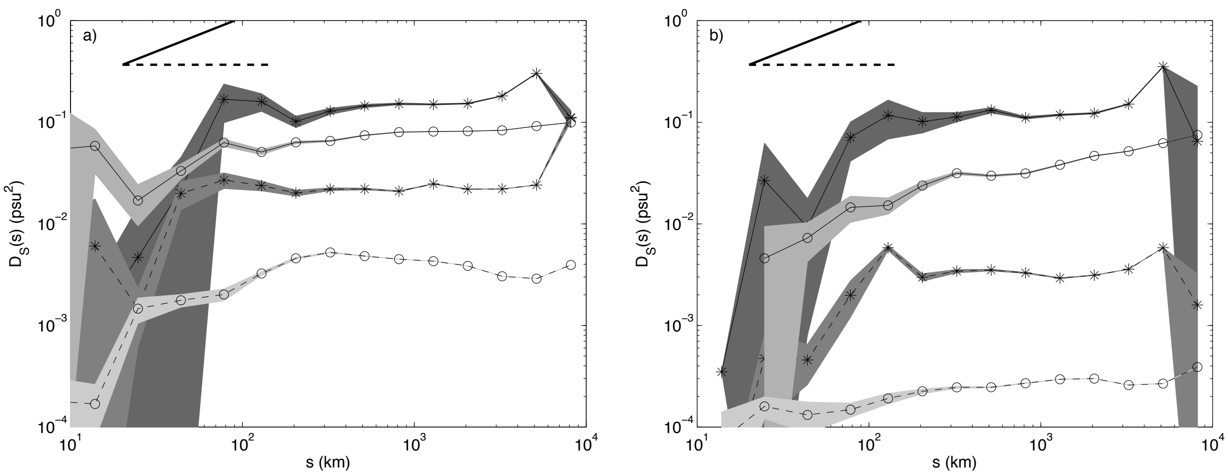

Figure 2.9: Salinity structure function, $D_S(s)|_p$, in the a) North (30-40N) and b) South (30-40S, right) Atlantic (star) and Pacific (circle) Oceans at 5 (solid) and 1000 (dashed) meters. Reference slopes of $\gamma = 0$ (dashed) and $\frac{2}{3}$ (solid) are shown in bold.

structure function in the high-EKE western boundary currents (Figures 2.8a and c) shows that the distinction of homogeneity does not affect the resulting structure functions. This could be a result of either choosing "homogeneous" variance regions that are still too heterogeneous, or else heterogeneous turbulence, as quantified by the structure function, is not substantially different from its homogeneous analog. In either case, these results suggest that if the relationship is to be made, that it may be made for any geographical region. This facts makes the structure function an even stronger metric than the usual turbulence spectrum, since the assumption of homogeneity is not required. The ability to extend the relationship even in the case of two structure function slopes shows that this tool is very useful for characterizing turbulence with discontinuous observations.

The major conclusion of this work is that it is possible to use the scattered, discontinuous Argo temperature and salinity data to calculate structure functions as a method of statistically describing the large-scale end of the inertial range of salinity (or temperature) variance in the oceans. The methodology of Frehlich and Sharman (2010b), with the theory of Webb (1964), allows the structure function slopes to be used to infer the slope of the salinity variance spectra in cases of isotropic, homogeneous turbulence, and we showed that the assumption of homogeneity is not necessary for calculating the structure function. In addition to including the up-to-date Argo measurements, incorporating additional data sources would increase the density of measurements, which would allow the structure function to be calculated over a larger range of scales, most specifically into the smaller scales of the inertial range. This method can now be applied to output from GCMs to determine how well they capture the large-scale turbulent behavior, especially at depth where other validation possibilities are much more limited. Despite the discontinuous and spotty nature of the observations that have discouraged many from using the extensive Argo dataset for turbulence analysis, this work shows that the Argo float network allows turbulence statistics to be calculated at depths and in geographic locations not examined previously, and the increasing size of the dataset will further the capabilities of this method.

Chapter 3

Observations of Tidal Turbulence from ADCP and ADV

With the growing interest in ocean renewable energy, a better understanding of the marine environment is needed in order to make further progress in research and development of these technologies. The Puget Sound, WA has the highest energy-harnessing potential in the United States, with its narrow channels, concentrating tidal flows that can produce 0.6 TWh/yr of extractable power (Haas, 2011). Previous analyses of the Puget Sound have included resource assessment (Epler et al., 2010), general site characterization (Gooch et al., 2009), site characterization with simple turbine models (Polagye and Thomson, 2013), and initial turbulence characterization (Thomson et al., 2012). Unfortunately, observing a tidal strait for all aspects that impact turbine placement and power production is virtually impossible. On this smaller scale, higher resolution measurements are needed, and on much smaller scales than those observed in Chapter 2. Here the use of acoustic Doppler instruments is more reasonable, with their ability to measure both mean and turbulent quantities on a faster time scale.

In this work, I performed a higher-order, detailed characterization of the turbulence at a prospective tidal energy site in the Puget Sound to gain a better understanding of the features of the flow that will impact a turbine and its power production. Turbulent "gusts," or coherent, intermittent eddies put particularly strong and variable stresses on turbine blades as they turn, leading to misalignment of the drive train and wearing of the gearbox (Ragheb and Ragheb, 2010). Therefore, a thorough site characterization with quantifications of coherent eddies can potentially prevent untimely, unexpected, and costly failures in turbines. Since tidal energy is still in its early stages of development, these savings can be invaluable to making this technology more accessible.

Using the acoustic Doppler observations from Thomson et al. (2012), this chapter examines three typical turbulent metrics (turbulence intensity, turbulent kinetic energy, and coherent turbulent kinetic energy), introduces another (anisotropy magnitude), and analyzes the dependence of several higher-order turbulent statistics on these metrics. These statistics include autocorrelations for time scale information, probability density functions for intermittency, and anisotropy tensor eigenvalues for quantification and a physical description of anisotropy of the flow. Each of these statistics was chosen from literature on laboratory and numerical experiments (Kolmogorov, 1941; Novikov and Stewart, 1964; Lumley and Newman, 1977), where the limitations of real-world observations do not apply. It will be shown that the parameters presented here, which are based on well-founded turbulence theory, provide a better *physical* description of the turbulence at a tidal energy site than the simple turbulence intensity used previously. The knowledge of the size, shape, and incidence of coherent structures in the tidal strait will allow for turbines to be designed to better withstand these events.

The results presented here are explained in detail in Appendix D and McCaffrey et al. (submitted, 2013). These results will be used in Chapter 4 for comparisons of turbulence from a stochastic turbulence simulator (the TurbSim model from the National Renewable Energy Laboratory (NREL), Jonkman and Kilcher (2012)), and large-eddy simulations (LES; an adaptation of the National Center for Atmospheric Research (NCAR) LES, Alexander and Hamlington (2014)).

3.1 ADCP and ADV Measurements

Two different instruments, an acoustic Doppler current profiler (ADCP) and an acoustic Doppler velocimeter (ADV), were used by Thomson et al. (2012) for the initial turbulence analysis at two tidal energy sites in the Puget Sound. An ADCP takes a vertical profile of velocities across four divergent acoustic beams (sampling volume $O(1m)$ in diameter, increasing with distance from the device), while an ADV measures three components of velocity at one point from three convergent beams (sampling volume $O(1cm)$ in diameter) (Nortek USA, LLC, 2014). See the right panel of Figure 3.1 for schematics of the instruments. Doppler noise is inherent to both instruments, but is much larger for the ADCP (Thomson et al. (2010) show the need to remove this noise from turbulence intensity from ADCP measurements). Unfortunately, the Doppler noise and beam spread inherent to the ADCP prevented its data from being used for the more extensive turbulence analysis done here (the ADV only measured at Nodule Point, so the Admiralty Head site was discarded). An analysis that lead to this conclusion is contained in Appendix E. It is possible to calculate turbulence statistics from the high-sampling frequency, less noisy ADV, so the results that follow are based off of these observations.

The ADV is located at Nodule Point, on the eastern side of Marrowstone Island in the Puget Sound, where Verdant Power^{TM} was considering building an array of turbines. The site, which is $22m$ deep and $10km$ wide, has a maximum current velocity of $1.8m\ s^{-1}$ at the proposed hub-height of $4.7m$ above the seabed. The observations span four days from 17 February to 21 February 2011 using an ADV sampling at $32Hz$ on the apex of a Tidal Turbulence Tripod at approximately hub-height. This includes 8 full tidal cycles during a spring tide, sufficient for an analysis of the small-scale turbulence. A map of the region with bathymetry and locations of both sites, along with pictures of the instruments deployed at each location is in Figure 3.1. These and more details on the observations can be found in Thomson et al. (2012).

Each of the three velocity components have been decomposed into a mean ($\overline{u}$) and per-

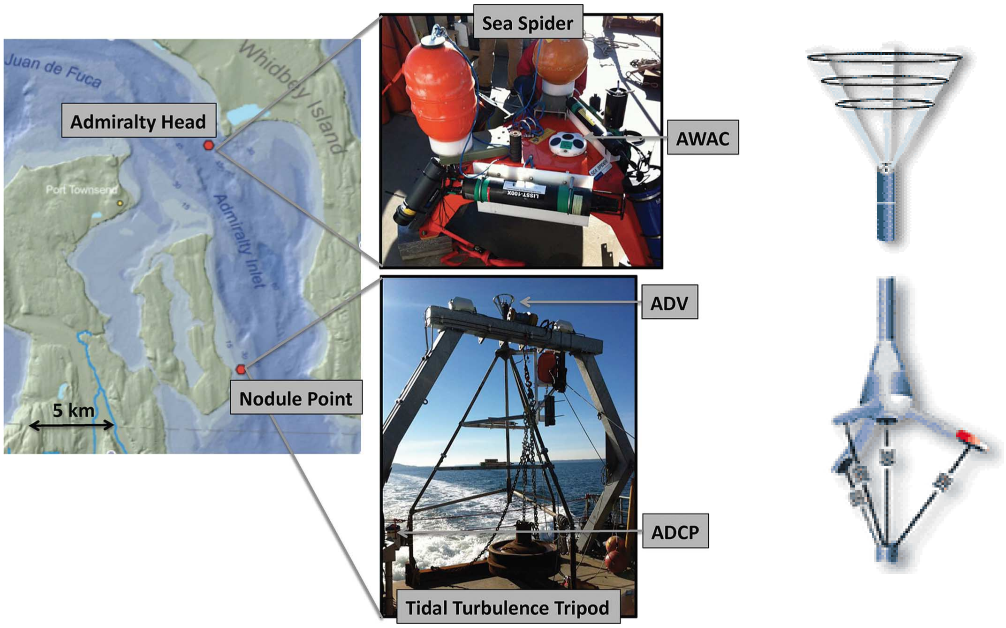

Figure 3.1: Left: Fig. 1 from Thomson et al. (2012): Regional map, bathymetry, and locations of two tidal energy sites in Puget Sound. At Admiralty Head, a Sea Spider was deployed on the seafloor to collect AWAC data. At Nodule Point, the Tidal Turbulence Tripod was deployed on the seafloor to collect ADV and ADCP data. The Sea Spider was ballasted with 800 lb of lead (ingots), and the Tidal Turbulence Tripod was ballasted with 1800 lb of steel (railroad wheels). Right: Basic schematics of an ADCP (top) and ADV (bottom).

turbation (u') as in Equation 1.2, where $\mathbf{u} = u\mathbf{i} + v\mathbf{j} + w\mathbf{k}$. The horizontal velocities are defined in perpendicular components, where $-\mathbf{i}$ is aligned toward the seaward principal flow direction, $\mathbf{j}$ is perpendicular to the principal flow direction, and $\mathbf{k}$ is in the vertical direction. As explained in Chapter 1, we used a 10-minute time mean (in contrast to the shorter 5-minute mean chosen by Thomson et al. (2012)) to retain the longest timescales of coherent turbulence structures in the perturbation, while capturing the tidal and diurnal variations in the mean. Assuming Taylor's hypothesis, this defines motions smaller than $\sim 1.08\ km$, or $1/10th$ of the channel width, as turbulent (for $1.8m\ s^{-1}$ mean velocities).

The three components of velocity from the ADV at Nodule Point are shown in Figure 3.2, with the observed velocities in gray, and the 10-minute mean in black. The dotted lines identify "slack conditions," when the velocity is not large enough to drive a turbine, defined as $\overline{u} \leq 0.8m\ s^{-1}$. Reynolds stresses (and their time-averaged covariances) are defined as $u_i'u_j'$ (shear stresses are when $i \neq j$, and normal stresses are when $i = j$). Coherent turbulent structures appear as bursts in these shear stresses in a well-mixed, homogeneous flow, such as a tidal strait (Kelley et al., 2000). Velocity perturbations, and the normal and shear stresses are shown Figures 3.3a, b, and c. Peaks occur periodically in each signal with the M2 (semidiurnal) tide dominated mainly by the normal stresses. Turbulent bursts can be seen in the shear stresses, also occurring at a roughly diurnal period, coincident with strong ebb and flood conditions. Some days have two turbulent bursts, with the stronger turbulence associated with the stronger flood. Diurnal variability is also typical as one large and one small (i.e., mixed semi-diurnal) flood or ebb per day. The w' fluctuations are considerably smaller than those in the other directions, as indicated by the very small vertical normal stress.

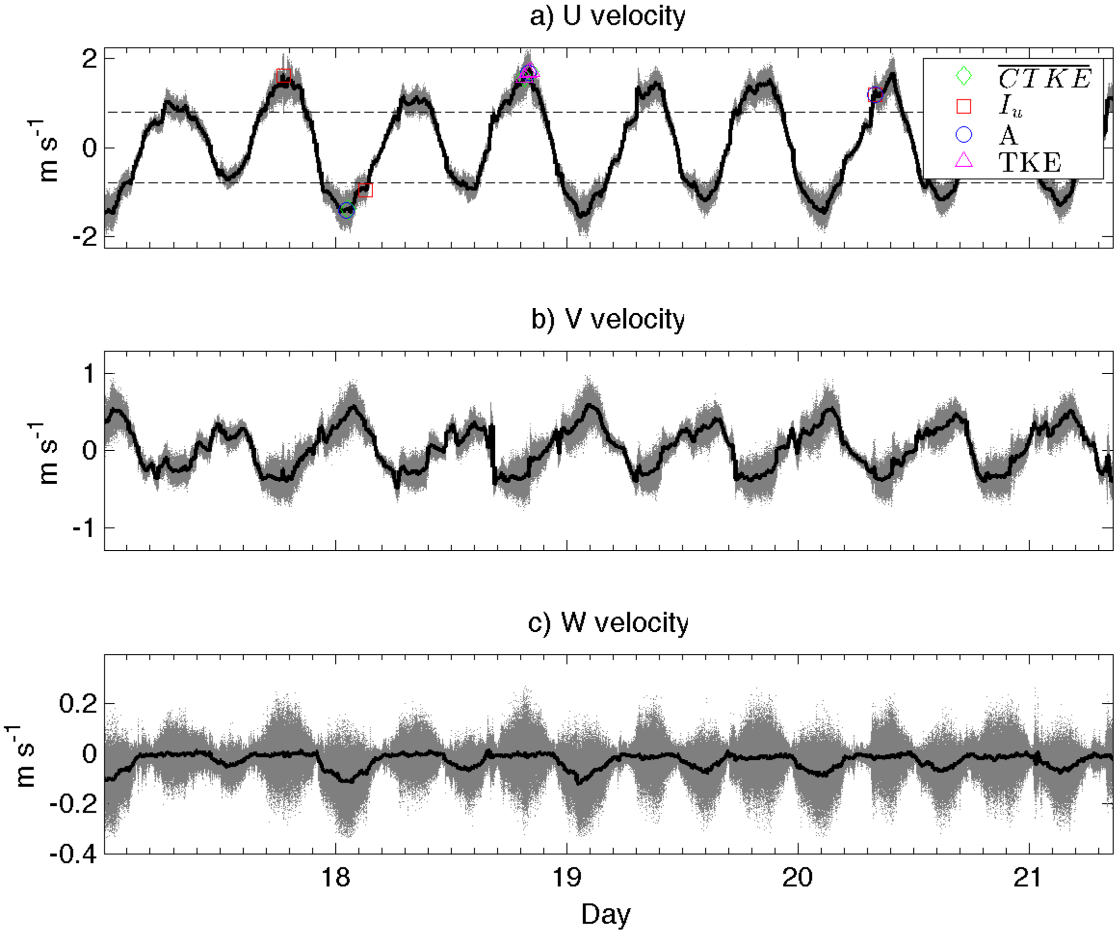

Figure 3.2: Velocities in the along stream (u; a), cross-stream (v; b), and vertical (w; c) directions from the ADV at Nodule Point from 17 Feb 2011 to 21 Feb 2011 at approximate hub-height depth of $4.7m$. Gray dots show instantaneous velocity measurements, and black lines show 10-minute averages. Dotted lines in a) show the slack condition criterion. Three 99th-percentile values of I_u, TKE, $\overline{CTKE}$, and A values when $\overline{u} > 0.8m\ s^{-1}$ are shown in the red squares, green diamonds, and blue circles, respectively on the u velocity plot.

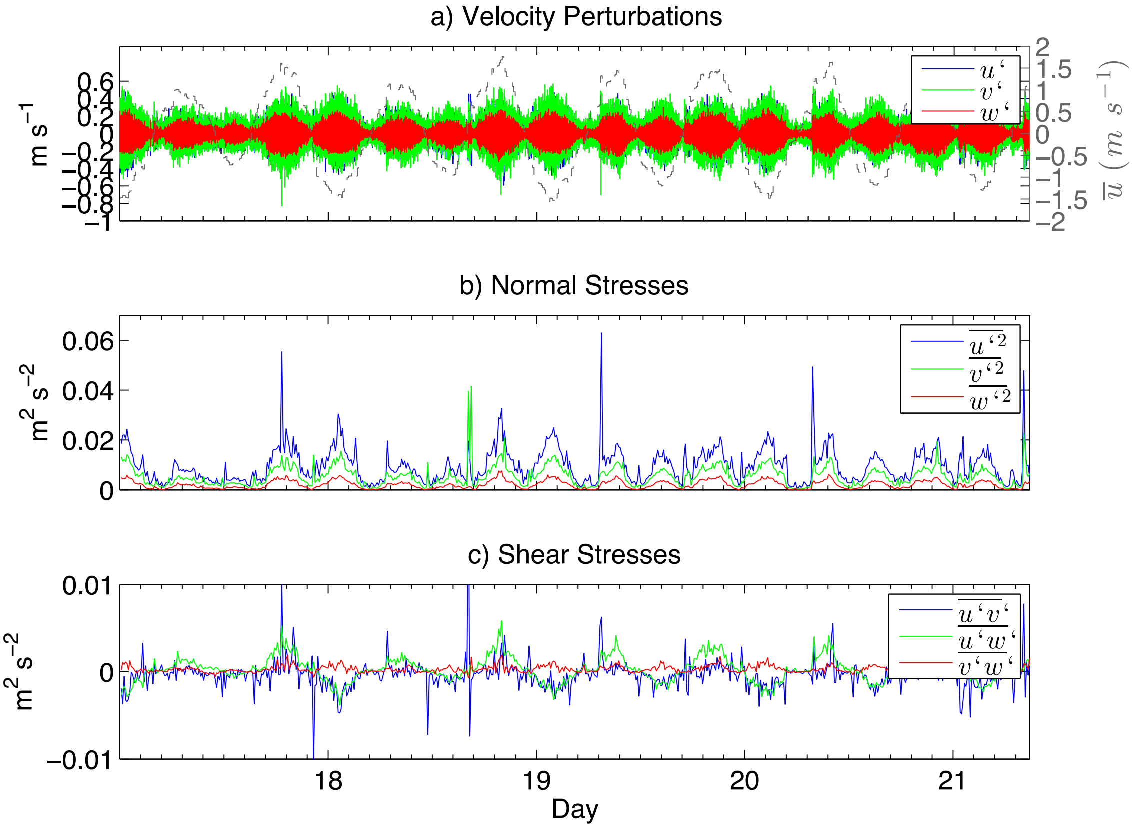

Figure 3.3: a) Velocity perturbations, b) turbulent kinetic energy components, and c) Reynolds shear stress components, from the Nodule Point ADV shown in Figure 3.2.

3.2 Turbulence Metrics: I_u, TKE, $CTKE$, and A

The turbulence metric most commonly used in the wind and tidal energy industries for site classification because of its impact on power generation and turbine loading (Elliott and Cadogan, 1990; Kaiser et al., 2007; Rareshide et al., 2009) is the turbulence intensity, defined as

$$I_u = \frac{\sigma_u}{\overline{u}} = \frac{\sqrt{\overline{u'^2} - n^2}}{\overline{u}}, \tag{3.1}$$

where the overline indicates a 10-minute average, and n is the instrument's Doppler noise (Thomson et al., 2012). Turbulent kinetic energy, (TKE or k) defined as one-half the sum of the normal stresses,

$$TKE = \frac{\overline{u_i u_i}}{2} = \frac{1}{2}\left(\overline{u'^2} + \overline{v'^2} + \overline{w'^2}\right), \tag{3.2}$$

has also been shown have a negative impact on power production (Wharton and Lundquist, 2012). Coherent turbulent kinetic energy, introduced by Kelley et al. (2000) as a metric that closely correlates with loads on a wind turbine, is defined as

$$CTKE = \frac{1}{2}\sqrt{(u'v')^2 + (u'w')^2 + (v'w')^2}. \tag{3.3}$$

These three metrics, plotted in Figure 3.4a, b & c, are the most popular for general descriptions of turbulence that affects a turbine. However, each of these metrics has a down-side. The turbulence intensity is simply a statistical descriptor and is dependent on the coordinate system chosen. Similarly, $CTKE$ is also dependent on coordinate system, and may therefore be skewed for flows with tidal flows that are not purely symmetrical. In addition, $CTKE$ is an instantaneous measure, so though it incorporates fluctuations in all three directions, there is no way to measure how long this "coherence" exists. Ideally, a true scalar, invariant of coordinate system, could be used to quantify turbulent events. TKE is tensor invariant, but does not describe the anisotropy between its components, or include the shear stresses. To this end, we created a new metric which we call the anisotropy magnitude, A, that captures the shear stress terms like the $CTKE$, but also the anisotropy from the normal stresses, like TKE.

Beginning with the anisotropy tensor (Lumley, 1978),

$$a_{ij} = \frac{\overline{u_i u_j}}{2k} - \frac{\delta_{ij}}{3}, \quad k = \frac{\overline{u_i u_i}}{2}, \tag{3.4}$$

and its three principal invariants (I, II, III),

$$\begin{aligned} I &= a_{ii} \equiv 0 \\ II &= a_{ij} a_{ji} \\ III &= a_{ij} a_{in} a_{jn}, \end{aligned} \tag{3.5}$$

with a sum implied to occur over repeated indices (Einstein notation), we have true scalars that are independent of coordinate system, dependent only on the asymmetries of the turbulence. Analyzing invariants II and III (I is zero by definition of a_{ij}) will show the departures from isotropy (often visualized by the classic Lumley Triangle of Lumley and Newman (1977)), since isotropic turbulence has the property that $I = II = III = 0$. From the scalars, k and II, we formed the coordinate-system invariant version of $CTKE$, the anisotropy magnitude:

$$A = k\sqrt{II} \equiv \tag{3.6}$$
$$= \sqrt{\frac{1}{2}\left(\overline{u'v'}^2 + \overline{u'w'}^2 + \overline{v'w'}^2\right) + \frac{1}{6}\left(\overline{u'^2}^2 + \overline{v'^2}^2 + \overline{w'^2}^2 - \overline{u'^2}\,\overline{v'^2} - \overline{v'^2}\,\overline{w'^2} - \overline{v'^2}\,\overline{w'^2}\right)}.$$

This metric has the following attributes: 1) Unlike TKE, but like $CTKE$, $A = 0$ for isotropic, uncorrelated turbulence. 2) Like $CTKE$ and TKE, A has the units of energy ($m^2 s^{-2}$). 3) A tends to grow with $CTKE$, approaching a version of $CTKE$ formed from the time-averaged shear stresses as $CTKE \gg k$. 4) Like $CTKE$ and TKE, A is real, and 5) unlike $CTKE$, A is a true, coordinate-independent scalar. The anisotropy magnitude, A, is therefore similar in meaning to the $CTKE$ in Equation 3.3, though improved. A allows instrument noise to be removed through the averaging, while it remains in the $CTKE$. The anisotropy magnitude, A, is plotted at Nodule Point in Figure 3.4d, exhibiting simultaneous, similarly-intermittent peaks as $CTKE$ between periods of low anisotropy. Figures 3.2, 3.4, 3.7, 3.10, 3.11, and 3.14 show three extreme values (in the 99th-percentile) of I_u, TKE, $\overline{CTKE}$, and A, and it is intriguing to note that the extreme occurrences of TKE co-occur with two peaks in $CTKE$, and one in A, but the peaks in A do not always co-occur with those of $CTKE$ or I_u. This highlights the fact that neither $CTKE$ nor I_u are reliable, coordinate-system independent indicators of turbulence or anisotropy, but that TKE and A capture the same features with a reliable, coordinate-system independent manner.

3.3 Physical Characterization

From the single-point measurements of velocity in time from an ADV, there are several temporal statistics that can inform us about the coherence, intermittency, and anisotropy of the flow. Using Taylor's hypothesis, these temporal analytics can be related to spatial properties. In the sections below, autocorrelations will be used as measures of coherence, probability density functions and higher-order moments will be used for intermittency, and the eigenvalue method of Banerjee et al. (2007) will be used to quantify anisotropy.

3.3.1 Coherence

With only a time series of velocities at one location in space, spatial correlations cannot be calculated, but the temporal autocorrelation can. The sampling frequency of $32Hz$ from the ADV allows the analysis of very small scales, up to the 10-minute scale. The temporal autocorrelation is defined as

$$\rho(\tau) = \frac{\overline{u'(t)u'(t+\tau)}}{\overline{u'^2}} \tag{3.7}$$

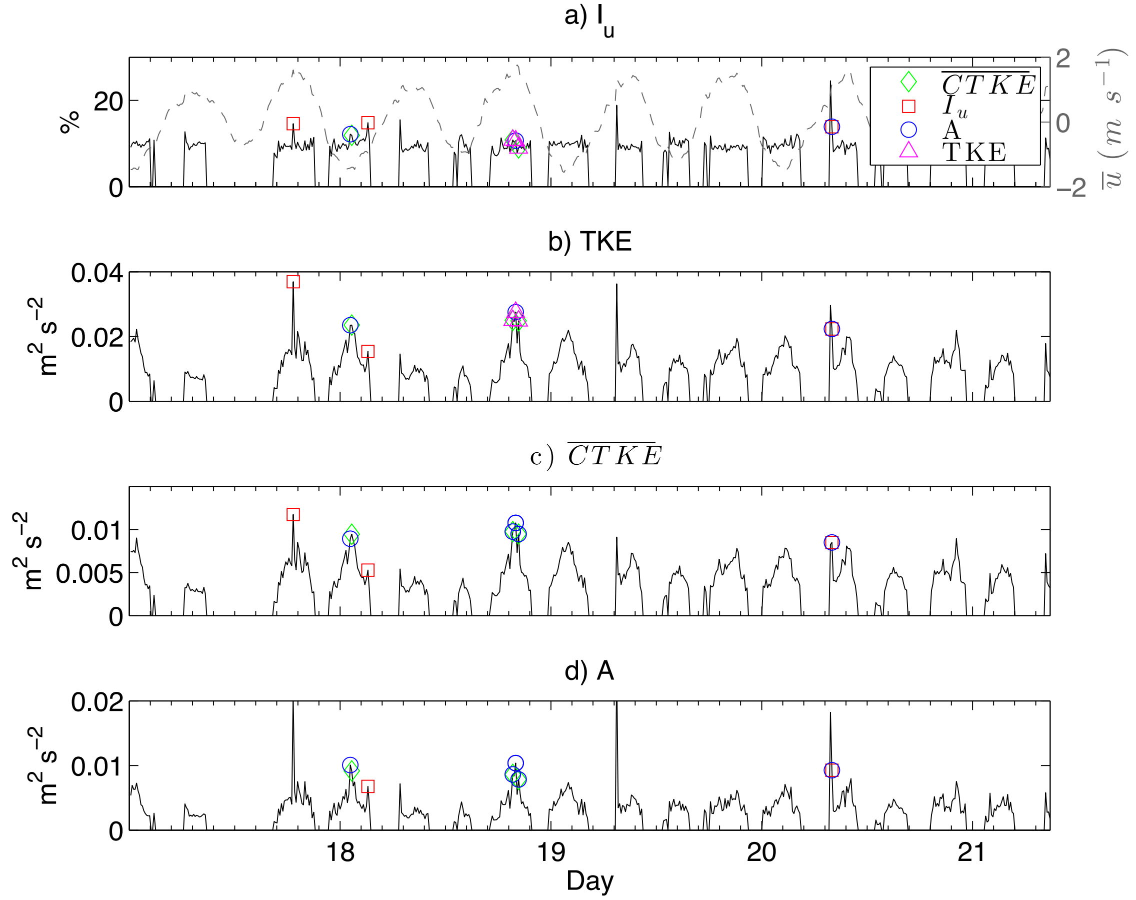

Figure 3.4: a) Turbulence intensity, b) turbulent kinetic energy, c) coherent turbulent kinetic energy, and d) anisotropy magnitude, A, from the Nodule Point data shown in Figures 3.2. Three 99th-percentile values of I_u, TKE, $\overline{CTKE}$, and A values when $\overline{u} > 0.8\ m\ s^{-1}$ are shown in the red squares, green diamonds, and blue circles, respectively, discussed in Section 3.2. The mean u-velocity is shown in a) as the gray dashed line.

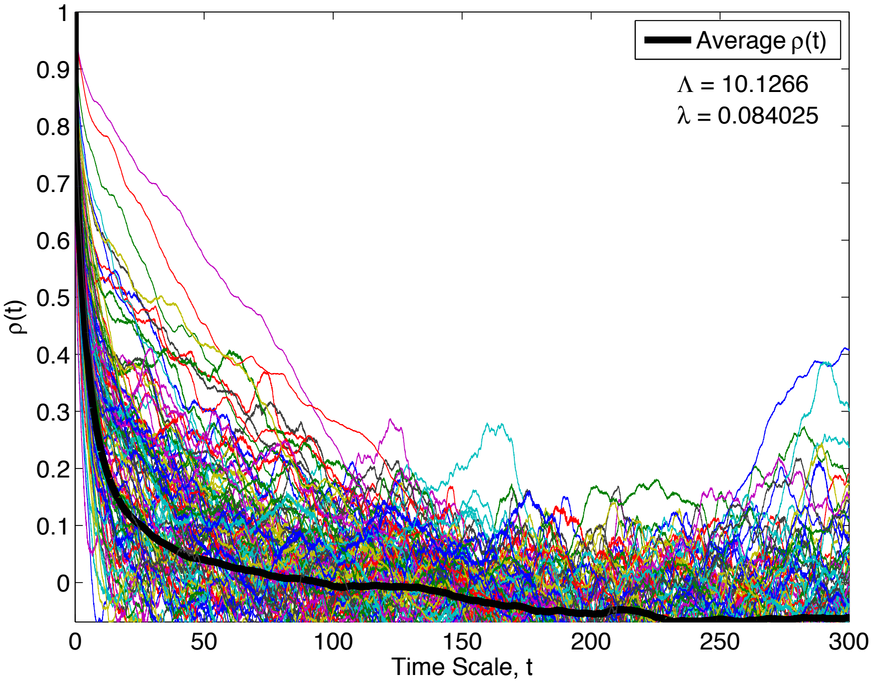

Figure 3.5: Autocorrelation functions for each 10-minute interval with $\overline{u} > 0.8\, m\ s^{-1}$ from the Nodule Point ADV. The individual intervals are colored lines and the average autocorrelation is shown in the bold black line.

where the overbar is the 10-minute mean. Figure 3.5 shows the resulting autocorrelation from all non-slack intervals, along with the mean autocorrelation (bold solid black line).

The Taylor, λ, and integral, Λ, scales are often used to quantify the longest time over which the turbulence stays correlated, and the time until the flow is uncorrelated, respectively (Pope, 2000). These scales are defined as

$$\lambda^2 = -2\left[\left.\frac{d^2\rho}{d\tau^2}\right|_{\tau=0}\right]^{-1}, \tag{3.8}$$

$$\Lambda = \int_0^\infty \rho(\tau)d\tau. \tag{3.9}$$

The average λ and Λ are shown in Figure 3.5. While most intervals become uncorrelated quickly, some intervals remain correlated up to 100 seconds. These intervals show themselves to be different from the normal behavior of the flow, highlighting coherent events. Using the average flow velocity of 0.83 $m\ s^{-1}$, the Taylor and integral scales relate to length scales of

$0.070m$ and $8.42m$, from Taylor's hypothesis. The intervals with the longest integral scales ($40 - 60$ s) tend to have horizontal speeds about 1 m s^{-1}, resulting in correlation length scales of $40 - 80m$. This compares reasonably well to the length scales of $75m$ obtained by Thomson et al. (2012) from Taylor's hypothesis applied to the "fractional" turbulence intensity. It is also interesting to note that 8 of the 10 longest integral scales and 7 of the 10 longest Taylor scales occur during flood tides.

3.3.2 Intermittency

The presence of these particularly coherent events that deviate from the normal conditions beckons an analysis of intermittency. The probability density function (pdf) of velocity increments ($\Delta u_\tau = u(t+\tau) - u(t)$ at time interval, τ), normalized by the standard deviation, is used for this analysis. A deviation from Gaussian behavior in the tails of the pdf indicates intermittency, or a higher probability of extreme events occurring. This indicates that higher order moments are necessary to describe the distribution, not just the mean and standard deviation or turbulence intensity. In addition, Mücke et al. (2011) showed the close correlation between the velocity increments and fluctuations in torque on turbine blades as seen in similar departures from Gaussian in the pdf tails of both quantities. The higher probability of alternating loads from torque fluctuations was therefore attributed to extreme wind events, or "gustiness." Figure 3.6 shows the pdfs of velocity increments with a dotted line showing the Gaussian (normal) distribution, and circles, squares, and diamonds representing $\Delta u'$, $\Delta v'$, and $\Delta w'$, respectively. The black shapes have a time interval of $\Delta t = 1/32s$. From Taylor's hypothesis, this represents motions at approximately $3cm$ scales, which is less impactful on a turbine, so the pdfs with $\Delta t = 3.6s$ (~ 3 m), and $\Delta t = 7.2s$ (~ 6 m) are also shown. The $\Delta t = 1/32s$ case is the closest to the Gaussian curve, with large intermittency (deviations from Gaussian) only in the vertical velocity. The scales associated with a half and whole turbine rotor diameter, however, exhibit more intermittent behavior in all directions, and equally. This behavior highlights the need for an inclusion of higher moments,

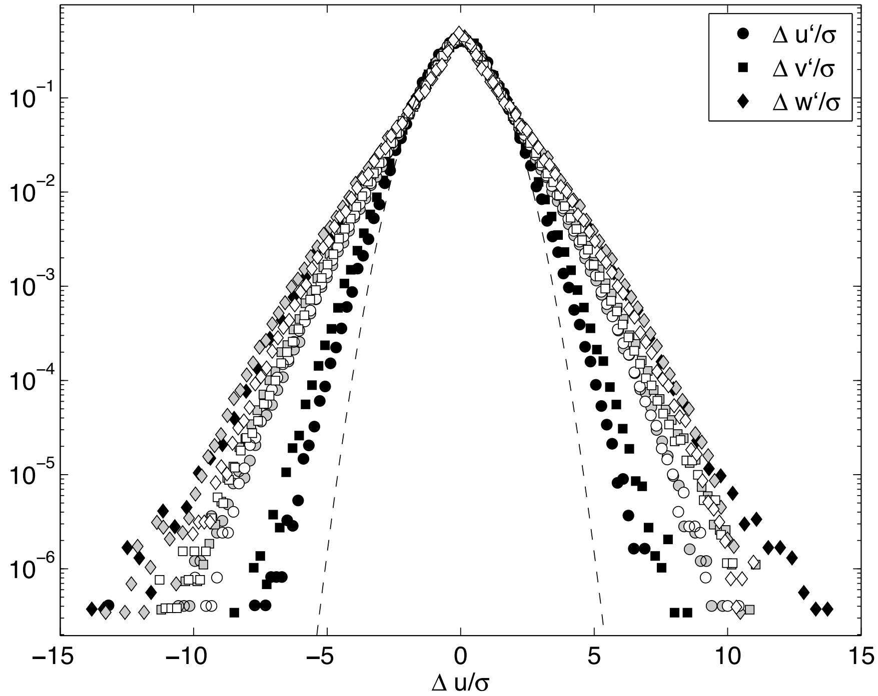

Figure 3.6: Probability density functions of the velocity perturbation increments, $\Delta u'$ (circles), $\Delta v'$ (squares), and $\Delta w'$ (diamonds) from Nodule Point ADV data, with Gaussian curves for reference (dashed). $\Delta u'$ (circles), $\Delta v'$ (squares), and $\Delta w'$ (diamonds): Black shapes have a time interval of $\Delta t = 1/32s$ ($\sim 3\ cm$), gray are $\Delta t = 3.6s$ ($\sim 3\ m$), and white are $\Delta t = 7.2s$ ($\sim 6\ m$).

since the mean and standard deviation do not suffice. The first four moments (mean, standard deviation, skewness, S, and excess kurtosis, $K - 3$), shown in Figure 3.7, support the lack of Gaussianity with the deviations from $S = 0$ and $K - 3 = 0$. The excess kurtosis is particularly meaningful since it is a measure of flatness of the probability distribution. Peaks in $K - 3$ show more peakedness at small increments, and wider tails. Therefore, the peaks in $K - 3$ support the results of the coherence analysis that shows that there are significant intermittent events in this flow.

3.3.3 Anisotropy

The differences in the pdfs of $\Delta u'$, $\Delta v'$, and $\Delta w'$ are indicators of anisotropy in the flow. Though the pdf indicates anisotropy, other tools may provide more information. For example,

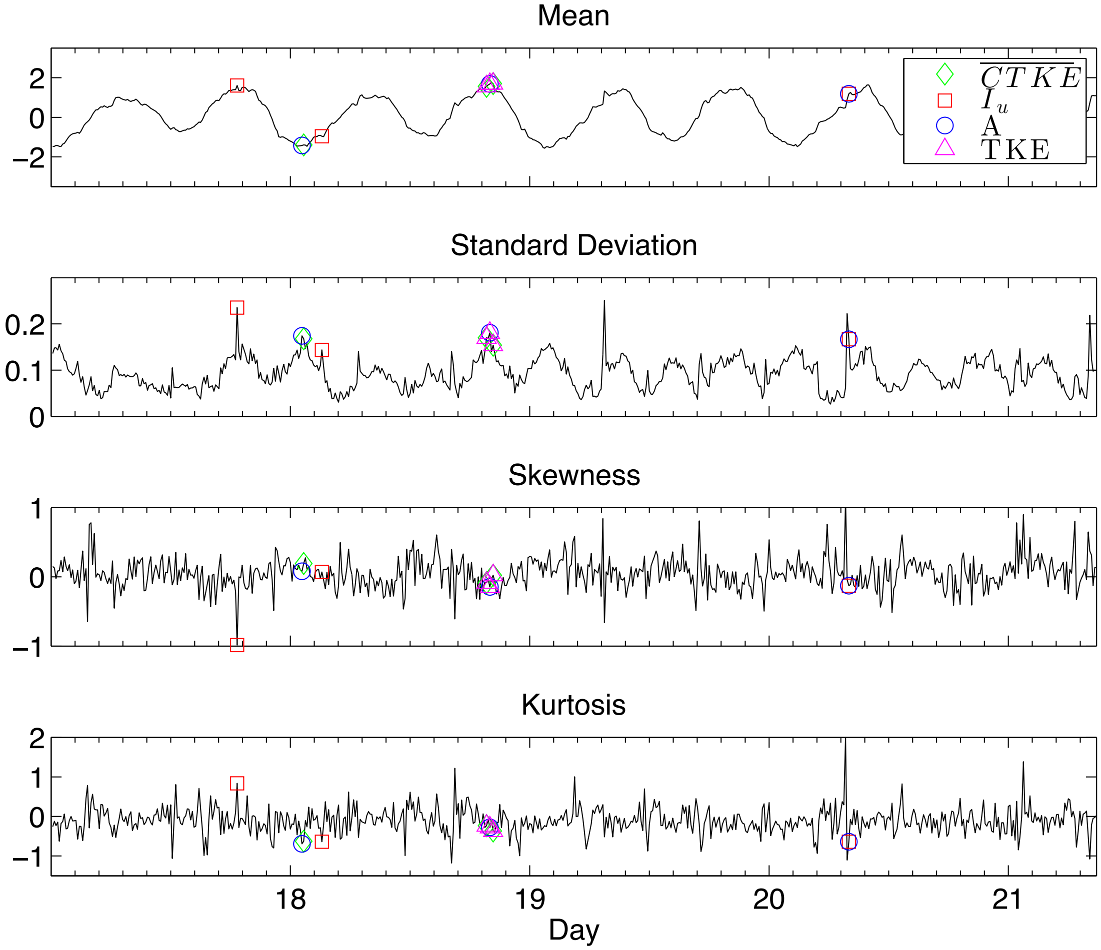

Figure 3.7: First four moments of the u-velocity from the Nodule Point ADV data, based on 10-minute intervals. Top-bottom: mean, standard deviation, σ, skewness, S, and excess kurtosis, $K-3$. Three 99th-percentile values of I_u, TKE, $\overline{CTKE}$, and A values when $\overline{u} > 0.8\ m\ s^{-1}$ are shown in the red squares, green diamonds, and blue circles, respectively.

the second-order temporal structure function of horizontal and vertical velocities can be compared. Similar to Equation 2.1, the second-order temporal structure function is defined as

$$D(\tau) = \overline{\left[u\left(t\right) - u\left(t+\tau\right)\right]^2}. \tag{3.10}$$

The structure function, which can be related to the wavenumber spectrum in isotropic, homogeneous turbulence, uses the 10-minute mean to determine the fluctuating velocity, u', and no difference appears in the structure function when linear de-trending is used for the perturbation. Figure 3.8 compares these temporal structure functions, with box plots representing the statistics of the structure functions of each non-slack 10-minute interval. The top plot shows the u-velocity structure functions, and the bottom plot shows the w-velocity. The solid line on each is the other's median, for better comparison. At small scales, the two lines are parallel, but at scales larger than about 3 seconds, the w-velocity structure functions flatten out, while the u-velocity continues with a slope of approximately $\gamma = \frac{2}{3}$. Anisotropy is manifest in the separation in slopes at the large scales.

Once it has been determined that coherent, intermittent features exist in the flow, and that the flow is sometimes anisotropic, it is possible to do an analysis using the anisotropy tensor (Equation 3.4) to quantify and physically describe those features. Banerjee et al. (2007) introduced a method of quantifying anisotropy as a function of the eigenvalues of the anisotropy tensor. The Cayley-Hamilton theorem proves that the eigenvalues may be found using only the tensor invariants (I, II, III) and *vice versa.* Therefore, the eigenvalues are coordinate-independent (Cayley, 1858).

The anisotropy is plotted on a "barycentric map," which is a ternary diagram with each of the three vertices representing a type of turbulence: one-dimensional (linear), two-dimensional (planar), and three-dimensional (fully isotropic). If the eigenvalues of the anisotropy tensor, a_{ij} are λ_1, λ_2 and λ_3, where $\lambda_1 \geq \lambda_2 \geq \lambda_3$, the coordinates of the barycen-

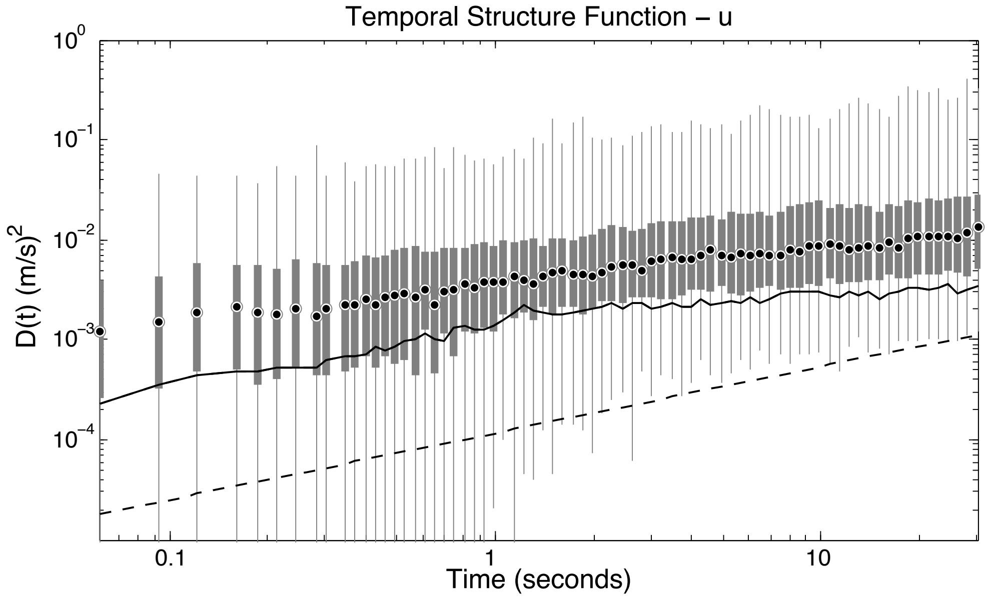

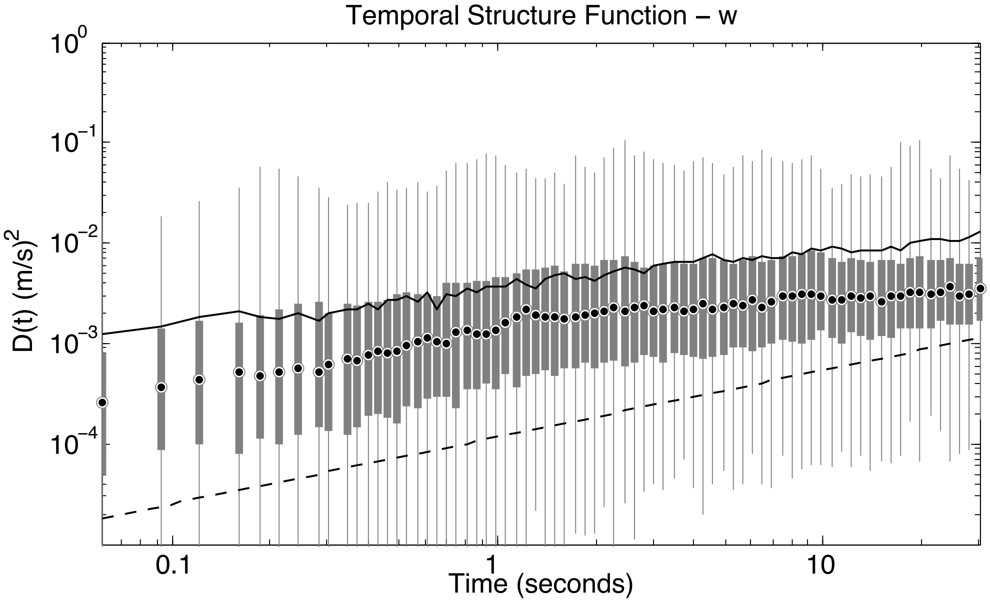

Figure 3.8: Box plots of the second-order temporal structure functions for each 10-minute interval with an $\overline{u} > 0.8\ m\ s^{-1}$ of the Nodule Point ADV data. Black circles are the median, the boxes show the 25th-percentile, and the vertical lines include the entire range. Top plot is the horizontal velocity structure function and the bottom is the vertical velocity structure function. For comparison, the solid line on the horizontal structure functions shows the median of the vertical velocity structure functions, and the line on the vertical structure functions shows the median of the horizontal velocity structure functions. The dotted line is a guideline with slope of 2/3, corresponding to the K41 turbulent cascade (Kolmogorov, 1941).

tric map are

$$
\begin{aligned}
C_{1c} &= \lambda_1 - \lambda_2, && (3.11)\\
C_{2c} &= 2\left(\lambda_2 - \lambda_3\right), && (3.12)\\
C_{3c} &= 3\lambda_3 + 1. && (3.13)
\end{aligned}
$$

To plot on a Cartesian plane where the vertices of the barycentric map are (x_{1c}, y_{1c}), (x_{2c}, y_{2c}), and (x_{3c}, y_{3c}), the location of each point is

$$x_{new} = C_{1c}x_{1c} + C_{2c}x_{2c} + C_{3c}x_{3c} \tag{3.14}$$

$$y_{new} = C_{1c}y_{1c} + C_{2c}y_{2c} + C_{3c}y_{3c}. \tag{3.15}$$

The barycentric map is shown in Figure 3.9, showing the one-, two-, and three-component limits at each vertex of the triangle (the barycentric map), with axis-symmetric and plane-strain limits shown as well. Each 10-minute interval falls someplace on that map, quantifying the distribution of the three types of turbulence. Points close to one vertex are strongly dominated by that turbulence type. The results show that the majority of intervals falls in the middle of the plot, but closer to the one- and two-component limits, with some significant events reaching closer to the one-component limit. The vast open space at the top of the barycentric map shows that the turbulence is never close to the isotropic limit between the sampling frequency and the 10-minute window. Interestingly, the slack conditions (plotted in gray) are even further from isotropic than the channeled flows, with one- and two-component turbulence at slack periods.

An additional benefit to the eigenvalue approach of quantifying anisotropy is that the eigenvectors associated with the ordered eigenvalues give the principal axes of the turbulence. In the one-component limit, the eigenvector associated with the largest eigenvalue is oriented in the (linear) direction of the flow, and the plane made by the eigenvectors of the two largest

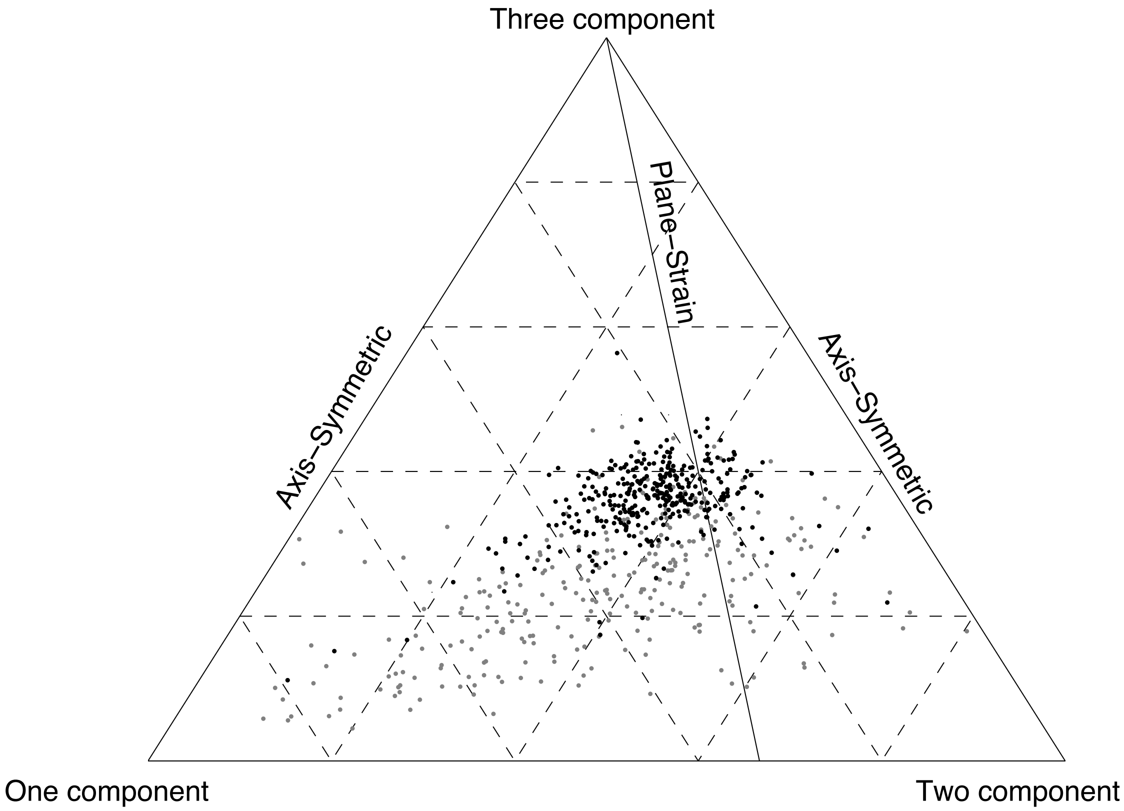

Figure 3.9: Barycentric map from Nodule Point ADV data, with the non-slack intervals in black and slack conditions in gray.

eigenvalues describes the two-component turbulence. This directional information could also come from the Reynolds stresses. Consistency between these approaches derives from the close relationship between the Reynolds stresses and the anisotropy tensor.

3.4 Parameterizations with Turbulence Metrics

Once a thorough turbulence characterization has been completed for coherence, intermittency, and anisotropy measures, a single parameter is desirable that will capture those events, without needing the entire analysis. This parameter will be useful for modeling and classification of tidal energy sites. To this end, the dependence on I_u, TKE, $\overline{CTKE}$, and A was determined for the physical characteristics.

A comparison between $\overline{CTKE}$ and A, with three values in the 99th-percentile of I_u, TKE, $\overline{CTKE}$, and A, is a first step to showing how one parameter can be used in place of a long list (Figure 3.10). The strong correlation between $\overline{CTKE}$ and A, which supports the generation of A as being similar to $CTKE$, suggests using the tensor invariant A in place of $CTKE$. Since $CTKE$ has been closely correlated to loads on a turbine, it is a natural conclusion that A would also have that impact, though further studies are needed to confirm this hypothesis.

The turbulence intensity versus mean speed plot gains a great deal of information when colored based on A, as in Figure 3.11. The $1/u$ behavior is expected from the definition of I_u, and the scatter in the points is informative, but color based on A highlights the points that will have the most impact on the turbine - with the highest I_u when the mean speed is highest. The 99th-percentile intervals of I_u, TKE, $\overline{CTKE}$, and A when $\overline{u} > 0.8\ m\ s^{-1}$ all occur in this region as well. Figures 3.10 and 3.11 both support the use of A over $CTKE$ and I_u, but a parameterization based on the physical properties of the flow is the greater goal of this work.

Parameterizing the intermittency with A is done in Figure 3.12, where the pdf of ve-

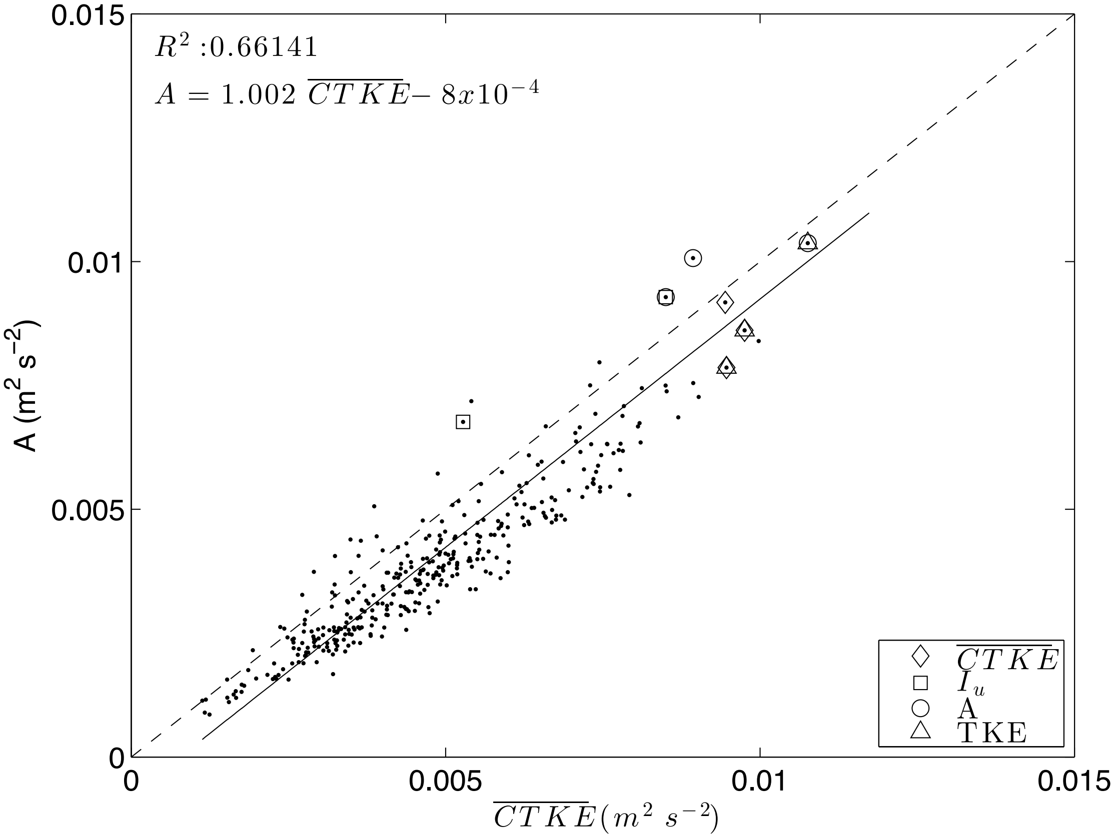

Figure 3.10: A versus mean $\overline{CTKE}$ for each 10-minute interval at Nodule Point. Linear best-fit and correlation coefficient are shown in the solid line, and the one-to-one dashed line is shown as well. Three 99th-percentile values of I_u, TKE, $\overline{CTKE}$, and A values when $\overline{u} > 0.8\ m\ s^{-1}$ are shown in the squares, diamonds, and circles, respectively.

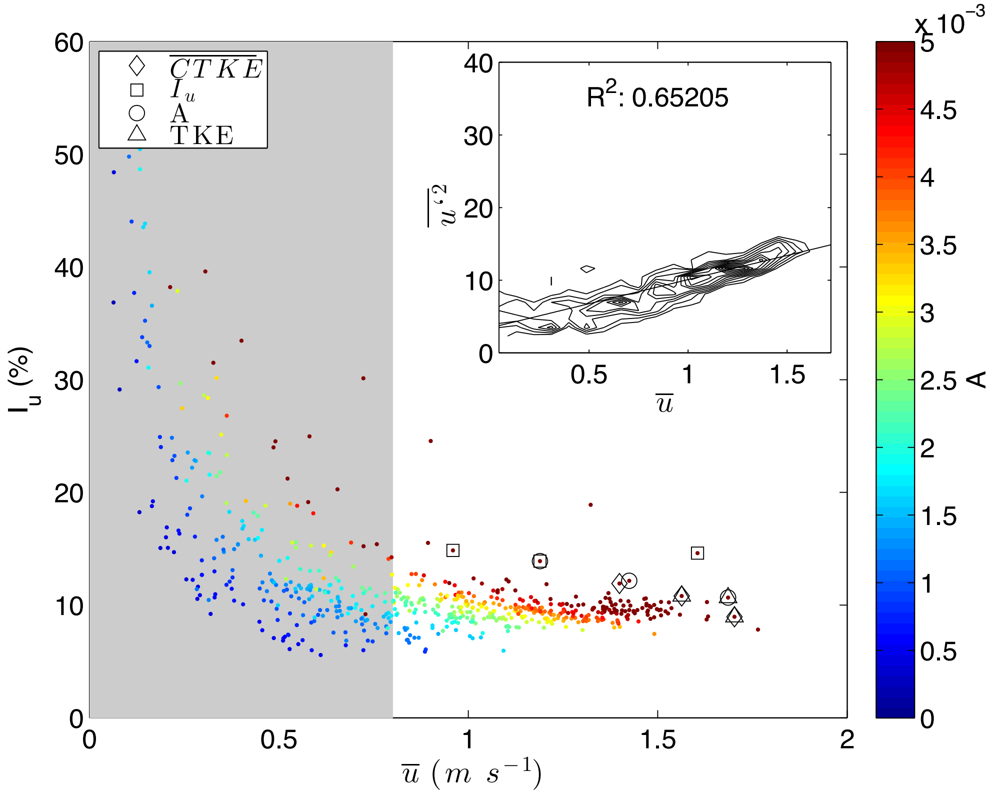

Figure 3.11: Turbulence intensity versus mean speed for each 10-minute interval at Nodule Point, with color based on$A$. The gray area indicates slack conditions. Three 99th-percentile values of I_u, TKE, $\overline{CTKE}$, and A values when $\overline{u} > 0.8$ m s^{-1} are shown in the squares, diamonds, and circles, respectively on each plot. Inset is the joint pdf of $\overline{u}$ vs $\overline{u'^2}$, with the best-fit line.

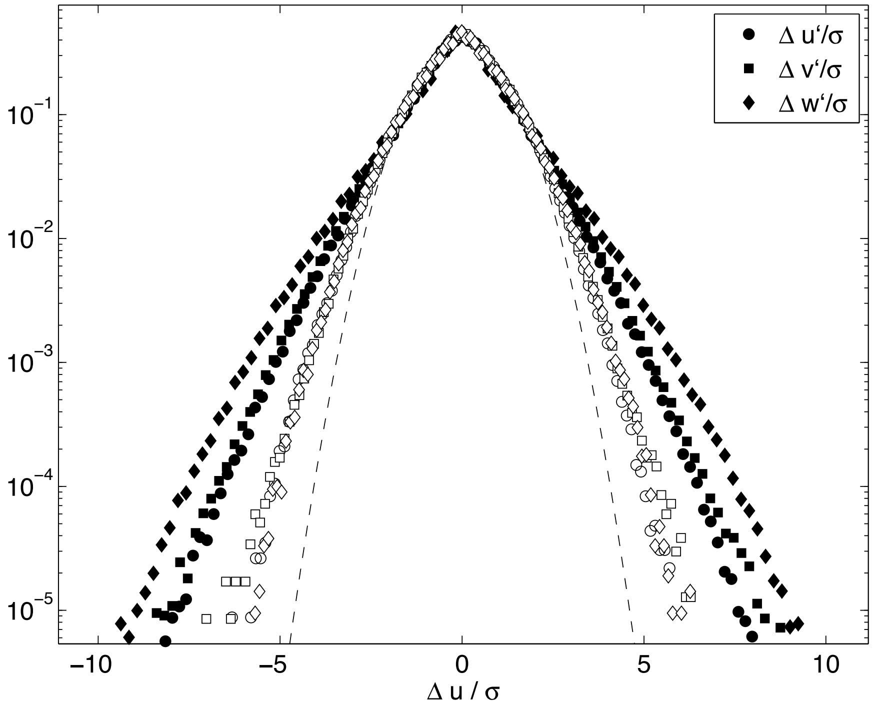

Figure 3.12: Probability density functions of the velocity perturbation differences, $\Delta u'$ (circles), $\Delta v'$ (squares), and $\Delta w'$ (diamonds) with a $\Delta t = 7.2s$ ($\sim 6\ m$) from Nodule Point ADV data, with Gaussian curves for reference (dashed). Black includes when $A < 0.005 m^2\ s^{-2}$, white includes when $A > 0.005 m^2\ s^{-2}$.

locity increments is computed for high versus low A (A greater or less than $0.005 m^2\ s^{-2}$), compared to low A. Although slightly counter-intuitive, this result suggests that within a single coherent structure, velocity increments are more Gaussian, but in differences spanning from one smaller-scale structure to the next, the intermittency appears. These results show that the coherent events at $\Delta t = 7.2s$ ($\Delta x \sim 6m$) are nearly random in all three directions, as is expected from the structure function analysis and the spectral results of Thomson et al. (2012), which are isotropic at this scale. It is possible that using the pdf to parameterize intermittency with A is not useful, since choosing Δt may be a larger indicator of intermittency, so the dependence on A does not appear.

Parameterizing coherence with I_u, TKE, $\overline{CTKE}$, and A is possible with regression analysis between each of these metrics and the integral and Taylor scales, Λ and λ. Table 3.1 shows these results, identifying A as most closely parameterizing coherence in the Taylor

	λ	Λ
I_u	0.596	0.450
TKE	0.747	0.079
$\overline{CTKE}$	0.680	0.017
A	**0.884**	0.317

Table 3.1: Coefficients of correlation, R^2, between Taylor scale, λ, and Integral scale, Λ, and I_u, TKE, $\overline{CTKE}$, and A from the Nodule Point ADV data.

scale, λ, while the coefficients of determination are lower for TKE, $\overline{CTKE}$ and I_u (i.e., poorly predicted). Figure 3.13 plots this relationship between A and λ. It makes sense that $\overline{CTKE}$ and A have stronger relationships with coherence time scales since they include more information about the cross-correlations and directional variability than I_u. The R^2 value of 0.884 supports this claim, suggesting that A is a better measure of coherence in a flow than TKE, $\overline{CTKE}$ or I_u. This also indicates that, since the longer time scales are more intermittent, these intervals are also higher in A.

Anisotropy is possibly the most important feature of the turbulence to parameterize since it is not captured at all by the currently-used turbulence intensity. The four different color schemes on the the barycentric map in Figure 3.14 highlight the dependencies of each parameter on the anisotropy. The peaks in all four quantities do happen when the flow is furthest from isotropic (three-component limit), but the overall coloring varies substantially. While turbulence intensity does have a strong relationship with anisotropy, it is misleading; since I_u only measures one component, it is defined to peak at the one component limit. The behavior of the $\overline{CTKE}$ and TKE on the barycentric map is fairly random, while the dependence on A is more related to the location on the map.

Using the comparisons made in this section, it is clear that A captures the behavior of $CTKE$, but provides more helpful information than I_u, while correlating closely with both the Taylor correlation scale and the proximity to the most anisotropic corner of the barycentric map. These results all support the use of A to parameterize turbulence in a tidal strait. If an additional parameter is to be calculated also, TKE shows the second strongest

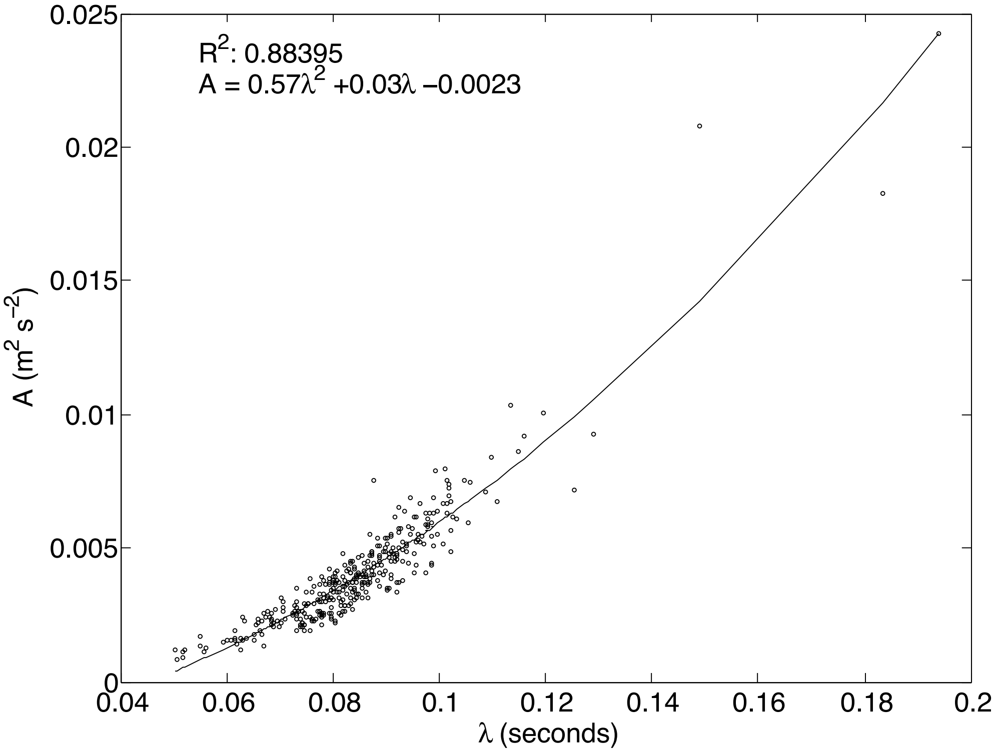

Figure 3.13: A versus Taylor scale, λ, for each 10-minute interval with $\overline{u} > 0.8$ m s^{-1} at Nodule Point with the quadratic fit line and R^2 value shown.

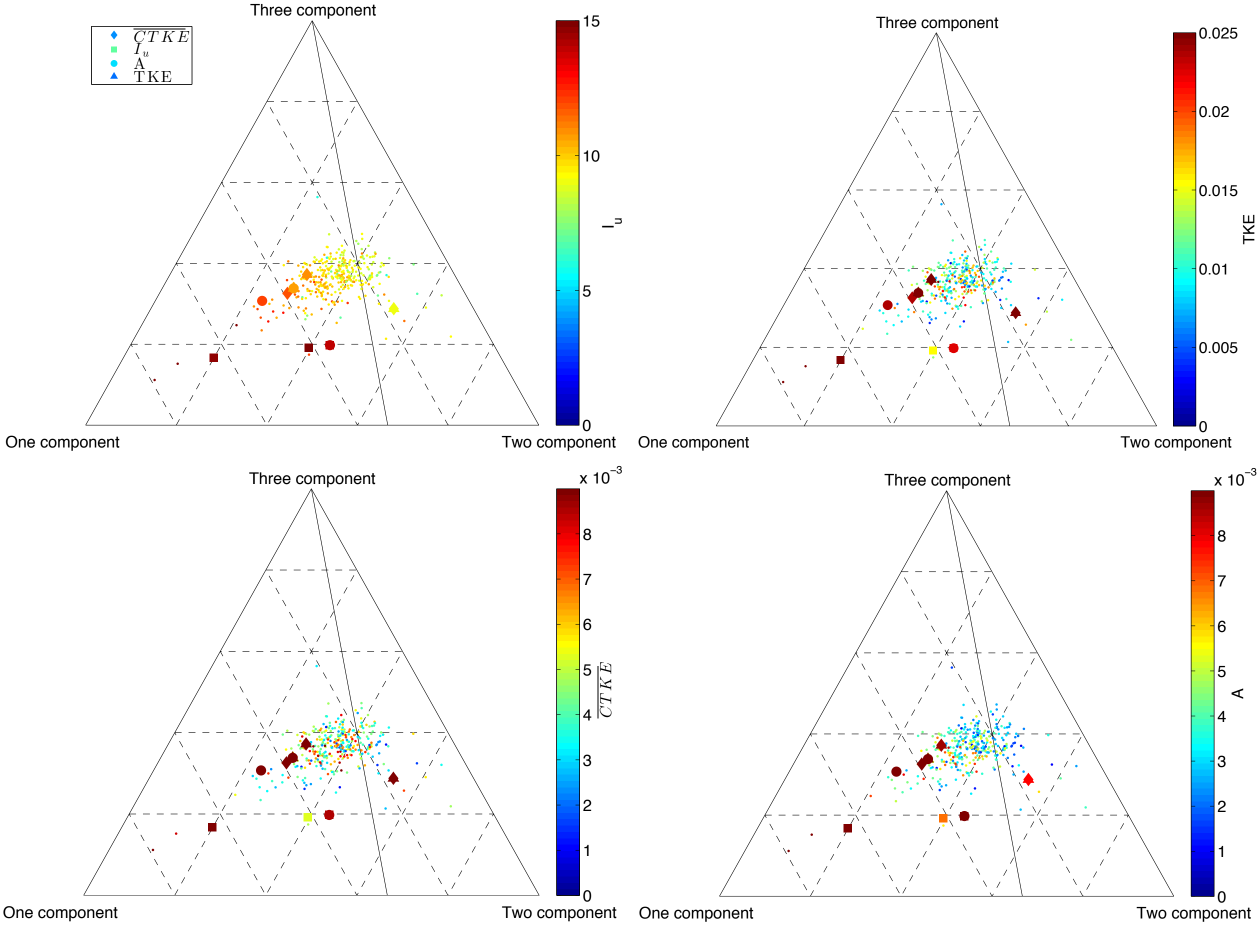

Figure 3.14: Barycentric maps based on C_{1c}, C_{2c}, and C_{3c} for the 10-minute intervals with $\overline{u} > 0.8\ m\ s^{-1}$ at Nodule Point. Clockwise from top left plots are colored based on turbulence intensity, I_u, TKE, A, and $\overline{CTKE}$. Three 99th-percentile values of I_u, TKE, $\overline{CTKE}$, and A values when $\overline{u} > 0.8\ m\ s^{-1}$ are shown in the squares, diamonds, and circles, respectively on each plot.

correlation to length scales, though anisotropy is lacking.

3.5 Conclusions from Tidal Turbulence

With the goal of more extensively characterizing the turbulence at a potential tidal energy site in the Puget Sound, I used ADV measurements to calculate turbulent properties like coherence, intermittency, and anisotropy. Making a comparison between the physical properties and the general turbulence metrics (I_u, TKE, $CTKE$, and A), we showed that the anisotropy magnitude, A, which we introduced, is the best for parameterizing the turbulent properties. Instead of calculating many different statistics, A can be used, independent of the chosen coordinate system, and the other characteristics can be inferred.

Though the ADV only measures velocities at one point in space, its high sampling frequency and low Doppler noise make it a viable tool for computing temporal turbulent statistics. With Taylor's hypothesis of frozen turbulence, these temporal statistics can be extended to spatial scales. However, real-world complexity may be hidden in this analysis by this hypothesis. In order to avoid the need for this assumption, measurements in time *and* in space are necessary. An array of ADVs can provide the spatial resolution, improving with the number of locations collecting simultaneous observations. Undoubtedly, new insight into the coherent, intermittent-in-time signals sensed here would result from information about their horizontal and vertical spatial coherence and intermittency.

The next chapter will compare the statistics of the observations to those of the output of turbulence from numerical models. The analysis here showed that turbulence in this region is strongly anisotropic, with coherent, intermittent events. A comparison between stochastic turbulence and turbulence created by a large-eddy simulation for this location will identify the strengths and weaknesses of each type of model in an effort to improve modeling capabilities for turbine design.

Chapter 4

Modeling Realistic Turbulence: TurbSim & LES

With the major disadvantage presented by the limited availability of observations of ocean turbulence, numerical models are invaluable to understanding of the energy transfer process in the oceans. Two models are presented here which use different foundational concepts to solve for a full flow field, including turbulence. The National Renewable Energy Laboratory's (NREL) HydroTurbSim (or TurbSim) model is based on the assumption of a kinetic energy spectrum with forcing and dissipation scales, and an inertial range in between (Figure 1.1), and an inverse Fourier transform is performed to obtain a time series of velocities (Jonkman, 2009). On the other hand, the National Center for Atmospheric Research's (NCAR) LES model is based on the pseudo-spectral, wave-averaged, non-hydrostatic, Boussinesq equations of fluid motion, where small-scale turbulence is parameterized (Moeng, 1984). First, output from the TurbSim model is compared to the observations from Nodule Point, using several of the metrics introduced in Chapter 3 as the indicator of goodness of the model. Then, the output from the NCAR LES is analyzed, and spatial correlations are compared between the two models.

Thyng et al. (2013) compared these ADV records and related observations in this region to a simulation using the hydrostatic, Boussinesq, sigma-coordinate Regional Ocean Modeling System (ROMS, Shchepetkin and McWilliams (2005)). Their results indicate that the large scale flow is adequately simulated, but the model resolution in their implementation is unable to fully reproduce the characteristics of the observed turbulence. They propose extensions to these parameterizations that can be used diagnostically and can guide future parameterization improvements. Models like TurbSim and NCAR LES are meant to resolve turbulence at smaller scales that ROMS relegates to parameterizations, so these models are expected to compare more closely to the observations.

Figure 4.1 shows a snapshot in time of velocity perturbation, u', from both models to be analyzed here. The TurbSim model produces low-resolution, cross-stream-vertical plane of velocities. The top border of the TurbSim output is aligned with a the top of the (hypothetical) rotor disk, shown as the dashed lines in the larger LES domain. From this figure, it appears that the LES has more coherence than TurbSim, so this is the main hypothesis of this work. It is expected that TurbSim will create turbulence that matches the lower-order statistics (i.e., mean and turbulence intensity), while the LES will create realistic coherent structures. Only one LES run has been performed, for a short time period, so the results here are preliminary, with better agreement with the observations to come with a longer time series from model data.

4.1 Introduction to Stochastically Modeled Turbulence

The NREL TurbSim model (Jonkman, 2009) is a stochastic model which creates two-dimensional flow fields in time. The method assumes an isotropic kinetic energy spectrum which is put through an inverse fast Fourier transform (ifft) to create a time series of velocities at the location of the hub. An example of a spectrum and its unique time series is shown in Figure 4.2. User-defined Reynolds stresses and a model-defined coherence function are used

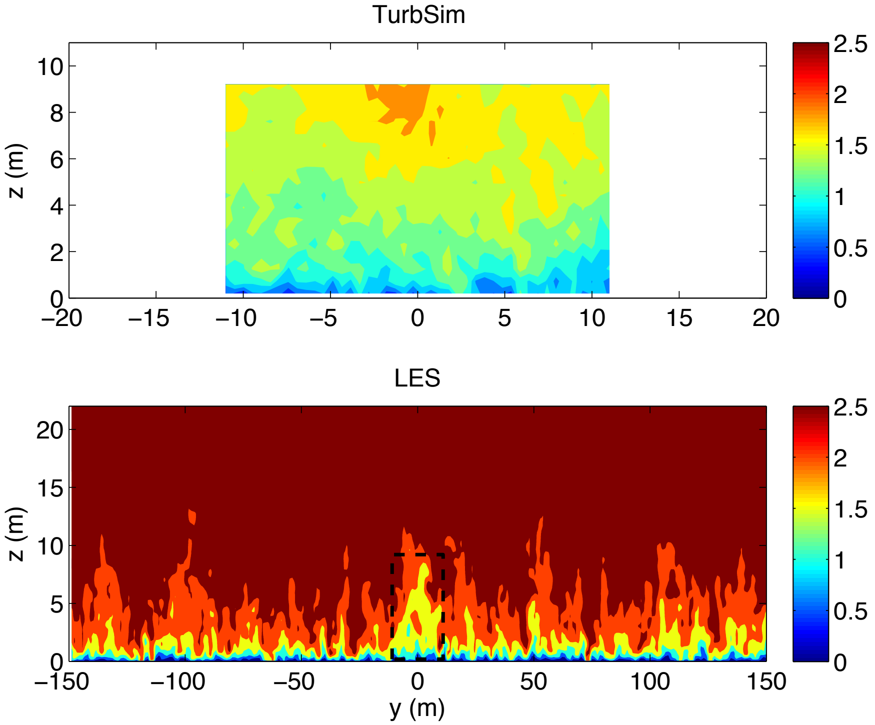

Figure 4.1: Cross-stream-vertical $(y-z)$ planes of u-velocity perturbation, u', from TurbSim (top) and the NCAR LES (bottom). The black dashed lines on the LES figure show the coverage of the TurbSim model.

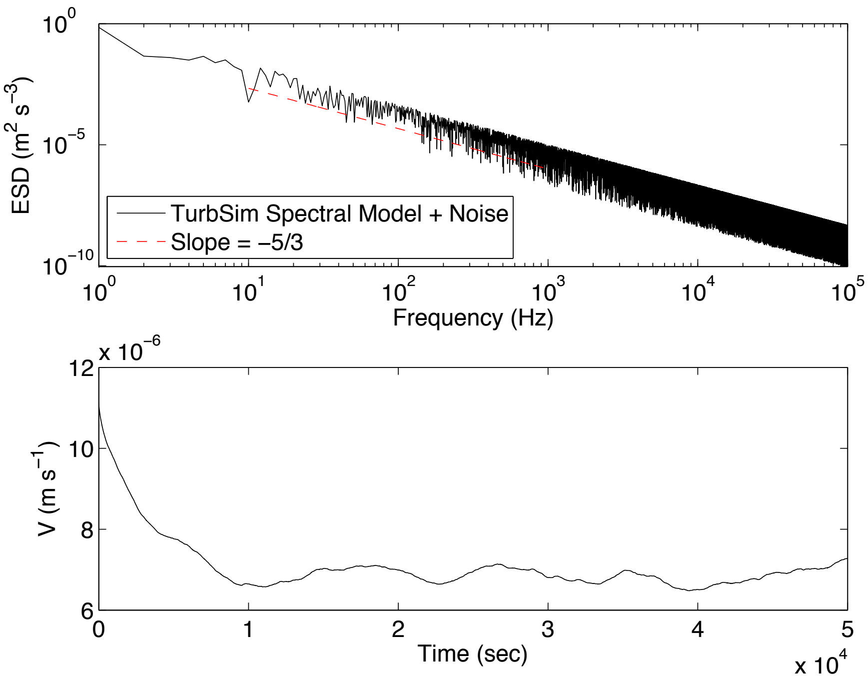

Figure 4.2: a) TurbSim spectral model for tidal turbulence for horizontal velocity at the hub, with a slope of $\lambda = -\frac{5}{3}$ from K41 shown in red for reference. b) Time series of the horizontal velocity associated with the kinetic energy spectrum in a).

to determine all three velocity components in the full $y - z$ plane (y is the horizontal coordinate, and z is the vertical, both tangent to the turbine rotor plane). TurbSim has recently been adapted for simulating tidal environments (and informally called HydroTurbSim), with specific spectral models and coherence functions with empirically derived coefficients from observations at Marrowstone Island, WA and the East River, NY (Jonkman and Kilcher, 2012). An overview of the method used in TurbSim is shown in Figure 4.3.

The spectral model form for velocity component K (i.e., $K = u,\ v$, or w) is

$$S_K(f) = \frac{\sigma_K^2 s_{1,K} \left[\frac{\partial u}{\partial z}\right]^{-1}}{1 + s_{2,K} \left[\frac{f}{\partial u/\partial z}\right]^{5/3}}, \tag{4.1}$$

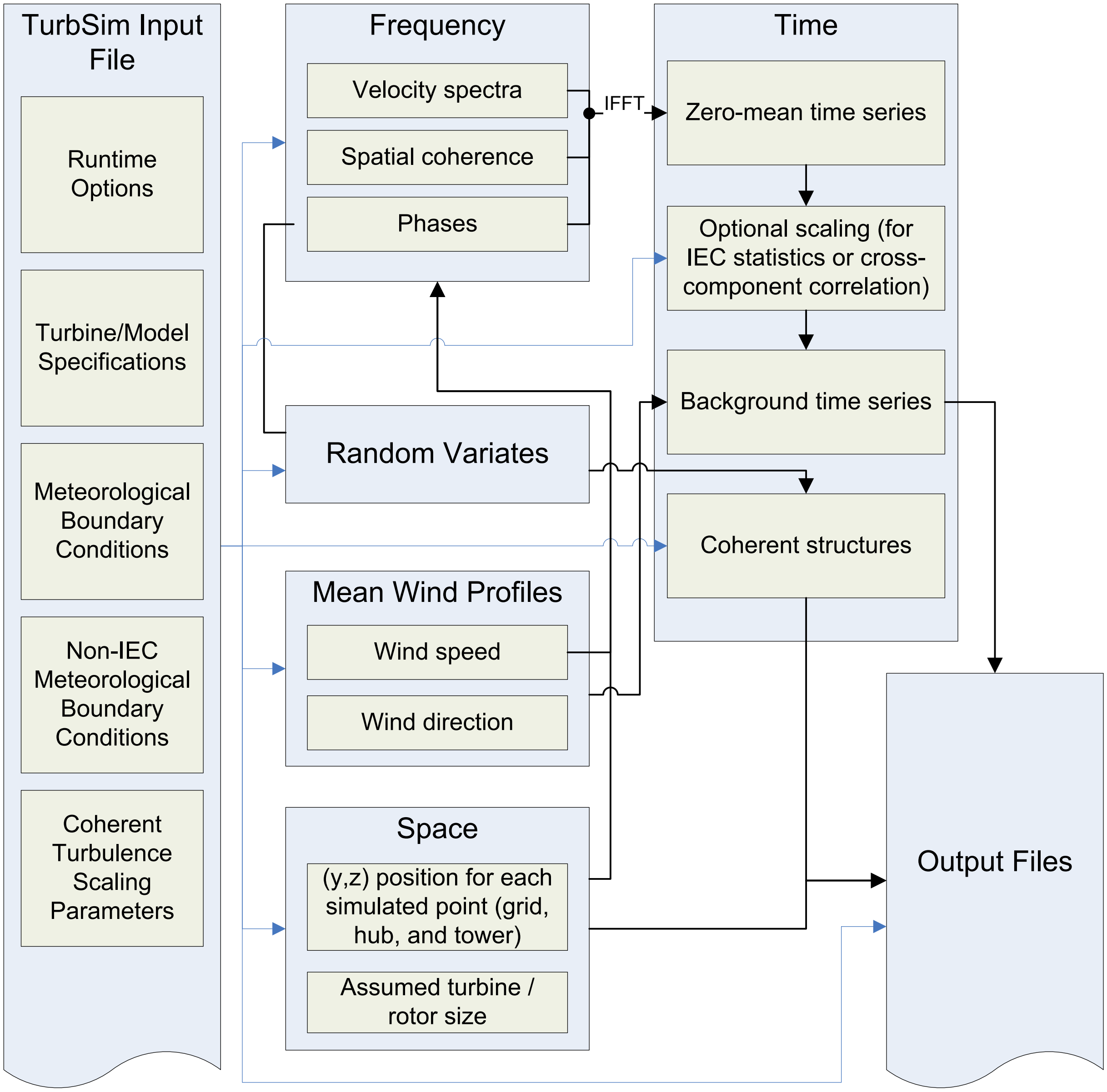

Figure 4.3: Figure C-1 of Jonkman and Kilcher (2012): Overview of the TurbSim simulation method; blue lines indicate processes influenced by input-file parameters; black lines indicate internal variables and processes. Note: coherent structures capability does not exist for tidal simulations.

where f is frequency, and the empirically defined coefficients are

$$\langle s_{1,K}, s_{2,K} \rangle = \begin{cases} \langle 1.21, 4.30 \rangle, & K = u \\ \langle 0.33, 0.50 \rangle, & K = v \\ \langle 0.23, 0.26 \rangle, & K = w. \end{cases} \tag{4.2}$$

The shear, $\partial u / \partial z$, is calculated from the specified mean velocity profile, and the component-TKE levels, σ_K^2, are determined based on an exponential profile proportional to $URef^2$ at a reference height, $RefHt$ (both user-defined):

$$\sigma_K^2 = (0.05URef)^2 \, \mu_K e^{-2z/RefHt}, \tag{4.3}$$

where $\mu_u = 4.5, \mu_v = 2.25, \mu_w = 0.9$ are empirically determined coefficients from Marrowstone Island, WA.

While still in frequency space, a spatial coherence function is applied to the spectrum of each velocity at the hub to create a two-dimensional plane of $u-, v-$ and w-velocities. The degree of spatial coherence between point i and j is defined in general as

$$Coh_{i,j}(f) = \frac{|S_{ij}(f)|}{\sqrt{S_{ii}(f) S_{jj}(f)}}, \tag{4.4}$$

where S_{ii} is the power spectral density, and S_{ij} is the cross-spectral density. For the specific spectral model used for tidal simulations, this relationship is estimated as

$$Coh_{i,j_K} = Exp\left(-a_K \left[\frac{r}{z_m} \right]^{CohExp} \sqrt{\left[\frac{fr}{u_m} \right]^2 + [b_K r]^2} \right), \tag{4.5}$$

where r is the distance between points i and j, f is cyclic frequency, $CohExp$ is a coherence exponent input parameter, and z_m and u_m are the mean height and wind speed of points i and j. The spatial coherence decrement, a, and offset parameter, b, are defined separately for each component wind speed.

At each location, a pseudorandom number generator is used to create random phases (one per frequency per grid point per wind component) for the velocity time series. To move from frequency space, where the flow is defined, to physical space, where the velocities are desired, an ifft is computed, and a zero-mean time series is created. This time series is then added to the background mean profile, defined as a logarithmic profile and plotted in Figure 4.11:

$$\overline{u}(z) = \frac{UStar}{\kappa} ln \left[\frac{z}{z_{ref}} \right] + URef, \tag{4.6}$$

where $\kappa = 0.41$ is von Karman's constant. The assumption of a log-layer profile is a strong assumption that is not able to be confirmed with the ADV observations at Nodule Point, but this profile is based on vertical profiles observed with an ADCP at other similar tidal locations, so the assumption is accepted for Nodule Point as well.

The TurbSim product is a two-dimensional plane of three components of velocity which change in time. The comparison to the observations is done by only using the model output at the location of the hub at all times. TurbSim was run with 34 different mean speeds from $-1.8\ m\ s^{-1}$ to $1.8\ m\ s^{-1}$, and Reynolds stresses defined from the observations (Figure 4.4). Each mean speed was run 10 times, to increase the amount of data used for calculation and presentation of statistics. Statistics are computed on each 10-minute run individually, and each run is independent of all others (the changing mean speeds are not meant to be part of a time series).

4.2 TurbSim results

The statistics used in Chapter 3 were computed from the TurbSim output, and the most informative results are shown here. The turbulence intensity versus mean speed plot (Figure 4.5) shows that, though the turbulence intensity is defined to have an inverse relationship with $\overline{u}$ ($I_u \sim 1/\overline{u}$), the turbulence intensity from TurbSim is constant. Though this is unre-

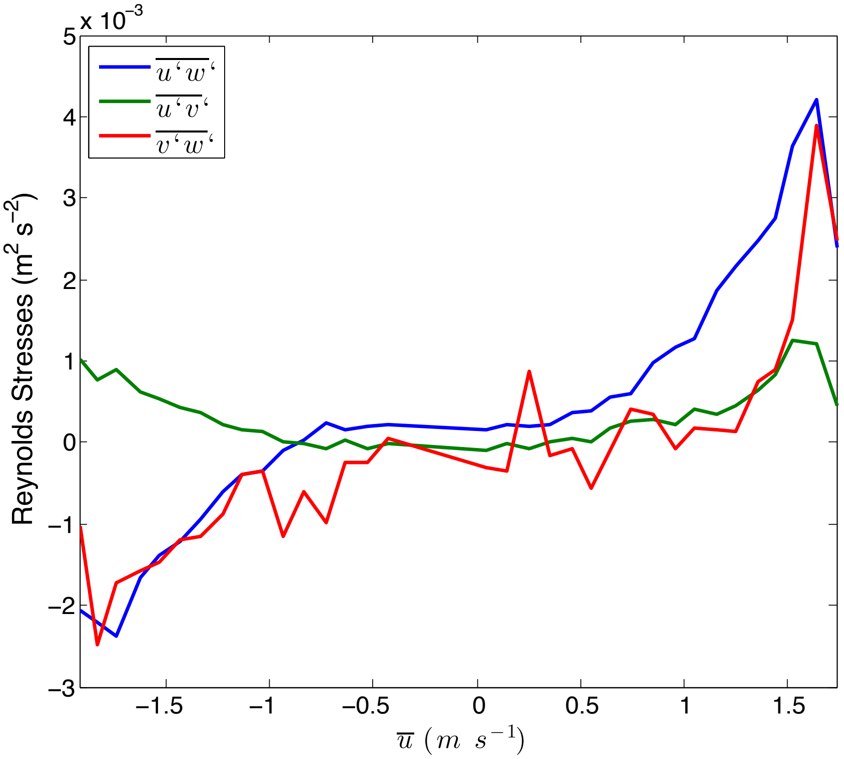

Figure 4.4: Average Reynolds stresses (blue - $\overline{u'w'}$, green - $\overline{u'v'}$, red - $\overline{v'w'}$) for differing mean velocities, $\overline{u}$, from ADV data at Nodule Point, which are input at hub height for TurbSim.

alistic (compare the colored dots to the averages from the Nodule Point ADV observations in black), above the cut-in speed of 0.8 $m\ s^{-1}$, the differences are small. Similar to the observations, however, the color based on anisotropy magnitude, A, highlights the intervals that have both the highest turbulence intensity as well as mean speed. When generating the spectra for the v- and w-velocities, TurbSim sets $\overline{v'^2}$ and $\overline{w'^2}$ to be constants proportional to $\overline{u'^2}$, defining k, and the anisotropy in the Reynolds normal stresses. The user defines the Reynolds shear stresses, so the anisotropy tensor, and therefore A, is comprised of a combination of model and user-defined quantities that are not changing realistically with the flow. The barycentric map (Figure 4.6) shows relatively similar locations of intervals from TurbSim and observations, suggesting that the anisotropy is dominated by the shear Reynolds stresses (user-defined to match observations), rather than normal stresses (defined by TurbSim). Later results will show how the anisotropy in the normal stresses is missing from the TurbSim data.

A comparison between $\overline{CTKE}$ and A (Figure 4.7) shows the correlation between TurbSim (blue dots) and the observations (red dots), with similar behavior between the two. The closer correlation between $\overline{CTKE}$ and A in TurbSim is also evidence of A being dominated by the shear-components of the anisotropy, which are the components that determine $CTKE$. The major difference between observations and TurbSim results is that *the most extreme events in* $\overline{CTKE}$ *and* A *are missing from the TurbSim data.*

This begs for further analysis into the coherent and intermittent events in TurbSim output. To this end, the temporal autocorrelation function and Taylor and integral scales were computed, and shown in Figure 4.8. It is immediately clear that the coherent events from the observations (the intervals with autocorrelations with much shallower slopes, that stay correlated longer) are missing in the autocorrelations from TurbSim. Every interval becomes uncorrelated at the same rate, which is also unlike the observations where some become immediately uncorrelated, while others remain. The Taylor and integral scales are indicative of this behavior also. Though the mean Taylor scale from TurbSim ($\overline{\lambda} = 0.59s$)

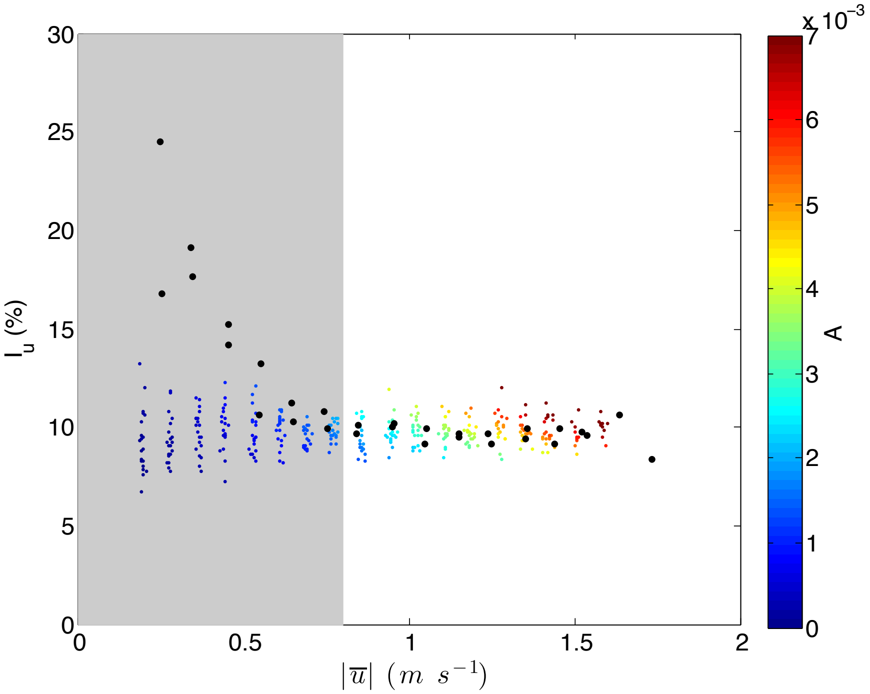

Figure 4.5: Turbulence intensity versus mean speed for the ADV observations from Nodule Point (averaged at each mean velocity where TurbSim was run; black dots), and from TurbSim (color, based on anisotropy magnitude, A). The slack conditions are shown in the grey box. LES results fall off the figure at mean speed of 3.2 $m\ s^{-1}$, with turbulence intensities of $12-15\%$.

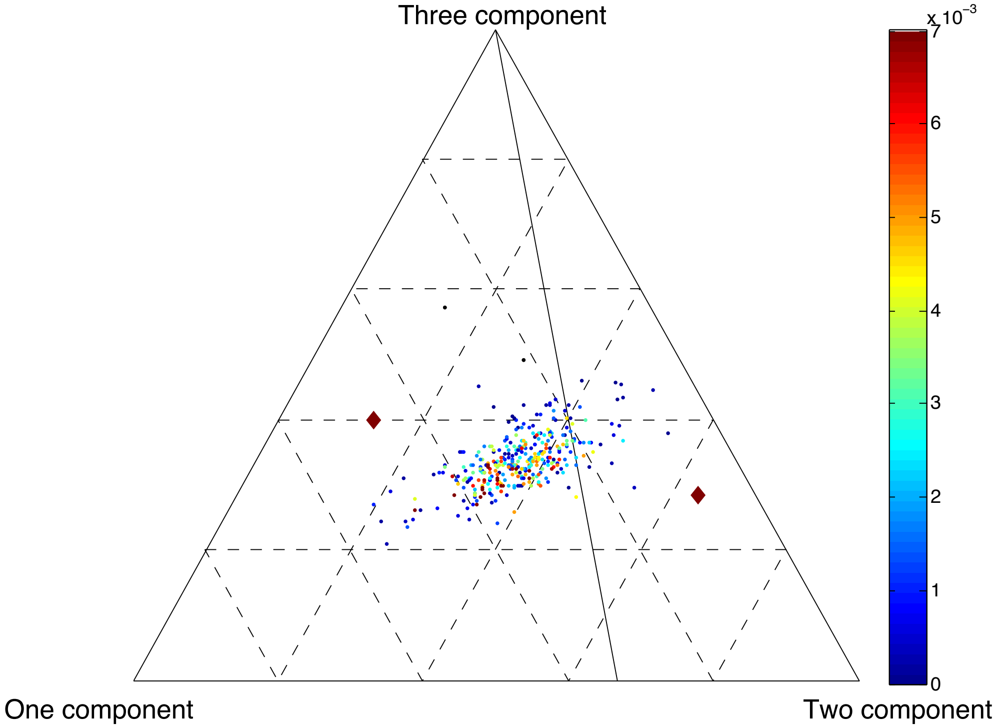

Figure 4.6: Barycentric map from TurbSim output with large diamonds from the two intervals from LES output, colored by the anisotropy magnitude, A.

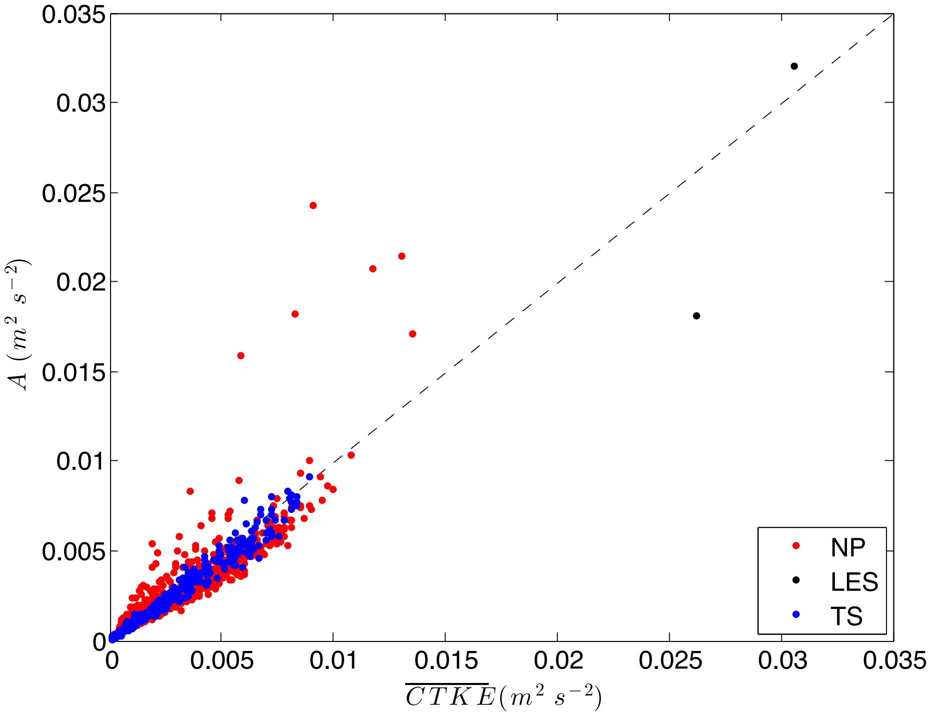

Figure 4.7: $\overline{CTKE}$ versus A from TurbSim output (blue), LES (black), and observations from Nodule Point (red) with the dashed one-to-one line for comparison.

is higher than that of the observations ($\overline{\lambda} = 0.08s$), the intervals that become uncorrelated faster in the observations are missing. The average integral scale is also similar to the observations (TurbSim: $\overline{\Lambda} = 8.197s$, ADV: $\overline{\Lambda} = 10.127s$), but an analysis of the distribution of integral scales shows a large contrast. Figure 4.9 compares the distributions of integral scales and their associated length scales (using Taylor's hypothesis and the mean velocity for each 10-minute interval) between the observations at Nodule Point (a and c) and the TurbSim output (b and d). The peaks (approximately the mean) of the histograms are located at a similar scale, but the tails are much larger in the observations, and cover a significantly longer range. The longer time scales that are missing from TurbSim are related, through Taylor's hypothesis, to the longer spatial scales, including the $75m$ scales seen by McCaffrey et al. (submitted, 2013) and Thomson et al. (2012).

The lack of coherent events is also seen in the probability density functions of velocity increments ($\Delta u_\tau = u(t+\tau) - u(t)$ at time interval, τ) shown in Figure 4.10. The pdf has

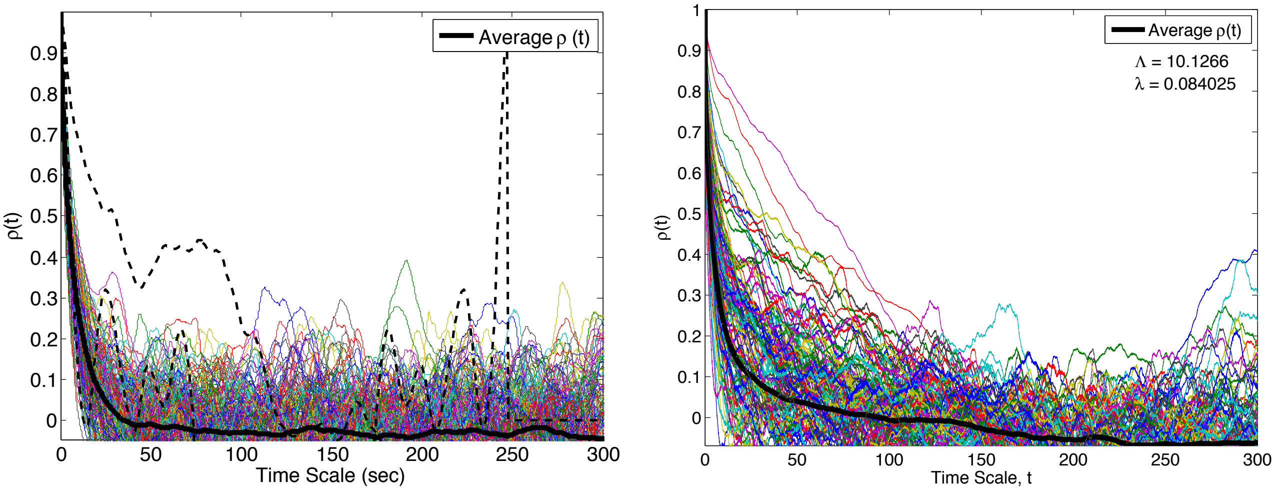

Figure 4.8: Left: Autocorrelation function for each 10-minute interval from TurbSim output, with the average shown in bold black. The two dashed lines are the autocorrelations from the two intervals from LES output. Right: Autocorrelations from the ADV observations at Nodule Point, with the average shown in bold black.

been used with TurbSim results in the atmosphere to show “gustiness” in the winds and the alternating loads on a wind turbine that result; strong differences or changes over time steps appear in the non-Gaussian tails of the pdf of both velocity increments and torque increments (Mücke et al., 2011). In observations (Figure 4.10a), these intermittent events are seen at longer time intervals ($\Delta t = 30$ and $60s$), but were not seen at $\Delta t = 1/10s$. In contrast, the pdfs of velocity increments from TurbSim output show a *decrease* in intermittency at $\Delta t = 30$ and $60s$. As shown in Mücke et al. (2011), it is important to model the intermittent events of the flow in order to accurately predict turbine loads, and these results show that TurbSim does not model these features. In addition, there is anisotropy in Δu, Δv, and Δw at the $\Delta t = 1/10s$ of the observations, but not so in TurbSim, which always assumes isotropic normal stresses.

In conclusion, the comparison between output from TurbSim and the ADV observations for Nodule Point show both positive and negative aspects of the stochastic model. In general, TurbSim accurately produces turbulence as it is defined by the model, including stresses and anisotropy shapes based on the barycentric map of Banerjee et al. (2007). However, the

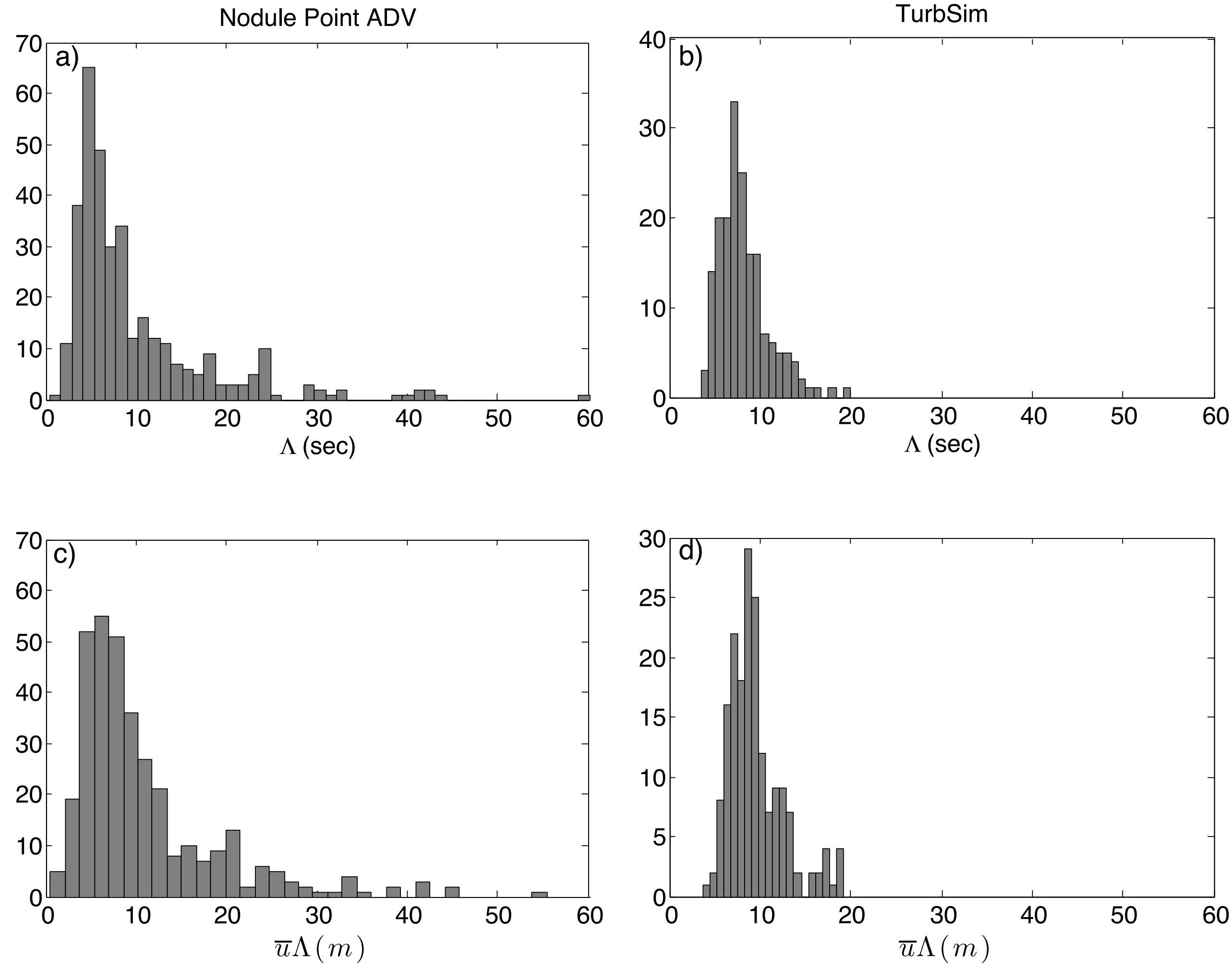

Figure 4.9: Histograms of the integral scale, Λ (a and b) and associated spatial scale from Taylor's hypothesis, $\overline{u}\Lambda$ (c and d), for the observations at Nodule Point (a and c) and Turbsim output (b and d).

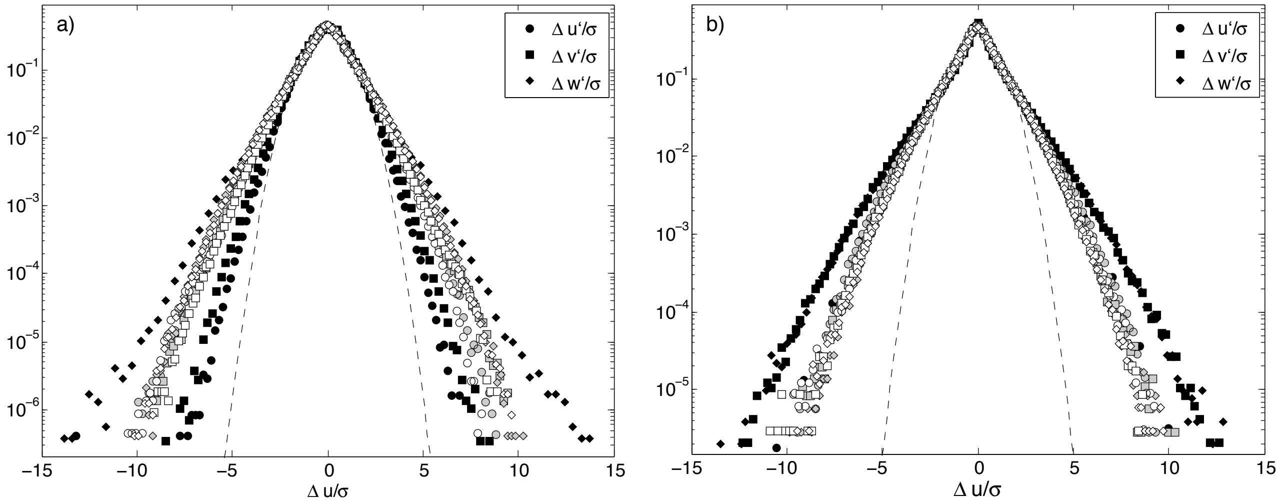

Figure 4.10: Probability density function of velocity increments (Δu - circles, Δv - squares, Δw - diamonds), normalized by each's standard deviation, in increasing time intervals: black is $\Delta t = 1/10s$, gray is $\Delta t = 30s$, and white is $\Delta t = 60s$, from observations at Nodule Point (a) and from TurbSim output (b).

most impact-ful coherent events are not created by the stochastic model. This is a known problem in TurbSim; in the atmospheric version of the model, empirically-derived, Kelvin-Helmholtz-like coherent structures are added to the final turbulent time series (Jonkman and Kilcher, 2012). A similar analysis to determine the appropriate method for including coherent structures in the tidal environment has not been completed, as it has for the atmosphere.

4.3 Introduction to NCAR LES

The previous section showed that coherent events are not created by a stochastic model, so a physical model, based on the NS equations, is a possible improvement. The model chosen here is the NCAR LES, introduced by Moeng (1984). Collaborators at the Turbulence and Energy Systems Laboratory (TESLa) at the University of Colorado Boulder have modified the model, previously adapted for ocean scenarios by McWilliams et al. (1997), to model the tidal channel at Nodule Point, WA (Alexander and Hamlington, 2014). This version of the model solves the filtered wave-averaged, Boussinesq equations (called the Craik-Leibovich equations) given by

$$\begin{aligned}
\frac{D\mathbf{u}}{Dt} + (\mathbf{f} + \omega) \times (\mathbf{u} + \mathbf{u}_s) &= -\nabla \pi - g\hat{z}\,(\rho/\rho_0) + \hat{\mathbf{x}}F_p + SGS, && (4.7)\\
\pi &= p/\rho_0 + \frac{1}{2}\left[|\mathbf{u} + \mathbf{u}_s|^2 - |\mathbf{u}|^2\right] && (4.8)\\
\frac{D\rho}{Dt} + \mathbf{u}_s \cdot \nabla \rho &= SGS, && (4.9)\\
\nabla \cdot u &= 0, && (4.10)
\end{aligned}$$

where $\mathbf{u}$ is the three-dimensional flow velocity, $\mathbf{f}$ is the Coriolis parameter, $\omega = \nabla \times \mathbf{u}$ is the vorticity, g is the acceleration due to gravity, ρ is the density, ρ_0 is a reference density, p is the pressure, F_p is a driving pressure term, and SGS represents subgrid-scale terms from the LES model. These equations include the effects of wave forcing by the additional Stokes velocity terms, $\mathbf{u}_s$, which is constant horizontally and super-exponentially decreases with depth. The pressure-driving force is constant in these runs, but will be used in the future to simulate changing magnitudes and directions of the mean flow in a tidal channel (Alexander and Hamlington, 2014). The SGS stresses, τ_{ij} are derived from the method of Sullivan et al. (1994) based on both the resolved-scale strain rate, S_{ij}, and the horizontally-averaged strain rate, $\overline{S_{ij}}$, as

$$\tau_{ij} = 2\nu_t \gamma S_{ij} - 2\nu_T \overline{S_{ij}}, \tag{4.11}$$

where ν_t and ν_T are turbulent and mean flow eddy viscosities, respectively, and $\gamma = S'/(S' + \overline{S'}$ is an isotropy factor written in terms of the strain rate magnitudes $S' \equiv \sqrt{2\overline{S'^2_{ij}}}$ and $S \equiv \sqrt{2\overline{S^2_{ij}}}$. The classic Smagorinsky model defines the turbulent eddy viscosity as

$$\nu_t = (C_s)^2 \sqrt{2 S_{ij} S_{ij}}, \quad C_s = \left(C_k \sqrt{\frac{C_k}{C_s}} \right)^{1/2}, \tag{4.12}$$

and the mean flow eddy viscosity as

$$\nu_T = (C_K L_m)^2 \sqrt{\left(\frac{\partial \overline{u}}{\partial z}\right)^2 + \left(\frac{\partial \overline{v}}{\partial z}\right)^2} \tag{4.13}$$

where u and v are horizontal velocities in the along-stream and cross-stream directions, and the model coefficients are $C_k = 0.1,\ C_e = 0.93$, and the product $C_K L_m$ is chosen to match Monin-Obukhov similarity theory near the wall (Sullivan et al., 1994). This work does not analyze the choice of SGS model, but rather focuses on the scales of the turbine $(1 - 100m)$.

The model was run by Alexander and Hamlington (2014) to simulate wind-, wave- and tidally-driven flow at Nodule Point, with a depth of $22m$, and has a max mean speed at the surface of 3.205 $m\ s^{-1}$. The model was spun up to allow the turbulence to develop fully, when the turbulence intensity matched the observations. An optional actuator disk turbine is available, though this analysis does not include that feature. The model has $256 \times 256 \times 320$ grid points for a $300m \times 300m \times 22m$ simulation ($1.17m$ resolution in the horizontal directions and $6cm$ in the vertical). With a varying time step of about $1s$, the data used span $848s$, giving one full 10-minute period, and half of a second. The results for these two intervals will be discussed, and future work will include a larger dataset in time.

4.4 LES Results

Figure 4.11 shows vertical profiles of mean u-velocity and turbulence intensity from the LES and TurbSim (TS), with the averages from the ADV observations at hub height at Nodule Point (ADV). The LES model creates a more realistic mean velocity profile of $\overline{u}$ (Figure 4.11a) that includes wall boundary profile that reaches 0 at the wall. The TurbSim model does not resolve the wall boundary. However, the LES run has mean speeds that are much faster than observed, so future model runs will be performed to produce a more realistic mean profile. The turbulence intensity profiles (Figure 4.11b) each have benefits over the other. TurbSim very accurately captures the turbulence intensity levels of the observations at hub

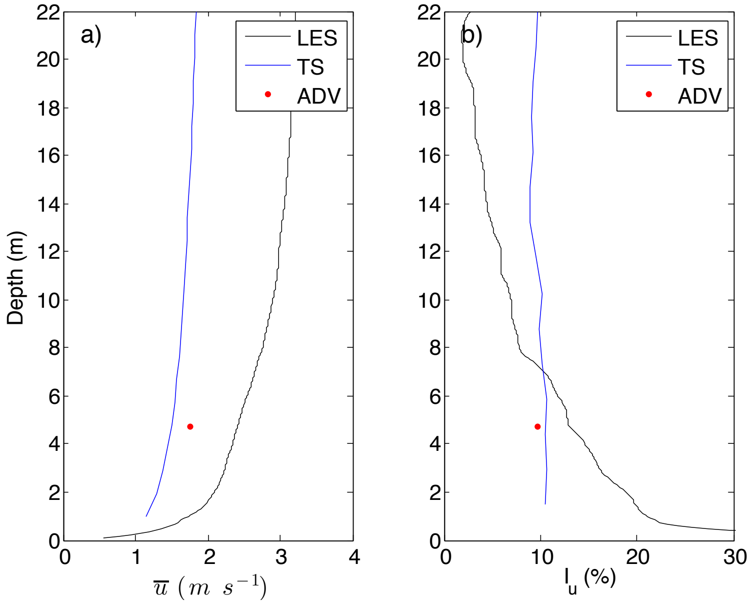

Figure 4.11: a) Vertical profile of the mean speed, $\overline{u}$, from LES (black) and TurbSim (blue), with the max u-velocity from all observations (ADV) shown in the red dot. b) Vertical profiles of turbulence intensity from LES (black), TurbSim (TS; blue), and the average turbulence intensity at hub height for intervals with $\overline{u} > 0.8$ m s^{-1} from observations (ADV; red dot).

height, but has a constant profile in z, independent of mean speed. The LES, on the other hand, captures the changing turbulence intensity with depth (including a slight increase at the surface from the wave and wind effects), but over-estimates I_u at hub height. The I_u profiles from the ADCP at Nodule Point in Thomson et al. (2012) show a higher average I_u at hub height from the ADCP than the ADV. The ADCP's profile is steeper than that of the LES, with minimum values of I_u at the surface of $8-9\%$, rather than $4-5\%$ in the LES.

The hope for using LES is to capture the intermittent, coherent structures in the flow. Using the same temporal statistics from the observational analysis, as well as spatial coherence, we can determine if LES does, in fact, generate more realistic turbulent features than TurbSim. The anisotropy eigenvalues were plotted on the barycentric map along with the TurbSim data in Figure 4.6, and also colored with the anisotropy magnitude, A. In general, the points match the observations and TurbSim results, as the points are closer to the one- and two-component limits than the isotropic limit. However, only having two

10-minute intervals is, unfortunately, not very helpful; more time information is needed to see the full range of anisotropy types and shapes. Knowing from the observations that there is also a dependence on the mean speed in the barycentric map (gray versus black points in Figure 3.9) requires longer model runs to identify the dependence in the LES data. From observations, the coherent structures appear to arrive during the slack conditions, but since the LES is not set up with the geographical details that are believed to force these features, they may not appear in the LES output.

When the LES intervals are plotted on the same color axis as the TurbSim data, they appear as very deep red, including the right-most point, which has a lower A, and is in the region that McCaffrey et al. (submitted, 2013) showed generally has lower A. This suggests that the LES data, with more time intervals included, should be plotted with its own scale for A to see the dependence. Figure 4.7 also supports this, with the two LES points (in black) far higher on the scale of $\overline{CTKE}$ and A. TurbSim results showed a lack in the highest values of $\overline{CTKE}$ and A; the LES output appears to capture these points, but the magnitude of both of the intervals suggests that the LES might, in fact, be *over*-estimating these quantities. Again, the conclusion to be made from these results is that we need many more intervals, again changing in mean speed, to determine the true behavior of A and $CTKE$ in the LES model.

Turning to the pdf for information on the intermittency in the LES model, the short times again become a problem. Figure 4.12 shows the pdfs of the velocity increments from the LES output. Only having $848s$ of data produces very noisy pdfs that do appear nearly Gaussian, but need more data to take form. Even the pdfs from the ADV data and TurbSim output with only $848s$ are scattered and more Gaussian than the pdfs with more data. However, the temporal autocorrelation can still be used to accurately identify the intermittent or constant behavior in the turbulence, represented by the distribution of coherence in the flow. Though there are only two intervals, a general idea can be gained by comparing the autocorrelations from the LES to that of TurbSim, as is done in Figure 4.8. The two dashed

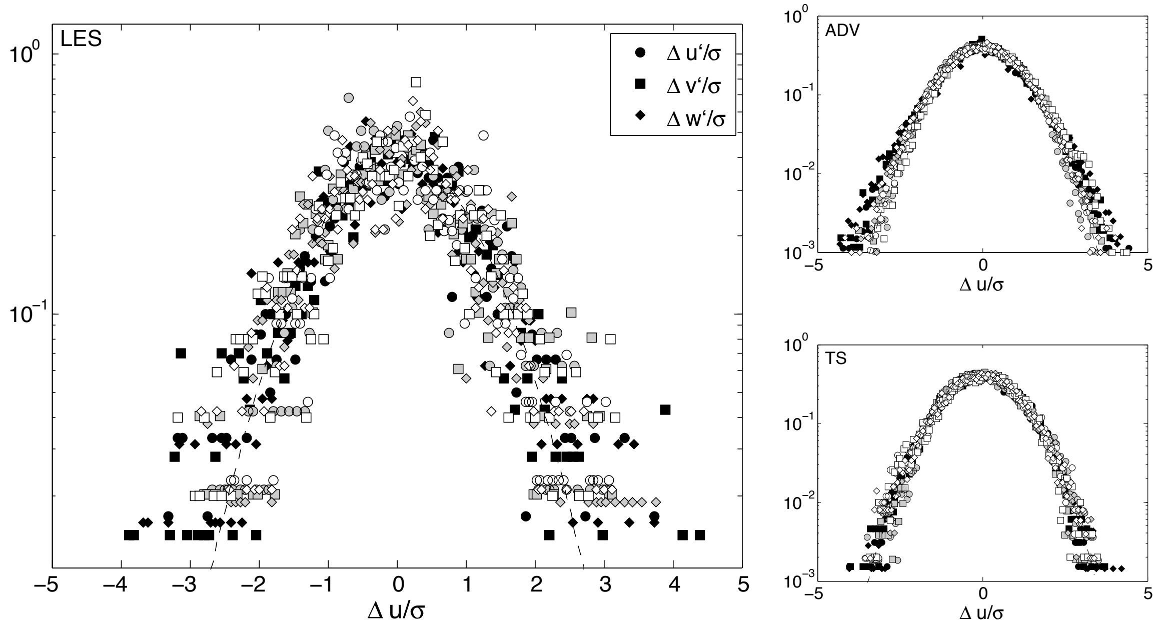

Figure 4.12: Left: Probability density function of velocity increments (Δu - circles, Δv - squares, Δw - diamonds), normalized by each's standard deviation, in increasing time intervals: black is $\Delta t = 1/10s$, gray is $\Delta t = 30s$, and white is $\Delta t = 60s$, from LES output. Example pdfs of $848s$ of the fastest mean velocities from the Nodule Point ADV observations and TurbSim output are shown on the right.

lines correspond to the two intervals of LES data (note that the second is only 248 seconds long, so $\rho(t > 248) = 0$), exhibiting differing levels of coherence, one of which is longer than every interval from TurbSim. The integral and Taylor scales for the first interval are $50.098s$ and $7.9647s$, and for the second interval they are $5.836s$ and $6.533s$, respectively. Using Taylor's hypothesis, this corresponds to a longest correlation length scale of $121.76m$. This length scale is very large, and is determined by the mean speed, which in this case, is much larger than observed. Therefore, in the case when the mean speed is 1.8 $m\ s^{-1}$, this length scale (assuming Λ doesn't change), is $90m$, which, though still slightly too large, is more reasonable and more consistent with the observations.

4.5 Spatial Correlations from LES

The advantage of having a numerical model is the spatial grid of velocities, not the limited data from an instrument. In order to assess the accuracy of using Taylor's hypothesis for estimating length scales, the spatial autocorrelation was calculated with the model output from the LES, and the results are shown in Figure 4.13. The spatial autocorrelation is defined as

$$\rho(r) \equiv \frac{\overline{u'(x,y,z)u'(x+r,y,z)}}{\overline{u'^2}}, \text{ or} \tag{4.14}$$

$$\rho(r) \equiv \frac{\overline{u'(x,y,z)u'(x,y+r,z)}}{\overline{u'^2}}, \tag{4.15}$$

where r is the separation distance in the streamwise (x, Figure 4.13a) or cross-stream (y, Figure 4.13b) direction and the overbar is an average in horizontal and vertical space. Since this method of estimating length scale uses the along-stream velocity, the spatial autocorrelation was first calculated in the along-stream-vertical plane. The spatial autocorrelations do not look very different from the temporal equivalents from the LES, but they do look quite different from the ADV observations' temporal autocorrelations. All lines become uncorrelated at about the same rate, and that is seen in the small range of Taylor scales ($2.9-4.3m$). Figure 4.14 compares the integral *length* scales from the observations and each model for the along- and cross-stream autocorrelations, either directly from the spatial autocorrelations or from Taylor's hypothesis of the temporal autocorrelation for the ADV and TurbSim (since its horizontal resolution is too small in the cross-stream case). The along-stream case for the ADV-TurbSim comparison was done above, but adding the LES to the analysis shows that, though the average integral scale is similar in all three cases, a strong bi-modal distribution is seen in the histogram of the LES results, with peaks at very small scales ($< 10m$) and large scales ($30-35m$). The mean integral scale of $18.5m$ is not indicative of the most common scales in the flow, making this an unreasonable parameter to use for characterizing the flow. The cause of this distribution is not clear from the physics of the model, which has no preferred scale at which turbulence is generated. The coherent features with length scales of greater than the water depth are all limited in the vertical direction, requiring the anisotropy to be high. Though it is desirable to have these coherent structures in the modeled flow, the distribution is not similar to the observations, so turbines built to withstand this turbulent environment would be "over-built," possibly losing the ability to generate power as efficiently. From this comparison between spatial and temporal autocorrelations, it appears that Taylor's hypothesis is not an accurate method of estimating length scales from time scales at these velocities, since the long time scales from $\rho(\tau)$ do not appear in $\rho(r)$.

The spatial coherence function from TurbSim, defined in Equation 4.5, is also plotted on Figure 4.13a. Since TurbSim does not create planes in the along-stream direction, this correlation function assumes isotropic turbulence in the along-stream and cross-stream directions so that the vector r between points i and j can be turned 90° (this may not be an accurate assumption, and will be discussed below). The TurbSim coherence function matches the LES output fairly well at the smaller scales, and appears to have the same behavior as the LES times with the integral scales at or below $10m$. The set coherence function does not allow for a bimodal distribution of integral scales, but at this point, it is not certain that the

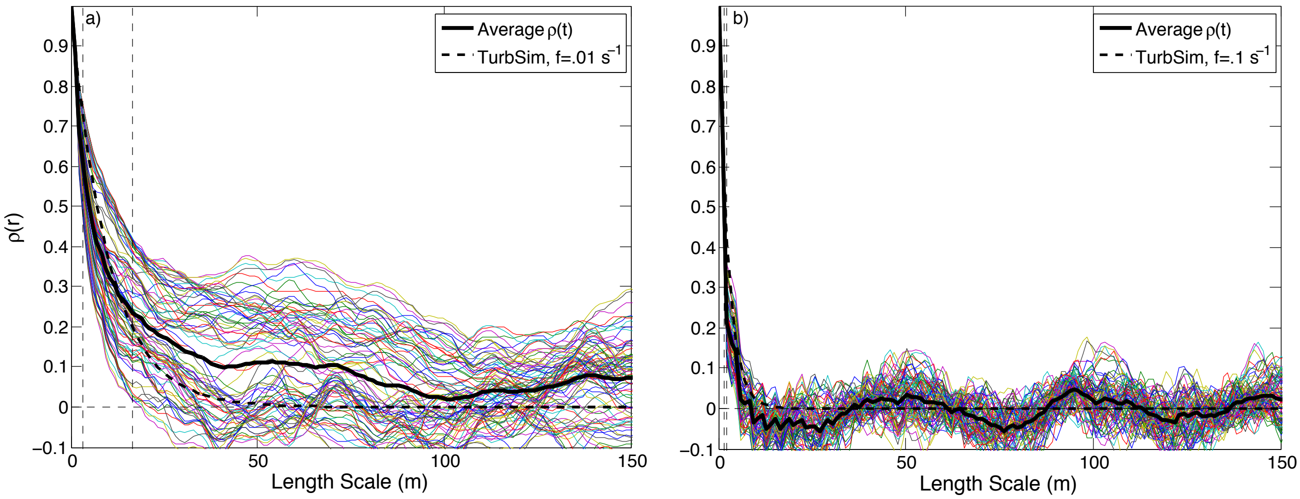

Figure 4.13: Spatial autocorrelation in the along-stream-vertical plane (a) and cross-stream-vertical plane (b) from the LES output (every 10 time steps shown for clarity), with the average for all times in the solid black line, and the coherence function from TurbSim (with $f = .01s^{-1}$ in a) and $f = .1s^{-1}$ in b) in the dashed line.

LES result is desirable anyway. Further observations with more than one location in space are needed for this confirmation.

Spatial correlations in the cross-stream direction are possible with both the LES output and the TurbSim coherence model. This information is completely impossible to obtain from either a vertical profile or a single-point collection of observations. Only multiple horizontal observations can provide the spatial correlations in this direction, since Taylor's hypothesis cannot be used when the mean flow is slow. Differences in the flow in this direction across a turbine rotor also induces torque and loads on the turbine (Alexander and Hamlington, 2014). The autocorrelation in this cross-stream direction is plotted in Figure 4.13b. These results are much less variable, with a range of only $3m$ for both the Taylor and integral scales. The correlation is much smaller in the cross-stream direction, which is consistent with the fact that the turbulence is being advected in the along-stream, but not cross-stream direction, introducing a favored direction of coherence. The distribution of integral scales (Figure 4.14b) does not exhibit the bimodal behavior of the along-stream direction. This result indicates that whatever physical process is causing the second peak in integral scales in the along-stream direction does not impact the cross-stream direction. The spatial coherence function for TurbSim has been plotted on the spatial autocorrelations from the LES in Figure 4.13 as well. On this plot, there is no directional transformation, nor assumptions necessary, since the TurbSim output is in the cross-stream-vertical plane. The TurbSim model fits the LES output very well with a value of f (frequency) an order of magnitude larger than in the along-stream direction, suggesting that higher frequency fluctuations dominate the turbulence in this direction. The better fit of the TurbSim coherence model in this direction may be an indicator that the isotropic assumption made to equate the coherence in the along-stream and cross-stream directions is incorrect, and the model should only be used in the $y-z$ plane, as in the TurbSim output. This is also consistent with the anisotropy of the barycentric map results in observations and LES. However, the integral length scales from TurbSim made with Taylor's hypothesis are unrealistic since there is essentially no mean v-velocity. Note that while all of the other x-axis ranges in Figure 4.14 extend to $60m$, the TurbSim cross-stream $\overline{u}\Lambda$ range only extends to $0.06m$. TurbSim will need to be run at a much higher resolution in order to calculate the spatial autocorrelations, and this work is planned for the future.

The availability of a grid of velocities is a great benefit that comes from numerically simulating a tidal strait, but model verification is still needed to support these results. An array of just two ADVs would provide an enormous amount of information to support the model results. Placing two horizontally-spaced ADVs would capture the horizontal coherent structures which dominate the anisotropy (from the barycentric map and turbulence intensity), and which induce pressure differences across the rotor plane. Vertically spaced ADVs would also capture the structures that vary in the vertical, though anisotropy in this direction is not as strong. The mean flow's vertical shear across the rotor plane can be measured by an ADCP to greater accuracy than two ADVs. Future field work will place two TTMs in the horizontal, cross-stream direction and then two in the horizontal, along-stream direction, with the option of having two ADVs on each TTM (Thomson, personal

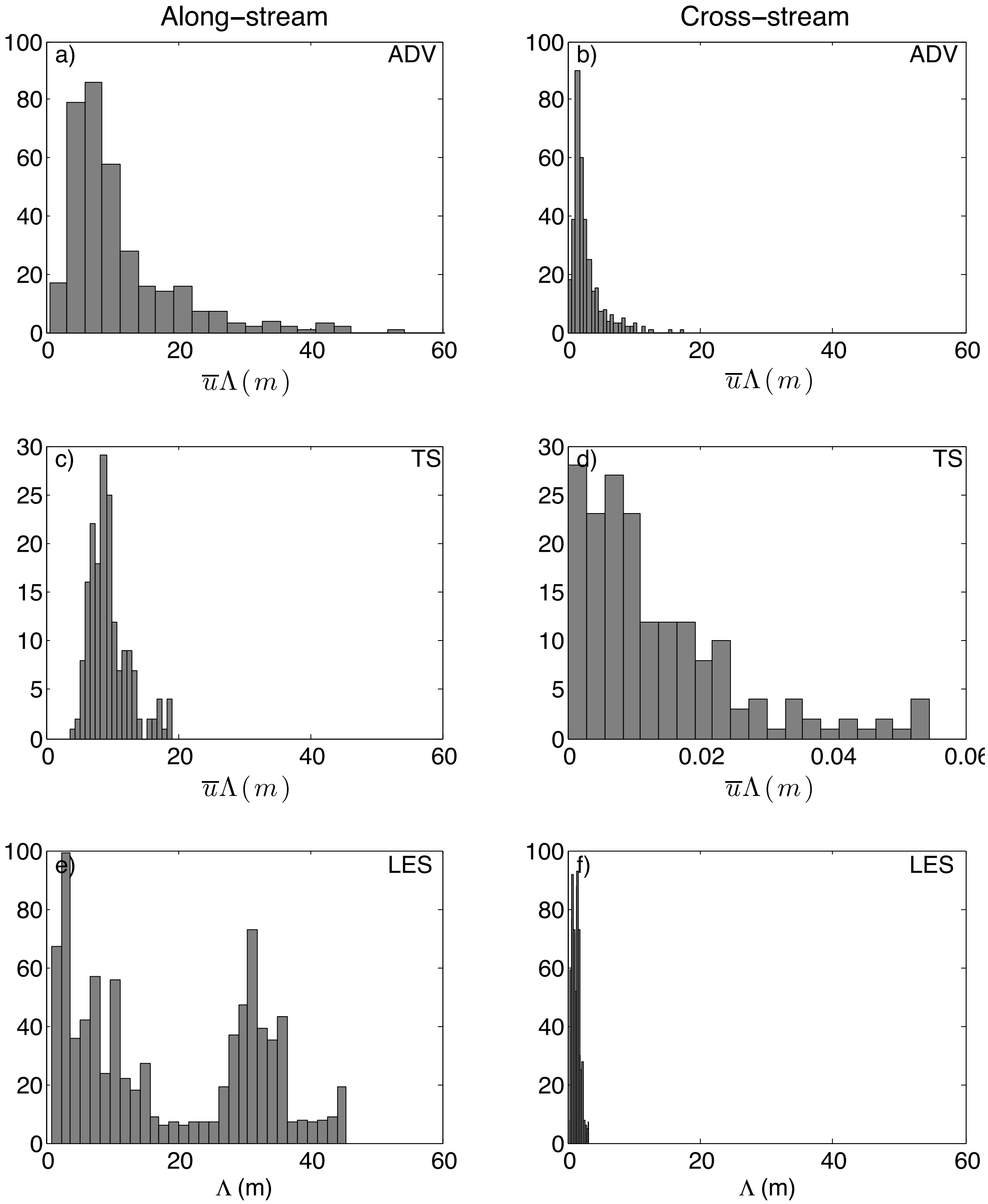

Figure 4.14: a) Histograms of spatial integral scales, $\overline{u}\Lambda$ or Λ, in meters, in the along-stream (a, c, and e) and cross-stream (b, d, and f) directions from the ADV observations (a and b), TurbSim (c and d), and LES (e and f).

communication). This data will provide valuable information as to which direction has the most impact on a turbine, and how quickly the turbulence changes with the mean flow, to assess the accuracy of Taylor's hypothesis.

4.6 Conclusions from Model Results

The two models presented here differ greatly in their basic make-up. The NREL TurbSim model is based on the assumption that turbulence is a stochastic process, and a time series of velocity perturbations is created out of a pre-defined kinetic energy spectrum. The LES model, on the other hand, is a physical model based on the Boussinesq Navier-Stokes equations including wave-, wind-, and tidal-forcing, where the largest eddies are resolved and the smallest turbulent scales are modeled. Each model brings advantages and disadvantages to the table as we attempt to create a full flow-field of realistic turbulence. TurbSim is much simpler and easier to run on one processor on a desktop computer (3200 mins of simulated time takes under 10 minutes of wall time), with several user-defined quantities to guarantee realism in those areas, such as the Reynolds stresses and turbulence intensity at hub height. However, there is no ability to include coherent structures in the current form of the tidal model, so the turbulent events that impact a turbine the most are missing from the turbulence created by this stochastic model. The LES requires a much more complicated model set-up and super-computing abilities to run in a manageable time (15 minutes of simulated time takes 24 wall hours on 768 processors). In exchange, the LES is based on realistic physics and accurately creates, without being defined by the user, realistic vertical profiles of quantities like Reynolds stresses and turbulence intensity.

A deeper look into the output from TurbSim and LES continued to show strengths and weaknesses in each model. While output from TurbSim captures the anisotropy in the Reynolds shear stresses, and thus has values for A similar to the observations, the largest, coherent intervals that are seen in the ADV data are not seen in TurbSim data.

Conversely, the two intervals analyzed from LES output showed values of A that are too large. The model-defined turbulence intensity in TurbSim does match the observations at hub-height, but there is no dependence on mean speed, so, while the model accurately creates the turbulence intensity it is defined to create, it is not realistic based on observations of changing mean flow velocities (both in time and in the vertical profile). With the current LES data, the changes in mean velocity are not modeled, but the vertical profile of mean speed and turbulence intensity are more realistic than those of TurbSim.

While investigating the creation of coherent events in TurbSim and LES, some expected and unexpected results were seen. The autocorrelations and pdfs from TurbSim supported the hypothesis that the model would not create coherent, intermittent events. The range of Taylor and integral scales did not capture the longer coherent events, and the pdfs did not increase in intermittency with longer time scales seen in the observations. Though it was predicted that the LES would capture these longer events, it did not appear as predicted. The temporal autocorrelation did show longer Taylor and integral scales on one of the two intervals analyzed, but the spatial autocorrelations in the along-stream direction, expected to mimic the behavior of the temporal autocorrelation, showed a very different, bimodal distribution of integral scales. Figure 4.15 shows an along-stream snapshot of the u-velocity perturbation, with the smaller scales $(5 - 10m)$ and larger scales $(30 - 40m)$ evident. It is unknown whether this bimodal distribution is realistic, however, and the current LES data is too short to see if the temporal scales are also bimodal. The cross-stream autocorrelations from the LES, compared to the coherence function in TurbSim were very similar, but unsupported by an array of observations.

The most immediate area for future work is to run a more realistic scenario of the LES, with longer times that cover at least one tidal cycle to include changes in the speed and direction of the tidal flow. A “simulated ADV” of sorts will be created, that will be a higher resolution, longer time series of velocities at one point in space for a direct comparison with the observations. This will introduce new challenges with more time necessary to run the

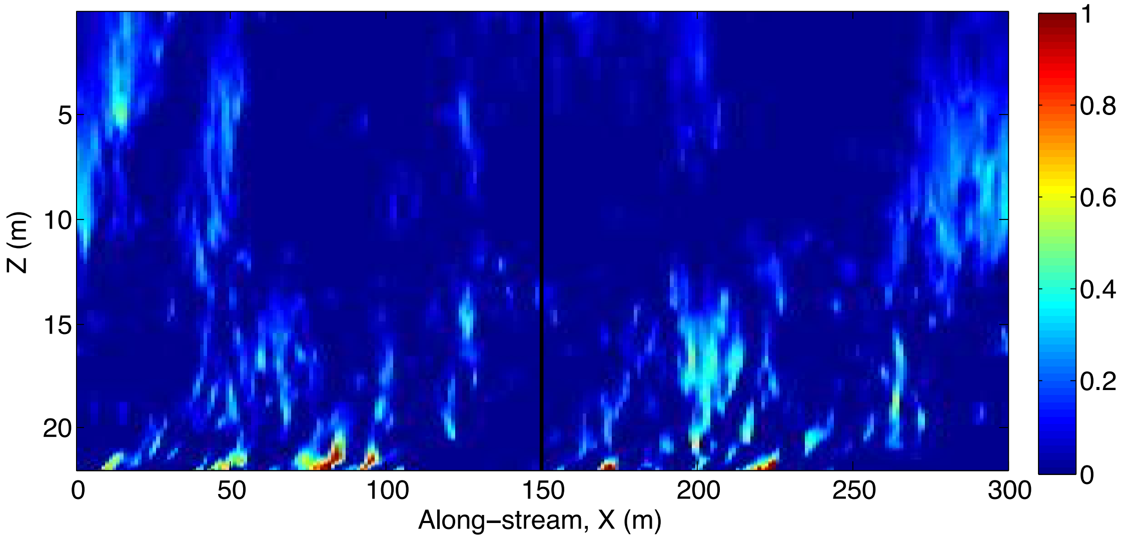

Figure 4.15: Streamwise-vertical plane of u-velocity perturbation, u' along the center line of the LES data, with the turbine plane shown in the solid line..

model, and more time and space needed to handle the larger datasets. These are obstacles that are worth waiting for, however, in order to achieve the realism necessary for the problem at hand. The combination of the temporal statistics and the spatial ones available from the 3-dimensional volumes will also help verify the instances when Taylor's hypothesis is and is not appropriate for these purposes and scales.

Though the model results provide additional information about the turbulence in the tidal strait that can be fed into a turbine model like NREL's Fatigue, Aerodynamics, Structures, and Turbulence (FAST), the current state of both the tidal TurbSim model, and the tidal NCAR LES is lacking important features of the flow. Thomson et al. (2012) hypothesized that a major influence on the turbulence at Nodule Point is the presence of a headland upstream of the proposed turbine site. A far-field feature such as this is very difficult to model. Nevertheless, without these models, there would be no way to predict loads on a turbine. Engineers must be aware of the faults of these models, but can still use their output to continue designing turbines to withstand the turbulent environment of a tidal energy site.

Chapter 5

Conclusions

This dissertation was motivated by a fascination with the incredibly complex, and often beautiful, nature of turbulence, and a desire to understand it more fully. The oceans support life on Earth, and impact all humans - regardless of how far from a coast they may be - because of its role in determining our climate, and providing us with many natural resources. Recognizing the importance of turbulence to applications such as climate change and ocean energy, I set out to explain as much as possible with the limited amount of data available to me. Despite the shortcomings of each of the datasets, I was able to use each for at least a preliminary analysis (I only needed to discard one dataset from the full analysis).

I introduced the topic of ocean turbulence based on the foundational theories that underly all modern turbulence work. The theoretical work of Kolmogorov, Kraichnan, and Batchelor have remained the starting point for other turbulence theories and observations. Parallel to the more classical turbulence work in the laboratory, oceanographers have been theorizing and observing the more complex systems, creating relevant theories to predict interior and surface quasi-geostrophic behavior, as well as tracer variance properties. The kinetic energy (and sometimes enstrophy) spectrum remains the most popular tool to understanding turbulent environments in both laboratories and oceans, so beginning with these theories is necessary to contributing to the modern knowledge of ocean turbulence. An introduction to some previous observations of ocean turbulence showed the gaps, which include global observations below the surface, as well as continued work in localized regions of interest. The body of my dissertation then focused on three methods of characterizing ocean turbulence, at both the global scale, and the very small, local scale.

Chapter 2 introduced a new method of characterizing ocean turbulence from a network of scattered, discontinuous vertical profiles from Argo floats. Previously thought to not be dense enough in its coverage in time and space, McCaffrey et al. (2014) showed that the data is sufficient for the structure function method, which had previously been used with rawinsondes in the atmosphere (Frehlich and Sharman, 2010b). The results of that chapter showed that it is possible to use temperature and salinity data from Argo floats to compute structure functions at spatial scales as small as $20km$ in some regions. While most previous ocean turbulence observations have been at the surface or in the mixed-layer, the Argo network provides a unique look at the deep ocean, with observations in profiles extending to $2000m$ depth. The basic assumptions of homogeneity and isotropy that allow the transformation between structure function (physical) space to spectral (wavenumber) space often do not hold in the ocean, but our results showed little change between more homogeneous and heterogeneous regions in terms of the *shape* of the structure functions, while the magnitude differed. This makes the structure function an even stronger tool for characterizing turbulence than the kinetic energy spectrum, since homogeneity and isotropy are not necessary for computation. The structure function itself is a useful diagnostic, which can be predicted with theories (e.g., Eyink (1996)), or compared directly to spectra computed in the same location in heterogeneous high-resolution ocean models.

Having shown success in calculating structure functions from Argo data, this method can now be applied to GCM data as an improved method of model validation beyond the simple point comparisons that Argo has provided up until now. These comparisons may be able to highlight regions in the oceans where the physics are inaccurate in the models. A subsequent project to follow this one would be to gather GCM output in vertical profiles to match the times and locations of Argo profiles, and compute structure functions, again on both isobars and isopycnals. Locations varying in latitude, depth, and levels of eddy activity and homogeneity will identify more clearly where GCMs fail and succeed at capturing the 3d turbulent processes that transfer energy from the large forcing scales to the small dissipation scales, or the 2d processes that transfer energy from the intermediate forcing scales to the large dissipative scales. Having observations of these processes can improve climate models, ultimately providing more reliable predictions of our future climate, and how we, as humans, can affect it.

Still motivated by the desire to understand the complexities of the oceans that affect our lives, Chapter 3 changed focus to the second major application of the turbulence research done here: ocean renewable energy. The ocean is capable of providing us with substantial amounts of energy, but the technology is new and the implications of extracting energy are still unknown, so research questions are still wide open. Understanding the turbulence at a potential tidal energy site is vital to its development and success. Taking advantage of the available observations in the Puget Sound, WA where two potential tidal energy sites are located, I performed a more extensive characterization of the turbulence than previously conducted. The goals were to identify the time and length scales of the strongest coherent features, physically describe them (i.e., what shape?), and parameterize them with simple turbulence metrics. Though velocity profiles are available from an ADCP, the less noisy ADV was used because its small sampling volume did not introduce the inherent beam spread of the diverging beams of an ADCP. This greatly limited the amount of information that we could gain about the turbulence because we lost access to the direct spatial information, and were left with only a time series of velocities at one point in space. This meant relying on Taylor's frozen turbulence hypothesis, which is only true for flows whose turbulent fluctuations happen at much faster timescales than the mean flow that advects them. Nonetheless, the high temporal resolution of the observations makes them perfect for the temporal statistics calculated here, which included autocorrelations, structure functions, probability density functions of the velocity increments, and the anisotropy properties. Using this collection of physical properties, I made a comparison between three basic turbulence metrics (turbulence intensity, turbulent kinetic energy, and coherent turbulent kinetic energy) to determine which is best at capturing the strong turbulent events. An additional metric, based on the anisotropy tensor and is a tensor invariant version of the coherent turbulent kinetic energy, which we called the anisotropy magnitude, A, was introduced and included in this comparison. This metric showed the closest relationship with the intermittency, coherence, and anisotropy as quantified by the physical parameters. This quantity parameterizes these properties of the flow much better than the previously used turbulence intensity.

This study is just the beginning of what could be a full career in site characterization for tidal energy sites, since there is such a wide variety of directions to go. First, and maybe most importantly, is the connection that remains to be shown in the water between turbulent characteristics and loads on a turbine. These comparison have been made in the atmosphere for wind turbines (Kelley et al., 2000; Mücke et al., 2011), and the correlation is expected to be the same. Unfortunately, there are very few tidal turbines in operation, and it is difficult to measure the loads in the water, so numerical models like the NREL Fatigue, Aerodynamics, Structures, and Turbulence (FAST) model are given the responsibility of providing these answers (Jonkman and Buhl, 2005). These temporal statistics also could be supported by additional observations that provide spatial information. The Tidal Turbulence Mooring (TTM), which can have multiple ADVs on a compliant mooring with an ADCP at the base, can be used for this purpose, and provide vertical spatial statistics (Thomson et al., 2013). Future field campaigns are planned which will include multiple TTMs for horizontally varying observations as well (Thomson, personal communication). Other future turbulence characterizations can also be conducted in the presence of an operating tidal turbine. While the turbulence impacts the turbine, the turbine also impacts the turbulence and the tidal channel, including the bottom bed and any biological organisms living there. Laboratory experiments and numerical simulations have addressed the questions of a turbine's influence on the tidal flow, but few observations have been made to support them thus far (Hill et al., 2013; Kang et al., 2012). Clearly, the need for further observations of turbulence for tidal energy applications is still great!

Since the list of needed observations for tidal energy applications is so long, numerical models are necessary to suffice in the meantime. As more observations come in, the models can continue to expand to construct a full tidal flow. The observations that informed the analysis in Chapter 3 were used in Chapter 4 to set up two very different numerical models of the tidal flow for this purpose. The first, the NREL HydroTurbSim (or TurbSim) model, is a stochastic turbulence generator performing an inverse Fourier transform on a pre-defined kinetic energy spectrum to obtain a turbulent time series to be added onto a mean flow profile. Calculating the same temporal statistics on the TurbSim output to compare to the ADV observations at Nodule Point, it was seen that the turbulence is created as defined: realistically in the anisotropy of the Reynolds shear stresses, but unrealistically in the anisotropy of the normal stresses. Additionally, the strong, coherent features of the flow are not seen. These results are as expected, since the physical mechanisms that create coherent structures in a flow are not included in a stochastic model. This model is user-friendly, very fast to run, and is generally useful for capturing the average turbulence intensity, which has been shown to have strong impacts on loads and power production (Rareshide et al., 2009), but for a more in-depth analysis, a physical model is needed at the expense of ease and time.

In search of a model that *does* create the realistic, coherent structures, we turned to large-eddy simulations of the tidal flow from Alexander and Hamlington (2014). Solving the wave-averaged, Boussinesq Navier-Stokes (Craik-Liebovich) equations in Equations 4.10 captures the wind-, wave-, and tidal-forcings in the modeled area. The output from the LES show a hint of more realistic coherent features, though the small amount of available data in time is not enough to see the full range of scales. Anisotropy values may be larger than observations because of the mean speeds that are unrealistic to the location (too fast), creating more shear than is present at Nodule Point. The spatial correlations that are available from models that are not possible from single-point observations were calculated with their resulting integral and Taylor scales. The spatial coherence scales did not match those obtained assuming Taylor's hypothesis from the temporal coherence scales from the ADV observations, most notably in the along-stream direction, where there are two dominant length scales in the LES data. Especially at the peaks in the tidal cycle when mean velocities are fastest, it appears that Taylor's frozen turbulence hypothesis is not appropriate, since the mean flow has such a strong impact on the turbulence. The difference in spatial correlations between the along-stream and cross-stream directions also indicates that the mean tidal flow determines the turbulent properties, so a full analysis needs to include a full tidal cycle, not just the fastest mean speed.

The most immediate future work is to run the LES model with more realistic velocities to match the observations closer, and run for a longer time to obtain more of the tidal signal. The output from the LES can also be used as input for the FAST model to identify the resulting loading on a turbine from the different properties of the flow, like scales and anisotropy. To accompany the future observations of turbulence in the presence of an operating turbine, this LES model, with its actuator disk capabilities, can be used to predict turbine array spacing and environmental affects. LES models often have the ability to include bottom topography (and terrain-following coordinates) that may account for some of the missing scales of turbulence in the current runs. Further development of the LES of Nodule Point and Admiralty Head is planned by Hamlington and Alexander (Hamlington, personal communication).

Just as the *in situ* observations have inherent shortcomings, all models do as well. The most general disadvantage with modeling is that only a small range of scenarios are possible to model. Only a model that includes every type of forcing, including human-caused and far-field motions, could create a nearly-accurate kinetic energy spectrum, but even then, the inability to *exactly* solve the fluid equations prevents a perfect prediction of a future turbulent state. Though this sounds very pessimistic, I hope that this dissertation has shown that there is always use in the data. The sometimes far-from-perfect data, whether from observations or models, are not a reason to give up on studying turbulence. Though it was sometimes discouraging to realize that what I set out to do was not possible with the data I had, I was forced to accept and even appreciate the bits of knowledge that *were* obtainable. Having specific hypotheses to test (theories of spectral slopes in Chapter 2, $CTKE$-load relationships in Chapters 3 and 4) allowed the limited data to cover a larger fraction of the questions at hand, rather than having open-ended or broad questions which could have required much more data. All observations and models give information otherwise unknown about turbulent flows. Only through continued research into and observations of each of these areas can we slowly increase our knowledge of the complex oceans.

When beginning this research more than four years ago, I quickly learned that observational data is not to be taken for granted, and is not very simple to work with. Difficulties in determining averaging intervals, grid sizes, appropriate methods of interpolation, and other unpredicted obstacles presented themselves along the way. I greatly appreciated the lessons I learned on a month-long CLIVAR research cruise aboard the *R/V Atlantis*, when I recognized the need for extreme detail while collecting and sampling ocean water at depth (e.g., during every-other profile, gloves must be worn by all scientists sampling before dissolved inorganic carbon!). Returning to my land-locked state to work with data gained through other people's hard work took on a new meaning; I became more aware of the importance of every result. Collecting the research done over the past five years has been a great chance to acknowledge how this work presents information about the ocean that was completely unknown to the world beforehand. I hope that this dissertation can be the beginning of a career of new realizations of the beauty of turbulence.

References

Alexander, S. and P. Hamlington, 2014: Study of turbulence statistics in large eddy simulations of ocean current turbine environments. *OMAE2014*, ASME.

Argo Science Team, 1998: On the design and implementation of argo. *International CLIVAR Project Office Rep. 21, GODAE Rep. 5.*

Banerjee, S., R. Krahl, F. Durst, and C. Zenger, 2007: Presentation of anisotropy properties of turbulence invariants versus eigenvalue approaches. *Journal of Turbulence*, **8 (32)**.

Bardina, J., J. Ferziger, and W. Reynolds, 1980: Improved subgrid-scale models for large-eddy simulation. *American Institute of Aeronautics and Astronautics Papers 80-1357.*

Batchelor, G. K., 1959: Small-scale variation of convected quantities like temperature in turbulent fluid .1. General discussion and the case of small conductivity. *Journal of Fluid Mechanics*, **5 (1)**, 113–133.

Blumen, W., 1982: Wave-interactions in quasi-geostrophic uniform potential vorticity flow. *Journal of the Atmospheric Sciences*, **39 (11)**, 2388–2396.

Broecker, W. S., 1991: The great ocean conveyor. *Oceanography*, **4 (2)**, 79–89.

Callies, J. and R. Ferrari, 2013: Interpreting energy and tracer spectra of upper-ocean turbulence in the submesoscale range (1-200 km). *Journal of Physical Oceanography*, **43 (11)**.

Cayley, A., 1858: A memoir on the theory of matrices. *Philosophical transactions of the Royal society of London*, **148**, 17–37.

Charney, J. G., 1971: Geostrophic turbulence. *Journal of Atmospheric Sciences*, **28**, 1087–1095.

Chelton, D. B., R. A. Deszoeke, M. G. Schlax, K. El Naggar, and N. Siwertz, 1998: Geographical variability of the first baroclinic rossby radius of deformation. *Journal of Physical Oceanography*, **28 (3)**, 433–460.

Cole, S. and D. Rudnick, 2012: The spatial distribution and annual cycle of upper ocean thermohaline structure. *Journal of Geophysical Research-Oceans*, **117**.

Corrsin, S., 1951: On the spectrum of isotropic temperature fluctuations in isotropic turbulence. *Journal of Applied Physics*, **22 (469)**.

Domaradzki, J. A. and E. M. Saiki, 1997: A subgrid-scale model based on the estimation of unresolved scales of turbulence. *Physics of Fluids (1994-present)*, **9 (7)**, 2148–2164.

Elliott, D. L. and J. Cadogan, 1990: Effects of wind shear and turbulence on wind turbine power curves. Tech. rep., Pacific Northwest Lab., Richland, WA (USA).

Epler, J., B. Polagye, and J. Thomson, 2010: Shipboard acoustic Doppler current profiler surveys to assess tidal current resources. *OCEANS 2010*, IEEE, 1–10.

Eyink, G. L., 1996: Intermittency and anomalous scaling of passive scalars in any space dimension. *Physical Review E*, **54 (2)**, 1497.

Ferrari, R. and D. L. Rudnick, 2000: Thermohaline variability in the upper ocean. *Journal of Geophysical Research: Oceans (1978–2012)*, **105 (C7)**, 16 857–16 883.

Forget, G., 2010: Mapping ocean observations in a dynamical framework: A 2004-06 ocean atlas. *Journal of Physical Oceanography*, **40**, 1201–1221.

Frandsen, S. T. et al., 2007: *Turbulence and turbulence-generated structural loading in wind turbine clusters*. Risø National Laboratory.

Frehlich, R. and R. Sharman, 2010: Climatology of velocity and temperature turbulence statistics determined from rawinsonde and ACARS/AMDAR data. *Journal of Applied Meteorology and Climatology*, in press.

Garrett, C. and W. Munk, 1972: Space-time scales of internal waves. *Geophysical Fluid Dynamics*, **2**, 225–264.

Germano, M., U. Piomelli, P. Moin, and W. H. Cabot, 1991: A dynamic subgrid-scale eddy viscosity model. *Physics of Fluids A: Fluid Dynamics (1989-1993)*, **3 (7)**, 1760–1765.

Gibson, C. and W. Schwarz, 1963: The universal equilibrium spectra of turbulent velocity and scalar fields. *Journal of Fluid Mechanics*, **16 (03)**, 365–384.

Gooch, S., J. Thomson, B. Polagye, and D. Meggitt, 2009: Site characterization for tidal power. *OCEANS 2009, MTS/IEEE Biloxi - Marine Technology for Our Future: Global and Local Challenges*, 1 –10.

Grant, H., R. Stewart, and A. Moilliet, 1962: Turbulence spectra from a tidal channel. *J. fluid Mech*, **12 (2)**, 241–268.

Haas, K. A., 2011: Assessment of energy production potential from tidal streams in the united states. Tech. rep., Georgia Tech Research Corporation.

Haney, S., et al., 2012: Hurricane wake restratification rates of one-, two-and three-dimensional processes. *Journal of Marine Research*, **70 (6)**, 824–850.

Hill, C., M. Musa, L. P. Chamorro, and M. Guala, 2013: Interaction between an axial-flow model hydrokinetic turbine and an erodible channel. *Bulletin of the American Physical Society*, **58**.

Jimenez, J., 1997: Oceanic turbulence at millimeter scales. *Scientia Marina*, **61**, 47–56.

Jonkman, B., 2009: Turbsim user's guide: Version 1.50. Tech. rep., National Renewable Energy Laboratory.

Jonkman, J. and L. Kilcher, 2012: Turbsim user's guide: Version 1.06. 00. *NREL/TP-xxx-xxxx (Draft Version), Golden, CO: National Renewable Energy Laboratory.*

Jonkman, J. M. and M. L. Buhl, 2005: FAST user?s guide. *Golden, CO: National Renewable Energy Laboratory.*

JPL, 2014: Jet Propulsion Laboratory Mission Control. $http://www.jpl.nasa.gov/missions$.

Kaiser, K., W. Langreder, H. Hohlen, and J. Højstrup, 2007: Turbulence correction for power curves. *Wind Energy*, Springer, 159–162.

Kanamitsu, M., W. Ebisuzaki, J. Woollen, S.-K. Yang, J. Hnilo, M. Fiorino, and G. Potter, 2002: Ncep–doe amip-ii reanalysis (r-2). *Bulletin of the American Meteorological Society*, **83 (11)**.

Kang, S., I. Borazjani, J. A. Colby, and F. Sotiropoulos, 2012: Numerical simulation of 3d flow past a real-life marine hydrokinetic turbine. *Advances in Water Resources*, **39**, 33–43.

Kelley, N., R. Osgood, J. Bialasiewicz, and A. Jakubowski, 2000: Using time-frequency and wavelet analysis to assess turbulence/roto interactions. Tech. rep., 19th American Society of Mechanical Engineers Wind Energy Symposium.

Klein, P., A. Treguier, and B. Hua, 1998: Three-dimensional stirring of thermohaline fronts. *Journal of Marine Research*, **56**, 589–612.

Klymak, J. M. and J. N. Moum, 2007: Oceanic isopycnal slope spectra. part i: Internal waves. *Journal of Physical Oceanography*, **37 (5)**, 1215 – 1231, URL `http://search.ebscohost.com/login.aspx?direct=true&db=aph&AN=25220492&site=ehost-live`.

Kolmogorov, A. N., 1941: The local structure of turbulence in incompressible viscous fluid for very large reynolds number. *Dokl. Akad. Nauk. SSSR*, **30**, 9–13.

Kraichnan, R. H., 1967: Inertial ranges in two-dimensional turbulence. *Physics of Fluids*, **16**, 1417–1423.

LaCasce, J. H. and A. Bower, 2000: Relative dispersion in the subsurface north atlantic. *Journal of Marine Research*, **58 (6)**, 863–894, doi:doi:10.1357/002224000763485737, URL `http://www.ingentaconnect.com/content/jmr/jmr/2000/00000058/00000006/art00002`.

Launder, B. E. and D. Spalding, 1974: The numerical computation of turbulent flows. *Computer methods in applied mechanics and engineering*, **3 (2)**, 269–289.

Le Traon, P.-Y., P. Klein, B. L. Hua, and G. Dibarboure, 2008: Do altimeter wavenumber spectra agree with the interior or surface quasigeostrophic theory? *Journal of Physical Oceanography*, **38 (5)**.

Legrand, C., 2009: *Assessment of Tidal Energy Resource: Marine Renewable Energy Guides*. European Marine Energy Centre.

Lomax, H. and B. Baldwin, 1978: Thin layer approximation and algebraic model for separated turbulent flows. *AIAA journal*, **(78-257)**.

Lumley, J., 1964: The spectrum of nearly inertial turbulence in a stably stratified fluid. *Journal of Atmospheric Sciences*, **21**, 99–102.

Lumley, J., 1978: Computational modeling of turbulent flows. *Advances in Applied Mechanics*, **18**, 123–176.

Lumley, J. and G. Newman, 1977: The return to isotropy of homogeneous turbulence. *Journal of Fluid Mechanics*, **82**, 161–178.

McCaffrey, K., B. Fox-Kemper, and G. Forget, submitted, 2014a: Estimates of ocean macroturbulence: Structure function and spectral slope from Argo profiling floats, I : Methods. *Journal of Physical Oceanography*.

McCaffrey, K., B. Fox-Kemper, and G. Forget, submitted, 2014b: Estimates of ocean macroturbulence: Structure function and spectral slope from Argo profiling floats, II: Global results. *Journal of Physical Oceanography.*

McCaffrey, K., B. Fox-Kemper, P. Hamlington, and J. Thomson, submitted, 2013: Characterizing turbulence anisotropy, coherence, and intermittency at a prospective tidal energy site. *Renewable Energy.*

McWilliams, J. C., P. P. Sullivan, and C.-H. Moeng, 1997: Langmuir turbulence in the ocean. *Journal of Fluid Mechanics*, **334**, 1–30.

Merriam-Webster.com, 2014: Turbulence. $http://www.merriam-webster.com.$

Moeng, C.-H., 1984: A large-eddy-simulation model for the study of planetary boundary-layer turbulence. *Journal of the Atmospheric Sciences*, **41 (13)**, 2052–2062.

Mücke, T., D. Kleinhans, and J. Peinke, 2011: Atmospheric turbulence and its influence on the alternating loads on wind turbines. *Wind Energy*, **14 (2)**, 301–316.

NASA, 2014: National aeronautics and space administration earth science missions. $http://climate.nasa.gov/nasa_role/missions.$

Nastrom, G. D. and K. S. Gage, 1985: A climatology of atmospheric wavenumber spectra of wind and temperature observed by commercial aircraft. *Journal of Atmospheric Sciences*, **42**, 950–960.

Nortek USA, LLC, 2014: Products. $http://www.nortekusa.com/usa.$

Novikov, E. and R. Stewart, 1964: The intermittency of turbulence and the spectrum of energy dissipation fluctuations (turbulence intermittency model to calculate spectrum of energy dissipation fluctuations). *1964.*

Obukhov, A. M., 1949: The structure of the temperature field in a turbulent flow. *Izv. Akad. Nauk. SSSR, Ser. Geog. and Geophys.*, **13 (58)**.

O'Rourke, F., F. Boyle, and A. Reynolds, 2010: Tidal energy update 2009. *Applied Energy*, **87 (2)**, 398–409.

Polagye, B. and J. Thomson, 2013: Tidal energy resource characterization: methodology and field study in Admiralty Inlet, Puget Sound, WA (USA). *Proceedings of the Institution of Mechanical Engineers, Part A: Journal of Power and Energy*, **227 (3)**, 352–367.

Pope, S. B., 2000: *Turbulent flows*. Cambridge University Press, Cambridge, URL `http://www.loc.gov/catdir/description/cam0210/99044583.html`.

Ragheb, A. and M. Ragheb, 2010: Wind turbine gearbox technologies. *Nuclear & Renewable Energy Conference (INREC), 2010 1st International*, IEEE, 1–8.

Rareshide, E., A. Tindal, C. Johnson, A. Graves, E. Simpson, J. Bleeg, T. Harris, and D. Schoborg, 2009: Effects of complex wind regimes on turbine performance. *Scientific Proceedings. American Wind Energy Association WINDPOWER Conference*.

Reid, J. L., 1994: On the total geostrophic circulation of the north atlantic ocean: Flow patterns, tracers, and transports. *Progress in Oceanography*, **33 (1)**, 1–92.

Richardson, L. F., 1922: *Weather prediction by numerical process*. Cambridge University Press.

Roullet, G., G. Maze, and X. Capet, 2013: Oceanic interior mesoscale turbulence revealed by argo floats. *EGU General Assembly Conference Abstracts*, Vol. 15, 2366.

Salmon, R., 1980: Baroclinic instability and geostrophic turbulence. 167–211 pp.

Scott, R. B. and F. Wang, 2005: Direct evidence of an oceanic inverse kinetic energy cascade from satellite altimetry. *Journal of Physical Oceanography*, **35**, 1650–1666.

Scotti, A. and C. Meneveau, 1999: A fractal model for large eddy simulation of turbulent flow. *Physica D: Nonlinear Phenomena*, **127 (3)**, 198–232.

Shchepetkin, A. F. and J. C. McWilliams, 2005: The regional oceanic modeling system (ROMS): a split-explicit, free-surface, topography-following-coordinate oceanic model. *Ocean Modelling*, **9 (4)**, 347–404.

Smagorinsky, J., 1963: General circulation experiments with the primitive equations: I. the basic experiment*. *Monthly weather review*, **91 (3)**, 99–164.

Stewart, R. H., 2004: *Introduction to physical oceanography.* Texas A & M University.

Stocker, T. F., Q. Dahe, and G.-K. Plattner, 2013: Climate change 2013: The physical science basis. *Working Group I Contribution to the Fifth Assessment Report of the Intergovernmental Panel on Climate Change. Summary for Policymakers (IPCC, 2013).*

Sullivan, P. P., J. C. McWilliams, and C.-H. Moeng, 1994: A subgrid-scale model for large-eddy simulation of planetary boundary-layer flows. *Boundary-Layer Meteorology*, **71 (3)**, 247–276.

Sutherland, H. J., 2002: Inflow and the fatigue of the LIST wind turbine. *2002 ASME Wind Energy Symposium*, 427–437.

Taylor, G. I., 1938: The spectrum of turbulence. *Proceedings of the Royal Society of London. Series A-Mathematical and Physical Sciences*, **164 (919)**, 476–490.

Thomson, J., L. Kilcher, M. Richmond, J. Talbert, B. Polagye, M. Guerra, and R. Cienfuegos, 2013: Tidal turbulence spectra from a compliant mooring. *Proceedings of the 1st Marine Energy Technology, Symposium (METS2013).*

Thomson, J., B. Polagye, M. Richmond, and V. Durgesh, 2010: Quantifying turbulence for tidal power applications. *Institute of Electrical and Electronics Engineers.*

Thomson, J., B. Polagye, M. Richmond, and V. Durgesh, 2012: Measurements of turbulence at two tidal energy sites in puget sound, wa. *Institute of Electrical and Electronics Engineers*, **37 (3)**, 363–374.

Thyng, K. M., J. J. Riley, and J. Thomson, 2013: Inference of turbulence parameters from a roms simulation using the¡ i¿ k¡/i¿-ε closure scheme. *Ocean Modelling*, **72**, 104–118.

Trenberth, K. E. and A. Solomon, 1994: The global heat balance: Heat transports in the atmosphere and ocean. *Climate Dynamics*, **10 (3)**, 107–134.

Vallis, G. K., 2006: *Atmospheric and Oceanic Fluid Dynamics : Fundamentals and Large-Scale Circulation*. Cambridge University Press, Cambridge.

Wang, D.-P., C. N. Flagg, K. Donohue, and H. T. Rossby, 2010: Wavenumber spectrum in the gulf stream from shipboard adcp observations and comparison with altimetry measurements. *Journal of Physical Oceanography*, **40 (4)**.

Webb, E. K., 1964: Ratio of spectrum and structure-function constants in the inertial subrange. *Quarterly Journal of the Royal Meteorological Society*, **90 (385)**, 344–345.

Wharton, S. and J. K. Lundquist, 2012: Atmospheric stability affects wind turbine power collection. *Environmental Research Letters*, **7 (1)**, 014 005.

Wunsch, C. and D. Stammer, 1995: The global frequency-wavenumber spectrum of oceanic variability estimated from topex/poseidon altimetric measurements. *Journal of Geophysical Research: Oceans*, **100 (C12)**, 24 895–24 910, doi:10.1029/95JC01783, URL `http://dx.doi.org/10.1029/95JC01783`.

Yeager, S. G. and W. G. Large, 2007: Observational evidence of winter spice injection. *Journal of Physical Oceanography*, **37**, 2895–2919, doi:DOI10.1175/2007JPO3629.1.

Appendix A

Frequently Used Abbreviations

ADCP Acoustic Doppler current profiler

ADV Acoustic Doppler velocimeter

CTKE Coherent Turbulent Kinetic Energy

EKE Eddy Kinetic Energy

GCM Global Circulation (or Climate) Model

K41 Kolmogorov (1941)

LES Large-eddy simulation

NCAR National Center for Atmospheric Research

NREL National Renewable Energy Laboratory

QG Quasi-Geostrophy

SGS Sub-grid scale

SQG Surface Quasi-Geostrophy

TKE Turbulent Kinetic Energy

TTM Tidal Turbulence Mooring

Appendix B

Hurricane wake restratification rates of one-, two- and three-dimensional processes

This work has been published in the Journal of Marine Research, and can be found here: http://dx.doi.org/10.1357/002224012806770937 .

Abstract The restratification of the cold wakes of Tropical Cyclones Fanapi, Frances, Igor, and Katrina are examined based on derived scalings for processes that can restore the hurricane wake toward the pre-cyclone conditions. The different restoration processes depend on the parameters of the wake: depth, width, buoyancy anomaly, and wind stress. The parameters needed are derived for each wake from satellite and climatological data. The scalings are based on model results and existing parameterizations, including air-sea heat fluxes (1d), Ekman buoyancy fluxes (2d), and mixed layer eddies (3d). The dominant surface restoration occurs by a combination of surface fluxes and Ekman buoyancy fluxes, while the submesoscale mixed layer eddy bolus fluxes are the dominant subsurface effect.

Appendix C

Observations of Ocean Macroturbulence: Structure Function Analysis from Argo Profiling Float Data.

This appendix contains the text of McCaffrey et al. (2014) and McCaffrey et al. (2014a), submitted to the *Journal of Physical Oceanography* in January, 2014.

Abstract - Estimates of Ocean Macro-turbulence: Structure Function and Spectral Slope from Argo Profiling Floats, I: Methods

The Argo profiling float network has repeatedly sampled much of the world's ocean. This study uses Argo temperature and salinity data to form the tracer structure function of ocean variability at the macro-scale ($10-1000$ km, mesoscale and above). Here, second-order temperature and salinity structure functions over horizontal separations are calculated along either pressure or potential density surfaces, which allows analysis of both active and passive tracer structure functions. Using Argo data, a map of global variance is created from

the climatological average and each datum. When turbulence is homogeneous, the structure function slope from Argo can be related to the ocean's temperature or salinity variance spectral slope. In the oceans, where turbulence is mostly heterogeneous, spectra may be misleading, but structure functions still provide statistical information that can be understood or used for model validation. This method is shown to match previous results from continuous glider observations in the Pacific Ocean.

Introduction

Understanding the nature of the turbulent processes in the atmosphere and ocean is crucial to determining large-scale circulation, and therefore climate prediction, but the relationship between large-scale circulation and small-scale turbulence is poorly understood. Atmospheric turbulence has been studied through spectral and structure function analyses for decades (Nastrom and Gage, 1985; Lindborg, 1999; Frehlich and Sharman, 2010a), and the results have been duplicated by high resolution General Circulation Models (GCMs) and mesoscale Numerical Weather Prediction (NWP) models as well (Koshyk and Hamilton, 2001; Skamarock, 2004; Frehlich and Sharman, 2004; Takahashi et al., 2006; Hamilton et al., 2008). As realistic ocean climate models become increasingly turbulent, a similar dataset to the Nastrom and Gage spectrum would be a perfect evaluation tool.

It is often assumed that constraining a horizontal power spectral density curve, or spectrum, requires a nearly-continuous synoptic survey, such as by satellite (Scott and Wang, 2005), tow-yo (Rudnick and Ferrari, 1999), ship (Callies and Ferrari, 2013), or glider (Cole and Rudnick, 2012). Near-surface spectra from tow-yo and satellite have been studied by the authors and collaborators among many others (Fox-Kemper et al., 2011), but a similar comprehensive analysis has not been done at depth because of the limited availability of continuous observations. However, the recent atmospheric rawinsonde method of Frehlich and Sharman (2010a) demonstrates that a collection of individual observations may be used to form the structure function, which is closely related to the power spectrum in stationary, isotropic, homogeneous turbulence. Structure function analysis is quite common in the engineering literature on turbulence (She and Leveque, 1994, is a well-known example).

With the increased density of Argo profiling floats sampling down to 2000 m over the past two decades, as well as the success of the rawinsonde method in the atmosphere, a new method is attempted to quantify large-scale turbulence in the oceans. Since spectra have not been computed from Argo data, point-by-point agreement between satellite and Argo (Gommenginger et al., 2010; Bhaskar et al., 2009) is sufficient to validate this utilization of surface Argo data, but the analysis here goes beyond what satellites alone can provide. In these previous analyses, satellite data was constrained to surface properties, while *in situ* estimates were of limited geographic and seasonal scope. These observations often yielded new insight, for example testing the predictions of quasigeostrophic turbulence theories and elucidating the importance and ubiquity of near-surface ocean fronts. Even without supporting theory, the structure function statistic is a useful constraint on high-resolution models, as structure functions are easy to calculate in a model from even a single output snapshot. In this study, temperature and salinity data from Argo are used to characterize large-scale turbulence at depth by constructing structure functions and, in some cases, inferring the related temperature and salinity variance spectra.

Previous ocean surface observations suggest that the spectral behavior for scales larger than about 1 km differs from smaller scale turbulence (e.g., Hosegood et al., 2006). Here, we call variability on this range of large scales “macro-turbulence” to emphasize that, aside from being large scale, little is known about what is being observed (see also Forget and Wunsch (2007)). While dynamical frameworks for mesoscale, quasigeostrophic turbulence spanning this spatial range at sub-inertial frequencies are heavily studied, they may not be complete in the description of data from the real ocean where temporal filtering has not been performed.

Macro-turbulence is considered between 10 and 10^4 km, including mesoscale eddy activity, internal waves, and other signals such as atmospheric forcing responses.

Structure Function - Spectrum Relationship

The tracer autocorrelation function, R_θ is a measurement of the similarity (or difference) between a point located at $\mathbf{x}$ and another separated by a distance vector, $\mathbf{s}$, defined as

$$R_\theta(\mathbf{s},\mathbf{x}) = \overline{\theta'(\mathbf{x})\theta'(\mathbf{x}+\mathbf{s})}, \tag{C.1}$$

where θ' is any tracer (e.g., potential temperature or salinity) deviation from an appropriate mean. The n^{th}-order tracer structure function, $D_{\theta,n}$, is similarly defined and the $n = 2$ form is related to the autocorrelation by

$$D_{\theta,n}(\mathbf{s},\mathbf{x}) = \overline{(\theta'(\mathbf{x}) - \theta'(\mathbf{x}+\mathbf{s}))^n}\ , \tag{C.2}$$

$$D_{\theta,2}(\mathbf{s},\mathbf{x}) = 2\left(\overline{\theta'^2} - R_\theta(\mathbf{s},\mathbf{x})\right). \tag{C.3}$$

In the case of isotropic turbulence, the structure function and autocorrelation are independent of direction (e.g., $D(\mathbf{s},\mathbf{x}) = D(s,x)$), and for homogeneous turbulence, they are independent of x (e.g., $D(s,x) = D(s)$). Exploiting the relationship in Equation (C.3) is of primary interest, so unless specified, $n = 2$ is assumed, and $D_\theta(s) = D_{\theta,2}(s)$.

In structure functions and spectra, the definition of “variance” and deviation from the “mean” must be clarified. Controlling noise, seasonality, and the resolution of chosen separation distances all detract from the use of a uniform bin average as mean, so instead the near-global mean monthly Ocean Comprehensive Atlas (OCCA) for the 3-year period from December 2003 through November 2006 (Forget, 2010) was used to approximate an appropriate turbulence-free mean for each location and each month. The temperature (salinity) variance is thus estimated as the difference between the observed temperature (salinity) and the climatological value, $\theta' = \theta_{Obs} - \theta_{Clim}$ ($S' = S_{Obs} - S_{Clim}$). While the Argo data is assimilated into the OCCA product, the model used for the assimilation is not high enough resolution to be eddy-permitting. In some sense, the "noise" of deviations from the OCCA climatology is the object of study here. However, these details aside, experimentation revealed the structure functions presented here did not change appreciably if a time average of all Argo data on a grid was used instead of this climatology.

If a given homogeneous, isotropic turbulence spectrum has power-law behavior over a range of wavenumbers, then a related scaling law for the structure function is expected (Webb, 1964). Suppose this power law is given by $B(k) = \alpha_B k^{\lambda}$, with spectral slope, λ. The structure function will also have a polynomial form: $D_\theta(s) = c_D s^{\gamma} + C_0$ with structure function slope, γ, and a constant C_0 representing contributions from other portions of the spectrum not adhering to the $B(k) = \alpha_B k^{\lambda}$ law (shown to be negligible in Webb (1964)). The relationship between the two slopes (derived in Appendix A)is

$$\gamma = -\lambda - 1. \tag{C.4}$$

However, structure functions calculated here often have a bend point with two slopes, so an analysis is needed to determine whether that was a sign of two separate power laws in the spectrum (a common example occurs in Nastrom and Gage (1985), where a spectral slope of $\lambda = -5/3$ is seen at the small scales, and $\lambda = -3$ is seen at large scales). A detailed examination of this case is shown in Appendix A. This analysis shows that, if spectral slopes of the two power-law scalings are λ_1 and λ_2, then the structure function can be written as

$$D_\theta(s) = c_1 s^{\gamma_1} + c_2 s^{\gamma_2}, \tag{C.5}$$

where the same relationship between structure function slope, γ, and spectral slope, λ (Equation C.4) applies between the large scale structure function slope versus small wavenumber spectral slope, and for the small scale structure function slope versus large wavenumber spectral slope. As long as the inertial range over which each power law applies is large enough and $\gamma_1 < \gamma_2$, the first term dominates the small scale, and the second term dominates the large scales. A primary goal of this paper will be to estimate γ from data over length scales where a single power law is suspected, or both γ_1 and γ_2 when a single linear fit is not apparent, and compare to theories that predict γ or a spectral equivalent.

Relevant Theory

Kolmogorov (1941) proposed the idea of an inertial range in isotropic, homogeneous turbulence, removed from frictional effects and removed from the scale of forcing. Through dimensional analysis, he arrived at a kinetic energy spectrum of $E(k) \propto k^{-5/3}$ in this range, and a corresponding velocity structure function slope of $\gamma = \frac{2}{3}$. Using Kolmogorov-like dimensional arguments, Obukhov (1949) and Corrsin (1951) predict a temperature spectrum with slope $\lambda = -\frac{5}{3}$ in the "intermediate" range where forcing is at a remote scale and dissipation is also distant (large Péclet number). The temperature structure function slope of $\gamma = \frac{2}{3}$ is expected for the Obukhov-Corrsin intermediate range.

It is important to note that velocity and temperature are active variables on constant pressure surfaces (isobars). The restoring to background stratification is a primary driver of internal waves, for example. However, strongly-stratified motions preferentially follow, not isobars, but potential density or neutral density surfaces to minimize energy expenditures (McDougall, 1987), although exact conservation is not possible (Nycander, 2011). Since temperature and salinity variance balance each other on isopycnals, temperature and salinity variations within the layer act as passive tracers.[1] A comprehensive study of temperature and salinity variations requires calculating turbulent statistics on both isobars and isopycnals (Cole and Rudnick, 2012) to analyze the properties of the variances as active versus passive tracers. Here isobaric structure functions will be contrasted with isopycnal structure functions, taken along surface-referenced potential density surfaces. Experimentation with

---

[1] Sometimes these variations are called 'spice', which is marked by compensating thermal and haline variations along a potential density surface, for example Yeager and Large (2007).

isoneutral structure functions and other reference levels for potential density yielded similar structure functions, so the simpler choice of fixed potential density with the surface reference pressure was made. Thus, the observations here will distinguish passive tracers from active, as should the predicted scalings. First, let us address the passive scalars, such as salinity variations on an isopycnal.

Due to rotation, stratification, and limited total depth, large-scale ocean flows are quasi-two-dimensional (dominantly horizontal). Two-dimensional turbulence scalings by Kraichnan (1967) of the kinetic energy slope of $E(k) \propto k^{-3}$ in the enstrophy cascade range (plus a logarithmic correction neglected here) at small scales and $E(k) \propto k^{-\frac{5}{3}}$ in the inverse energy cascade at large scales could potentially describe barotropic motions. The eddy-turnover timescale for stirring by the largest eddies ($\tau_k \propto (k^3 E(k))^{-1/2}$) is therefore a single dominant value for the entire enstrophy cascade where $E(k) \propto k^{-3}$, and varies for the inverse energy cascade where $E(k) \propto k^{-\frac{5}{3}}$. As barotropic flow is not strongly affected by salinity and temperature variations, scalars in regions where barotropic cascades are dominant should behave as passive tracers.

Batchelor (1959) theorized that in 2- or 3-dimensional velocity fields, between the viscous and diffusive scales, a passive tracer follows $\lambda = -1$ and thus, $\gamma = 0$. The scales observed in this study, however, are much larger, so the Batchelor spectrum does not apply directly. However, Batchelor (1959) and Vallis (2006) argue that in turbulence where each wavenumber is dominated by a single eddy-turnover timescale, a passive tracer spectrum should exhibit a slope of $\lambda = -1$ ($\gamma = 0$). For example, the Vallis scaling likely applies for separation distances larger than the largest eddies. Two cases where such a scaling applies should be kept in mind. First, as just explained, the 2d enstrophy cascade is expected to have a single dominant timescale and thus behave in this way. Within the range of scales of a 2d energy cascade no dominant timescale exists, and the Obukhov-Corrsin spectrum is expected to apply. However, if the inverse energy cascade only goes over a limited range of scales (Scott and Wang, 2005), then all scales larger than the largest eddies of this cascade are again dominated by a single eddy turnover time, and $\lambda = -1$ ($\gamma = 0$) applies for these largest scales.

Spectral behavior in quasi-geostrophic (QG) flows is more complex, as passive and active tracers have distinct behavior. Charney (1971), Salmon (1982), and Blumen (1978) all describe kinetic energy spectra for the quasi-geostrophic flows. For all cases, passive tracers should behave as Obukhov-Corrsin predict when $E(k) \propto k^{-5/3}$, or as the single eddy-turnover timescale result of $\lambda = -1$ ($\gamma = 0$) when $E(k) \propto k^{-3}$. However, the wavenumber range where these spectral slopes should appear in quasi-geostrophic flow is unclear as the effects of 'surface' QG (SQG) and 'interior' QG differ strongly by forcing and depth (Tulloch and Smith, 2006; Callies and Ferrari, 2013).

In QG and SQG, active tracers are related to the potential energy spectrum that accompanies the kinetic energy spectrum. The relationship between potential energy and kinetic energy differs between QG and SQG, however. Unfortunately, tracers observed by the method here can shed little light on these scalings without additional knowledge of the kinetic energy. Callies and Ferrari (2013) address the kinetic energy spectrum and its comparison to QG and SQG scalings with distance and depth from cruise data where velocities are directly observed.

The difficulty with QG and SQG active tracer scalings is that other phenomena occur that may affect the scalings which do not occur in QG or SQG dynamics. For example, the Garrett and Munk (1975) spectrum of internal waves is thought to often dominate the isobaric temperature and salinity variability, but the quasigeostrophic equations filter out these waves. Using mooring data, it may be possible to separate the sub-inertial motions from the faster ageostrophic modes, but such data is very sparse. Argo data do not afford this possibility. Another example is frontogenesis, which forms too slowly in QG (Williams, 1972). The presence of fronts has a direct influence on both the tracer and kinetic energy spectra. Klein et al. (1998) theorized that jumps in velocity and tracers would lead to a $\lambda = -2$ slope, and Bernstein and White (1974) and others observed a spectral slope of

$\lambda = -2$ above 400 m which they attribute to frontogenesis. Cole and Rudnick (2012) observe $\lambda = -2$ for isopycnal salinity spectra down to nearly 1000 m depth in the central subtropical North Pacific. A comparison with that data is below. Callies and Ferrari (2013) find strong effects that they attribute to waves–not eddies–over submesoscale separation scales (below about 20 km) in the Gulf Stream region.

A summary of this section is shown in Table 2.1.

Note on Homogeneity and Isotropy

All of the spectral theories above assume isotropy and homogeneity. Even without assuming homogeneity and the subsequent connection to spectra, the structure function is still an interesting diagnostic of ocean turbulence–unlike the traditional Fourier spectrum. Heterogeneous turbulence requires special care beyond Fourier methods, such as wavelet analysis or Wiener filters. Here it is shown that the assumption of homogeneity is not always, and maybe never be, valid, and the results from various regions with different levels of heterogeneity will be analyzed.

In situations where data are easily found, such as a simulation of turbulence, a heterogeneous, anisotropic turbulent flow could be analyzed conditionally by position and angle. That is, the structure function $D_\theta(\mathbf{s}, \mathbf{x})$ would remain a function varying along with six independent variables (two vectors, six components). With output from a model, structure functions could be calculated at every location, only averaging over time steps to maintain all six degrees of freedom. However, in the ocean, data are not so easily had, so a compromise is taken for the first analysis of the present data.

As seen by the large range of values in the salinity variance map in Figure C.1, the salinity variance is not homogeneous over much of the oceans. A particularly heterogeneous region was chosen in the central Equatorial Pacific to show the importance of the differentiation. Figure C.2 shows the isobaric salinity structure function for the whole region (bold), and then each four subregions, as shown in Figure C.1. The 95% confidence interval for the entire region shows the statistical significance of the differences between the average and its more homogeneous subgroups. However, the confidence intervals (see Table C.2 in Appendix B) are much larger for the four subgroups, making it harder to determine an accurate slope. Furthermore, the longest separation distances can only be studied in the larger box of the entire region. Therefore, in heterogeneous regions, a connection to a spectral slope is not made, as scaling laws are likely to vary significantly and interpretation of spectra in such cases would be questionable. The structure function can be interpreted directly in such cases, by preserving the $\mathbf{x}$ and $\mathbf{s}$ dependences. However, in noisy data, the structure function must still be averaged over limited areas, which reduces the number of independent variables at the cost of smoothing out the data. As Argo data continue to accumulate, it will become possible to reduce this effect by binning the averaging regions more and more finely, and only the testable assumption of statistical stationarity remaining.

Similarly, isotropy is also rare, both in flow analysis and sampling. To minimize biases in sampling in a few directions from an anisotropic field, all directions of pairs were weighted equally, even when some directions had fewer observations. For example, in a region chosen as a rectangle, there were more pairs in the major-axis direction, so they were weighted less to balance with the fewer minor-axis pairs. If more than 10% of the pairs were in the same direction (binned in 18° bins), then a weight was applied. This approach reduces the imbalance caused by an anisotropic distribution of pairs in particular directions, but may increase noise due to increased weights for less well-sampled orientations. Again, as the number of Argo observations increases, the added data can be used to isolate directional information by binning into smaller and smaller directional spans. Here we choose to average over all directions, which reduces precision, but increases accuracy of a clearly defined metric that converges to the sole metric in the case of isotropy.

Finally, it is possible, or even likely that sampling biases are inherent in the style of sampling based on passive float technology. That is, floats will be unlikely to drift into or out of coherent structures, and are likely to be ejected from regions of high eddy activity

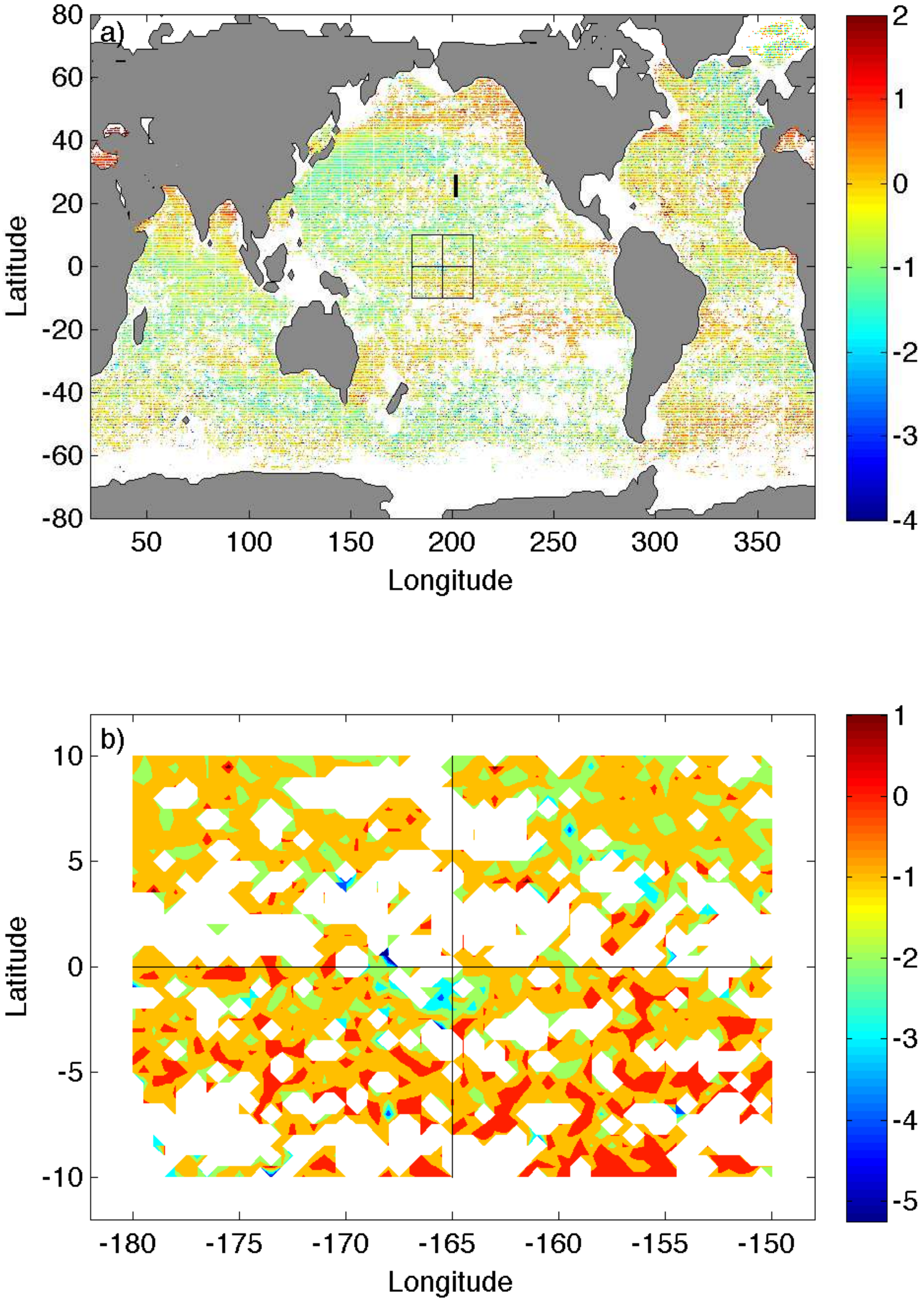

Figure C.1: The log of salinity “variance” at 5 m. a) shows the global variability of salinity variance, with the box showing the heterogeneous region examined in Figure C.2, and the bold line showing the location of the C&R observations. b) The heterogeneous region - note the different colorbar - and its four sub-regions.

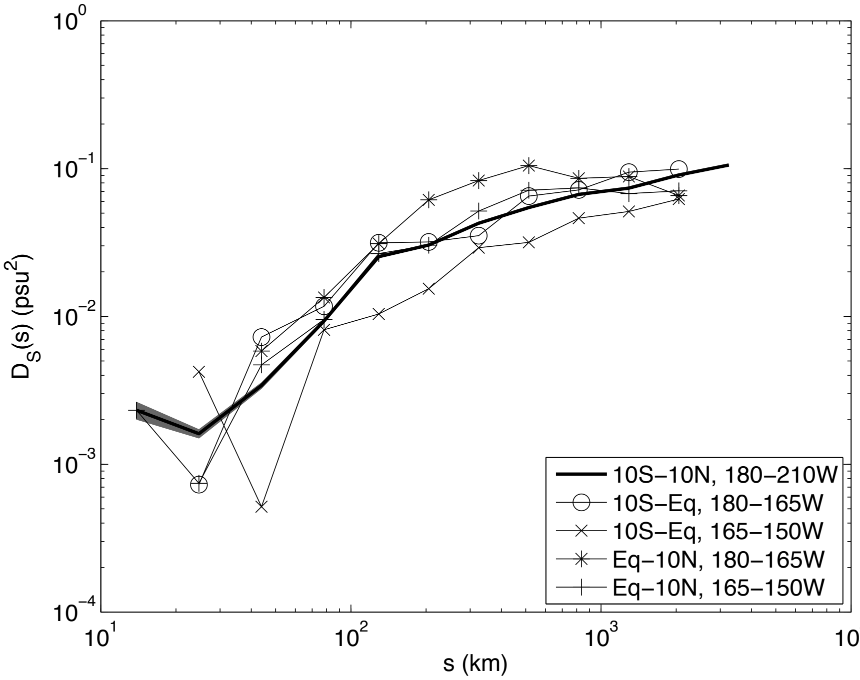

Figure C.2: Isobaric salinity structure function in the central Equatorial Pacific between 10S and 10N and 180W and 150W. The bold line is the structure function computed for the entire region, with a 95% confidence interval in gray shading, and each of the four lines is a subregion: star - 10S-Eq, 180-165W; diamond - 10S-Eq, 165-150W; circle - Eq-10N, 180-165W; square - Eq-10N, 165-150W toward lower energy regions (e.g., Davis, 1991). Without a substantially higher density of observations, such sampling biases due to heterogeneity are not easily detected generically and so are neglected here. However, all structure functions result from a large number of observational pairs (see Appendix B), and instrument error analysis and bootstrapping confidence intervals are used to verify these assumptions (see Appendices B and C).

Data Analysis Techniques

The data used in this analysis were obtained from the ∼3600 Argo floats located around the world in all oceans, from 2000 to 2013. Argo is to "provide an enhanced real-time capability for measurement of temperature and salinity through the upper 2000 m of the ocean and contribute to a global description of the seasonal cycle and inter-annual variability of the upper ocean thermohaline circulation" (Argo Science Team, 1998). The extensive float network introduced the first systematic sampling of temperature and salinity of the global ocean on a large spectrum of scales with accuracy of approximately .01°C and .01 psu, respectively. Each Argo float takes a vertical profile of temperature and salinity as it ascends from 2000 m to the surface, where it transmits the obtained data to a satellite before descending and drifting for 9 days. Calibration is done on all profiles at one of the national data centers, and though an incorrect or missing calibration could skew the statistics computed here, they are assumed to be correct (Carval et al., 2011). These data were collected and made freely available by the International Argo Program and the national programs that contribute to it (http://www.Argo.ucsd.edu, http://Argo.jcommops.org). A simple quality-control scheme was applied to the data before analysis began. In processing the data, we relied on the Argo delayed-mode procedures for checking sensor drifts and offsets in salinity, and made use of the Argo quality flags. Density was computed for each Argo temperature/salinity profile, which was then interpolated to density levels, $\sim 24.0 - 27.8\ kg\ m^{-3}$ in intervals of $0.1\ kg\ m^{-3}$, and depth levels, $5m$ at the surface, with increasing intervals down to $2000m$.

The structure function for potential temperature and salinity are computed as follows:

$$D_\theta(s) = \overline{(\theta'(x) - \theta'(x+s))^2}, \tag{C.6}$$

$$D_S(s) = \overline{(S'(x) - S'(x+s))^2}. \tag{C.7}$$

Overbar here implies spatiotemporal averaging, with weighting to balance among orientations. If the flow is heterogeneous or anisotropic, this procedure can only provide the spatial average of the structure function. Horizontal structure functions are computed here, so only observations at the same vertical level were used, either on pressure levels standard to Argo data, or in 0.1 $kg\ m^{-3}$ potential density bands. When separations were taken along pressure surfaces, these isobaric structure functions will be denoted $D_\theta(s)|_p$, or for separations along potential density contours, the isopycnic structure function will be written as $D_\theta(s)|_\sigma$. Structure functions are plotted on a graph with logarithmic axes with the separation distance, s, on the horizontal and $D(s)$ on the vertical, while a power spectral density is usually plotted with wavenumber, k, on the horizontal axis. On these log-log structure function plots, the slope of the line is γ (sometimes equated to the spectral slope minus one, from Equation (C.4).

In order to maximize coverage, data collected over the whole time period were included. The separation distance, s, for each data pair was calculated with the known location of the floats. Since few (or no) Argo floats measure at the exact same time, a limiting velocity, c_{max}, was chosen to select observations that occur close enough together in time (Δt) and over sufficient spatial separation (s) that effective simultaneity is expected, i.e. a typical ocean signal could not travel between the two locations. Thus, only separations where $s > c_{max}\Delta t$ were considered "simultaneous," and used for analysis (following Frehlich and Sharman, 2010a). A slow c_{max} is desirable in order to include more data pairs in the analysis, but if, for example, a float samples the same eddy in subsequent profiles, and the limiting velocity is too slow, the same eddy would be sampled twice. This results in overly-correlated pairs and biased structure functions. On the other hand, sampling points that are too far apart in time and space become uncorrelated and virtually random, so the structure functions became flat. When experimenting with different c_{max} values, the high values created structure functions that were too noisy, with too few pairs being included in the computation. When c_{max} was too low, the structure functions became more smooth (desirable), but the slopes changed (undesirable). Therefore, the velocity chosen made the structure functions as smooth as possible before the slope changed. A speed of $c_{max} = 1\ m\ s^{-1}$ was chosen to be likely to exceed the propagation speed of all large-scale, unidirectional signals, though the exact chosen c_{max} had little effect on the resulting structure functions.

As mentioned, the structure functions are calculated on both isobars and isopycnals. Potential density (σ_θ, the density of a parcel of water brought to the surface to eliminate compressive effects (Stewart, 2008)) was calculated with the Thermodynamic Equation of Seawater toolbox (McDougall, 2011) with the temperature, depth and salinity measured by each Argo float, using a reference pressure of the surface (σ_0). Potential density was chosen as the density coordinate instead of neutral density because the path-dependence of neutral density introduces inconsistencies in structure function interpretation at large s. However, by calculating structure functions with both neutral and potential density coordinates with the same data, only minor differences in the average $D(s)$ occurred, so the results presented are not overly sensitive to this choice. For reference, Figure C.3 shows the calculated potential density from the OCCA climatology with depth in the western Atlantic (a) and central Pacific (b) Oceans.

Structure Function Results

It is of immediate importance to note that it is possible to use the Argo data to retrieve the structure function over macro-scale separation distances. Due to lack of simultaneous nearby

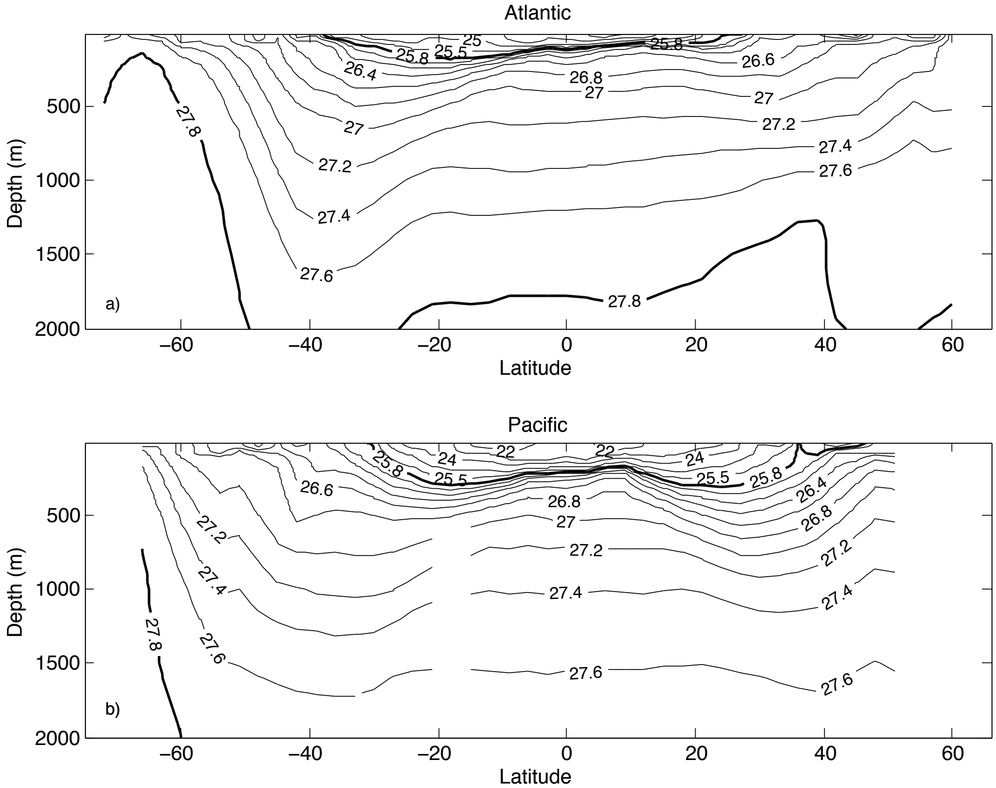

Figure C.3: Potential density (in $kg\ m^{-3}$) along 23.5W in the eastern Atlantic Ocean (a) and 180W in the Pacific (b), calculated from the OCCA climatology of temperature, salinity, and pressure with the Thermodynamics Equation of Seawater.

observations at scales smaller than $O(10km)$, the structure function is noisy and slope is not discernible for submesoscales, but at scales larger than $O(10km)$, a clear slope can be seen. Cole and Rudnick (2012) (hereafter referred to as C&R) calculated salinity spectra on 7 isopycnal bands along 158W from 22.75-29N, and observed a spectral slope of $\lambda = -2$ (see Figure 9 of C&R). Taking advantage of the Argo data in that region (156-160W, 10-40N), the structure function was computed on the same potential density bands and including the same region and is shown in Figure C.4. A slope of $\gamma = 1$ is seen, consistent with the spectral slope of $\lambda = -2$ of C&R. The magnitudes and slopes from C&R were used and the amplitude of the corresponding structure function was calculated, and the equivalent (model) structure function is shown as the dashed line in Figure C.4a, and the thin lines in Figure C.4b. The range of scales represented in C&R (the length of the bold line) is surpassed by the use of Argo data. The difference in magnitude can be attributed to the inclusion of several years of data (and therefore inter-annual variability), while C&R only have one year. The seasonal spectra in C&R were also duplicated and matched in magnitude quite well (Figure C.4b). However, C&R has more data for each individual month in this region, so the Argo structure functions (even using a larger area from 0-50N) for the seasons are noisier. The close match provides confidence to continue and calculate both isobaric and isopycnal structure functions, as is done extensively in the companion paper (McCaffrey et al., 2014a).

Conclusions

The first conclusion worthy of attention is that the Argo float network's observations of temperature and salinity are a useful tool to understand the temperature and salinity variance spectrum in the ocean, and with the addition of velocity data, this method can be used for the kinetic energy structure function as well. Following the methodology of Frehlich and Sharman (2010a), using individual observations varying in height (or depth, for the ocean), structure functions can be calculated and sometimes used to infer the spectral slope of the

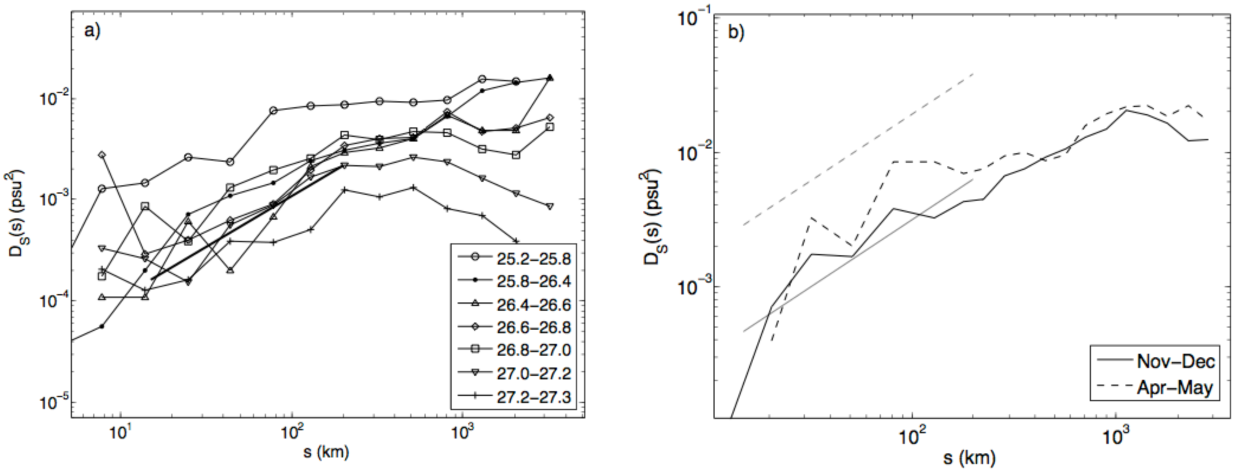

Figure C.4: a) Salinity structure function, $D_S(s)|_\sigma$, along 158W for 10-40N along isopycnals of $25.2-25.8\ kg\ m^{-3}$, $25.8-26.4\ kg\ m^{-3}$, $26.4-26.6\ kg\ m^{-3}$, $26.6-26.8\ kg\ m^{-3}$, $26.8-27.0\ kg\ m^{-3}$, $27.0-27.2\ kg\ m^{-3}$, $27.2-27.3\ kg\ m^{-3}$. Bold line is a fit to the structure function model equivalent to the spectrum found by C&R. b) Structure functions at $25.2-25.8\ kg\ m^{-3}$ for the seasons specified in C&R. April-May: solid, Nov-Dec: dashed. Thin solid and dashed lines are the structure function model equivalent to a fit of C&R's spectrum for the April-May and Nov-Dec, respectively.

tracer variance spectrum, depending on homogeneity. Even with discontinuous and spotty temperature or salinity measurements, an appreciation of the turbulence statistics at greater depths and over broader geographic regions than previously observed is now possible, and will only improve with the growth of the Argo dataset. The ability to get back a spectrum from a structure function, even in a case where two distinct structure function slopes are present and data is filled with gaps, shows how powerful a tool the structure function is.

Another strength of the structure function is its ability to be used for heterogeneous flows. The more classical spectrum requires the flow to be homogeneous to identify a spectral slope. Because the oceans are not homogeneous (the variance in even the most homogeneous regions of the ocean still varies by more than an order of magnitude), the structure function is often a better tool to use than the variance spectrum. However, the primary limitation to this approach is data density, as spatial refinement reduces the amount of observation pairs that can be used.

Two primary validation techniques have been presented here. First, the point-by-point agreement between satellite measurements and Argo (Gommenginger et al., 2010; Bhaskar et al., 2009) implies that a satellite-based structure function would provide similar answers to those from Argo, but would be limited to surface temperatures only. Second, the Argo data are in agreement in slope, magnitude, and seasonal variability when compared to the Cole and Rudnick (2012) glider data. However, the Argo data is easily extended over longer time and spatial scales, as it has already been collected on a near-global basis for many years. This study also shows that even unevenly spaced, discontinuous salinity and temperature measurements in the ocean are capable of producing turbulent statistics that may be similarly interpreted instead of, or along with, the traditional tracer spectra.

This work has opened many possibilities for future studies beyond the results already presented. Alongside the increasing number of Argo floats measuring at depth, it would be beneficial to include other sources of data to fill in the spatial gaps in Argo's network that would allow the structure function to be calculated further into the inertial range of the oceans at smaller scales (e.g., mooring data). This method can also be extended to velocity observations in order to directly measure the kinetic energy structure function.

Acknowledgments This paper was inspired by conversations with Rod Frehlich. We wish that there had been more time with Rod, so that we could learn more from him. The Argo Program is part of the Global Ocean Observing System. KM was supported by the CIRES/NOAA-ESRL Graduate Research Fellowship. BF-K was supported by NSF 0855010 and 1245944 and GF was supported in part through NASA project "Estimating the Circulation and Climate of the Ocean (ECCO) for CLIVAR" and NSF 1023499.

Appendix A

LargeStructure Function - Spectrum Relationship, In Depth

The spectral and structure function theory will be addressed starting from the isotropic temperature variance spectrum, $B(k)$, found similarly to the approach used in Webb (1964):

$$\overline{\theta'^2} = \int_0^\infty B(k)dk. \tag{C.8}$$

for wavenumbers, k, where θ' is temperature variance, defined in Section C. The salinity variance spectrum is the same as Equation C.8, with S' instead of θ', and from here on, temperature variance and salinity variance will be discussed interchangeably. The temperature variance autocorrelation function, $R(s)$, and n^{th}-order structure function, $D_\theta(s)$, for spatial separation, s, are defined by

$$\begin{aligned} R(s) &= \overline{\theta'(x)\theta'(x+s)}, && \text{(C.9)} \\ D_\theta(s) &= \overline{(\theta'(x) - \theta'(x+s))^n}. && \text{(C.10)} \end{aligned}$$

The second-order ($n = 2$) structure function, which will most often be calculated here, has the unique relationship to $R(s)$ by

$$D_\theta(s) = 2(\overline{\theta'^2} - R(s)). \tag{C.11}$$

The autocorrelation may be represented spectrally for isotropic, homogeneous turbulence by

$$R(s) = \int_0^\infty B(k)\cos[ks]\mathrm{d}k. \tag{C.12}$$

Using the relationship between the autocorrelation and structure function from (C.11), and the spectral definition of autocorrelation in (C.12), the structure function can be written spectrally by

$$D_\theta(s) = 2\int_0^\infty B(k)\,(1-\cos[ks])\,\mathrm{d}k. \tag{C.13}$$

As mentioned in Section C, for a given spectrum, $B(k) = \alpha_B k^\lambda$, with a single spectral slope, λ, over a range from $k_{min} < k < k_{max}$ and a given structure function, $D_\theta(s) = \alpha_D s^\gamma$, with a single structure function slope, γ, a change of variables ($ks \rightarrow \xi$) yields

$$\begin{aligned} D_\theta(s) &= 2\int_0^\infty \alpha_B k^\lambda\,(1-\cos[ks])\,\mathrm{d}k \\ &= 2\alpha_B s^{-\lambda-1}\int_0^\infty \xi^\lambda\,(1-\cos\xi)\,\mathrm{d}\xi \\ &= s^\gamma\Big[2\alpha_B\int_0^\infty \xi^\lambda\,(1-\cos\xi)\,\mathrm{d}\xi\Big]. \end{aligned} \tag{C.14}$$

This shows that $\gamma = -\lambda-1$, relating the slope of the structure function, γ, to the spectral slope, λ. Webb (1964) shows that outside of the inertial range $[k_{min}, k_{max}]$, the contribution to the spectrum is small, so (C.14) can be truncated and written as

$$D_\theta(s) = s^\gamma\Big[2\alpha_B\int_{k_{min}}^{k_{max}} \xi^\lambda\,(1-\cos\xi)\,\mathrm{d}\xi\Big]. \tag{C.15}$$

One could make the same argument for the kinetic energy spectrum, $E(k)$, and velocity structure function, $D_U(s)$. Thus,

$$\overline{U^2} = \int_0^\infty E(k)dk \tag{C.16}$$

$$D_U(s) = \overline{(u(x)-u(x+s))^2}. \tag{C.17}$$

Following the same method, $D_U(s) \propto s^{\beta_D}$ and $E(k) \propto k^{\beta_E}$ produce the same relationship:

$\beta_D = -\beta_E - 1$.

In the case of a tracer variance spectrum with a direct and indirect cascade producing two power-law scalings (as is the case in Nastrom and Gage (1985)), (C.13) can be split into four pieces spanning intervals in k:

$$\begin{aligned} D_\theta(s) &= 2\int_0^\infty B(k)\left(1-\cos[ks]\right)\mathrm{d}k \\ &= 2\left(\int_0^{k_{min}} B(k)\left(1-\cos[ks]\right)\mathrm{d}k + \int_{k_{min}}^{k_1} \alpha_1 k^{\lambda_1}\left(1-\cos[ks]\right)\mathrm{d}k\right) + \\ &\quad 2\left(\int_{k_1}^{k_{max}} \alpha_2 k^{\lambda_2}\left(1-\cos[ks]\right)\mathrm{d}k + \int_{k_{max}}^{\infty} B(k)\left(1-\cos[ks]\right)\mathrm{d}k\right). \end{aligned} \tag{C.18}$$

Since the first and the last integrals are definite and negligible (Webb, 1964), inserting the continuity of $B(k)$ ($\alpha_1 k_1^{\lambda_1} = \alpha_2 k_1^{\lambda_2}$) produces

$$D_\theta(s) = 2\alpha_1\left(\int_{k_{min}}^{k_1} k^{\lambda_1}\left(1-\cos[ks]\right)\mathrm{d}k + k_1^{\lambda_1-\lambda_2}\int_{k_1}^{k_{max}} k^{\lambda_2}\left(1-\cos[ks]\right)\mathrm{d}k\right) \tag{C.19}$$

Assuming each of the two inertial ranges is large ($k_{min} << k_1 << k_{max}$) the structure function is dominated by only one of the two integrals in (C.19), depending on scale of s when compared with the wavenumber ($k_{min} < 1/s < k_1$ or $k_1 < 1/s < k_{max}$). Performing the change of variables as done above for the single power law case, gives the structure function in terms of s,

$$D_\theta(s) = 2\left(\alpha_1 s^{-\lambda_1-1}\int_{k_{min}s}^{k_1 s} \xi^{\lambda_1}\left(1-\cos[\xi]\right)\mathrm{d}\xi + \alpha_2 s^{-\lambda_2-1}\int_{k_1 s}^{k_{max}s} \xi^{\lambda_2}\left(1-\cos[\xi]\right)\mathrm{d}\xi\right). \tag{C.20}$$

Thus, when the inertial ranges are deep, the structure function is closely approximated by a polynomial with two terms:

$$D_\theta(s) = c_1 s^{\gamma_1} + c_2 s^{\gamma_2}, \tag{C.21}$$

with $\gamma_1 = -\lambda_2 - 1$ and $\gamma_2 = -\lambda_1 - 1$. The analysis of Nastrom and Gage (1985) confirmed that the bend point where the structure function switches from being dominated by the second to the first term happens near $s \approx 1/k_1$, although this result was much clearer when the inertial ranges were made wider than those in the actual observations of Nastrom and Gage (1985). Other prototypical dual cascade spectra were also tested, yielding similar results (e.g., the direct and indirect cascades of 2D turbulence from Kraichnan, 1967).

Appendix B

Structure Function Details

The tables included here show the details of the structure function calculations, including the numbers of float profiles in each calculation, the number of "simultaneous" pairs used, and the 95% bootstrap confidence intervals for the structure functions.

The 95% bootstrap confidence interval was calculated because the population of pairs that contribute to the average in the structure function are not normally distributed, so the standard deviation of the observations is not sufficient. Using the Central Limit Theorem (Devore, 2009), which states that the means, $\overline{x}_n$ from n samples of a population (here, the pairs of simultaneous observations), are normally distributed, and therefore, the population mean (μ, the true quantity of the structure function) is the mean of the sample means ($\mu = \overline{\overline{x}_n}$). Therefore, the confidence interval is the area with a 95% probability that it contains the true structure function value. This theorem is only true when n is sufficiently large (usually larger than $n = 30$, though some populations may require more), so $n = 200$ was used here.

Region	# of profiles	# of pairs
10S-10N, 180W-150W	14236	1098734
10S-Eq, 180-165W	3537	29194
10S-Eq, 165-150W	3758	39664
Eq-10N, 180-165W	3484	32588
Eq-10N, 165-150W	3456	32509

Table C.1: Number of profiles and pairs used to compute the structure function in the heterogeneous region analysis in Figure C.2.

Region	10S-10N, 180W-150W	10S-Eq, 180-165W	10S-Eq, 165-150W	Eq-10N,W 180-165W	Eq-10N, 165-150W
s (10^3 km)					
0.0139	2.3±0.3069	NaN	NaN	NaN	0.9±0.3068
0.0247	1.6±0.1153	0.7±NaN	4.2±NaN	NaN	0.7±0.0846
0.0439	3.4± 0.1492	7.2±0.4158	0.5±0.0203	5.8±0.3515	4.7±0.2722
0.0781	9.3±0.2352	11.7±0.9514	8.1±0.2947	13.4±0.6854	9.5±0.4817
0.1292	25.4±0.2157	31.5±0.6355	10.4±0.1810	31.1±0.6352	26.6±0.4008
0.2048	30.4±0.1330	31.9±0.2762	15.4±0.1035	61.4±0.4863	30.3±0.3192
0.3246	42.7±0.1127	35.2±0.2894	29.1±0.1250	83.0±0.4407	51.6±0.2703
0.5145	54.5±0.0728	65.2±0.1959	31.7±0.0779	104.8±0.2505	71.5±0.1970
0.8155	66.9±0.0393	71.7±0.1704	46.2±0.0550	85.9±0.1561	74.0±0.1290
1.2924	73.7±0.0266	94.6±0.1830	51.3±0.0645	88.5±0.1539	67.8±0.1037
2.0484	90.5±0.0252	99.3±0.6636	62.2±0.2756	65.7±0.4382	70.6±0.3711
3.2465	105.8±0.0426	NaN	NaN	NaN	NaN

Table C.2: The structure function plus/minus the 95% bootstrap confidence interval for the structure function in the heterogeneous region analysis in Figure C.2. All values are 10^{-3} psu^2.

Appendix C

Error Analysis An important aspect of structure function analysis that must be included is an understanding of random noise. Lester et al. (1970) showed that the structure function of Gaussian white noise has a slope of $\gamma = 0$, so those results were replicated with a randomly generated dataset of temperatures and salinities with changing standard deviations. The same calculation was particularly important to determine the noise level generated by measurement error. Results of this analysis are shown in Figure C.5. Using the square of the known standard error of the Argo measurements of temperature and salinity

Depth	# of profiles	# of pairs
25.5	3649	34228
26.1	4549	60546
26.4	4620	65251
26.6	4608	65894
26.8	4668	66417
27.0	4768	67930
27.2	4764	67848

Table C.3: Number of profiles and pairs used to compute the structure function in Figure C.4.

density ($kg\ m^{-3}$)	25.5	26.1	26.4	26.6	26.8	27.0	27.2
s ($10^3\ km$)							
0.0139	1.5±0.099	1.5±0.029	0.1±0.003	0.3±0.023	0.9±0.048	0.3±0.029	0.1±0.014
0.0247	2.6±0.100	0.7±0.018	0.6±0.027	0.4±0.019	0.4±0.040	0.2±0.009	0.2±0.002
0.0439	2.4±0.077	1.1±0.031	0.2±0.008	0.6±0.019	1.3±0.052	0.6±0.022	0.4±0.008
0.0781	7.5±0.100	1.5±0.031	0.7±0.021	0.9±0.022	2.0±0.026	0.9±0.022	0.4±0.007
0.1292	8.4±0.092	2.4±0.023	2.1±0.024	1.9±0.025	2.6±0.024	1.7±0.017	0.5±0.005
0.2048	8.8±0.078	3.1±0.030	2.9±0.034	3.4±0.037	4.4±0.039	2.2±0.016	1.2±0.016
0.3246	9.5±0.035	3.6±0.014	3.3±0.024	4.0±0.023	3.9±0.018	2.1±0.008	1.1±0.007
0.5145	9.1±0.032	4.0±0.016	4.1±0.017	4.1±0.018	4.8±0.016	2.6±0.007	1.3±0.005
0.8155	9.7±0.021	6.7±0.012	6.8±0.014	7.3±0.013	4.6±0.009	2.4±0.004	0.8±0.001
1.2924	15.6±0.023	11.9±0.012	4.8±0.009	4.7±0.007	3.1±0.005	1.6±0.002	0.7±0.002
2.0484	14.7±0.024	14.5±0.014	4.9±0.009	5.0±0.009	2.7±0.007	1.2±0.003	0.4±0.003
3.2465	NaN	16.1±0.046	16.1±0.017	6.4±0.013	5.2±0.0072	0.9±0.001	0.1±0.000

Table C.4: The structure function plus/minus the 95% bootstrap confidence interval for the structure functions in Figure C.4. All values are $10^{-3}\ psu^2$.

(.01 degree Celsius and .01 psu, respectively) as the standard deviation, and a typical temperature and salinity value for the mean, a Gaussian dataset was created, and the structure function was calculated. A noise floor for the structure function including the error from the climatology was also considered, using the total standard deviation, $\sigma_{tot} = \sqrt{\sigma^2_{Argo} + \sigma^2_{clim}}$. This more realistic noise floor (dashed line in Figure C.5) of $O(10^{-4})$ is still below the structure functions calculated, allowing this analysis of turbulence from Argo data to continue without fear of data measurement errors interfering.

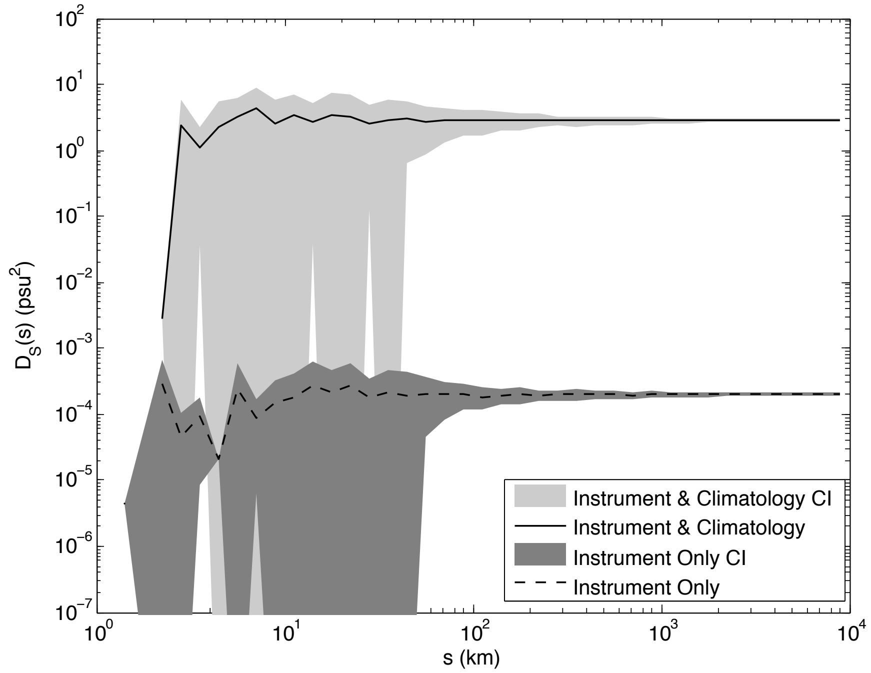

Figure C.5: Structure function of a Gaussian random synthetic dataset with standard error of the Argo instruments (dark gray) and climatology (light gray).

References

Argo Science Team, 1998: On the design and implementation of argo. *International CLIVAR Project Office Rep. 21, GODAE Rep. 5.*

Batchelor, G. K., 1959: Small-scale variation of convected quantities like temperature in turbulent fluid .1. General discussion and the case of small conductivity. *Journal of Fluid Mechanics*, **5 (1)**, 113–133.

Bernstein, R. and W. White, 1974: Time and length scales of baroclinic eddies in the central North Pacific Ocean. *J. Phys. Oceanogr.*, **4**, 613–624.

Bhaskar, T. U., S. Rahman, I. Pavan, M. Ravichandran, and S. Nayak, 2009: Comparison of amsr-e and tmi sea surface temperature with argo near-surface temperature over the indian ocean. *International Journal of Remote Sensing*, **30 (10)**, 2669–2684.

Blumen, W., 1978: Uniform potential vorticity flow .1. Theory of wave interactions and 2-dimensional turbulence. *Journal of the Atmospheric Sciences*, **35 (5)**, 774–783.

Callies, J. and R. Ferrari, 2013: Interpreting energy and tracer spectra of upper-ocean turbulence in the submesoscale range (1-200 km). *Journal of Physical Oceanography*, in press.

Carval, T., et al., 2011: Argo user's manual, version 2.31. Tech. rep., Argo Data Management.

Charney, J. G., 1971: Geostrophic turbulence. *Journal of the Atmospheric Sciences*, **28**, 1087–1095.

Cole, S. and D. Rudnick, 2012: The spatial distribution and annual cycle of upper ocean thermohaline structure. *Journal of Geophysical Research-Oceans*, **117**.

Corrsin, S., 1951: On the spectrum of isotropic temperature fluctuations in isotropic turbulence. *Journal of Applied Physics*, **22 (469)**.

Davis, R. E., 1991: Lagrangian ocean studies. *Annual Review of Fluid Mechanics*, **23 (1)**, 43–64.

Devore, J., 2009: *Probability and Statistics for Engineering and the Scientes, Seventh Edition*. Brooks/Cole, Belmont, CA.

Forget, G., 2010: Mapping ocean observations in a dynamical framework: A 2004-06 ocean atlas. *Journal of Physical Oceanography*, **40**, 1201–1221.

Forget, G. and C. Wunsch, 2007: Estimated global hydrographic variability. *Journal of Physical Oceanography*, **37 (8)**, 1997–2008, doi:DOI10.1175/JPO3072.1.

Fox-Kemper, B., et al., 2011: Parameterization of mixed layer eddies. III: Implementation and impact in global ocean climate simulations. *Ocean Modelling*, **39**, 61–78, doi:10.1016/j.ocemod.2010.09.002, URL `http://dx.doi.org/10.1016/j.ocemod.2010.09.002`.

Frehlich, R. and R. Sharman, 2004: Estimates of turbulence from numerical weather prediction model output with applications to turbulence diagnosis and data assimilation. *Monthly Weather Review*, **132**, 2308–2324.

Frehlich, R. and R. Sharman, 2010: Climatology of velocity and temperature turbulence statistics determined from rawinsonde and ACARS/AMDAR data. *Journal of Applied Meteorology and Climatology*, **49 (6)**, 1149–1169.

Garrett, C. and W. Munk, 1975: Space-time scales of internal waves: A progress report. *Journal of Geophysical Research*, **80 (3)**, 291–297.

Gommenginger, C. P., C. J. Banks, M. A. Srokosz, and H. M. Snaith, 2010: Observations of atmosphere-ocean freshwater input with in situ and satellite measurements of surface salinity and rain.

Hamilton, K., Y. O. Takahashi, and W. Ohfuchi, 2008: Mesoscale spectrum of atmospheric motions investigated in a very fine resolution global general circulation model. *Journal of Geophysical Research*, **118**.

Hosegood, P., M. C. Gregg, and M. H. Alford, 2006: Sub-mesoscale lateral density structure in the oceanic surface mixed layer. *Geophysical Research Letters*, **33 (L22604)**, doi:10.1029/2006GL026 797.

Klein, P., A. M. Treguier, and B. L. Hua, 1998: Three-dimensional stirring of thermohaline fronts. *Journal of Marine Research*, **56 (3)**, 589–612.

Kolmogorov, A. N., 1941: The local structure of turbulence in incrompressible viscous fluid for very large reynolds number. *Dokl. Akad. Nauk. SSSR*, **30**, 9–13.

Koshyk, J. N. and K. Hamilton, 2001: The horizontal kinetic energy spectrum and spectral budget simulated by a high-resolution troposphere-stratosphere mesosphere gcm. *Journal of Atmospheric Sciences*, **58**, 329–348.

Kraichnan, R. H., 1967: Inertial ranges in two-dimensional turbulence. *Physics of Fluids*, **16**, 1417–1423.

Lester, P., E. Reiter, and C. S. U. D. of Atmospheric Science, 1970: *The Application of Shear Functions in the Study of the Meso- and Microstructure of the Atmosphere*. Atmospheric science paper, Department of Atmospheric Science, Colorado State University, URL `http://books.google.com/books?id=F\_nVSgAACAAJ`.

Lindborg, E., 1999: Can the atmospheric kinetic energy spectrum be explained by two-dimensional turbulence? *Journal of Fluid Mechanics*, **388**, 259–288.

McCaffrey, K., B. Fox-Kemper, and G. Forget, 2014a: Estimates of ocean macro-turbulence: Structure function and spectral slope from argo profiling floats, i: Global results. *Journal of Physical Oceanography*, submitted.

McCaffrey, K., B. Fox-Kemper, and G. Forget, 2014b: Estimates of ocean macro-turbulence: Structure function and spectral slope from argo profiling floats, i: Methods. *Journal of Physical Oceanography*, submitted.

McDougall, T. J., 1987: Neutral surfaces. *Journal of Physical Oceanography*, **17**, 1950–1964.

McDougall, T. J., 2011: *Getting started with TEOS-10 and the Gibbs Seawater (GSW) Oceanographic Toolbox*, Vol. 7.

Nastrom, G. D. and K. S. Gage, 1985: A climatology of atmospheric wavenumber spectra of wind and temperature observed by commercial aircraft. *Journal of the Atmospheric Sciences*, **42**, 950–960.

Nycander, J., 2011: Energy conversion, mixing energy, and neutral surfaces with a nonlinear equation of state. *Journal of Physical Oceanography*, **41 (1)**, 28–41, doi:DOI10.1175/2010JPO4250.1.

Obukhov, A. M., 1949: The structure of the temperature field in a turbulent flow. *Izv. Akad. Nauk. SSSR, Ser. Geog. and Geophys.*, **13 (58)**.

Rudnick, D. L. and R. Ferrari, 1999: Compensation of horizontal temperature and salinity gradients in the ocean mixed layer. *Science*, **283 (5401)**, 526–529.

Salmon, R., 1982: Geostrophic turbulence. *Topics in Ocean Physics*, A. R. Osborne and P. M. Rizzoli, Eds., Proceedings of the International School of Physics Enrico Fermi (July 1980), Course LXXX.

Scott, R. B. and F. Wang, 2005: Direct evidence of an oceanic inverse kinetic energy cascade from satellite altimetry. *Journal of Physical Oceanography*, **35**, 1650–1666.

She, Z.-S. and E. Leveque, 1994: Universal scaling laws in fully developed turbulence. *Physical Review Letters*, **72**, 336–339.

Skamarock, W. C., 2004: Evaluating mesoscale nwp models using kinetic energy spectra. *Monthly Weather Review*, **132**, 3019–3032.

Stewart, R. H., 2008: *Introduction to Physical Oceanography*. R. H. Stewart (online website self-publication), URL `http://oceanworld.tamu.edu/ocean410/ocng410_text_book.html`.

Takahashi, Y. O., K. Hamilton, and W. Ohfuchi, 2006: Explicit global simulation of the mesoscale spectrum of atmospheric motions. *Geophysical Research Letters*, **33**.

Tulloch, R. and K. S. Smith, 2006: A theory for the atmospheric energy spectrum: Depth-limited temperature anomalies at the tropopause. *Proceedings of the National Academy of Sciences*, **103 (40)**, 14 690 14 694.

Vallis, G. K., 2006: *Atmospheric and Oceanic Fluid Dynamics : Fundamentals and Large-Scale Circulation*. Cambridge University Press, Cambridge.

Webb, E. K., 1964: Ratio of spectrum and structure-function constants in the inertial subrange. *Quarterly Journal of the Royal Meteorological Society*, **90 (385)**, 344–345.

Williams, R., 1972: Quasi-geostrophic versus non-geostrophic frontogenesis. *Journal of Atmospheric Sciences*, **29**, 3–10.

Yeager, S. G. and W. G. Large, 2007: Observational evidence of winter spice injection. *Journal of Physical Oceanography*, **37**, 2895–2919, doi:DOI10.1175/2007JPO3629.1.

Abstract - Estimates of Ocean Macro-turbulence: Structure Function and Spectral Slope from Argo Profiling Floats, II: Global Results

Previous studies have shown that a second-order structure function can be computed from discontinuous, scattered observations to describe the kinetic energy or tracer variance in both the atmosphere and the ocean. Taking advantage of the global coverage of the Argo profiling float network, this study extends the structure function method to examine the depth, latitude, eddy kinetic energy, and basin dependence of salinity anomalies. An analysis of homogeneous versus heterogeneous regions, based on salinity variance, is also completed. Structure functions are computed along both isobars and isopycnals to differentiate between the active and passive tracer variance spectra. In homogeneous regions, the active tracer structure function slopes of approximately $\gamma = \frac{2}{3}$ at small scales flatten out to 0 (related to spectral slopes of $\lambda = -\frac{5}{3}$ and -1, respectively) as separation distance increases, with a strong amplitude dependence on depth. These slopes are consistent with scaling arguments originating from Obukhov, Corrsin, and Batchelor. The passive tracer structure function is also flat at large scales, but with a shallower small-scale slope. In heterogeneous regions where the relation to spectral slope breaks down, structure function slopes of $\gamma = 0$ are seen, with amplitude decaying with depth. Structure function amplitude changes with latitude, differing at the surface and at depth. The amount of eddy activity also impacts the structure functions, both in slope and in amplitude. Turbulence intermittency could be detected with present Argo observations via the tails of the probability distribution, but reliable computation of higher order structure functions will require more observations.

Introduction

In an attempt to gain a better understanding of the transfer of large-scale ocean energy to smaller scales, spectral and structure function analyses can be invaluable. Atmospheric turbulence has been studied through spectral and structure function analyses for decades (Nastrom and Gage, 1985; Lindborg, 1999; Frehlich and Sharman, 2010a), and the results have been duplicated by high resolution General Circulation Models (GCMs) and mesoscale Numerical Weather Prediction (NWP) models as well (Koshyk and Hamilton, 2001; Skamarock, 2004; Frehlich and Sharman, 2004; Takahashi et al., 2006; Hamilton et al., 2008). As realistic ocean climate models become increasingly turbulent, a similar dataset to the Nastrom and Gage spectrum would be a perfect evaluation tool. Unfortunately, continuous observations are sparse in the oceans.

The recent rawinsonde method of Frehlich and Sharman (2010a) proved that calculating second-order structure functions from scattered individual rawinsondes can be used to infer a spectral slope that matches the results of Nastrom and Gage. In the companion paper, McCaffrey et al. (2014) adapt this method for use with the temperature and salinity observations from Argo profiling floats. There, it was shown that a discernible slope can be identified, and that structure functions from Argo salinity data matches observed salinity variance spectra from Cole and Rudnick (2012). The success of that work allows the expansion of the method to answer questions as to how salinity variance changes geographically. In the current work, the second-order salinity structure function is calculated in regions varying in depth, latitude, eddy activity, and level of homogeneity. Several theories have predicted the spectral and structure function slopes of turbulent regimes, and those results are summarized in Table 2.1. The results of the current analysis show some consistency with the scaling laws derived by assuming a continuous transfer of kinetic energy and temperature variance between many scales of motion. Intriguingly, these results differ by region, offering a greater diversity of possibilities that those explored in more regional studies.

Two prominent recent examples which will be contrasted against are the observations of Cole and Rudnick (2012) and Callies and Ferrari (2013). Those analyses used glider salinity and temperature and ship-based velocity measurements to form turbulence spectra over a range of scales covered by the analysis herein. The results here show that while consistency is found with those observations with Argo data selected from the same region and time, these spectral shapes *are not* present in all regions. Few general principles are found that apply globally, and some sense of the diversity is demonstrated here. The patterns that do arise are found in regions grouped by latitude, depth, and eddy kinetic energy magnitude.

Data Analysis Techniques

As described in detail in McCaffrey et al. (2014), the temperature, salinity, and pressure data used for this analysis were attain by the Argo profiling float network from 2000 to 2013. Potential density was computed for each Argo temperature/salinity profile using the Thermodynamic Equation of Seawater toolbox (McDougall, 2011), and interpolated to constant levels, $\sim 24.0 - 27.8\ kg\ m^{-3}$ in intervals of $0.1\ kg\ m^{-3}$. Argo observations are made at depth levels from $5m$ at the surface down to $2000m$, with increasing intervals with depth. See Appendix A for details on the depth and density bins.

The second-order potential temperature and salinity structure functions are defined as

$$D_\theta(\mathbf{x},\mathbf{s}) = \overline{(\theta'(\mathbf{x}) - \theta'(\mathbf{x}+\mathbf{s}))^2}, \tag{C.22}$$

$$D_S(\mathbf{x},\mathbf{s}) = \overline{(S'(\mathbf{x}) - S'(\mathbf{x}+\mathbf{s}))^2}. \tag{C.23}$$

Notation is as in McCaffrey et al. (2014), but here the $\mathbf{s}$ represents separation vector along the chosen vertical coordinate, $\mathbf{x}$ position vector, θ is potential temperature, and S is salinity. Here horizontal separations will be taken along pressure surfaces (isobaric structure functions) or along potential density surfaces (isopycnal structure functions). As discussed in McCaffrey et al. (2014), a compromise must be reached between the available data density and the regional specificity of the structure functions. For this reason, only one structure function will be evaluated in each region and it will be averaged over all angles, with the assumption that this average is sensible and meaningful (e.g., the expected value of $D_\theta(\mathbf{x},\mathbf{s}) \approx D_\theta(s)$). The resulting structure functions have a relatively simple shape (piecewise linear when in log (ordinate) and log (range), i.e., dual power law), so a least-squares fit is performed on the logarithm of each structure function to estimate the slope, bend point, and amplitude of each line. An in-depth explanation of this process can be found in Appendix B. Throughout Section C, results from this line-fitting regime will be discussed alongside the structure functions as a quantification for comparison purposes. A 95% confidence interval was also computed by bootstrapping for the structure functions, though for readability, only a few are shown here (e.g., Figure 2.9). The confidence intervals show that the slopes reported are statistically significant at some scales, based on the number and agreement of observations available (given in Appendix A).

Structure Function Results

Homogeneous Regions: Depth Dependence

As turbulence homogeneity and isotropy are desirable for analysis, an attempt was made first to locate the largest regions of homogeneous, isotropic behavior. Salinity variance was mapped in search of regions with "uniform" variance.[2] Variance was considered "uniform" if less than two orders of magnitude spanned the variance in the region. As seen in Figure C.6, there is large variation in salinity variance in both basins shown. The most uniform regions (see solid boxes in Figure C.6), chosen along the 5 m isobar and 25.8 $kg\ m^{-3}$ isopycnal, were used for initial structure function calculations, where homogeneity was assumed. In other more heterogeneous regions, like the dotted lined region in Figure C.6, the link between the structure function and spectrum was not exploited, since it is bound to be less reliable, so spectral slopes are not inferred from structure functions.

While making the assumption of homogeneous flow, the observed structure function slope can be related to the spectral slope. At the surface, two regions of uniform variance were

---

[2] As discussed in the companion paper, here variance is defined as the squared magnitude of deviations from the Ocean Comprehensive Atlas (OCCA) (Forget, 2010) climatology.

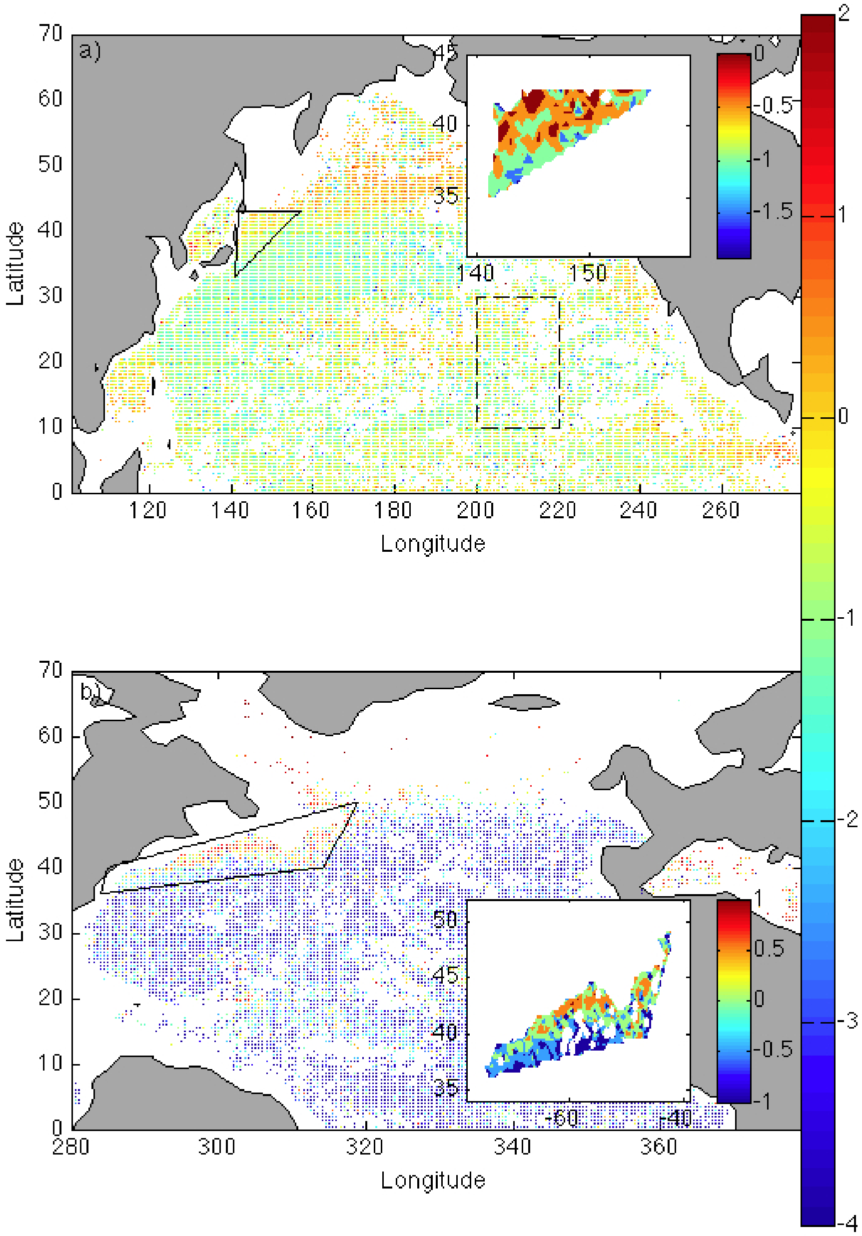

Figure C.6: The log of salinity "variance" at (a) 5 m and (b) 25.8 $kg\ m^{-3}$ with solid boxes around the chosen homogeneous regions in the western boundary currents, and a dotted line around the heterogeneous region in the central Pacific.

chosen, one along an isobar and the other along an isopycnal, and both happened to be in the western boundary currents. On isobars, the uniform region of the Kuroshio Current was chosen, and the isobaric salinity structure function was calculated on every depth level down to 2000 m, as shown in Figure 2.3a. Additional details of all structure functions, including the borders of the homogeneous regions and the number of profiles at each depth level, are included in Appendix A. Two distinct structure function slopes are seen in these results, so the two power-law behavior is expected in the equivalent salinity variance spectra. There is a slope near $\gamma = \frac{2}{3}$ in the smaller scales, with no dependence on depth (Figure 2.3b). This corresponds to the spectral slope of $\lambda = -\frac{5}{3}$ predicted by the theory of 3-dimensional turbulence of Kolmogorov (1941), as well as the theory of the surface quasi-geostrophic (SQG) temperature cascade by Blumen (1978) and the inverse energy cascade of 2d and quasigeostrophic turbulence of Kraichnan (1967) and Salmon (1980). In this location, as in the SQG theory (Callies and Ferrari, 2013), the structure function amplitude decays exponentially with depth. This intriguing result differs from that of (Callies and Ferrari, 2013), which offers the possibility that an exponential decay, as in SQG theory, may apply in this location but not in the shallow section repeatedly observed by the *Oleander*. Note however, that the SQG theory would also predict a sharp drop or rolloff of structure function at small separation distances which is not observed here. At larger scales, the structure function slope flattens out to $\gamma = 0$ at all depths, with a bend at approximately 200 km. This may be indicative of the energy injection scale at the size of the largest eddies, above which no additional energy is added, resulting in a flat structure function. The amplitude (Figure 2.3c) does, however, decrease with depth, and the mixed layer is discernible above 300 m where the structure function amplitude remains fairly constant.

A difference is seen in the isopycnal structure function results (Figure 2.4a) in the Gulf Stream homogeneous region, but again, two distinct slopes are seen at some depths. The isopycnals also decrease in structure function amplitude when moving deeper into the water column, but the behavior of the slopes is slightly different from the isobars. Only at intermediate depths at small scales is the slope $\gamma = \frac{2}{3}$ with large scale slopes of $\gamma = 0$. The scale when the change in slope takes place is 100 km. The $\gamma = \frac{2}{3}$ behavior may be described by the theory of passive tracer variance of Obukhov (1949) and Corrsin (1951), with structure function slopes equivalent to a spectral slope of $\lambda = -\frac{5}{3}$. In the mixed layer, the large scale slope of $\gamma = 0$ is seen, but the small scales are too noisy to extract a slope. The deepest isopycnals have a slope of $\gamma = 0$ at all scales, possibly signifying a new regime of activity at depths deeper than about 27.5 $kg\ m^{-3}$. At larger scales, the slope of $\gamma = 0$ is equivalent to a spectral slope of $\lambda = -1$, which coincides with the extension by Vallis (2006) of a scaling from (Batchelor, 1959) to the passive tracer cascade (see also McCaffrey et al. (2014)). This theory would suggest that the largest eddies are the size of the onset of the $\gamma = 0$ regime, around 100 km. The extension of $\gamma = 0$ slope to smaller scales would therefore indicate that the largest scale of eddies deep in the Gulf Stream region is smaller than the scales measured by the Argo salinity structure functions. The isobaric structure function in this Gulf Stream region has no depth dependence on the location of the bend point, with shapes similar to those of the isobaric structure functions in the Kuroshio.

The differences seen in the isobaric and isopycnal structure functions could be attributed to the internal wave signal that is substantially weaker in the isopycnal structure function, or the difference in eddy activity along and across isopycnals. The general fact that isobaric structure function slopes are weakly dependent of depth, but isopycnal structure function slopes *strongly* change with depth shows the difference that the chosen coordinate, and probably internal waves, make. Similar behavior is seen in the isopycnal structure function in this Kuroshio region, where at the surface, the slopes flatten to $\gamma = 0$ at large scales only at the surface, but have a slope of $\gamma = \frac{2}{3}$ at all scales at depth. Internal waves most likely dominate the isobaric structure function at large scales (Klymak and Moum, 2007), whereas on isopycnals, only the eddy activity remains at large scales, and that changes with depth. This hypothesis could be further investigated by calculating a prediction from the Garrett-Munk spectrum (Garrett and Munk, 1972) of internal waves across this region, but this process is beyond the scope of the current paper. The larger scale for persistence of the $\gamma = \frac{2}{3}$ slope deep in the water column is an indicator of the energy (and therefore tracer) cascade to larger scales as a function of depth.

One may contrast these results against those of Callies and Ferrari (2013) and Cole and Rudnick (2012). An approximate analog of the potential energy spectrum of Callies and Ferrari (2013) (where the SQG signature was not seen) is the isobaric potential density structure function. The isobaric potential density structure function in Figure C.7 does show the expected SQG behavior, with a flattening of the structure function at large scales at depth (equivalent to a steeper potential energy spectrum at large wavenumber) but not at the surface. However, this behavior is not found everywhere in the structure function, and the rolloff of spectral slope is weaker at small scales than expected in SQG. It is our inference that the ocean does not have only one potential energy spectral shape, and neither the isobaric potential density structure function in the Kuroshio nor the results of Callies and Ferrari (2013) appear generically applicable. Similarly, the clear spectral slope observed by Cole and Rudnick (2012) across all the scales they observe is seen here to change on scales around a few hundred kilometers to a different slope. In Figure 2.4, the break point is not even a constant "largest eddy" scale, but rather a function of depth. The next sections leave behind homogeneity, and thus the direct connection to spectral slopes, to find general patterns in structure functions that apply globally.

Heterogeneous Regions: Depth Dependence

Once the assumption of homogeneity has been removed, the slope of the structure function no longer has a relationship to the spectral slope, but comparisons of structure functions between depths, latitudes, levels of eddy activity, and ocean basin become interesting problems in themselves. Beginning this new assessment of ocean turbulence with the structure function as its own statistic, both isobaric and isopycnal structure functions were calculated at different depths. While some patterns emerge from the depth variations of structure functions, no

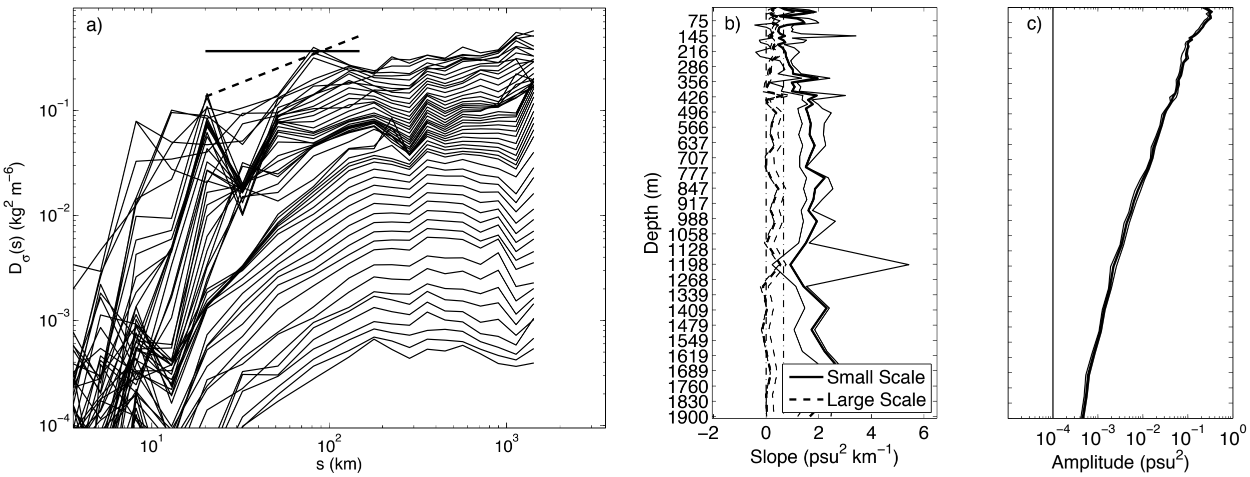

Figure C.7: Isobaric potential density structure function, $D_S(s)|_p$, (a) in the Kuroshio uniform variance region at depths from 5 m (top-most line) to 2000 m (bottom-most). Bold reference lines show a slope of $\gamma = \frac{2}{3}$ (dashed) and 0 (solid). The slopes of the small scale (solid) and large scale (dashed) fit lines (b), and the amplitude (c) is plotted with depth in pressure in meters. A 95% bootstrap interval is also shown in thin lines in (b) and (c) for slopes and amplitude.

globally consistent patterns emerge. Thus, in contrast to the SQG-based or other theories that predict rapid decay in variance with depth with faster decay at small scales, so a steepening of the structure function slope is expected, some regions show changes in slope with depth, while others show nearly constant slopes at all depths. This indicates that subtle variations in stratification, interior potential vorticity, topography, etc., lead to a diversity of results. Some of the more common patterns will be shown here.

In heterogeneous regions, where eddies do not dominate the flow, the depth dependence holding pressure versus density constant can highlight the internal wave activity at depth. Figure 2.5 shows the isobaric (a) and isopycnal (b) structure function in the central North Pacific, covering a region that includes locations with high and low variance (see the dotted lined region in Figure C.1). At the surface, both isobaric and isopycnal structure functions have a slope of $\gamma = \frac{2}{3}$ at all scales. Deeper, however, the two differ; isobaric results show flattening all the way to $\gamma = 0$ at large scales, and small scales have slopes steeper than $\gamma = 0$, but shallower than the slope of $\gamma = \frac{2}{3}$ seen at the surface. The slopes of the isopycnal structure functions slightly flatten to just below $\gamma = \frac{2}{3}$, but only the deepest few density levels show a slope of $\gamma = 0$. These differences between pressure and density surfaces can be instructive about the effects of internal waves and eddies on the structure function. Along isopycnals where internal waves are excluded, it makes sense that a region with heterogeneous variance would have a uniform slope over all scales, since no particular scale dominates the spectrum. On isobars, the internal waves impose a scale relation of separation distance versus correlation magnitude that does not carry over to along-isopycnal variability.

Heterogeneous Regions: Latitude Dependence

Latitude is anticipated to be a determining factor in the structure function slope and amplitude, because the Rossby deformation radius decreases with latitude (Chelton et al., 1998), and other geographical features like sub-tropical and sub-polar gyres vary with latitude. Figure 2.6 shows the isobaric salinity structure function in 10 degree latitude bands in the Atlantic Ocean at 5 m (a) and 1900 m (b). Immediately, it is important to note the different vertical scales on these two plots, as the deep locations have a significantly lower amplitude of structure function, and its changes with latitude are within different orders of magnitude than those at the surface. This is consistent with results from the previous section, where deeper isobars have a lower amplitude than the surface locations.

At the surface, the equator has the highest amplitude, indicating high eddy and internal wave activity, while 25-35 N and S have the lowest amplitude, possibly due to their central location in the subtropical gyres. Here, a slope greater than $\gamma = 0$ is seen at the equator and low latitudes, but the slope never reaches $\gamma = \frac{2}{3}$. This slope extends to large scales in low latitudes, but at high latitudes, the slope flattens out to $\gamma = 0$. At a depth of 1900 m, nearly opposite results are seen. The higher latitudes have the highest amplitude, with a minimum at the equator and low latitudes. A strong symmetry can be seen in the latitude dependence of the structure function. The changes in amplitude are almost directly correlated to latitude, with the strongest variations between 35-45 N and S. Approaching the equator, however, the temperature variance decreases, to a minimum at low latitudes. Most latitude bands have a slope of $\gamma = 0$, with a small (approximately $\gamma = \frac{1}{3}$) slope at the non-equatorial, low latitudes.

Latitude dependence along isopycnals shows interesting behavior, and encourages more study into its mechanics. Figure 2.6 shows the isopycnal structure functions in 10-degree latitude bands in the Atlantic Ocean at 25.7 $kg\ m^{-3}$ (a) and 27.7 $kg\ m^{-3}$ (b). The isopycnal of 25.7 $kg\ m^{-3}$ is used to compare the latitudes where it is near the surface, to those where it is below the thermocline (see Figure 3 in McCaffrey et al. (2014)). At higher latitudes, this isopycnal is closer to the surface, and its amplitude acts accordingly. There is, however, a peak at the equator as well, possibly indicating either a shallower isopycnal, or increased eddy activity at depth. This peak is weaker than the equatorial peak seen in the isobaric structure function, however. The asymmetry between the northern hemisphere and southern hemisphere shows that it is not just the depth (or the amount of time that this isopycnal is in the mixed layer) that determines the structure function amplitude, since isopycnal depth is fairly symmetrical with latitude. The deeper isopycnal at 27.7 $kg\ m^{-3}$ has a significant asymmetry with latitude, with flatter structure functions with larger amplitudes in the Northern Hemisphere. A hypothesis for this behavior is that the amplitude is due to the levels of temperature and salinity changes along isopycnals (called “spice”). The theory proposed by Yeager and Large (2007) states that seasonal injections of spice in the North Atlantic increase the salinity variability on density surfaces that are then subducted and transported southward by the meridional overturning circulation. The map of the depth density levels shows that the 27.7 $kg\ m^{-3}$ isopycnal is closer to the surface in the northern hemisphere, which means that it is more likely to reach the deeper wintertime mixed layer where spice is injected. That variability is then transferred along the isopycnal southward, which may explain the continuous southward decrease in structure function amplitude. Despite the isopycnal reaching the surface again in the southern hemisphere, the structure function only increases slightly, suggesting that an additional forcing is experienced in the northern hemisphere that does not occur in the south–perhaps eddy shedding from North Atlantic deep water or salty Mediterranean eddies. The map of isopycnal depth, as well as the latitude dependence of this isopycnal structure function could therefore support this theory. This behavior is not relevant along pressure surfaces, so this signal is missing altogether from the structure functions in Figures 2.6a and b.

Heterogeneous Regions: Eddy-Rich vs. Eddy-Poor

In order to identify the effect of eddies in the isopycnal structure function, regions where eddy activity is very high are compared to regions where the activity is much smaller. Figure 2.7 identifies the regions where eddy activity is small (gray) and large (black), based on the Aviso eddy kinetic energy. The altimeter maps were produced from data distributed by Aviso (http://www.aviso.oceanobs.com/), as part of the Ssalto ground processing segment. The structure functions in this section are all calculated along isopycnals to isolate the eddy activity and show the difference that their level of kinetic energy may make on the structure function.

The high-EKE and low-EKE regions along isopycnals are compared in Figure 2.8. Eddy-poor regions (Figure 2.8b and d) have slopes of $\gamma = \frac{2}{3}$ at all scales at the surface. At larger scales, deeper in the water column, the slopes flatten out, but not completely; few density levels show a slope of $\gamma = 0$, but most stay just above flat. In the high-EKE regions (Figure 2.8a and c), two different stories are needed. At the surface in both regions, a slope of $\gamma = \frac{2}{3}$ is seen at small scales with a slope of $\gamma = 0$ at large scales. However, in the Gulf Stream, the slope of $\gamma = \frac{2}{3}$ extends to the largest scales measured in this region. In the Kuroshio current, the surface slopes extend deeper, but instead of the small scale slope extending to larger ones, here the large scale slope of $\gamma = 0$ extends into the small scales. However, it is possible that the noise at small scales is distorting the slope.

When making a comparison between high-EKE and low-EKE behavior, one can see that the amplitude is higher at the surface in the high-EKE regions, which is indicative of its higher variance from eddies. The deeper isopycnals in high-EKE regions show very similar structure function behavior to the low-EKE regions, suggesting that the stirring below the surface is much weaker than at the surface, and no energy is injected above $\sim 100\ km$. The deep isopycnals in both high-EKE and low-EKE regions exhibit the same behavior, including amplitude, except in the Gulf Stream, where the amplitude remains higher.

Returning to the previous results in the depth dependence Sections 3C & C in light of the discussion of the high-EKE and low-EKE regions reveals an important fact. The homogeneous regions were both in western boundary currents, where eddies are strong, and the heterogeneous region is in the eastern basin where eddies would be scarce. Therefore, comparing the homogeneous isopycnal structure function (Figure 2.4a) to Figures 2.8a and c, and the homogeneous isobaric structure function (Figures 2.5b) to Figures 2.8b and d, it is clear that the homogeneous regions have the same structure function behavior as the heterogeneous eddy regions. The same can be said for the low-EKE regions on isopycnals. The conclusion can be made that the structure function slopes and amplitudes do not differ qualitatively between homogeneous and heterogeneous regions. An exact quantitive comparison is impossible since our definition of “homogeneous” versus “heterogeneous” is subjective. This could be an indicator of one of two things: either not even the chosen “uniform” variance regions are homogeneous, or else heterogeneous turbulence, as quantified by an averaged structure function as done here, is not substantially different from a homogeneous analog.

Heterogeneous Regions: Basin Dependence

Particular features of ocean basins can also be distinguished through the use of isobaric structure functions. Deep water formation occurs in the North Atlantic, but not the Pacific, so this behavior is investigated in the structure function. Figure 2.9 compares the deep and shallow isobaric structure functions for the North and South Atlantic and Pacific. A consistent small-scale slope of approximately $\gamma = \frac{2}{3}$ and large-scale slope of $\gamma = 0$ is shared by all structure functions, independent of depth, latitude, or basin (the 95% confidence intervals shown support statistical significance of these results). The surface structure functions (solid lines) have nearly identical amplitude behavior across basins, but at depth, a difference can be seen. At depth in the North Atlantic, the structure function amplitude is much larger, and approximately equal to that of the surface in the Pacific. The deep North Pacific is much weaker, as is expected due to the decrease in variance with depth there. In the Southern oceans, the deep structure functions are both much lower in amplitude than the surface, highlighting the difference that the deep North Atlantic exhibits (potentially either eddy effects or spice injection). This could be a signature of the highly saline deep water which is formed in this region.

Higher Order Structure Functions and Intermittency

Kolmogorov's 4/5th's law states that: "In the limit of infinite Reynolds number, the third order (longitudinal) [velocity] structure function of homogeneous isotropic turbulence, evaluated for increments, s small compared to the integral scale, is given in terms of the mean energy dissipation per unit mass ε (assumed to remain finite and non-vanishing) be $\overline{(u(x) - u(x+s))^3} = \text{-}\frac{4}{5}\varepsilon s$" (Frisch, 1995). Because of its exact and nontrivial nature, this means that if a third-order velocity structure function does *not* have the $\gamma = -\frac{4}{5}$ slope, one, if not both, of the assumptions (isotropy and homogeneity) must be violated. The equivalent theory for passive tracers, θ, found by Yaglom (1949) states

$$\overline{[u(x) - u(x+s)][\theta(x) - \theta(x+s)]^2} \quad = \quad -\frac{4}{5}\,\varepsilon\, s. \tag{C.24}$$

With the addition of velocity data–perhaps even from float displacement measurements–estimates of this third-order structure function might be used to directly test the assumptions of isotropy and homogeneity. In addition, higher-order structure functions would differentiate between structure functions with a slope of $\gamma = 0$ because of a single eddy-turnover timescale, and those with slopes of $\gamma = 0$ from random origin. A single timescale of stirring ultimately randomizes the flow, but the higher moments would appear in the higher-order structure functions differently from random data.

Higher order structure functions ($D_{\theta,3}(s), D_{\theta,4}(s), D_{\theta,5}(s)$, etc) are often computed alongside probability density functions (pdfs) of the salinity(/temperature/velocity) differences to identify intermittent signals, as well as to verify the existence of finite higher-order moments (Frisch, 1995). In the inertial range, the turbulent cascade should result in a normal distribution of differences, with non-normal intermittent behavior appearing in the tails of the pdf. Figure C.8 illustrates that using the pdf can be an additional descriptive characteristic of turbulence in a particular region. The pdf of salinity differences at 5 m depth in the Kuroshio (a), which was chosen for being (nearly) homogeneous, is much closer to being normally distributed (shown by the dashed line) than the Equatorial Atlantic (b), which is expected to see intermittent eddy activity. In order for the higher moments to exist, the tail of the pdf must be exponential, instead of diverging algebraically. Though the behavior in the tails shown here appears to be exponential, it is also noisy, so a strong conclusion cannot be made, discouraging further computation of higher-order structure functions.

Conclusions and Summary

Supported by the previous results of Frehlich and Sharman (2010b) and McCaffrey et al. (2014), the structure function method has been applied for the analysis of salinity variance in the world's oceans. Although the assumption of homogeneity does not seem to apply based on salinity variance maps, the results of the structure functions do not vary in homogeneous and heterogeneous regions. This is encouraging because the assumption of homogeneity would be a severe limitation, and without this limitation, future studies may continue calculating spectral slopes from structure functions. The ability to get back a spectrum from a structure function, even in a case where two distinct structure function slopes are present and data is

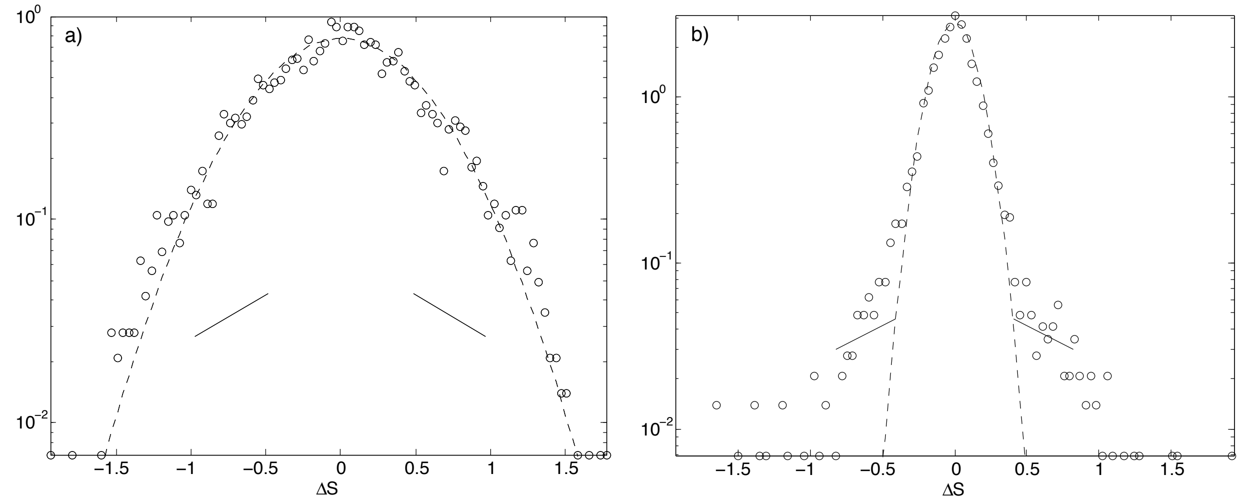

Figure C.8: Normalized probability distribution functions of ΔS in the inertial range of 10 to 300 kilometers at 5 m depth in the uniform variance region of the a) Kuroshio and b) in the Equatorial Atlantic.

filled with gaps, shows how powerful a tool the structure function is.

Isobaric structure functions show most significantly an amplitude decrease with depth. Slopes of $\gamma = \frac{2}{3}$ at all scales along isopycnals, and on isobars at small scales and $\gamma = 0$ at larger scales are seen at depth. These results support the theories of the energy cascades of Kolmogorov (1941) and Kraichnan (1967), and the passive tracer cascade of Obukhov (1949) and Corrsin (1951), which are all based on simple dimensional analyses of the energy and tracer variance equations. Latitude variations show variable behavior along isobars and isopycnals, and at depth and on the surface. Along isobars near the surface, structure functions are largest in magnitude near the equator and have slopes at all scales consistent with Kolmogorov spectra. Along deeper isobars, structure function magnitude is greater away from the equator (although less than surface values at all latitudes), and tend to flatten out at larger separation distances. Along isopycnals, deep surfaces resemble the deep structure functions along isobars which may demonstrate weak internal wave activity at depth.. Near-surface isopycnals do not show equatorial strengthening and tend to level off at larger scales. Comparing high-EKE and low-EKE regions show strong eddy activity at the surface which decreases with depth. It is also possible to use the structure function to investigate ocean characteristics, like the location of deep water formation and spice injection in the North Atlantic.

Though it is beyond the scope of the work here to definitively explain the causes of these variations, models and theories of geographic variations in mesoscale eddy and internal wave statistics should capture their patterns. For this reason, some care is taken in Appendix A to provide reproducibility details that can be directly checked against realistic eddy-permitting and finer resolution models.

With the growing amount of observations from the Argo dataset, the strength of this method will only increase. Including other observations (i.e., moorings, gliders, and cruise data), the knowledge of smaller scales of ocean turbulence will be observable as well.

Acknowledgments This paper was inspired by conversations with Rod Frehlich. We wish that there had been more time with Rod, so that we could learn more from him. The Argo Program is part of the Global Ocean Observing System. KM was supported by the CIRES/NOAA-ESRL Graduate Research Fellowship. BF-K was supported by NSF 0855010 and 1245944 and GF was supported in part through NASA project "Estimating the Circulation and Climate of the Ocean (ECCO) for CLIVAR" and NSF 1023499.

Appendix A

Structure Function Details

This appendix includes the detailed information for each structure function herein, including the number of profiles in the selected region at each depth and the number of "simultaneous" measurement pairs. In addition, the regions defined as homogeneous and heterogeneous are identified:

Kuroshio homogeneous region, "uniform" at $5m$:

SW: lon = 141; lat= 33;

NW: lon = 142; lat= 43;

SE: lon = 155; lat= 42;

NE: lon = 157; lat= 42;

Gulf Stream homogeneous region, “uniform” at $25.9 kg\ m^{-3}$:

SW: lon = -76; lat= 36;

NW: lon = -75; lat= 40;

SE: lon = -46; lat= 40;

NE: lon = -41; lat= 50;

Heterogeneous region, “non-uniform” at $25.9 kg\ m^{-3}$ and $5m$:

SW: lon = -160; lat= 10;

NW: lon = -160; lat= 30;

SE: lon = -140; lat= 10;

NE: lon = -140; lat= 30;

Appendix B

Line-Fitting Algorithm

In order to quantify the differences among structure functions, a line-fitting algorithm was created to extract the slopes of the structure functions with one (or two) linear fit(s). A test was first performed to decide whether more than one linear fit was needed. On the structure functions with only one slope, a least-squares method of linear regression was performed, using the bootstrap method of sampling to obtain a confidence interval. The advantage of using the bootstrap method for the confidence interval is that the assumption of normality for the individual observations is not necessary.

Since the relationship to the spectral slope no longer holds in heterogeneous regions, there could be two separate linear slope regimes with no relation to the spectrum. In this case, the same linear regression was performed, but in steps so as to find the amplitude and approximate bend point where a change in slope occurs. A bootstrap analysis was completed for this process. First, randomly chosen data points were fitted by two lines with the bend point at each separation distance bin. A least-squares error was calculated for the lines fit for each bend point, and the bend point with the smallest error was chosen (s_{bend}). Using that bend point, all data points were then considered for the best-fit line. Another bootstrap regime was then run, choosing random data points and calculating the resulting slopes of the best-fit lines for the sub-sets of the original data. A bootstrap interval using 200 subsamples was calculated from these results, providing a confidence interval for the chosen best fit from all points.

In the homogeneous regions where two structure function slopes are discerned, the same linear fitting regime was used, and the relation to the spectral slope was applied to the results. The bend point for the spectral slope was computed to be $k_1 = 1/s_{bend}$.

Depth	No. profiles	No. pairs	Depth	No. profiles	No. pairs
5m	3927	19383	360m	5665	43034
15m	5747	51574	380m	5743	44320
25m	6209	62357	400m	5561	42531
35m	6292	62408	420m	4378	26605
45m	5966	61334	440m	4589	31627
55m	6278	61816	460m	5200	39488
65m	6208	61002	480m	5182	37971
75m	6017	58401	500m	5370	41386
85m	6111	56751	550m	5381	41204
95m	6110	54444	600m	5365	40905
105m	5532	45353	650m	5119	36565
115m	5806	44674	700m	5257	39031
125m	5592	42608	750m	5096	36193
135m	5611	44095	800m	5304	39631
145m	5590	42647	850m	5020	35310
155m	5834	44958	900m	5260	39069
165m	5380	41946	950m	4937	34395
175m	5802	44475	1000m	4917	36343
185m	5577	42378	1100m	4796	34845
200m	5838	45174	1200m	4627	32091
220m	5840	45391	1300m	4551	31028
240m	5840	45135	1400m	3573	22269
260m	5712	43950	1500m	3428	20762
280m	5783	44871	1600m	3319	20461
300m	5014	31869	1700m	3270	20042
320m	5704	43439	1800m	3187	19231
340m	5828	44912	1900m	2831	14045

Table C.5: Number of profiles and profile pairs used to compute the isobaric structure function for each depth in the “uniform” region of the Kuroshio, shown in Figure 2.3.

Density	No. profiles	No. pairs		Density	No. profiles	No. pairs
$24.9kgm^{-3}$	381	1015		$26.4kgm^{-3}$	2626	23940
$25.0kgm^{-3}$	433	1086		$26.5kgm^{-3}$	3233	31730
$25.1kgm^{-3}$	470	1323		$26.6kgm^{-3}$	3618	37997
$25.2kgm^{-3}$	497	1536		$26.7kgm^{-3}$	3800	41771
$25.3kgm^{-3}$	617	2112		$26.8kgm^{-3}$	4430	50953
$25.4kgm^{-3}$	615	2135		$26.9kgm^{-3}$	4551	54158
$25.5kgm^{-3}$	756	2971		$27.0kgm^{-3}$	4971	61753
$25.6kgm^{-3}$	889	3889		$27.1kgm^{-3}$	5191	67238
$25.7kgm^{-3}$	969	4475		$27.2kgm^{-3}$	5256	69048
$25.8kgm^{-3}$	1136	5831		$27.3kgm^{-3}$	5321	70538
$25.9kgm^{-3}$	1271	7173		$27.4kgm^{-3}$	5309	70638
$26.0kgm^{-3}$	1515	9189		$27.5kgm^{-3}$	5411	73461
$26.1kgm^{-3}$	1772	12426		$27.6kgm^{-3}$	5375	72775
$26.2kgm^{-3}$	1909	14009		$27.7kgm^{-3}$	5201	67818
$26.3kgm^{-3}$	2380	20055				

Table C.6: Number of profiles and profile pairs used to compute the isopycnal structure function for each density level in the “uniform” region of the Gulf Stream, shown in Figure 2.4.

Depth	No. profiles	No. pairs		Depth	No. profiles	No. pairs
5m	10139	365192		360m	13013	614256
15m	14736	825454		380m	14582	815007
25m	14740	822307		400m	13260	660630
35m	14735	822046		420m	9254	344965
45m	14757	824696		440m	14720	816694
55m	14795	830618		460m	9454	334480
65m	14781	828257		480m	9462	342825
75m	14809	832856		500m	14387	783612
85m	14832	835247		550m	14166	769917
95m	14813	833364		600m	14219	768681
105m	14848	837059		650m	14418	779360
115m	14856	837475		700m	13688	688283
125m	14903	841562		750m	14092	744171
135m	14930	843148		800m	14224	753096
145m	14198	748041		850m	13346	668227
155m	14897	841062		900m	13198	635600
165m	13027	615750		950m	12705	600324
175m	14883	840231		1000m	10303	452745
185m	12432	555375		1100m	9591	385024
200m	14888	839387		1200m	8155	258947
220m	13800	702299		1300m	8131	257549
240m	13586	696020		1400m	7545	218515
260m	14153	743979		1500m	6931	183331
280m	13486	685195		1600m	6925	182970
300m	13798	708247		1700m	6902	181216
320m	14885	838701		1800m	6880	179759
340m	13768	698935		1900m	6827	176746

Table C.7: Number of profiles and profile pairs used to compute the isobaric structure function for each depth in the heterogeneous region of the Pacific, shown in Figure 2.5a.

Density	No. profiles	No. pairs
$24.9kgm^{-3}$	11652	483239
$25.0kgm^{-3}$	11997	512881
$25.1kgm^{-3}$	11823	496640
$25.2kgm^{-3}$	11483	470120
$25.3kgm^{-3}$	11034	425446
$25.4kgm^{-3}$	10927	424389
$25.5kgm^{-3}$	10987	427971
$25.6kgm^{-3}$	11129	443197
$25.7kgm^{-3}$	11547	480032
$25.8kgm^{-3}$	11680	488667
$25.9kgm^{-3}$	12160	538459
$26.0kgm^{-3}$	12490	571559
$26.1kgm^{-3}$	13101	637287
$26.2kgm^{-3}$	13621	700790
$26.3kgm^{-3}$	13905	733375
$26.4kgm^{-3}$	13841	736917
$26.5kgm^{-3}$	13928	739101
$26.6kgm^{-3}$	13956	741433
$26.7kgm^{-3}$	14043	748687
$26.8kgm^{-3}$	14169	761025
$26.9kgm^{-3}$	14373	782291
$27.0kgm^{-3}$	14340	771766
$27.1kgm^{-3}$	14320	767621
$27.2kgm^{-3}$	14358	772878
$27.3kgm^{-3}$	14287	765540
$27.4kgm^{-3}$	10154	439285
$27.5kgm^{-3}$	8155	259510
$27.6kgm^{-3}$	6932	183701
$27.7kgm^{-3}$	26	3

Table C.8: Number of profiles and profile pairs used to compute the isopycnal structure function for each density level in the heterogeneous region of the Pacific, shown in Figure 2.5b.

References

Batchelor, G. K., 1959: Small-scale variation of convected quantities like temperature in turbulent fluid .1. General discussion and the case of small conductivity. *Journal of Fluid Mechanics*, **5 (1)**, 113–133.

Blumen, W., 1978: Uniform potential vorticity flow .1. Theory of wave interactions and 2-dimensional turbulence. *Journal of the Atmospheric Sciences*, **35 (5)**, 774–783.

Callies, J. and R. Ferrari, 2013: Interpreting energy and tracer spectra of upper-ocean turbulence in the submesoscale range (1-200 km). *Journal of Physical Oceanography*, in press.

Chelton, D. B., R. A. Deszoeke, M. G. Schlax, K. El Naggar, and N. Siwertz, 1998: Geographical variability of the first baroclinic rossby radius of deformation. *Journal of Physical Oceanography*, **28 (3)**, 433–460.

Cole, S. and D. Rudnick, 2012: The spatial distribution and annual cycle of upper ocean thermohaline structure. *Journal of Geophysical Research-Oceans*, **117**.

Corrsin, S., 1951: On the spectrum of isotropic temperature fluctuations in isotropic turbulence. *Journal of Applied Physics*, **22 (469)**.

Forget, G., 2010: Mapping ocean observations in a dynamical framework: A 2004-06 ocean atlas. *Journal of Physical Oceanography*, **40**, 1201–1221.

Frehlich, R. and R. Sharman, 2004: Estimates of turbulence from numerical weather prediction model output with applications to turbulence diagnosis and data assimilation. *Monthly Weather Review*, **132**, 2308–2324.

Frehlich, R. and R. Sharman, 2010a: Climatology of velocity and temperature turbulence statistics determined from rawinsonde and ACARS/AMDAR data. *Journal of Applied Meteorology and Climatology*, **49 (6)**, 1149–1169.

Frehlich, R. G. and R. D. Sharman, 2010b: Equivalence of velocity statistics at constant pressure or constant altitude. *Geophysical Research Letters*, **37**, doi:DOI10.1029/2010GL042912.

Frisch, U., 1995: *Turbulence: The Legacy of A. N. Kolmogorov*. Cambridge University Press, Cambridge.

Garrett, C. and W. Munk, 1972: Space-time scales of internal waves. *Geophysical Fluid Dynamics*, **2**, 225–264.

Hamilton, K., Y. O. Takahashi, and W. Ohfuchi, 2008: Mesoscale spectrum of atmospheric motions investigated in a very fine resolution global general circulation model. *Journal of Geophysical Research*, **118**.

Klymak, J. M. and J. N. Moum, 2007: Oceanic isopycnal slope spectra. part i: Internal waver. *Journal of Physical Oceanography*, **37 (5)**, 1215–1231, doi:DOI10.1175/JPO3073.1.

Kolmogorov, A. N., 1941: The local structure of turbulence in incrompressible viscous fluid for very large reynolds number. *Dokl. Akad. Nauk. SSSR*, **30**, 9–13.

Koshyk, J. N. and K. Hamilton, 2001: The horizontal kinetic energy spectrum and spectral budget simulated by a high-resolution troposphere-stratosphere mesosphere gcm. *Journal of Atmospheric Sciences*, **58**, 329–348.

Kraichnan, R. H., 1967: Inertial ranges in two-dimensional turbulence. *Physics of Fluids*, **16**, 1417–1423.

Lindborg, E., 1999: Can the atmospheric kinetic energy spectrum be explained by two-dimensional turbulence? *Journal of Fluid Mechanics*, **388**, 259–288.

McCaffrey, K., B. Fox-Kemper, and G. Forget, 2014: Estimates of ocean macro-turbulence: Structure function and spectral slope from argo profiling floats, i: Methods. *Journal of Physical Oceanography*, submitted.

McDougall, T. J., 2011: *Getting started with TEOS-10 and the Gibbs Seawater (GSW) Oceanographic Toolbox*, Vol. 7.

Nastrom, G. D. and K. S. Gage, 1985: A climatology of atmospheric wavenumber spectra of wind and temperature observed by commercial aircraft. *Journal of the Atmospheric Sciences*, **42**, 950–960.

Obukhov, A. M., 1949: The structure of the temperature field in a turbulent flow. *Izv. Akad. Nauk. SSSR, Ser. Geog. and Geophys.*, **13 (58)**.

Salmon, R., 1980: Baroclinic instability and geostrophic turbulence. *Geophysical & Astrophysical Fluid Dynamics*, **15 (1)**, 167–211.

Skamarock, W. C., 2004: Evaluating mesoscale nwp models using kinetic energy spectra. *Monthly Weather Review*, **132**, 3019–3032.

Takahashi, Y. O., K. Hamilton, and W. Ohfuchi, 2006: Explicit global simulation of the mesoscale spectrum of atmospheric motions. *Geophysical Research Letters*, **33**.

Vallis, G. K., 2006: *Atmospheric and Oceanic Fluid Dynamics : Fundamentals and Large-Scale Circulation*. Cambridge University Press, Cambridge.

Yaglom, A., 1949: Local structure of the temperature field in a turbulent flow. *Doklady Akademii Nauk*, **69 (6)**, 743–746.

Yeager, S. G. and W. G. Large, 2007: Observational evidence of winter spice injection. *Journal of Physical Oceanography*, **37**, 2895–2919, doi:DOI10.1175/2007JPO3629.1.

Appendix D

Characterizing Turbulence Anisotropy, Coherence, and Intermittency at a Prospective Tidal Energy Site.

This appendix contains the text of McCaffrey et al. (submitted, 2013), submitted to *Renewable Energy* in October, 2013. The figures not included in Chapter 3 are included here.

Abstract

As interest in marine renewable energy increases, observations are crucial for understanding the environments that prospective turbines will encounter. Data from an acoustic Doppler velocimeter in Puget Sound, WA are used to perform a detailed characterization of the turbulent flow encountered by a turbine in a tidal strait. Metrics such as turbulence intensity, structure functions, probability density functions, intermittency, coherent turbulence kinetic energy, anisotropy invariants, and a new scalar measure of anisotropy are used to characterize the turbulence. The results indicate that the scalar anisotropy magnitude can

be used to identify and parameterize coherent, turbulent events in the flow. An analysis of the anisotropy characteristics leads to a physical description of turbulent stresses as being primarily one- or two-dimensional, in contrast to the isotropic, three-dimensional small scale turbulence predicted by classical Kolmogorov theory. A new measure of the anisotropy magnitude is introduced to quantify the level of anisotropic, coherent turbulence in a coordinate-independent way. These diagnostics and results will be useful for improved realism in modeling the performance and loading of turbines in realistic ocean environments.

Introduction

With the growing interest in ocean renewable energy, a better understanding of the marine environment is needed in order to make further progress in research and development. In many respects, progress made in the wind energy industry presages ocean energy developments, from the shape and mechanics of marine hydro-kinetic (MHK) turbines to metrics used for site characterization. The European Marine Energy Commission Assessment of Tidal Energy Resource recommends turbulence in its list of metrics for site characterization (though it is not required) (Legrand, 2009), and the comprehensive assessment of tidal in-stream devices by the Electric Power Research Institute briefly recognizes that turbulence is harmful to turbines (Bedard et al., 2005). However, the importance of turbulence effects on wind and tidal turbines is becoming increasingly appreciated since intense coherent turbulent structures can be structurally harmful to turbines, can decrease the capacity to generate power, and can increase the overall cost of power production (Frandsen et al., 2007; Mücke et al., 2011; Kaiser et al., 2007; Rareshide et al., 2009).

The International Electrotechnical Commission (IEC) standard metric for quantifying the level of turbulence at wind energy sites is the turbulence intensity (addressed in SectionD) (IEC, 2005). However, this metric does not address all turbulent events that may affect generation and safety, such as coherent structures and intense eddies. Hand et al. (2003) used an array of turbulence intensity measurements to assess coherence and turbulence length scales, while Sutherland (2002) performed a multi-variable regression analysis of the equivalent fatigue loads of a turbine, finding that the vertical component of the inflow velocity has most impact.

To date, studies of MHK sites have continued to use the turbulence intensity as the primary metric for characterizing ocean turbulence environments (Elliott and Cadogan, 1990; Gooch et al., 2009; Epler et al., 2010; Polagye and Thomson, 2013). However, atmospheric and oceanic turbulence differ due to the distinct tidal, seasonal, and diurnal forcings of each fluid. Some of the most comprehensive characterizations, such as Thomson et al. (2012), Thomson et al. (2013), and Gunawan et al. (sion) have furthered the characterization of ocean turbulence by also examining energy spectra and spatial structure functions. A more detailed description of MHK sites using higher order statistics will reveal additional insights into the turbulent environment of a tidal strait.

In the present study, a higher-order, detailed characterization of ocean observations is performed in order to obtain more accurate predictions of loading and power production from a tidal turbine. This information is useful for comparisons of turbulence observations with numerical turbulence simulators (like the TurbSim model from the National Renewable Energy Laboratory (NREL) (Jonkman and Kilcher, 2012)), which currently use only turbulence intensity and a power spectral density curve to create more realistic turbulent environments for turbine simulator models (like FAST). Turbulence manifested in gusts, or coherent, anisotropic, and intermittent eddies puts particularly strong and variable stresses on a turbine as it turns, leading to misalignment of the drive train and wearing of the gearbox (Ragheb and Ragheb, 2010). As a result, a site characterization that quantifies the incidence and properties of intense, coherent, anisotropic turbulent eddies has the potential to prevent untimely, unexpected, and costly failures in turbines.

Using velocity measurements from the Puget Sound, WA, this paper examines several higher-order metrics in order to characterize and identify extreme turbulence eddies (or "events") in a tidal strait. These metrics include velocity structure functions for time scale information, probability density functions for intermittency, and anisotropy tensor eigenvalues for quantification and physical description of anisotropy. The specific metrics chosen are drawn from the laboratory and numerical experiment literature, where collection of data is simpler than in real-world ocean observations (Kolmogorov, 1941; Novikov and Stewart, 1964; Lumley and Newman, 1977). However, these metrics are demonstrated here to be suitable for application to observational data as well. Higher-order statistics and a parameterization more grounded in turbulence theory are proposed to improve the classification of anisotropy at potential tidal energy sites. An easily understood visualization of anisotropy proposed by Banerjee et al. (2007) is presented as well. With an improved set of parameters that provide a better physical description of the flow, it will be shown that more accurate predictions of turbulence coherence can be obtained. Knowledge of turbulence coherence will allow turbines to be better designed to withstand the particular scales of turbulence that cause the largest loads and put the most strain on gear boxes. This paper is organized as follows: Section 2 characterizes the flow with several statistical parameters; Section 3 proposes a new parameterization based on the characterization; and Section 4 concludes with a discussion of the implications of this work to the marine energy industry.

Characterization of Turbulence

The data used in this analysis were collected from an acoustic Doppler velocimeter (ADV) device at Nodule Point, on the eastern side of Marrowstone Island in the Puget Sound (Thomson et al., 2012). The site, which is 22 m deep, was under consideration for an array of Verdant Power$^{\text{TM}}$ turbines and has a maximum current velocity of 1.8 $m\ s^{-1}$ at the proposed hub-height of 4.7 m above the seabed. The measurements examined here were collected from February 17th to February 21, 2011 using an ADV sampling at 32 Hz on the apex of a Tidal Turbulence Tripod at approximately hub-height. The location is well-mixed, with minimal stratification as measured from a CTD (conductivity-temperature-depth sensor). More detail on the observations and how they were performed can be found in Thomson et al. (2012).

Velocity Decomposition and Statistics

Each of the three velocity components have been decomposed into a mean ($\overline{u}$) and perturbation (u'):

$$\mathbf{u} = \overline{\mathbf{u}} + \mathbf{u}', \tag{D.1}$$

where $\mathbf{u} = u\mathbf{i} + v\mathbf{j} + w\mathbf{k}$. The horizontal velocities are defined in perpendicular components, where $-\mathbf{i}$ is aligned toward the seaward principal flow direction, $\mathbf{j}$ is perpendicular to the principal flow direction, and $\mathbf{k}$ is in the vertical direction. Wave motions are neglected for the location analyzed here, although they may be important in other locations since they introduce coherent structures that appear in the variance. The mean used here is a 10-minute time mean, by contrast to the shorter 5-minute mean chosen by Thomson et al. (2012). The 10-minute interval was chosen in an attempt to retain the longest timescales of coherent turbulence structures in the perturbation, while capturing the tidal and diurnal variations in the mean. Within each averaging interval, the mean flow was assumed to be steady, which can create discontinuities at interval edges. Experimentation with a range of averaging intervals suggested that 5 to 10 minute variability is appropriately categorized as turbulent (see Appendix). Assuming Taylor's frozen turbulence hypothesis (Taylor, 1938), this allows motions smaller than $\sim 1.8\ km$ at Nodule Point (for $1.8\ m\ s^{-1}$ mean velocities).

Figure 3.2 shows the three components of velocity at Nodule Point from 17 Feb 2011 to 21 Feb 2011 at approximately hub-height depth ($4.7\ m$), with the observed velocities in gray, and the 10-minute mean in black. "Slack conditions," where the velocity is not large enough to drive a turbine, are defined as $\overline{u} \leq 0.8\ m\ s^{-1}$ (shown with dotted lines on Figure **??**), and occur at high and low tides. This is in contrast to ebb and flood tides when velocities are larger. Velocity perturbations, the individual components of turbulent kinetic energy

($TKE = \frac{1}{2}\left(\overline{u'^2} + \overline{v'^2} + \overline{w'^2}\right)$), and total TKE are shown Figures 3.3a, b, and c. Peaks occur periodically in each signal with the M2 (semidiurnal) tide dominated mainly by the $\overline{u'^2}$ and $\overline{v'^2}$ components of the TKE. Diurnal variability is also typical as one large and one small (i.e., mixed semi-diurnal) flood or ebb per day. The w' fluctuations are considerably smaller than those in the other directions, as indicated by the very small $\overline{w'^2}$ component of the TKE.

Reynolds shear stresses are defined as $\overline{u_i'u_j'}$. In a well-mixed, homogeneous flow such as a tidal strait, coherent turbulent structures appear as bursts in the Reynolds shear stresses (Kelley et al., 2000). Figure 3.3d shows the covariances, where turbulent bursts can be seen occurring at a roughly diurnal period. Outside of the turbulent burst, all three components are approximately zero with only occasional peaks in one component. Some days have two turbulent bursts, both during flood tide, with the stronger turbulence associated with the stronger flood.

Turbulence Intensity and Coherent Turbulent Kinetic Energy

The metric most commonly used in the wind industry to characterize the turbulent environment is the turbulence intensity, I (ISO 4354, 1997). Turbulence intensity, shown in Figure D.1a, is the ratio of the standard deviation of the velocity to the mean with a noise-corrected term subtracted for acoustic Doppler measurements, and is defined as

$$I = \frac{\sigma_u}{\overline{u}} = \frac{\sqrt{\overline{u'^2} - n^2}}{\overline{u}}, \tag{D.2}$$

where the overline indicates a 10-minute average ($I_u \approx \frac{\sqrt{\frac{2}{3}k - n^2}}{\overline{u}}$ for isotropic turbulence) (Thomson et al., 2012). Although in much of the wind literature turbulence intensity is calculated from wind speeds (often measured by cup anemometers) (Elliott and Cadogan, 1990), turbulence intensity can be calculated in all three directions (I_u, I_v, I_w), but the along-stream intensity, I_u, is used here. Figure D.2 shows turbulence intensity plotted versus mean flow speed for the entire sampling period at Nodule Point. The highest turbulence

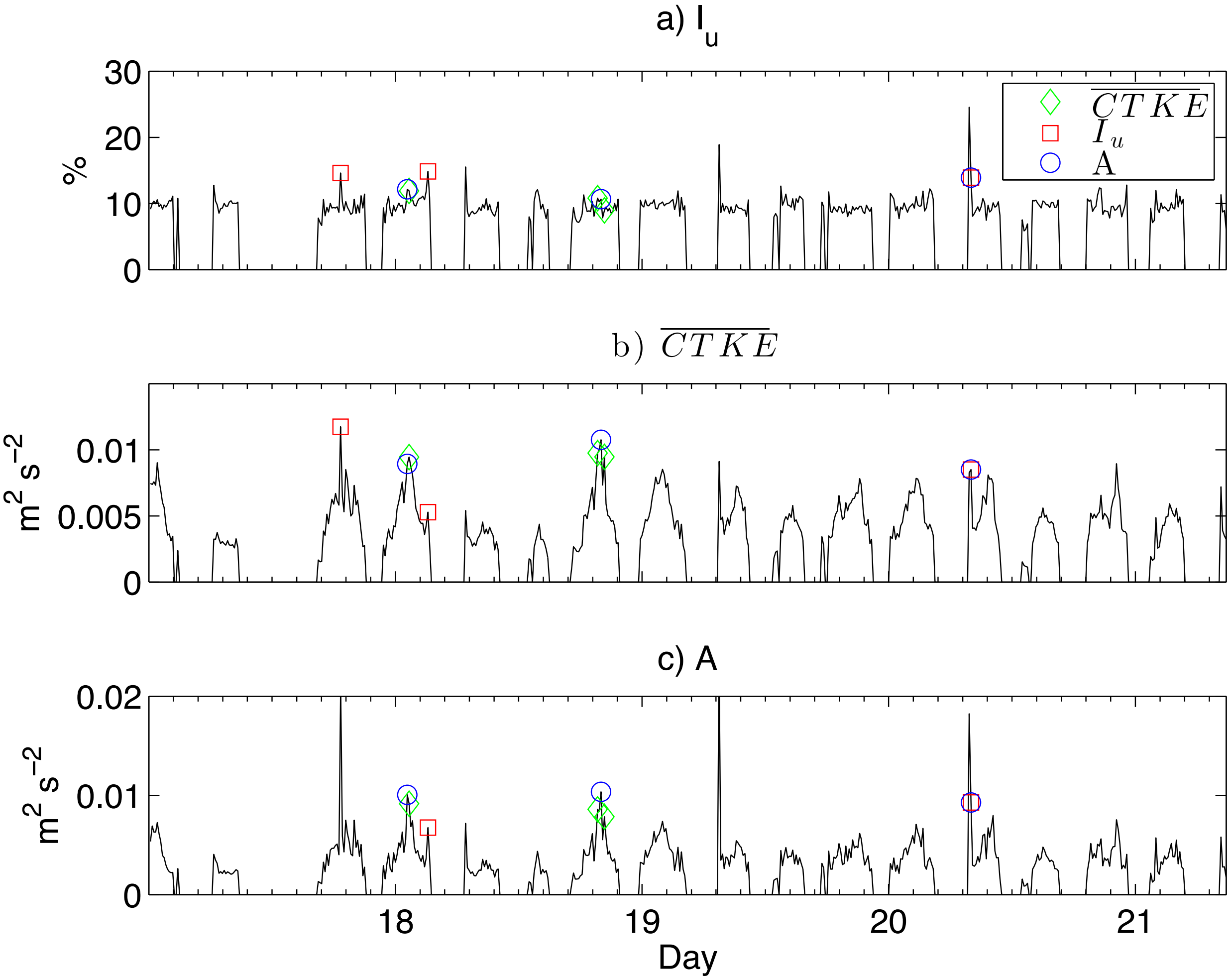

Figure D.1: a) Turbulence intensity, b) coherent turbulent kinetic energy, and c) anisotropy magnitude, A, from the Nodule Point data shown in Figures 3.2 and 3.3. Three 99th-percentile values of I_u, $\overline{CTKE}$, and A values when $\overline{u} > 0.8\ m\ s^{-1}$ are shown in the red squares, green diamonds, and blue circles, respectively.

intensities occur below 0.8 m/s, which are considered slack conditions when the turbine would be motionless. The fastest mean velocities at Nodule Point ($\sim 2\ m\ s^{-1}$) see turbulence intensities around 10%, while slower mean velocities see turbulence intensities that reach up to 20%. This behavior is consistent with the $I_u \sim 1/\overline{u}$ relationship, which has been removed in the inset of Figure D.2 where $\overline{u'^2}$ vs. $\overline{u}$ is shown. This encourages further analysis into what causes the turbulence intensity to peak, since the large spread suggests that local values of $\overline{u}$ are not a good predictor of σ_u.

Although turbulence intensity is a helpful metric for determining loads on a turbine (Mücke et al., 2011), a more detailed characterization of the *type* of turbulence will show individual turbulent events like a large, anisotropic eddy passing through the region. Coherent turbulent kinetic energy ($CTKE$; the magnitude of the instantaneous Reynolds shear stresses) is another common metric in the wind literature used to identify coherent turbulent events (Gooch et al., 2009; Jonkman, 2009), and is defined as

$$CTKE = \frac{1}{2}\sqrt{(u'v')^2 + (u'w')^2 + (v'w')^2}. \tag{D.3}$$

CTKE identifies the instances when the Reynolds shear stresses peak, while the turbulence intensity identifies only one component of the kinetic energy. The use of the cross terms identifies the spatially coherent features in the flow (though CTKE is an instantaneous quantity, so the temporal coherence remains unknown).

The method employed by Kelley et al. (2000) & Kelley et al. (2005) to describe coherent turbulent structures uses wavelet analysis to decompose the Reynolds stresses and coherent turbulent kinetic energy alongside observed loads on wind turbines to characterize the time and frequency behavior of the coherent structures and their effect on the turbines. These results have shown that bursts of $CTKE$ at scales $6\% - 23\%$ of the rotor diameter induce higher structural loads on both stiff and flexible-blade wind turbines. Although observations of loads are not available for a tidal turbine, Reynolds stresses and $CTKE$ from ADV

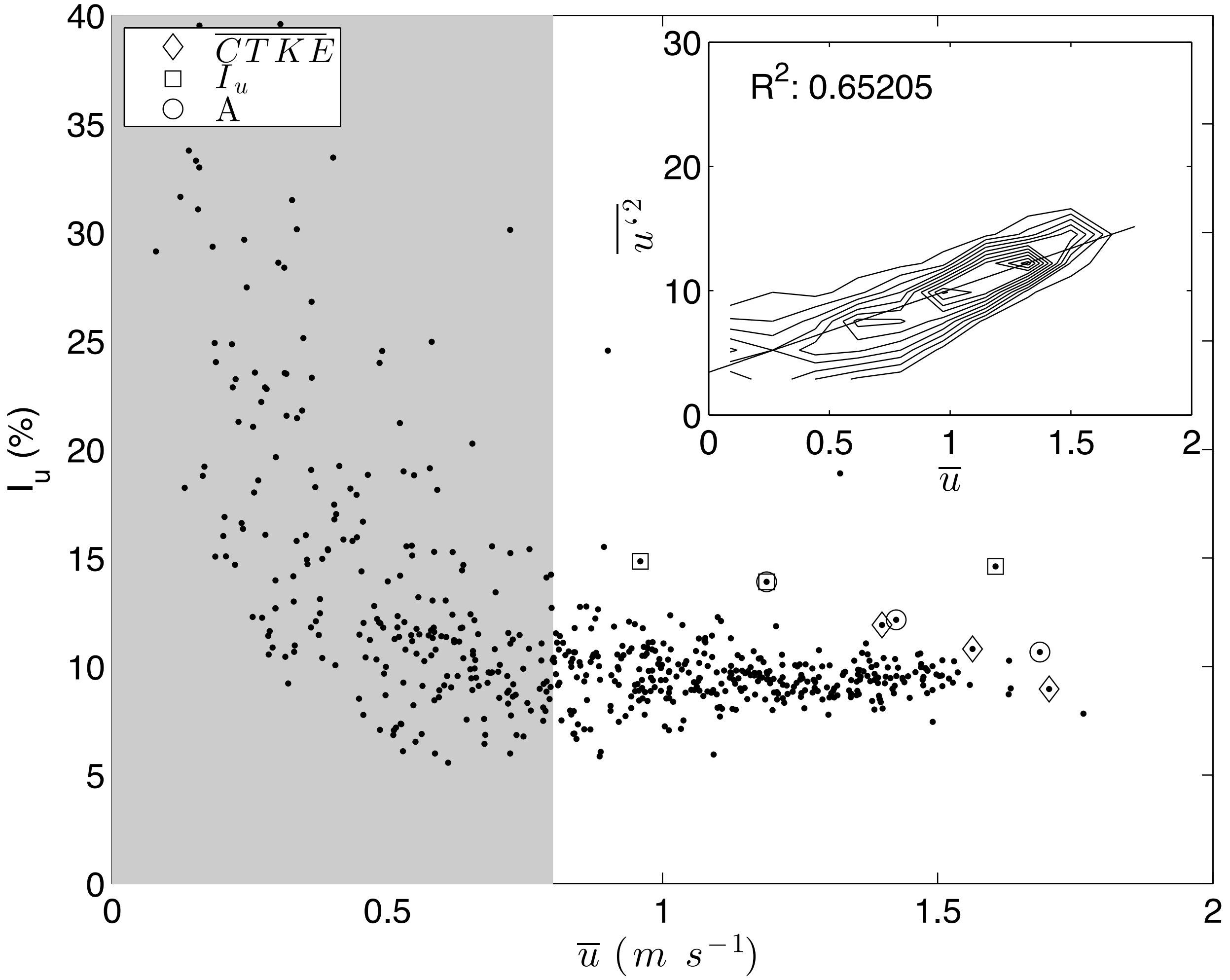

Figure D.2: Turbulence intensity versus mean speed for each 10-minute interval at Nodule Point. The gray area indicates slack conditions. Three 99th percentile values of I_u, $CTKE$, and A values when $\overline{u} > 0.8\ m\ s^{-1}$ are shown in the squares, diamonds, and circles, respectively on each plot. Inset is the joint pdf of $\overline{u}$ vs $\overline{u'^2}$, with the best-fit line.

measurements can be used to infer expected loading events.

CTKE is shown in Figure D.1b, and will be used as an additional metric for parameterization of turbulence at this location. An alternative to $CTKE$, the anisotropy magnitude A (Eq. D.11), that is more firmly grounded in turbulence theory is shown in Figure D.1c and presented in Section D. Three illustrative intervals in the largest 99th percentile of I_u, $\overline{CTKE}$, and A when $\overline{u} > 0.8\ m\ s^{-1}$ were chosen to highlight the meaning of these diagnostics. These intervals are also indicated in Figures 3.2, D.1, D.2, 3.7, 3.9, and 3.10.

Correlation and Length Scales

Turbulence intensity is a poor descriptor of the spatial and temporal structure of turbulence in the tidal channel, so quantifying the scales of motion leading to large I_u is a natural next step. Spatial and temporal correlation scales can also give a much better physical description of the turbulence than is possible with turbulence intensity so velocity autocorrelations were calculated to infer the time (and, using Taylor's hypothesis, length) scales of the turbulence. The temporal autocorrelation is defined as

$$\rho(\tau) = \frac{\overline{u'(t)u'(t+\tau)}}{\overline{u'^2}} \tag{D.4}$$

where the overbar is the 10-minute mean, and results are shown in Figure 3.5. The coherence function used in TurbSim is also plotted (with $a = 8.8, L = 2.454.7, f = .0001$ Jonkman (2009)), showing the stretched exponential form used to include coherent structures in the model. Although the model significantly under predicts the coherence for certain intervals, it does capture the mean observed at this location quite well.

The Taylor, λ, and integral, Λ, scales are used to quantify the longest time over which the turbulence stays correlated, and the time until the flow is uncorrelated, respectively (Pope, 2000). These scales are defined as

$$\lambda = -2\left[\frac{d^2\rho}{d\tau^2}\right]^{-1}, \tag{D.5}$$

$$\Lambda = \int_0^\infty \rho(\tau)d\tau. \tag{D.6}$$

These correlation time scales were calculated for each 10-minute interval where $\overline{u} > 0.8$ in Figure 3.5. The average correlation length scales are shown, though Figure 3.5 clearly shows intervals with much higher λ and Λ than the mean. Using Taylor's frozen turbulence hypothesis with the mean horizontal velocity and Λ for each 10-min segment, the average correlation length scale is 11.6 m, with the longest correlation equivalent to 81 m. Thomson et al. (2012) calculated a dominant length scale of $2-3$ times the water depth (average of $75\ m$) at Nodule Point from the “fractional” turbulence intensity, with a large spread.

Frequency Analysis: Structure Functions

Structure functions of each 10-minute interval with $\overline{u} > 0.8\ m\ s^{-1}$ were computed in order to study the relationship of correlation over the longer and shorter timescales, analogous to an energy spectrum. Structure functions are especially useful for problems with uneven measurements in space or in time, but they are used here with the even time-series of observations in order to directly relate to the correlation time scales from the previous section. The second-order temporal structure function is defined as (Webb, 1964)

$$D(\tau,t) = \overline{\left[u\left(t\right) - u\left(t+\tau\right)\right]^2}, \tag{D.7}$$

which has a slope (γ_D) that is related to the slope of the energy spectrum (γ_E) by

$$\gamma_D = -\gamma_E - 1. \tag{D.8}$$

This relationship can be used to define the energy spectrum of simulated turbulence used as input into a computational fluid model of a turbine. Structure functions provide spectral information about a range of timescales, as opposed to λ and Λ which provide single correlation scales. Spatial structure functions have also been used to infer energy dissipation rates, as done in Wiles et al. (2006) and Thomson et al. (2012).

Figure D.3 compares the temporal structure function of the horizontal (top) and vertical (bottom) velocities from the Nodule Point ADV. For easier comparison, the solid line in the horizontal structure function plot is the median of the vertical structure functions, and vice versa. The slope of nearly $\gamma_D = 2/3$ seen in both directions up to a time scale in the $1-5\ sec$ range matches the scaling theory of three-dimensional, isotropic turbulence from Kolmogorov (1941). The structure function slope of $\gamma_D = 2/3$ is equivalent to the frequency spectral slope of $f^{-5/3}$. The structure function median in one direction is almost always outside of the 25th percentile of the other direction's structure function (see solid lines on each plot), exhibiting the preference for larger horizontal velocity covariance at these time scales. At first glance, this difference in amplitude between the vertical and horizontal velocity structure functions seems to suggests that the covariances are not isotropic, but McCaffrey et al. (tion) show that the transformation from frequency to temporal space introduces an integration constant that may explain the offset in structure function amplitude seen here. Thus, only the slope of the structure function is meaningful in this context, not the magnitude. A slight flattening occurs on the vertical structure function at about 3 *sec* that does not occur in the horizontal structure function. This supports the results of Thomson et al. (2012) for frequency spectra with 5-minute windows, which exhibit isotropy from $1 - 10$ *sec* scales. At lower frequencies, the vertical spectra flatten out, showing the large-scale anisotropy. A random phase signal has a structure function slope of 0, suggesting that over the longest timescales vertical velocities are not associated with a turbulent cascade. Note that the $\gamma_D = 2/3$ slope of these structure functions (and the related kinetic energy spectrum slope) is *not* a unique indicator of an energy cascade in three-dimensional turbulence –indeed the inverse energy cascade in two-dimensional turbulence of Kraichnan (1967) would also follow $\gamma_D = 2/3$. Consistency of the structure function with Λ is indicated by the point where the structure functions flattens out being on the order of the average integral scale from Figure 3.5.

Intermittency from Probability Density Functions

The flow diagnosis reveals distinctions among different 10-minute intervals, which likely extends to turbulence intermittency. A useful tool used to analyze turbulent behavior is the velocity difference probability density function (pdf), which can quantify the intermittency of turbulence (e.g. coherent structures and eddies). Comparing pdfs in each direction further uncovers the anisotropy. Gaussian turbulence should manifest itself as a collection of velocity differences that are normally distributed for small differences, with intermittent events

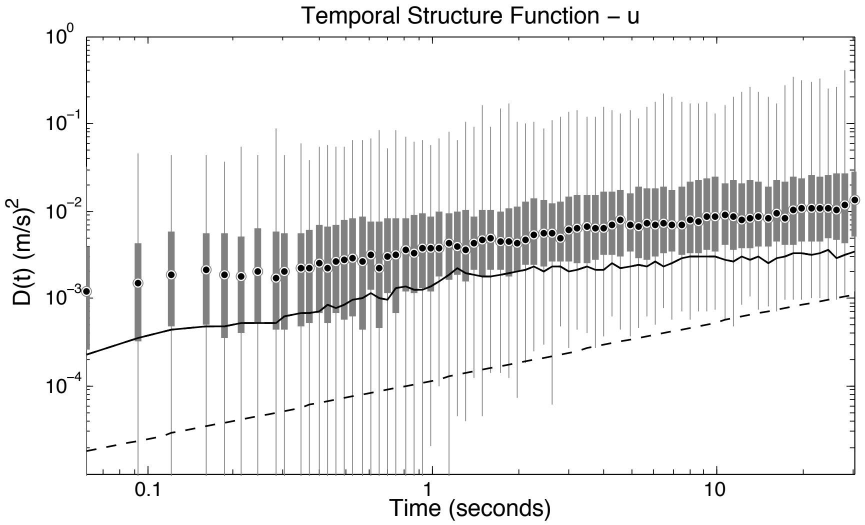

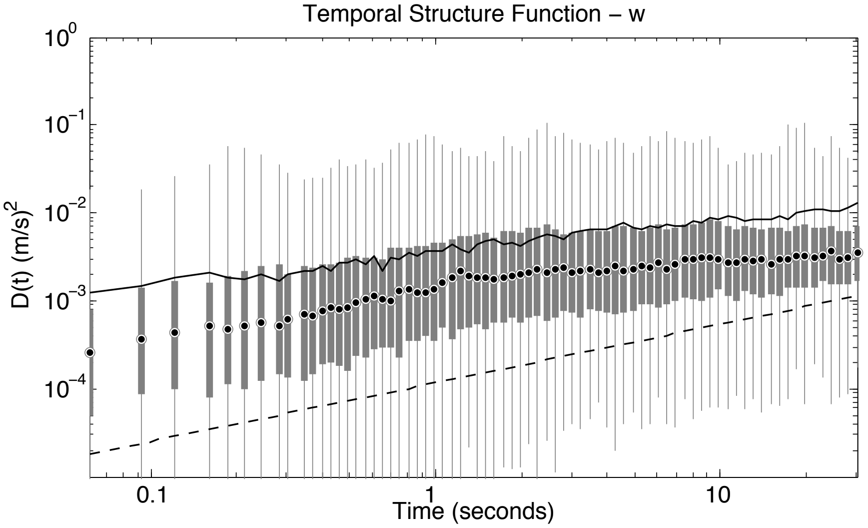

Figure D.3: Box plots of the second-order temporal structure functions for each 10-minute interval with an $\overline{u} > 0.8\ m\ s^{-1}$ of the Nodule Point ADV data. Top plot is the horizontal velocity structure function and the bottom is the vertical velocity structure function. For comparison, the solid line on the horizontal structure functions shows the median of the vertical velocity structure functions, and the line on the vertical structure functions shows the median of the horizontal velocity structure functions. White circles are the median, the boxes show the 25th-percentile, and the vertical lines include the entire range. The dotted line is a guideline with slope of 2/3.

appearing as deviations from Gaussian distributions in the tails (Frisch, 1995). Although the small velocity differences in all pdfs shown in Figure 3.6 do follow the Gaussian curve (dashed lines), the strong departure from Gaussian in the tails indicates that there is a significant amount of intermittency in this flow.

Higher statistical moments were calculated for each velocity component (subscript i) also in 10-minute intervals (mean, variance, skewness S, and kurtosis K, respectively) in order to provide more quantitative measures of intermittency. Moments of the u-velocity at Nodule Point are plotted in Figure 3.7. A purely random, Gaussian flow would have moments $S_i = 0$ and $K_i = 3$. It is clear from the skewness and kurtosis (shown here as deviations from Gaussian, $K - 3$) that many intervals deviate from normally distributed, random velocity perturbations. The departure from Gaussian in the pdfs expands consistently on the departure from 0 in the skewness and kurtosis (minus 3) in Figure 3.7. The differences between the pdfs of $\Delta u', \Delta v'$, and $\Delta w'$ highlight the anisotropic nature of this flow. The larger frequency in the tails of the pdf of $\Delta w'$ is the strongest sign of anisotropy.

A single observation at Nodule Point covers 1/32 of a second, so looking at velocity differences over slightly longer intervals will accentuate persistent features. Figure 3.6 compares the pdfs using $\Delta t = 1$ (1/32 sec), 115 (115/32 sec) and 230 (230/32 sec), corresponding to the smallest features captured by the ADV, and at 3 m and 6 m, which are potential half- and full-rotor diameters, assuming Taylor's hypothesis (with the overall average of the flow speed as the velocity scale). As the time interval increases, the intermittency increases for u and v velocities but decreases for w. Thus, as in the structure function analysis, horizontal velocities are more coherent on longer timescales than vertical, and now we may associate those correlations as well with intermittency. There is only a small difference in intermittency between the 3 and 6 m-scales, suggesting that the intermittent structures occur on a scale larger than the turbine rotor.

Tensor Invariant Anisotropy Magnitude

The metrics analyzed thus far indicate that turbulence at this location in the Puget Sound features anisotropy and coherence. However $CTKE$ is, like I_u, not a true scalar as it depends on the coordinate system chosen. In the case of CTKE, the dependence on coordinate system is not obvious, but direct calculation using this data and alternative coordinate system choices, such as a rotation of the u-v coordinates by 45^o, results in an altered value of CTKE. By aligning the u-velocity with the along-stream direction and w with the vertical as done here, one arrives at a unique definition of $CTKE$. However, the turbulent structures that arrive at the study location may observe coordinate-invariance symmetries not shared by $CTKE$ (e.g., non-horizontal planar or axial symmetries). Locations where the ebb and flood flow directions are not anti-parallel, are likely to cause inconsistencies in the interpretation of $CTKE$. Here we construct a quantity similar to CTKE, but formed from true scalars so that coordinate-independence is achieved.

The flow at Nodule Point has been determined to be anisotropic and to possess intermittent coherent structures. A coordinate-system-invariant metric of anisotropy in the presence of such structures is therefore desirable. A more detailed anisotropy analysis can be done using the anisotropy tensor (Lumley, 1978):

$$a_{ij} = \frac{\overline{u_i u_j}}{2k} - \frac{\delta_{ij}}{3}, \;\; k = \frac{\overline{u_i u_i}}{2}, \tag{D.9}$$

and its three principal invariants (I, II, III),

$$\begin{aligned} I &= a_{ii} \equiv 0 \\ II &= a_{ij} a_{ji} \\ III &= a_{ij} a_{in} a_{jn}, \end{aligned} \tag{D.10}$$

with a sum implied to occur over repeated indices (Einstein notation). Like the turbulent kinetic energy, k, these invariants are true scalars independent of coordinate system–they depend only on the symmetry, or lack thereof, of the turbulence itself. An analysis of the invariants II and III (since $I = 0$ by the definition of a_{ij}) provides a method of quantifying anisotropy in a turbulent flow and physically describing the departures from isotropy, independent of the chosen coordinate axis. Isotropic turbulence with uncorrelated orthogonal velocity fluctuations has the characteristic that $I = II = III = 0$, and deviations away from this point describe different turbulent regimes, as illustrated by the classical Lumley Triangle (Lumley and Newman, 1977). The next section illustrates an updated version of the Lumley Triangle due to Banerjee et al. (2007).

The coordinate-system invariant scalar magnitude of the anisotropy similar to the $CTKE$, denoted A, is constructed from the scalars II and k as

$$A = k\sqrt{II} \equiv \sqrt{\frac{1}{4}\left(2[\overline{u'v'}^2 + \overline{u'w'}^2 + \overline{v'w'}^2] + \overline{u'^2}^2 + \overline{v'^2}^2 + \overline{w'^2}^2\right)}. \tag{D.11}$$

This definition possesses the following attributes: 1) Like $CTKE$, $A = 0$ for isotropic, uncorrelated turbulence. 2) Like $CTKE$, A has the units of energy (k). 3) A tends to grow with $CTKE$, approaching a version of $CTKE$ formed from the time-averaged shear stresses as $CTKE \gg k$. 4) Like $CTKE$, A is real, and 5) unlike $CTKE$, A is a true, coordinate-independent scalar. The anisotropy magnitude, A, is therefore similar in meaning to the $CTKE$ in Equation D.3, though not identical because $CTKE$ is an instantaneous measure, and A uses the 10-minute means of the Reynolds stresses. This allows instrument noise to be removed through the averaging, while it acts to enhance $CTKE$. The anisotropy magnitude, A, is plotted at Nodule Point in Figure D.1c, exhibiting simultaneous, similar intermittent peaks as $CTKE$ between periods of low anisotropy. However, it is intriguing to note that the extreme occurrences of A do not always co-occur with those of $CTKE$ or I_u, as seen in Figures 2-4. Thus, we may conclude that neither I_u or $CTKE$ is a reliably coordinate-independent indicator of extreme turbulence or anisotropy, and that A accentuates the same features but in a quantitatively reliable manner.

Anisotropic Barycentric Map

Banerjee et al. (2007) introduce a visualization of anisotropy that contains additional information beyond A, based on the eigenvalues of the anisotropy tensor as opposed to the invariants. The "barycentric map" is a ternary diagram with vertices representing purely one-component (linear), two-component (planar), and three-component (isotropic) turbulence. This map is easier to read than the Lumley Triangle since the three turbulent states are equally spaced, and each have one point to represent them. The Cayley-Hamilton theorem proves that the eigenvalues may be found using only the tensor invariants (I, II, III) and *vice versa*. Thus like the invariants, the eigenvalues (and the barycentric map) are coordinate-independent (Cayley, 1858). The axis-symmetric and plain-strain limits are represented by straight lines on the barycentric map.

If the eigenvalues of the anisotropy tensor, a_{ij} are λ_1, λ_2 and λ_3, where $\lambda_1 \geq \lambda_2 \geq \lambda_3$, the coordinates of the barycentric map are

$$C_{1c} = \lambda_1 - \lambda_2, \tag{D.12}$$

$$C_{2c} = 2\left(\lambda_2 - \lambda_3\right), \tag{D.13}$$

$$C_{3c} = 3\lambda_3 + 1. \tag{D.14}$$

To plot on a Cartesian plane where the vertices of the barycentric map are (x_{1c}, y_{1c}), (x_{2c}, y_{2c}), and (x_{3c}, y_{3c}), the location of each point is

$$x_{new} = C_{1c}x_{1c} + C_{2c}x_{2c} + C_{3c}x_{3c} \tag{D.15}$$

$$y_{new} = C_{1c}y_{1c} + C_{2c}y_{2c} + C_{3c}y_{3c} \tag{D.16}$$

The barycentric map is shown in Figure 3.14, with four color schemes to be discussed in

Section D: turbulence intensity, I_u, $CTKE$, A, and $\sqrt{II}$. These results show that the vast majority of the flow is in the middle of the map, extending closer to the one- and two-component limits. The large empty space on the top part of the triangle highlights that this flow is never in the isotropic turbulent regime for scales between the sampling frequency and the 10-minute window.

The eigenvectors of the anisotropy tensor, when ordered, give the principal axes of the turbulence. In the one-component limit, the eigenvector associated with the largest eigenvalue orients the (linear) direction of the flow, and the plane made by the eigenvectors of the two largest eigenvalues describes the two-component turbulence. It is also possible to gain the directional information from Figure 3.3d and 3.3e to see which of the Reynolds stress components dominates the $CTKE$ signal. Consistency between these approaches derives from the close relationship between the Reynolds stresses and the anisotropy tensor.

Parameterization of Extreme Turbulence

A single parameter, or small set of parameters, to describe the turbulence at a particular location is desired for modeling and classification of tidal turbine locations. The turbulence intensity has been the parameter used, and only briefly has $CTKE$ been introduced to discuss coherence in a flow. Here, the metrics discussed in Section D are compared in order to identify the best parameter to characterize turbulence.

The 10-minute intervals with I_u, $\overline{CTKE}$, and A in the 99th percentile (when $\overline{u} > 0.8\ m\ s^{-1}$) are marked on most plots. The peaks in $CTKE$ do not appear as peaks in I_u or A, as seen clearly in Figure D.2, highlighting that these quantities correspond to different *kinds* of turbulent events that an analysis of only one quantity would miss. $CTKE$ peaks when two or more velocity components have large fluctuations, while I_u peaks with only one, differentiating between a shear stress and a linear stress. The differences in $\overline{CTKE}$ and I_u in Figures D.2 & 3.7 show that the turbulence intensity peaks occur during slow, near-slack tides. The anisotropy magnitude, however, sometimes peaks with I_u, and sometimes $\overline{CTKE}$. While all three quantities coincide with intervals with a large standard deviation in u', I_u appears in the highest peaks (since I_u is directly proportional to the standard deviation). All three quantities appear with kurtosis less than 3, representing a probability density function that is flatter than Gaussian, indicating intermittency.

The ability to parameterize coherence with I_u, $\overline{CTKE}$, and A is examined through regression analysis between each metric and λ and Λ. The resulting correlation coefficients are shown in Table D.1. The intervals with high I_u, A, and $\overline{CTKE}$ are associated with longer turbulent timescales λ and Λ (see Section D). However, quadratic regressions between I_u, and $\overline{CTKE}$ (most often used for this purpose; Jonkman (2009)) and λ or Λ do not yield statistically significant coefficients of determination (i.e., poor predictability). Thus, if we consider our long turbulent timescales to indicate coherent structures, then the extremal intervals do indicate the presence of coherent structures, but the metrics I_u and $\overline{CTKE}$ are not only a measure of coherence. However, the quadratic relationship between A and the Taylor scale, λ is very strong, with an R^2 value of 0.884. This relationship is plotted in Figure 3.13. $CTKE$ and A include more information about cross-correlations and directional variability than the turbulence intensity, so it is perhaps not surprising that they give a better physical description of the flow and a less noisy prediction of other measures of coherence in the turbulence, which is the goal of this study. The advantage of turbulence intensity over $CTKE$ and A is that directional velocity observations are not needed, only a current speed. However, without directional information, I_u is a poor predictor of coherence, and one should consider adding other measures of coherence, such as λ, in addition to I_u.

Understanding the intermittency of coherent structures is beneficial for predictions of loads on a turbine. Using A as a measure of coherence, supported by Figure 3.13, and comparing the larger A events ($A > 0.002$) to the total flow on a probability density function, the A events appear as smaller deviations from Gaussian in the tails (see figure 3.12). Although slightly counter-intuitive, this result suggests that within a single coherent structure,

Table D.1: Coefficients of correlation, R^2, between Taylor scale, λ, and Integral scale, Λ, and I_u, $\overline{CTKE}$, and A from the Nodule Point ADV data.

	λ	Λ
I_u	0.596	0.450
$\overline{CTKE}$	0.680	0.017
A	**0.884**	0.317

velocity differences are more Gaussian, but in differences spanning from one smaller-scale structure to the next, the intermittency appears. These results show that the coherent events at $\Delta t = 230$ samples, $\Delta x \sim 6m$ are nearly random in the u and v directions, but intermittent in the w direction. Again, the anisotropy seen in Figure 3.6 appears in the pdf differences in the three directions.

Anisotropy is an important feature that is potentially problematic to a turbine (introducing an uneven strain on the blades), and a characteristic that is not currently modeled, so the comparison between the measures of turbulence or coherence and anisotropy can give a much more accurate description of the flow. The three color schemes in Figure 3.9 highlight the differences between turbulence metrics and their relationships to anisotropy on the barycentric map. The extreme events in I_u, $CTKE$, and A occur on the edge of the scatter farthest away from the isotropic limit. The tendency in all three metrics is such that higher values often occur when the turbulence is most toward the one-dimensional limit, although the extreme events are distributed among the scatter in each variable.

The turbulence intensity exhibits a strong relationship with anisotropy, with high I_u events approaching the one-component limit. This shows that at this location, the strongest component of the turbulence is aligned in the along-stream direction that is used in the turbulence intensity. Not shown, but important to note, are the intervals during slack tides which fall closer to the lower lefthand corner of the barycentric map, closer to the one-component limit than the faster intervals. Since turbulence intensity increases with decreasing mean velocity, these results are in agreement, although it is counter-intuitive that the slack tides would exhibit one-component turbulent behavior more than the fast tides.

The color based on $\overline{CTKE}$ shows a much weaker relationship with anisotropy, with peaks in $\overline{CTKE}$ scattered throughout the map's domain. The anisotropy magnitude, A, is similar to $\overline{CTKE}$, as expected, but with a slightly stronger correlation in predicting the dimensionality of the turbulence. By analyzing $\sqrt{II}$, which contributes to A, the relationship between II and the one-component limit becomes evident. The fact that A does not follow this behavior indicates that k, the turbulent kinetic energy in all three directions (as opposed to the single direction captured in the turbulence intensity), dominates the anisotropy at these scales; $\sqrt{II}$ is therefore a better metric for measuring anisotropy in the one-component limit. The correlation was calculated between $\sqrt{II}$ and the correlation time scales, Λ and λ, with resulting correlation coefficients of 0.601 and 0.436 respectively. While the correlation between $\sqrt{II}$ and Λ is larger than the other metrics, $\sqrt{II}$ and λ is much lower than the strong correlation between A and λ.

When comparing $\overline{CTKE}$ and A in Figure 3.10, a very strong relationship exists (since A was derived to be the invariant form of $CTKE$), and the highest I_u, $\overline{CTKE}$ and A intervals all appear in the high end of the plot. This supports the use of A as opposed to $\overline{CTKE}$ in characterizing intense turbulent events since it similarly captures anisotropic, coherent events, but is a tensor invariant quantity better supported by turbulence theory than $\overline{CTKE}$. Since $CTKE$ has been demonstrated to correlate with turbine loading, and A is closely related, further studies must be conducted to determine whether the $\sqrt{II}$ (anisotropic turbulence) or the k (intense turbulence) factors of coherence turbulence measured by A are most closely related to loading.

The occurrence of one-component "turbulence" may be a sign that some residual of the tidal flow itself continues to be categorized as "turbulence" using 10-minute averages–unfortunately some mixing of mean and turbulence is inevitable when Reynolds averaging is used in turbulent flows without clear scale separation.

Concluding Remarks

The tidal site of Nodule Point shows strong signs of turbulent events that are expected to impact tidal energy conversion devices. Some of these events have peaks in coherent turbulent kinetic energy, some have peaks in turbulence intensity, and most exhibit one-component anisotropic behavior. The presence of this type of turbulence means that a preferred direction to the loading events is to be expected, putting a particular orientation of strain on the turbine. In order to predict these impacts, an analysis of turbulence should include turbulence intensity, either in its traditional or coordinate-system invariant form (the ratio of the full TKE to the mean kinetic energy), and a measure of anisotropy. Both $CTKE$ and I_u are useful metrics for measuring turbulence, but when all three velocities are available, the coordinate-independent measures A, k, and the invariants or eigenvalues of the anisotropy tensor are a preferred physical description that include many details about the directions of the one- and two-components of the turbulence. Other measures of intermittency and coherence, such as the pdfs and structure functions, can be important diagnoses of the degree to which Kolmogorov-like scalings for turbulent cascades hold for the environment of interest.

The observed anisotropy at Nodule Point can possibly be attributed to the shallow depth that does not allow isotropy above scales larger than the water depth. In addition, two-dimensional turbulence may be created by topographic vortex shedding, which would produce an inverse energy cascade with a slope of $\gamma_D = 2/3$ as was observed here. However, high resolution surface measurements (e.g. SAR, HF radar, or ocean color) are necessary to confirm this hypothesis. Stratification is unlikely to be forcing the two-dimensional flow, since the tidal strait is well-mixed. Therefore, it is predicted that tidal straits in general will have two-dimensional turbulence at scales larger than their depth, although observations at more sites are needed to support this hypothesis.

A next step will compare the statistics of the observations to those of the output of turbulence simulators and turbine models. The observations show strongly that turbulence in this region is *not* isotropic, even outside of the peaks in turbulence metrics. Turbulence simulators like TurbSim create isotropic turbulence and then add on an optional coherence function (Jonkman, 2009). A comparison between the resulting loads and efficiencies for turbines in stochastic turbulence and turbulence created by a physical ocean model (like the Regional Ocean Modeling System of Shchepetkin and McWilliams (2005)) or large-eddy simulation (like the National Center for Atmospheric Research LES model of Sullivan et al. (1994)) for this location will identify the strengths and weaknesses of each type of model in an effort to improve modeling capabilities for turbine design. Thyng et al. (2013) compare these ADV records and related observations in this region to a simulation using ROMS. Their results indicate that the large scale flow is adequately simulated, but the subgrid parameterizations in their implementation are unable to fully reproduce the characteristics of the observed turbulence. They propose extensions to these parameterizations that can be used diagnostically and can guide future parameterization improvements.

Additional complexity in real-world turbulence at this and similar sites may be hidden in this analysis by the assumption of Taylor's frozen turbulence hypothesis. Several statistics calculated here utilized this hypothesis to estimate spatial information from temporal data. In order to relax that assumption, measurements in time *and* in space are necessary. An array of ADVs can provide the spatial resolution, improving with the number of locations collecting simultaneous observations. Undoubtedly, new insight into the coherent, intermittent in time signals sensed here would result from information about their horizontal and vertical spatial coherence and intermittency.

Acknowledgments Thanks are due to Levi Kilcher of the National Renewable Energy Laboratory for his input. Also, the APL-UW staff for help in field data collection: Joe Talbert, Alex deKlerk, and Capt. Andy Reay-Ellers. And Brian Polagye (UW) and Marshall Richmond (PNNL) for experiment planning. JT was partially supported by DOE Northwest National Marine Renewable Energy Center. BF-K and PH are partially supported by NSF 1258907 and 0934737. KM is supported by the NOAA-ESRL/CIRES Graduate Research

Fellowship.

Appendix A

Time window choice

In decomposing the velocity signal into mean and perturbation, the goal is to capture the small-scale (in time and space) turbulent effects aside from the large-scale (in time and space) tidal effects. Taylor's hypothesis of the relationship between the time and length scales is assumed, which states that for a given turbulent velocity scale, $\hat{u}$, the time and length scales are related as L/T. This requires that for turbulence at larger spatial scales, a longer time scale is needed to capture the motions. With a goal of capturing the large, coherent structures in the tidal flow, the largest δt possible is desirous. However, the tidal signal impacts the flow at longer time scales, so a careful analysis was needed to separate the two.

The power spectrum of the along stream velocity in Figure **??**a shows significant peaks at very low frequency, and at tidal frequencies of 2 and 4 cycles per day (diurnal and semi-diurnal tides). Figure **??**b shows spectra of the along-stream velocity perturbation obtained through different time windows. With a 60-minute window, the tidal frequencies are still apparent, but with decreasing δt, the peaks decrease. By $\delta t =$ 5-minutes, the tidal signal is imperceptible.

Figure 1.3a shows a 10.5-hour segment of velocities with different δt means, and the resulting perturbations with 60, 30, and 20-minute δt are shown in Figure 1.3b and 10 and 5-minute intervals in Figure 1.3c. From these plots, it is clear that the 60, 30 and 20-minute averages are too long because a significant linear trend remains over the intervals where the tide is changing direction. That linear trend is therefore being included in the "turbulence," though it is actually the tidal signal. The 10- and 5-minute averages do not show this remaining signal.

The variance, σ, for each interval in the entire sample for different δt values was computed, and is shown in Figure 1.4. For the smallest values of δt, there are higher variances seen, with a decrease as δt increases to about $\delta t = 5$. Ignoring the outliers, the range of variances stays about constant until approximately $\delta t = 35$ when it increases again. Using this range of ideal δt values, as well as the information in Figure 1.3, the higher end of this range is known to be too large. Therefore, after this analysis, the interval length, δt, for the mean-perturbation decomposition was chosen to be 10 minutes. This captures the largest scales of turbulence without contaminating it with the tidal signal.

References

C. Legrand, Assessment of Tidal Energy Resource: Marine Renewable Energy Guides, European Marine Energy Centre, 2009.

R. Bedard, M. Previsic, O. Siddiqui, G. Hagerman, M. Robinson, Survey and characterization tidal in stream energy conversion (TISEC) devices, EPRI North American Tidal In Stream Power Feasibility Demonstration Project (2005).

S. T. Frandsen, et al., Turbulence and turbulence-generated structural loading in wind turbine clusters, Risø National Laboratory, 2007.

T. Mücke, D. Kleinhans, J. Peinke, Atmospheric turbulence and its influence on the alternating loads on wind turbines, Wind Energy 14 (2011) 301–316.

K. Kaiser, W. Langreder, H. Hohlen, J. Højstrup, Turbulence correction for power curves, in: Wind Energy, Springer, 2007, pp. 159–162.

E. Rareshide, A. Tindal, C. Johnson, A. Graves, E. Simpson, J. Bleeg, T. Harris, D. Schoborg, Effects of complex wind regimes on turbine performance, in: Scientific Proceedings. American Wind Energy Association Windpower Conference, 2009.

IEC, Iec 61400-1: Wind turbines part 1: Design requirements, International Electrotechnical Commission (2005).

M. M. Hand, N. D. Kelley, M. J. Balas, Identification of wind turbine response to turbulent inflow structures, in: Proceedings of the 4th ASME JSME Joint Fluids Engineering Conference, Renewable Energy Symposium, 2003, pp. 6–10.

H. J. Sutherland, Inflow and the fatigue of the list wind turbine, in: 2002 ASME Wind Energy Symposium, 2002, pp. 427–437.

D. L. Elliott, J. Cadogan, Effects of wind shear and turbulence on wind turbine power curves, Technical Report, Pacific Northwest Lab., Richland, WA (USA), 1990.

S. Gooch, J. Thomson, B. Polagye, D. Meggitt, Site characterization for tidal power, in: OCEANS 2009, MTS/IEEE Biloxi - Marine Technology for Our Future: Global and Local Challenges, 2009, pp. 1 –10.

J. Epler, B. Polagye, J. Thomson, Shipboard acoustic Doppler current profiler surveys to assess tidal current resources, in: OCEANS 2010, IEEE, 2010, pp. 1–10.

B. Polagye, J. Thomson, Tidal energy resource characterization: methodology and field study in Admiralty Inlet, Puget Sound, WA (USA), Proceedings of the Institution of Mechanical Engineers, Part A: Journal of Power and Energy 227 (2013) 352–367.

J. Thomson, B. Polagye, M. Richmond, V. Durgesh, Measurements of turbulence at two tidal energy sites in Puget Sound, WA, IEEE Journal of Ocean Engineering 37 (2012) 363–374.

J. Thomson, L. Kilcher, M. Richmond, J. Talbert, A. deKlerk, B. Polagye, M. Guerra, R. Cienfuegos, Tidal turbulence spectra from a compliant mooring, in: Proceedings of the 1st Marine Energy Technology, Symposium (METS2013), 2013.

B. Gunawan, V. Neary, J. Colby, Tidal energy site resource assessment in the east river, ny (usa), Renewable Energy (in revision) (In revision).

J. Jonkman, L. Kilcher, Turbsim user's guide: Version 1.06. 00, Golden, CO: National Renewable Energy Laboratory (2012).

A. Ragheb, M. Ragheb, Wind turbine gearbox technologies, in: Nuclear & Renewable Energy Conference (INREC), 2010 1st International, IEEE, 2010, pp. 1–8.

A. N. Kolmogorov, The local structure of turbulence in incompressible viscous fluid for very large Reynolds number, Dokl. Akad. Nauk. SSSR 30 (1941) 9–13.

E. Novikov, R. Stewart, The intermittency of turbulence and the spectrum of energy dissipation fluctuations (turbulence intermittency model to calculate spectrum of energy dissipation fluctuations), 1964. (1964).

J. Lumley, G. Newman, The return to isotropy of homogeneous turbulence, Journal of Fluid Mechanics 82 (1977) 161–178.

S. Banerjee, R. Krahl, F. Durst, C. Zenger, Presentation of anisotropy properties of turbulence invariants versus eigenvalue approaches, Journal of Turbulence 8 (2007).

G. I. Taylor, The spectrum of turbulence, Proceedings of the Royal Society of London. Series A-Mathematical and Physical Sciences 164 (1938) 476–490.

N. Kelley, R. Osgood, J. Bialasiewicz, A. Jakubowski, Using Time-Frequency and Wavelet Analysis to Assess Turbulence/Rotor Interactions, Technical Report, 19th American Society of Mechanical Engineers Wind Energy Symposium, 2000.

ISO 4354, Wind Actions on Structures, 1997.

B. Jonkman, TurbSim User's Guide: Version 1.50, Technical Report, National Renewable Energy Laboratory, 2009.

N. Kelley, B. Jonkman, G. Scott, J. Bialasiewicz, L. Redmond, The Impact of Coherent Turbulence on Wind Turbine Aeroelastic Response and Its Simulation, Technical Report, National Renewable Energy Laboratory WindPower Conference, 2005.

S. B. Pope, Turbulent flows, Cambridge University Press, Cambridge, 2000. URL: `http://www.loc.gov/catdir/description/cam0210/99044583.html`.

E. K. Webb, Ratio of spectrum and structure-function constants in the inertial subrange, Quarterly Journal of the Royal Meteorological Society 90 (1964) 344–345.

P. Wiles, T. Rippeth, J. Simpson, P. Hendricks, A novel technique for measuring the rate of turbulent dissipation in the marine environment, Geophysical Research Letters 33 (2006).

K. McCaffrey, B. Fox-Kemper, G. Forget, Estimates of ocean macro-turbulence: Structure function and spectral slope from argo profiling floats, In preparation to be submitted to Journal of Physical Oceanography (in preparation).

R. H. Kraichnan, Inertial ranges in two-dimensional turbulence, Physics of Fluids 16 (1967) 1417–1423.

U. Frisch, Turbulence: The Legacy of A. N. Kolmogorov, Cambridge University Press, Cambridge, 1995.

J. Lumley, Computational modeling of turbulent flows, Advances in Applied Mechanics 18 (1978) 123–176.

A. Cayley, A memoir on the theory of matrices, Philosophical transactions of the Royal society of London 148 (1858) 17–37.

A. F. Shchepetkin, J. C. McWilliams, The regional oceanic modeling system (ROMS): a split-explicit, free-surface, topography-following-coordinate oceanic model, Ocean Modelling 9 (2005) 347–404.

P. P. Sullivan, J. C. McWilliams, C.-H. Moeng, A subgrid-scale model for large-eddy simulation of planetary boundary-layer flows, Boundary-Layer Meteorology 71 (1994) 247–276.

K. M. Thyng, J. J. Riley, J. Thomson, Inference of turbulence parameters from a ROMS simulation using the k-ε closure scheme, Ocean Modelling (2013).

M. T. Stacey, S. G. Monismith, J. R. Burau, Measurements of reynolds stress profiles in unstratified tidal flow, Journal of Geophysical Research 104 (1999) 10933–10.

J. Thomson, B. Polagye, M. Richmond, V. Durgesh, Quantifying turbulence for tidal power applications, Institute of Electrical and Electronics Engineers (2010).

Appendix E

Justification for Rejection of ADCP Data for Turbulent Statistics

The ADCP used for this analysis is located at Admiralty Head. The site is $56m$ deep, and has maximum current velocity of $3.2m\ s^{-1}$ at the proposed hub-height of $8.1m$. The ADCP observations were taken from 9 May to June 11, 2011 at a sampling frequency of $1Hz$. The ADCP takes a vertical profile from $1.1m$ to $20.1m$ with $1m$ vertical resolution. The beam spread at hub height is $6.8m$. This may introduce substantial biased in the calculation of the velocities, since this diameter is more than a potential turbine diameter (!). All turbulent motions smaller than this width get averaged, smoothing out a significant amount of turbulence. This averaging prevents statistics like the autocorrelation from being calculated, since the most correlated, small-scale features are averaged over. The autocorrelations calculated from this data shown an immediate drop off, and integral and Taylor scales much smaller than this beam spread diameter, confirming the inability to use this statistic with these data.

In addition to the biases that averaging introduces, the inhomogeneity between beams prevents correlations between velocity components (Reynolds stresses) from being accurate. Stacey et al. (1999) acknowledged the need for a method of calculating Reynolds stresses and TKE from ADCP data without the bias from Doppler noise. They introduced a method that uses the raw, along-beam velocities instead of the three-components which require averaging across the beam spread area. With a four-beam ADCP with each beam aligned at angle, θ, from the vertical, the velocities can be computed as

$$\begin{aligned} u_1 &= v\ sin\theta + w\ cos\theta && \text{(E.1)} \\ u_2 &= -v\ sin\theta + w\ cos\theta && \text{(E.2)} \\ u_3 &= u\ sin\theta + w\ cos\theta && \text{(E.3)} \\ u_4 &= -u\ sin\theta + w\ cos\theta. && \text{(E.4)} \end{aligned}$$

This is an over-determined system that produces an "error velocity" that can be a check of homogeneity across beams (i.e., if w computed from beams 1 and 2 is not equal to w computed from beams 3 and 4, the flow is not homogeneous across beams, and the velocity is not acceptable). Using these definitions of the velocities, and a Reynolds decomposition (Equation 1.2) to get the perturbation velocities, the Reynolds stresses can be defined as

$$\begin{aligned} \overline{u'w'} &= \frac{\overline{u_3'^2} - \overline{u_4'^2}}{4sin\theta cos\theta} && \text{(E.5)} \\ \overline{v'w'} &= \frac{\overline{u_1'^2} - \overline{u_2'^2}}{4sin\theta cos\theta} && \text{(E.6)} \\ \overline{u'v'} &= \frac{\overline{u_1'^2} + \overline{u_2'^2}}{4sin\theta cos\theta} \text{ -or- } \frac{\overline{u_3'^2} + \overline{u_4'^2}}{4sin\theta cos\theta}. && \text{(E.7)} \end{aligned}$$

A comparison between the Reynolds stresses computed with the different definitions of w is shown in Figure E.1. The deviation away from the one-to-one line shows that there is considerable error, and therefore inhomogeneity between beams. This was a strong determining factor in the rejection of the ADCP data for computations of the Reynolds stresses, and subsequently, the anisotropy tensor and magnitude.

An additional problem with the ADCP is caused by the Doppler noise, rather than the beam spread. Thomson et al. (2010) showed the need to remove the noise (determined by the instrument's manufacturer) from the calculation of turbulence intensity, and even after

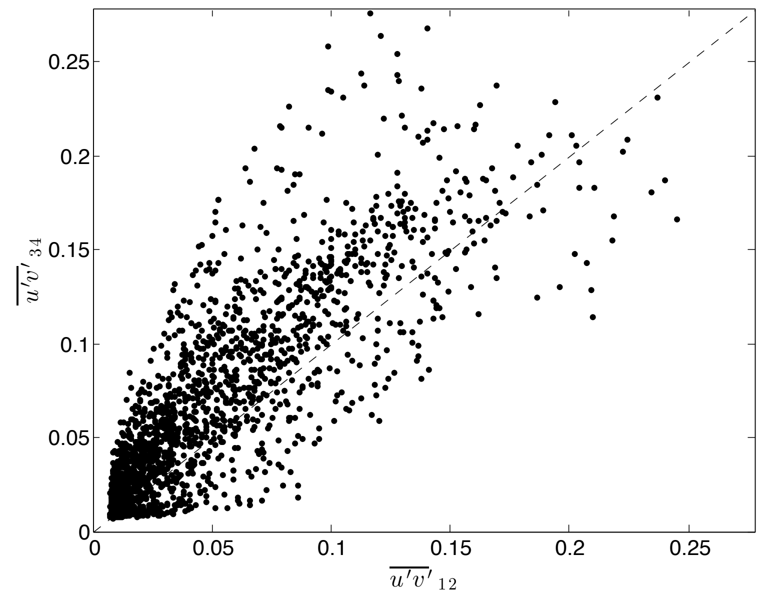

Figure E.1: Reynolds shear stress component, $\overline{u'v'}$, computed with w computed from beams 1 and 2 ($\overline{u'v'}_{12}$) and w computed from beams 3 and 4 ($\overline{u'v'}_{34}$). the dotted line shows the one-to-one relationship, and the solid line is the line fit to the data.

that was removed, an additional biased remained. The Doppler noise level of the Admiralty Head ADCP is $n = 0.112$, which also interferes with the calculation of the power spectrum and structure functions, which have magnitudes at and lower than the noise level.

Because of the large Doppler noise and beam spread that prevent calculated the autocorrelation, structure function, and anisotropy statistics from ADCP data, I determined that this dataset is not sufficient for characterizing turbulence as described in Chapter 3.